

An Ultracold Gas of Bosonic  
 $^{23}\text{Na}^{39}\text{K}$  Ground-State Molecules

VON DER FAKULTÄT FÜR MATHEMATIK UND PHYSIK DER  
GOTTFRIED WILHELM LEIBNIZ UNIVERSITÄT HANNOVER

zur Erlangung des Grades  
DOKTOR DER NATURWISSENSCHAFTEN  
– DR. RER. NAT. –

genehmigte Dissertation  
von

M.Sc. Kai Konrad VOGES  
Geboren am 02.01.1990,  
Gehrden

2020



1. Gutachterin: Prof. Dr. S. OSPELKAUS  
Institut für Quantenoptik,  
Leibniz Universität Hannover
2. Gutachter: Prof. Dr. K. HAMMERER  
Institut für Theoretische Physik und  
Institut für Gravitationsphysik  
(Albert-Einstein-Institut)  
Leibniz Universität Hannover
3. Gutachter: Prof. Dr. H.-C. NÄGERL  
Institut für Experimentalphysik und  
Zentrum für Quantenphysik,  
Universität Innsbruck

Tag der Promotion:  
26.10.2020



## Abstract

Ultracold bialkali polar molecules play a leading part at the frontline of quantum physics. They recently attract a lot of attention in the field of ultracold quantum chemistry, quantum many-body physics and quantum simulations. The key for their success is the rich internal level structure with rotational and vibrational degrees of freedom and their large electric dipole moments. Still, only a handful of molecular species are available at ultracold temperatures until now, although it is highly desirable to produce new molecular species to further expand the range of applications.

Besides direct laser cooling methods for molecules, the assembly of heteronuclear ground-state molecules from ultracold atomic mixtures is the most promising approach for the creation of polar molecules. It includes the formation of weakly bound Feshbach molecules from the diatomic mixture and the subsequent two-photon stimulated Raman adiabatic passage (STIRAP) transfer to the rovibrational ground state. This creation strategy has been successfully demonstrated for the first time in the pioneering experiments at JILA with ultracold  $^{40}\text{K}^{87}\text{Rb}$  molecules. Since then, only a few more molecular species from different alkali atoms have been created, namely  $^6\text{Li}^{23}\text{Na}$ ,  $^{23}\text{Na}^{40}\text{K}$ ,  $^{23}\text{Na}^{87}\text{Rb}$  and  $^{87}\text{Rb}^{133}\text{Cs}$ .

In this thesis, I report the successful creation of a new species of ultracold polar ground-state molecules:  $^{23}\text{Na}^{39}\text{K}$ .

Starting from an ultracold mixture of bosonic  $^{23}\text{Na}$  and  $^{39}\text{K}$  atoms, weakly bound molecules are created. For this purpose, a Feshbach resonance in a high angular momentum scattering channel is chosen, experimentally identified and characterized. Close to this resonance the weakly bound Feshbach molecules are formed using resonant radio frequency radiation.

For the two-photon ground-state transfer, a unique, highly specialized two-color laser system is designed and realized. It is used for one- and two-photon spectroscopy to identify the relevant transitions for the ground-state transfer. Based on the obtained data, a local model of the singlet-triplet mixed excited state manifolds is developed, with which the hyperfine structure and the magnetic field dependence is predicted with high accuracy.

According to these findings, a suitable pathway to a single hyperfine ground state is chosen considering selection rules and experimental conditions such as laser polarization and beam alignment. To precisely determine the two-photon resonance condition for STIRAP, electromagnetically induced transparency measurements are performed. The ground-state transfer is then performed using STIRAP. The experimental findings regarding the STIRAP are successfully supported theoretically by a model based on a five-level master equation.

The pure molecular gas shows evidence for two-body dominated loss mechanisms, such as sticky four-body collisions. The molecule-atom mixture of  $^{23}\text{Na}^{39}\text{K}+^{39}\text{K}$  reveals an unexpectedly low loss rate coefficient although sticky three-body collisions are assumed to occur. This behavior demands further investigations regarding different hyperfine collisional channels and magnetic field regions.

**Keywords** ultracold atoms and molecules, Bose gases, Feshbach resonances, Feshbach molecules, molecular spectroscopy, stimulated Raman adiabatic passage (STIRAP), polar molecules, ultracold collisions



# Contents

<b>1</b>	<b>Introduction</b>	<b>1</b>
1.1	Creation of Ultracold Polar Molecules . . . . .	5
1.2	The Thesis and its Framework . . . . .	8
<b>2</b>	<b>Feshbach Molecule Creation</b>	<b>11</b>
2.1	Creation of Weakly Bound Dimers . . . . .	11
2.2	Feshbach Molecules in Heteronuclear Atomic Mixtures . . . . .	14
2.3	P1: <i>Formation of ultracold weakly bound dimers of bosonic <math>^{23}\text{Na}^{39}\text{K}</math></i> . . . . .	19
<b>3</b>	<b>A Laser System for STIRAP</b>	<b>27</b>
3.1	Stimulated Raman Adiabatic Passage in a Molecular System . . . . .	27
3.1.1	A Three-Level $\Lambda$ -System . . . . .	27
3.1.2	Transfer Protocol . . . . .	29
3.1.3	Losses . . . . .	31
3.1.4	Constraints and Limits . . . . .	32
3.2	Construction of the Raman Laser . . . . .	34
3.2.1	High Finesse Reference Cavity . . . . .	37
3.2.2	Laser Light Generation . . . . .	43
3.2.3	Locking and Pulse Application . . . . .	55
<b>4</b>	<b>Optical Spectroscopy of the Excited and Ground States</b>	<b>63</b>
4.1	The Role of the Excited State . . . . .	63
4.2	Spectroscopy of NaK Molecules . . . . .	65
4.3	P2: <i>A pathway to ultracold <math>^{23}\text{Na}^{39}\text{K}</math> ground state molecules</i> . . . . .	67
4.4	Additional Results of the Excited States Spectroscopy . . . . .	76
<b>5</b>	<b>Ultracold Trapped <math>^{23}\text{Na}^{39}\text{K}</math> Ground-State Molecules</b>	<b>81</b>
5.1	STIRAP in Molecular Systems . . . . .	81
5.2	Ultracold Molecular Scattering Physics . . . . .	84
5.3	P3: <i>Ultracold Gas of Bosonic <math>^{23}\text{Na}^{39}\text{K}</math> Ground-State Molecules</i> . . . . .	87
<b>6</b>	<b>Conclusion and Outlook</b>	<b>99</b>
	<b>Bibliography</b>	<b>I</b>



# Chapter 1

## Introduction

Quantum mechanics is one of the most fundamental theories in physics. Atomic and molecular quantum experiments contribute a major part to its testing and understanding, thanks to their excellent controllability, particle scalability, and physical purity and simplicity. Recent experiments are able to create ultracold atomic ensembles with temperature in the pK regime [1]: the coldest temperatures mankind can engineer nowadays. In addition, a multitude of trapping geometries, from simple round confinement to advanced three-dimensional structures, can be realized. Moreover, scattering properties between the particles can be tuned in intensity and carried from the short to long-range realm, by adding dipole-dipole interaction (DDI). The versatility for those experiments is almost unlimited and can be adapted to many quantum mechanical problems.

The first idea to use radiative forces for the manipulation of the motion of sodium atoms sprouted in the 1970s by Hänsch and Schawlow [2]. The development and implementation of new techniques quickly proceeded during the next decades: Zeeman-deceleration [3], magneto-optical trapping (MOT) [4], optical molasses cooling [5], and forced evaporative cooling in magnetic and optical traps [6, 7]. The rapid progress peaked with the assignment of the Nobel prize in 1997 to Steven Chu, Claude Cohen-Tannoudji, and William D. Phillips “for [the] development of methods to cool and trap atoms with laser light” [8]. For all forthcoming quantum gas experiments these breakthroughs are the starting point for the preparation and manipulation of ultracold ensembles.

Since then, the field of ultracold matter yields the possibility to implement quantum mechanical systems and problems. Many more atomic species with different physical properties have been explored. To date, experiments are using alkali, earth-alkali, numerous lanthanides and transition metal atoms as well as atom combinations in mixtures.

Many experiments rely on the production of quantum-degenerate matter: Bose-Einstein condensates (BEC) [9] or quantum-degenerate Fermi gases [10]. For some atomic species, for example certain potassium isotopes [11], the background scattering properties are unfavorable and have to be changed to achieve this goal anyway. In the vicinity of Feshbach resonances, the interaction between the constituents is widely tunable by magnetic fields ranging from the non-interacting to the strongly correlated regime [12]. The tunability of ultracold quantum gases features a wide spectrum of observable quantum phenomena. Some highlights are the formation of self-bound quantum droplets in otherwise collapsing BECs [13, 14], quantum density fluctuations in an ideal superfluid for simulations of the expansion of the early universe [15] and solitonic excitations like vortices or planar solitons [16, 17].

The origin of Feshbach resonances, the coupling of atomic and molecular scattering channels, also features the fascinating possibility to enter into the physics of ultracold molecules. By applying adiabatic magnetic field ramps or resonant transfer schemes [12] molecule forma-

tion is conducted which makes it possible to study chemical reactions [18] and the BCS-BEC quantum phase transition [19, 20]. Even the existence of three-body Efimov bound states was proven [21].

Ultracold ensembles are also well suited for precision measurement applications. Matter wave interference experiments are used to build quantum sensors to measure accelerations or test the universality of free fall [22, 23]. In present days, the experiments extended to become standard technologies such as gravimeters and atomic clocks. To take one example, the SI unit definition of the time is given by a microwave transition in Cs atoms measured in a cold atom fountain [24]. Nowadays, new standard candidates which overpass the standard clock use optical transitions, such as the Sr lattice clock [25] and will replace the old time standard in the long term.

Another experimental extension on neutral atoms are optical lattices, adding periodic boundary conditions to the quantum gas. Interfering laser beams generate standing wave patterns, in which the ultracold atoms are confined, thus Hubbard models known from solid-state physics can be emulated. Integrating advanced techniques of high resolution quantum gas microscopy, single lattice sites can be imaged and manipulated individually [26, 27]. Another approach to manipulate the trap geometry are optical tweezers [28]. They give the opportunity to produce all kinds of exotic conditions, ranging from 1D chains to complex 3D arrays and enable their dynamic change.

The diversity of quantum gas experiments using neutral particles seems to be endless. Nevertheless, it can be further extended by additional long-range interactions, adding new knobs on the controllability and tunability to quantum gases. Especially the above mentioned anisotropic DDI

$$V_{\text{dd}}(r) = \frac{C_{\text{dd}}}{4\pi} \cdot \frac{1 - 3 \cos^2(\theta)}{r^3} \quad (1.1)$$

is of particular interest as it originates naturally from the dipole moments of certain particles. In Eq. 1.1, the constant  $C_{\text{dd}}$  represents the interaction strength of the dipoles and  $\theta$  and  $r$  define the angle and distance between the two dipoles, respectively.

In this regard, most commonly used dipolar systems are Rydberg atoms, highly magnetic atoms and polar molecules. All of them feature unique properties, such as the interaction strength  $C_{\text{dd}}$ , lifetimes and short-range interactions and exhibit a spectacular progress in the last years.

## Rydberg Atoms

Rydberg atoms possess a highly excited electronic state with principle quantum number  $n \gg 1$ , which locates the electron far away from its nucleus. This leads to several features, making Rydberg atoms unique [29]. The weakly bound electronic state is very sensitive to any distortions from external disturbances. On the one hand, this is challenging to account for, on the other hand, Rydberg atoms could be used as sensitive field sensor quantum devices, for example for electric fields [30].

The lifetime of the metastable excited state itself is about several  $100 \mu\text{s}$ . This is long compared to low- $n$  excitations, but is fairly small in contrast to the lifetimes of magnetic atoms or polar molecules [31].

Nevertheless, the dipole moment of Rydberg atoms outperforms the ones from atoms and molecules. In recent years, Rydberg atoms received notable attention, especially since the Rydberg blockade from dipolar interactions between two atoms was observed [32]. Hence,

entangling schemes for quantum information applications were shown between two neutral atoms [33] and recently between whole atom arrays [34]. The interaction also leads to the observation of Rydberg molecules [35], which emerge from a new type of chemical bonding.

## Magnetic Atoms

In contrast to Rydberg atoms, magnetic atoms provide a permanent dipole moment in their electronic ground states which leads to a very comfortable situation in terms of stability and lifetime of the ensemble. On the other hand, their magnetic dipole moments are fairly small. As they originate from the non-closed electronic shell structure, the magnetic dipole moments are in the order of the Bohr magneton  $\mu_B$ . To date, several atomic species have been cooled to quantum degeneracy, such as Cr [36], Dy [37], Er [38] and Tm [39] and trapping experiments for Ho [40] have been performed.

Due to their high mass and their fairly high dipole moments the group of lanthanides prove to be fruitful long-range interaction candidates and led to the observation of fascinating quantum many-body phenomena. For both, Er and Dy, the formation of dipolar droplets originating from quantum fluctuations was observed [41, 42]. The properties of these droplets were extensively studied, such as scissor modes [43] or phase transitions to macrodroplets [41]. In this respect, a dipolar striped state is strongly hinting towards the realization of supersolid states [44]. Excitingly, the supersolid state was realized for the first time in systems of Er and Dy [45, 46]. Moreover, in these dipolar systems, more promising experiments were realized, like the excitation spectrum of the roton quasiparticle [47] and anisotropic superfluid behavior in a dipolar condensate [48]. Nevertheless, for those experiments the dipolar length scale  $a_{dd} = C_{dd}m/12\pi\hbar$  has to reach the short-range interaction length which is typically done by reducing the atomic short-range scattering length  $a$  drastically. Effects which require a strong dipole interaction, such as applications in an optical lattice, for example, where the long-range dipolar length has to be in the order of the lattice spacing, are hardly accessible with dipolar atoms. In this case ultracold polar ground-state molecules are advantageous.

## Bialkali Polar Molecules

The stepping stone for the creation of bialkali polar ground-state molecules are dual-species quantum gas experiments, where alkali atoms are assembled to weakly bound molecules and subsequently transferred to the ground state; for more details see Sec. 1.1. For heteronuclear bialkali molecules there are ten different molecular species available: LiNa, LiK, LiRb, LiCs, NaK, NaRb, NaCs, KRb, KCs and RbCs, all composed from the 5 different stable alkali metal atomic species; see Fig. 1.1, namely  ${}^6,7\text{Li}$ ,  ${}^{23}\text{Na}$ ,  ${}^{39,40,41}\text{K}$ ,  ${}^{85,87}\text{Rb}$  and  ${}^{133}\text{Cs}$ . Due to the different isotopes for the alkali metal atoms, some molecules have several isotopologues, which add up to in total 31 different heteronuclear molecules. In recent years just a handful of different ground-state molecules have been created, which are the fermionic  ${}^{40}\text{K}{}^{87}\text{Rb}$  [49],  ${}^{23}\text{Na}{}^{40}\text{K}$  [50] and  ${}^6\text{Li}{}^{23}\text{Na}$  [51] and the bosonic  ${}^{87}\text{Rb}{}^{133}\text{Cs}$  [52, 53] and  ${}^{23}\text{Na}{}^{87}\text{Rb}$  [54]. These molecules feature unique properties, such as their high electric dipole moments, chemical (in)stability and collision properties.

The NaK molecules,  ${}^{23}\text{Na}{}^{39}\text{K}$ ,  ${}^{23}\text{Na}{}^{40}\text{K}$  and  ${}^{23}\text{Na}{}^{41}\text{K}$ , are a group of both, fermionic and bosonic chemically stable molecules. The only other species which provide this combination

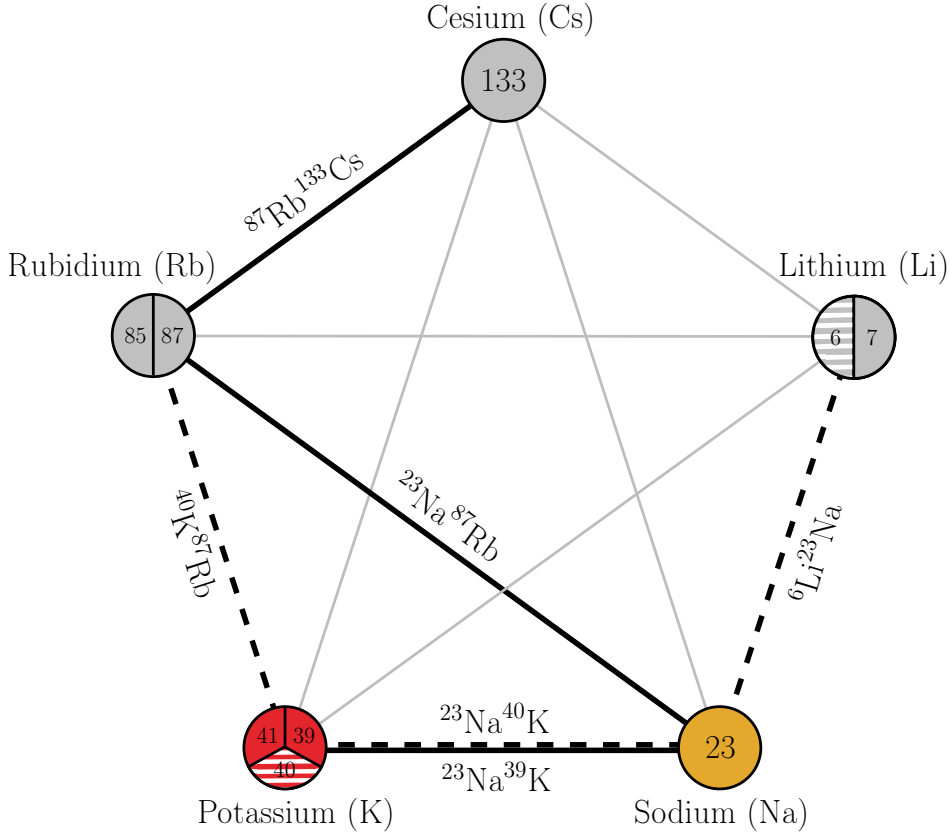


**Figure 1.1:** Summary of the possible bialkali molecule. This diagram shows the different combinations for bialkali molecules. Among the quintuple of stable alkali species (circles), K and Li are the only ones which possess fermionic (dashed filling) and bosonic (full filling) isotopes. The thick black lines indicate the already realized molecular species. Dashed lines show fermionic molecules, full lines show bosonic molecules. NaK is the only molecule available as both, fermion and boson. Thin gray lines represent missing combinations.

are the KCs molecules. NaK and KCs are therefore very interesting candidates in view of comparability. They can easily be compared to their counterparts with the respective other quantum statistics, or additionally to other molecular species with similar properties. The dipole moments of the different molecules differ a lot, from 0.65 D for LiNa over 2.76 D for NaK to 5.52 D for LiCs in their singlet ground states [55]. Even so, the interaction strengths of polar molecules are orders of magnitude higher than the ones of magnetic atoms and overcome the critical length scale  $a_{dd}$ , such as lattice spacing easily. Some molecules, for example LiNa, KRb and LiCs, suffer from chemical instability originating from atom exchange reactions [56]. The most prominent example is the KRb molecule, where chemical reactions were limiting the lifetime of the trapped ensemble [57]. The reaction takes place, when two molecules get close to each other. To prevent this, and therefore control the reaction kinetics, several approaches were proposed and realized. By polarizing the molecules using DC electric fields the anisotropic dipole-dipole interaction (DDI) between the molecules is introduced. In head-to-tail collisions, the DDI is attractive whereas in side-to-side collisions the DDI is repulsive. This leads to the appearance of a centrifugal barrier for higher partial waves which alter the collision dynamics according to the collisional entrance direction relative to the applied electric field [58, 59]. Similarly, resonant microwave radiation between rotational states introduces a dipole moment, which should also lead to shielding in molecular collisions [60, 61]. Moreover, collisions can be prevented by loading the molecules into

individual sites of an optical lattice. For an even more elaborate approach, molecules can be directly created in the optical lattice which can lead to a higher creation efficiency and filling fraction of the lattice as it was done in the case of KRb ground-state molecules [62] and RbCs Feshbach molecules [63]. With the molecules in the lattice, fascinating prospects for quantum simulations with spin-exchange models arise [64, 65]. On the other hand, collisions of ground-state molecules lead to the formation of four-body complexes. In a photoionization study on ultracold fermionic KRb the formation of these long-lived collision complexes has been directly observed [66]. Similarly, in nonreactive bosonic RbCs ensemble evidence on sticky collisions has been found [67]. Recently, the excitation of the four-body complexes by the trapping light was observed by applying stroboscopic optical trapping conditions [68–70], which opens a completely new research field towards ultracold four-body compounds. Lately, the creation of a quantum degenerate ensemble of fermionic ground-state molecules of KRb has been reported [71]. This marks a milestone in the preparation of ground-state molecules and shows the feasibility to prepare molecular gases with the same quality as it is standard for atomic gases. To date, a bosonic degenerate gas of heteronuclear molecules is still missing. Nevertheless, recent success on sympathetic cooling of fermionic LiNa molecules with  $^{23}\text{Na}$  atoms [72] may suggest to apply a similar technique for a bosonic molecule, as it might be possible for  $^{23}\text{Na}^{39}\text{K}$ .

## 1.1 Creation of Ultracold Polar Molecules

Cold and ultracold polar molecules can be created in mainly two different ways, by direct cooling or by assembling the molecules from an ultracold atomic quantum gas mixtures.

The first approach is under current investigations in many research groups where laser cooling and evaporation techniques known for atoms are applied to molecules. Indeed, molecules feature a much richer and more complicated level structure than atoms which makes the entire cooling process more challenging and technically laborious.

The second approach, the assembly of ultracold molecules, is a well known and established procedure; see Fig.1.2. Nevertheless, the molecule creation for any atom mixture combination is vastly unique and requires a detailed investigation and understanding, which is represented by the 0<sup>th</sup> step in Fig.1.2. On top of that, the basis for any molecule assembly is a dual-species quantum gas apparatus which is by itself a technical and operational expense. The assembly process for polar ground-state molecules follows the pathway originally shown for the first time at JILA for fermionic  $^{40}\text{K}^{87}\text{Rb}$  molecules [49]. It consists of two major parts, namely the creation of weakly bound molecules (commonly known as Feshbach molecules) [12]; see Fig. 1.2, 1<sup>st</sup> step, and the subsequent transfer of these molecules to their ground state by using a STImulated Raman Adiabatic Passage (STIRAP) [73]; Fig. 1.2, 3<sup>rd</sup> step. For the detailed knowledge of all the involved states during Feshbach molecule creation and STIRAP extensive spectroscopic studies are needed in terms of magnetic field Feshbach studies and optical molecular spectroscopy; Fig. 1.2, 2<sup>nd</sup> step.

The first experiments on the creation of trapped ultracold weakly bound heteronuclear Feshbach molecules have been reported by Ospelkaus *et al.* [74] on fermionic  $^{40}\text{K}^{87}\text{Rb}$  in an optical lattice. Later, more findings have been reported by Klempt *et al.* (2008) [75] and Zirbel *et al.* (2008) [76] for bulk systems. Following these pioneering approaches, other atomic species combinations have been investigated:  $^6\text{Li}^{40}\text{K}$  (2010) [77],  $^{23}\text{Na}^{40}\text{K}$  (2012) [78],  $^6\text{Li}^{23}\text{Na}$  (2012) [79],  $^{87}\text{Rb}^{133}\text{Cs}$  (2013) [80],  $^{23}\text{Na}^{87}\text{Rb}$  (2015) [81].

From all of these weakly bound molecules, except for  $^6\text{Li}^{40}\text{K}$ , also ground-state molecules have been created by using STIRAP. For the STIRAP, excited states play a major role, so in-

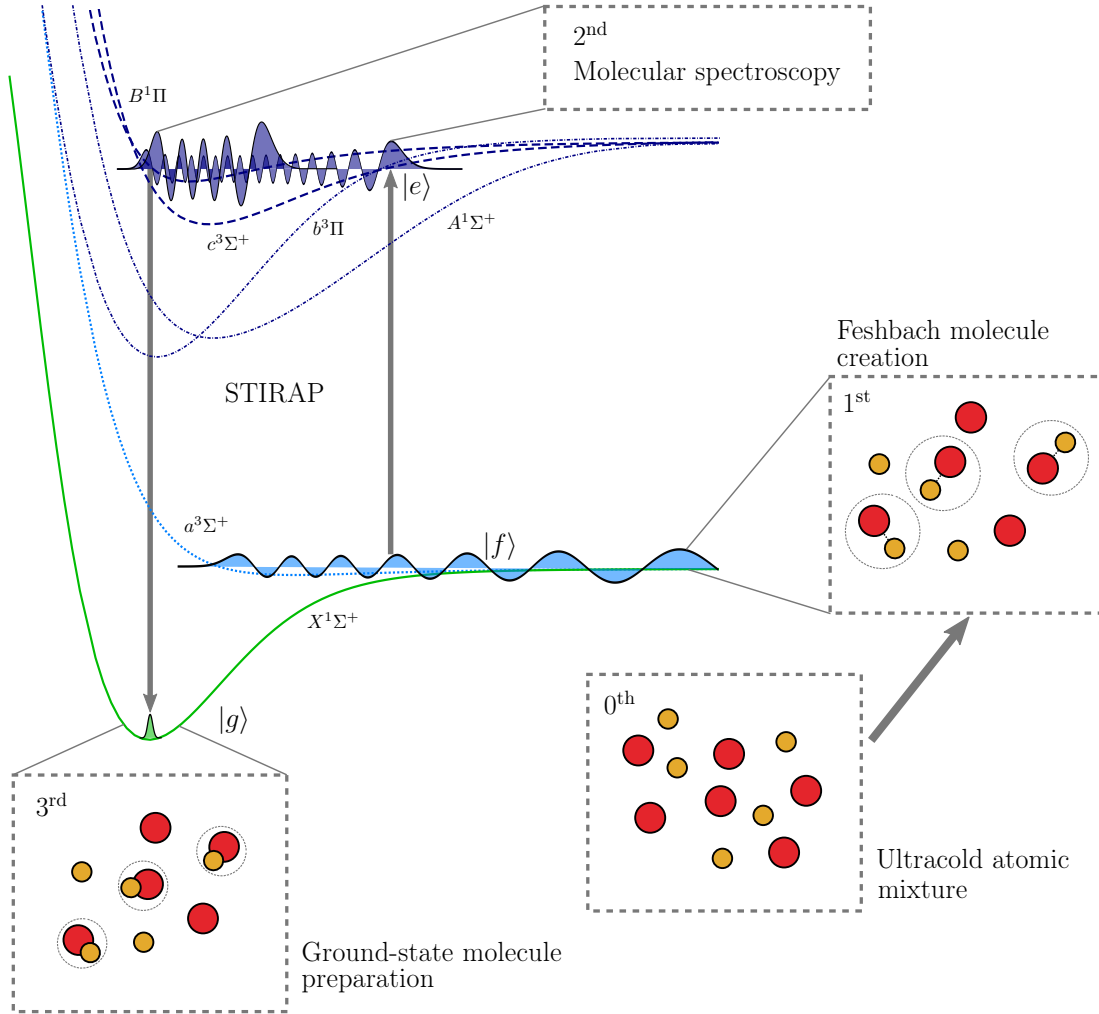


**Figure 1.2:** Molecule assembly process. In this picture, an overview of the alkali ground-state molecule assembly process from an ultracold atomic mixture is shown, orientated along the molecular potential energy curves. The entire process is analog to the original one for the  $^{40}\text{K}^{87}\text{Rb}$  molecules [49]. The essential steps (0<sup>th</sup> - 3<sup>rd</sup>) are labeled according to the succession of this thesis.

tensive spectroscopic studies have been performed to find the ideal pathway to the ground state. Typically, the spectroscopy is done starting from a Feshbach molecule state, searching for excited states and the ground state by utilizing loss measurements including dark resonance (Autler-Townes) and dark state (electromagnetically induced transparency, EIT) effects. The findings are reported for example for  $^{40}\text{K}^{87}\text{Rb}$  [49],  $^{23}\text{Na}^{40}\text{K}$  [82],  $^{23}\text{Na}^{87}\text{Rb}$  [83, 84] and  $^6\text{Li}^{40}\text{K}$  [85]. The excited states are chosen in a way that they provide a decent admixture of singlet and triplet character and therefore offer a good coupling strength to the mainly  $a^3\Sigma^+$  Feshbach molecule state as well as to the pure  $X^1\Sigma^+$  ground state. For the STIRAP in  $^{40}\text{K}^{87}\text{Rb}$  and  $^{23}\text{Na}^{40}\text{K}$  strongly coupled states from the  $c^3\Sigma^+$  and  $B^1\Pi$  potentials are used. In  $^{87}\text{Rb}^{133}\text{Cs}$  and  $^{23}\text{Na}^{87}\text{Rb}$  states from the  $A^1\Sigma^+$  and  $b^3\Pi$  potentials are utilized; see Fig. 1.2. For  $^{23}\text{Na}^{40}\text{K}$  molecules an alternative pathway is known [86], in which the STIRAP is performed by using states from the excited  $D^1\Pi$  and  $d^3\Sigma^+$  potentials. In case of  $^6\text{Li}^{23}\text{Na}$  a strong singlet-triplet coupling in the excited state is not necessary, because the ground-state molecule is prepared in the  $a^3\Sigma^+$  ground state and therefore the STIRAP does not rely on any singlet-triplet bridge. Recently, an alternative, pure singlet pathway for  $^6\text{Li}^{40}\text{K}$  have been

discovered [85], which starts from a singlet potential dominated Feshbach resonance making a detailed understanding of the excited states unnecessary. This approach is pioneering in the sense of simplicity for the STIRAP state transfer and may overcome issues like the weak coupling of the Feshbach molecule state to the excited state. On the other hand, STIRAP processes utilizing singlet-triplet coupled excited states are very well understood and established. For the  $^{40}\text{K}^{87}\text{Rb}$  molecule, for example [71], STIRAP was done within  $4\ \mu\text{s}$  and with efficiencies of about 90%. The singlet-pathway approach might be an interesting tool for upcoming molecules and may be extended to high angular momenta molecules.

## 1.2 The Thesis and its Framework

Within this thesis, I present the entire creation process for bosonic  $^{23}\text{Na}^{39}\text{K}$  ground-state molecules, from Feshbach molecule creation via molecular spectroscopy to ground-state molecule creation and first collisional investigations. Along the described creation process of Sec. 1.1 and Fig. 1.2, the work is divided into three main parts, where each part is based on a peer reviewed publication P1-3:

- Formation of weakly bound molecules and their characterization; Chap. 2, P1: [87]
- Spectroscopy for the identification of the excited and ground states; Chap. 4, P2: [88]
- STIRAP and collision studies of the ground-state molecule quantum gas; Chap. 5, P3: [89]

An additional chapter describes the construction and characterization of the two-color STIRAP laser system; see Chap. 3, which is a key element for molecular spectroscopy (Chap. 4) and ground-state molecule creation (Chap. 5).

My thesis work builds on a dual-species quantum gas apparatus which has been realized for ground-state molecule creation and the investigation of molecular quantum gases. Furthermore, it is based on the detailed investigation of scattering properties of the  $^{23}\text{Na}+^{39}\text{K}$  mixture and the first time realization of a dual-species quantum degenerate gas of  $^{23}\text{Na}$  and  $^{39}\text{K}$ . A large part of this preliminary work has also been done during my time as a PhD student and I contributed to this work (see the list of publication during my PhD time below). Details can be found in the PhD thesis of M. Gempel [90], T. A. Schulze [91] and T. Hartmann [92] and peer-review publications which I co-authored. In the following I briefly summarize their content. The list of publications is given below.

A description of the design and construction of the experiment is given in the PhD thesis of Matthias W. Gempel [90]. The design process includes a high-resolution single-atom single-site quantum gas microscope [93] and an advanced electrode system based on transparent ITO [94] for the molecule polarization.

In the thesis of Torben A. Schulze [91], the construction of the experimental apparatus as well as the preparation of dual-species Bose-Einstein condensate are described. Additionally, the scattering properties of the initial ultracold  $^{23}\text{Na}+^{39}\text{K}$  mixture have been investigated [95]. The description of the assembly of the main experimental apparatus is completed in the PhD thesis of Torsten Hartmann [92]. Moreover, intensive studies on the Feshbach resonance spectrum and scattering properties in different hyperfine spin mixtures of  $^{23}\text{Na}+^{39}\text{K}$  have been performed, which led to a new potential energy curve description of the  $^{23}\text{Na}^{39}\text{K}$  molecule [96], laying the headstone for the present thesis.

## List of publications

- M.W. Gempel, T. Schulze, T. Hartmann, **K.K.V.**, A. Zenesini, S. Ospelkaus, “*Versatile electric fields for the manipulation of ultracold NaK molecules*”, New J. Phys. **18** 045017, 2016 [94]
- T. Schulze, T. Hartmann, **K.K.V.**, M.W. Gempel, A. Zenesini, E. Tiemann, S. Ospelkaus, “*Feshbach spectroscopy and dual-species Bose-Einstein condensation of  $^{23}\text{Na}$ - $^{39}\text{K}$  mixtures*”, Phys. Rev. A **97** 023623, 2018 [95]
- T. Hartmann, T. Schulze, **K.K.V.**, P. Gersema, M.W. Gempel, E. Tiemann, A. Zenesini, S. Ospelkaus, “*Feshbach resonances in  $^{23}\text{Na}$ + $^{39}\text{K}$  mixtures and refined molecular potentials for the NaK molecule*”, Phys. Rev. A **99** 032711, 2019 [96]
- M.W. Gempel, T. Hartmann, T. Schulze, **K.K.V.**, A. Zenesini, S. Ospelkaus, “*An adaptable two-lens high-resolution objective for single-site resolved imaging of atoms in optical lattices*”, Rev. Sci. Instrum. **90**, 053201, 2019 [93]
- **K.K.V.**, P. Gersema, T. Hartmann, T. Schulze, A. Zenesini, S. Ospelkaus, “*A pathway to ultracold bosonic  $^{23}\text{Na}^{39}\text{K}$  ground state molecules*”, New J. Phys. **21** 123034, 2019 [88]
- E. Tiemann, P. Gersema, **K.K.V.**, T. Hartmann, A. Zenesini, S. Ospelkaus, “*Beyond Born-Oppenheimer approximation in ultracold atomic collisions*”, Phys. Rev. Res. **2** 013366, 2020 [97]
- **K.K.V.**, P. Gersema, T. Hartmann, T. Schulze, A. Zenesini, S. Ospelkaus, “*Formation of ultracold weakly bound dimers of bosonic  $^{23}\text{Na}^{39}\text{K}$* ”, Phys. Rev. A **101** 042704, 2020 [87]
- **K.K.V.**, P. Gersema, M. Meyer zum Alten Borgloh, T. Schulze, T. Hartmann, A. Zenesini, S. Ospelkaus, “*Ultracold Gas of Bosonic  $^{23}\text{Na}^{39}\text{K}$  Ground-State Molecules*”, Phys. Rev. Lett. **125** 083401, 2020 [89]



## Chapter 2

# Feshbach Molecule Creation

This chapter summarizes the  $^{23}\text{Na}^{39}\text{K}$  Feshbach molecule creation from a dual-species quantum gas mixture of  $^{23}\text{Na}$  and  $^{39}\text{K}$  atoms. First I will introduce the important concept of the Feshbach resonance and detail the creation techniques for the preparation of weakly bound Feshbach molecules close to such a resonance; see Sec. 2.1. Then I will explain the challenges of Feshbach molecule creation in heteronuclear mixtures and describe the basis for the  $^{23}\text{Na}+^{39}\text{K}$  mixture and the selection of a suitable Feshbach resonance; see Sec. 2.2.

The successful creation of  $^{23}\text{Na}^{39}\text{K}$  Feshbach molecules is then presented in the peer-reviewed publication P1: *Formation of ultracold weakly bound dimer of bosonic  $^{23}\text{Na}^{39}\text{K}$*  [87] in Sec. 2.3.

### 2.1 Creation of Weakly Bound Dimers

The assembly of ground-state molecules from ultracold atoms follows the pioneering experiments in 2008 of the JILA group [49]. It is including the two-photon Raman passage transfer of molecular populations between the ground state and the weakly bound molecular state and, prior to this, the weakly bound molecular Feshbach state preparation; see Sec. 1.1. The Feshbach molecule preparation is done by the association of two atoms from the atomic ensemble to a dimer, which are called Feshbach molecules. Creating Feshbach molecules prior to the ground state transfer has two major advantages.

First, the Feshbach molecules, in contrast to free colliding atoms, narrow the spread of the collisional wavefunction and locate a major part of it inside the molecular potential. This increases the two-photon transitions strength of the Raman process and makes the state exchange highly efficient. Second, the weakly bound molecule creation can itself reach high efficiencies. From experiments with degenerate atomic ensembles [71] or with optical lattice applications [62], the Feshbach molecule creation efficiency can exceed 50%, making the entire molecule creation process highly efficient.

#### Feshbach Resonances

The description of ultracold atomic scattering physics is done by using molecular potentials of the scattering particles. For two colliding atoms, the electronic molecular potential can be expressed as a potential energy  $V(R)$  dependent on the internuclear distance  $R$  of the two particles; compare Fig. 2.1. In the limit of very high internuclear distance the two atoms can be treated as unperturbed in their respective hyperfine states. At short range the underlying molecular potential alters the individual atomic behavior and governs the background scattering properties, which are typically expressed in terms of the scattering length  $a$ . A negative scattering length corresponds to attractive interaction, while a positive scattering

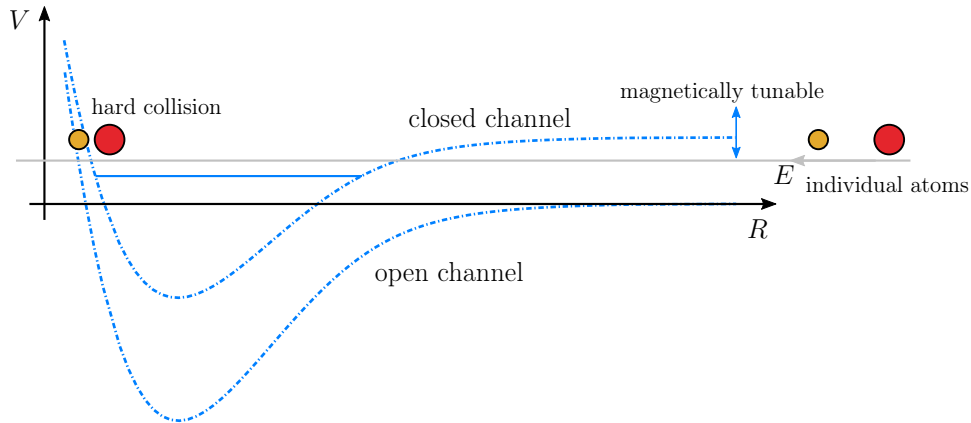


**Figure 2.1:** Sketch of involved molecular potentials in a Feshbach resonance. This picture shows a sketch for the understanding of the emergence of Feshbach resonances. Free atoms in a collisional process (red and yellow circles) experience the background scattering properties of the open channel. The relative energy difference between the diatomic scattering state (gray line) and the bound molecular state from the closed channel potential (horizontal blue line) can be tuned by a magnetic field. When the two energies match, a Feshbach resonance appears. The closed channel can be populated by sweeping the bound state across the diatomic scattering energy or by bridging the energy via rf/mw or an optical Raman transition; see Fig. 2.2. Energy scales are exaggerated. This representation is taken from [12].

length is a repulsive interaction; see Fig. 2.2.

The molecular potential itself supports several rotational and vibrational bound states. For Feshbach resonances and the creation process of weakly bound Feshbach molecules from free atoms, the least bound vibrational states of the molecular potentials are of interest.

When two individual free atoms collide, their total energy  $E$  is above the diatomic asymptotic molecular dissociation threshold. This scattering channel is called *open*, as the two atoms during their collision enter the molecular potential and leave it again; see Fig. 2.1. At the same time, other molecular potentials exist, which are associated with other hyperfine states of the atoms. A molecular hyperfine potential with a bound state close to the diatomic scattering energy of the atoms in the open channel is called *closed*; see Fig. 2.1. When the two electronic hyperfine potential couple to each other and the energies of the free atoms in the open channel and the bound state in the close channel match, a Feshbach resonance occurs. Typically, the energy of the hyperfine structure of atoms is magnetic field dependent. Therefore, the hyperfine structure of the molecular potentials and accordingly the vibrational bound states are also magnetically tunable. Thus, the energy match between the closed and open channel can be adjusted by magnetic fields and individual Feshbach resonances can be approached. This also changes the coupling between the open and closed channel and their admixture.

As a consequence for the atoms, the scattering length  $a$  can be tuned. At a Feshbach resonance, the scattering length exhibits a pole at the magnetic field  $B_0$ , where its absolute value approaches infinity but the sign flips between positive and negative. Close to the resonance, the scattering adapts to the background scattering length where on one side of the resonance the scattering length crosses zero at  $B'$ ; see Fig. 2.2 upper panel. The difference  $\Delta = B_0 - B'$  is often named the width of the resonance. For a more complete description of scattering theory and atomic Feshbach resonances refer to [12, 92].

Feshbach resonances are one of the most important tools in the field of ultracold atomic and molecular scattering physics [12]. The free tunability of the scattering properties allows

to investigate weakly and strongly correlated quantum gases [16, 17], to reach quantum degeneracy of several atomic species [11] and to enter molecular bound states [74], which also leads to the observation of BCS-BEC phase transitions [19, 20].

This preparation of molecular bound states is one of the important steps for the creation of ground-state molecules; compare Fig. 1.2, 1<sup>st</sup> step, and will be discussed in the following section.

## Creation Techniques

The key for preparing molecular states from ultracold atomic quantum gases are Feshbach resonances. At the position of the resonance, a molecular state and a diatomic one are crossing each other. Close to this resonance both states couple and create an avoided crossing; see Fig. 2.2 blue state in the lower panels in (a) and (b). On the positive scattering length side of the resonance, where the molecular state exists energetically below the diatomic dissociation threshold; see Fig. 2.2, the two atoms can enter the molecular state, when they are in a collision process with each other and change their energy accordingly.

This case can be used for the two main approaches for the creation of weakly bound molecules, the direct state transfer and the adiabatic creation through magnetic field ramps; see Fig. 2.2.

Magnetic field ramps utilize the avoided crossing of a Feshbach resonance. At the pole of a Feshbach resonance a molecular state enters from the continuum into an atomic scattering channel. The coupling between the two states as well as their differential magnetic moment dictate the width of the resonance [12]. The molecular state can be populated, when

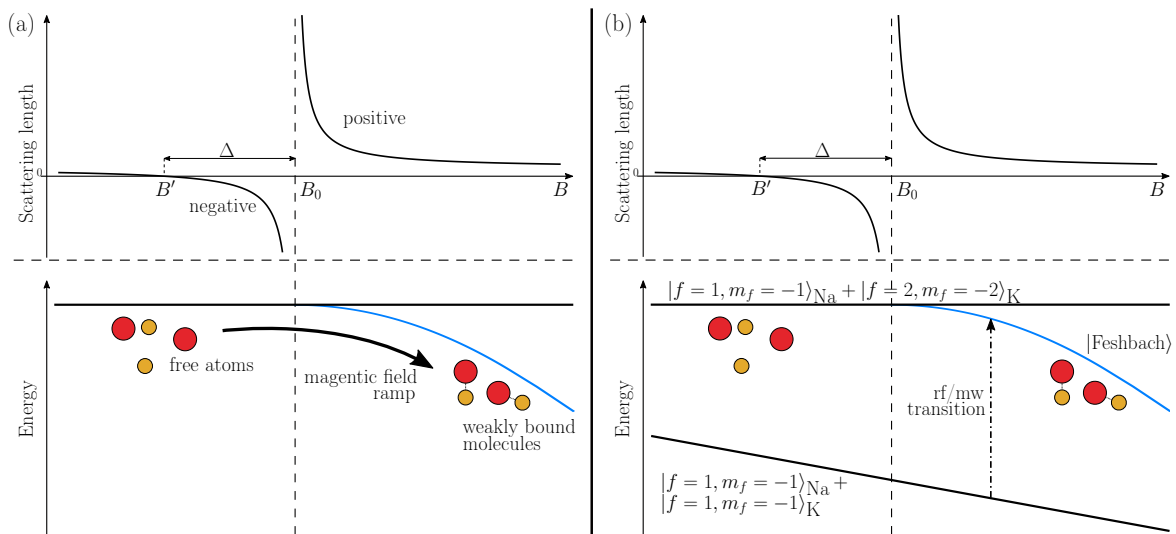


**Figure 2.2:** Sketch of possible ways for Feshbach molecule creation. (a) This picture shows the Feshbach molecule creation with a magnetic field ramp. Starting with free atoms in a prepared hyperfine state (black line lower panel) on the negative scattering length side of a Feshbach resonance with pole position  $B_0$  (upper panel), the magnetic field is swept across the resonance to the positive scattering length side. Atoms can follow the molecular state (blue, lower panel) and form weakly bound molecules. Labels are according to the text. (b) Feshbach molecules can also be associated by a direct transfer from free atoms (black line, lower panel) to bound molecules (blue line, lower panel) by radio frequency (rf) or microwave (mw) transitions (dashed-dotted arrow). Also possible are optical Raman transition, which are not shown here. The atomic and molecular states shown in this example are labeled as the ones actually used in [87].

the atomic gas is prepared on the negative scattering length side and the magnetic field is ramped adiabatically to the positive scattering length side across the resonance. Atoms, which experience a collision, follow their diatomic scattering state over the avoided crossing and end up in the molecular bound state. This method is commonly used for small-width Feshbach resonances, since long sweeps across a broad resonance would lead to strong atomic three-body losses from the increased scattering length value close to resonance; see upper panels of Fig.2.2(a). Therefore, a decently fast ramp across the resonance is needed. Moreover, a magnetic field ramp is fairly easy to implement in an experiment and makes the creation process reliable and robust.

Direct methods transfer atoms from an atomic scattering state to the molecular state by inducing a transition via resonant radiation. This can be done by magnetic field modulation, microwave (mw) and radio frequency (rf) application [12] and optical Raman transitions [98]. To utilize these approaches, the default scattering channel has to provide scattering properties allowing for a holding time of the atoms long enough to perform the creation process. In case of the magnetic field modulation, the initial state is the same as the one the Feshbach resonance is located in. For rf/mw and Raman association; see Fig.2.2(b), a different initial scattering channel is used. Besides, the transition linewidth for rf/mw is quite narrow, within several tenth of kHz, which prescribes the magnetic field to be stable. Depending on the atomic species and quantum states, this can be quite challenging. Therefore, often Feshbach resonances with a large width are used, because their involved molecular states change less drastically with respect to the magnetic field than resonances with a small width.

## 2.2 Feshbach Molecules in Heteronuclear Atomic Mixtures

Atomic quantum gas mixture experiments have to overcome several obstacles regarding the behavior of the different atomic species during the different stages of the experiment; see the for example [91, 92, 94]. Concerning heteronuclear Feshbach molecule creation, the challenges arise from the trap configuration and the inter and intra atomic scattering scenarios.

This section is dedicated to the restriction coming from the optical trap. It details different cases and possible solutions regarding the optical trap parameters and the resulting density distributions of the atoms as well as the creation rates. Furthermore, it summarizes the experimental basis of the atomic scattering scenario of  $^{23}\text{Na}$  and  $^{39}\text{K}$  and the envisioned Feshbach resonance.

### Trap Parameters and Density Distributions

For the creation of heteronuclear molecules from an atomic mixture, the density distribution in the trap and the atom number ratio between the two species are important. Molecule creation is most efficient when the density distributions overlap and thus the atom numbers of both species are equal. However, in a single-wavelength optical dipole trap both species experience different trapping conditions due to different dynamical polarizabilities and masses. Consequently, the number density distributions for the two species differ from each other and their spacial distributions do not overlap completely. To circumvent this, the atom number ratio can be adjusted to approach the optimal situation of similar averaged densities. Since the density distributions still have different width, an equal mean atom number can be reached by preparing a number imbalanced mixture.

Additionally, in cases of mixtures with a high mass ratio, such as Li + Cs or Na + Cs, the gravitational sag plays a major role. At low temperatures, especially close to or even at

quantum degeneracy and weak trapping potentials, the atomic clouds can separate in the direction of the gravitational field and reduce their spacial overlap, leading to a decreased molecule association efficiency. This can be compensated by a multi-color optical dipole trap or magnetic field gradients, which can cancel the effect of gravity between the species. Regarding spatial separation, phase separation due to unfavorable interspecies scattering lengths may be an obstacle, especially in the case of direct molecule association through rf/mw radiation; see Fig. 2.2(b), where the initial atomic state has to be prepared cautiously.

The trap parameters and the resulting density distributions of the atomic clouds have to be controlled and understood cautiously. In the following publication in Sec. 2.3 [87], the effect of the density distribution discrepancy for the  $^{23}\text{Na}+^{39}\text{K}$  mixture has been investigated. To maximize the molecule creation efficiency in the single-wavelength optical dipole trap an atom number imbalanced mixture towards  $^{23}\text{Na}$  has been prepared.

### Creation Rate

One other important parameter for the creation process is the lifetime of the created dimers. Feshbach molecules typically have very short lifetimes. For bosonic ensembles with relatively high densities, the lifetime can be of the order of ms. The lifetime is influenced by vibrational quenching of the molecules in molecule-molecule and molecule-atom collisions and is typically determined by the density of the molecular and atomic ensembles. After molecule creation it is therefore recommended to remove remaining atoms from the trap and remain with a pure molecular ensemble to suppress inelastic collisional processes as much as possible.

However, an atom removal is not possible during the molecule creation process. There, a competition between molecule creation and molecular loss due to collisions takes place. Thus, a strong dependence of the molecule creation efficiency on the density of the initial atomic ensembles is expected. For low atomic densities, the molecular association rate is very small and can easily be overcome by losses. A large atomic density results in a large molecular creation rate, however, also inelastic losses will increase. Thus, the largest molecular ensembles are expected to be created in the intermediate density regime.

In direct association through rf/mw radiation from a diatomic state to a weakly bound state (see Fig. 2.2(b)) a similar effect is expected to occur during the creation time dynamics. At a given atomic density and creation rate through the rf/mw radiation power the molecule density increases over time. While the molecule density rises, also the losses from collisions between the molecules and atoms increase due to the enhanced molecular density. Hence, the most efficient pulse duration for the rf/mw radiation is expected when the loss compensates the creation rate.

The creation rate determines the overall achievable molecule number. In the following publication in Sec. 2.3 [87], the time dynamics for a fixed rf/mw power and an optimized atom number imbalance have been investigated. The dynamics have been modeled by a set of differential equations for the molecule and atom number change. The model agrees with the experimental data.

### The Experimental Basis

Finally, a favorable Feshbach resonance has to be chosen. For the selection, the preceding work on a detailed understanding of scattering properties between  $^{23}\text{Na}$  and  $^{39}\text{K}$  in different spin channels and the detailed knowledge of the interaction potential between the two

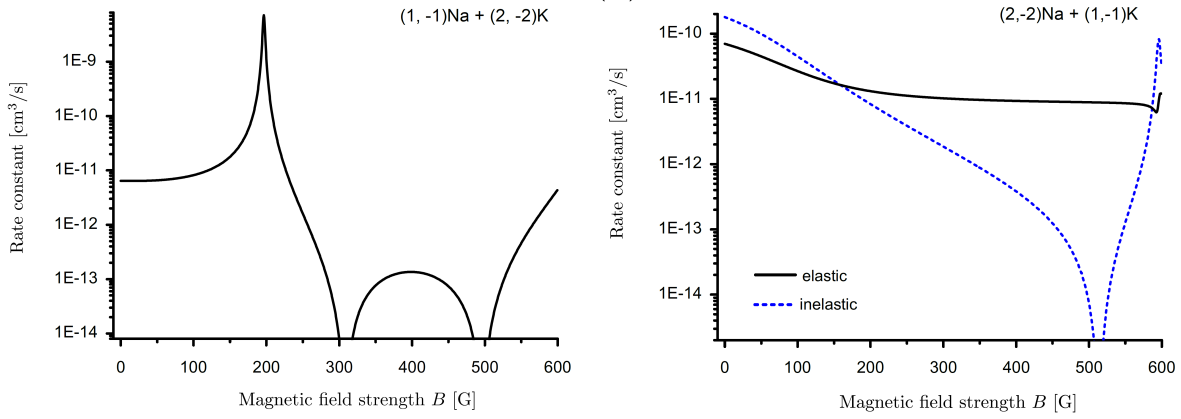


**Figure 2.3:** Prediction of the scattering rates for the  $M_F = -3$  scattering channels dependent on the magnetic field strength, provided by E. Tiemann using the refined potentials from [96]. (a)  $|F = 2, m_F = -2\rangle_{\text{Na}} + |f = 1, m_f = -1\rangle_{\text{K}}$  states, (b)  $|f = 1, m_f = -1\rangle_{\text{Na}} + |f = 2, m_f = -2\rangle_{\text{K}}$  states. The picture is taken from [92].

species are beneficial [95, 96].

In view of ground-state molecule creation, a scattering channel with very low or a very high total angular momentum is preferable, to also create ground-state molecules in a low or high spin state, respectively. Note that for singlet ground-state molecules only nuclear spins contribute, since the ground state is located in the singlet potential, where the electron spins pair up and do not contribute to the hyperfine structure.

Regarding the creation process itself, a small-width Feshbach resonance would be favorable, as in this case a simple magnetic field ramp would be applicable. From Hartmann *et al.* [96] it is known, that there are resonances with a small width in various spin channels, especially with a total angular momentum of  $M_F = 0, 1, 2$ . However, the ultracold ensemble is initially prepared in the  $|f = 1, m_f = -1\rangle_{\text{Na}} + |f = 1, m_f = -1\rangle_{\text{K}}$  state which has a total angular momentum of  $M_F = -2$ . Thus, to access one of the narrow Feshbach resonances would require at least two state transfers, during which atom losses are expected.

Broad resonances, on the other hand, are available in all possible spin channels of the  $^{23}\text{Na}+^{39}\text{K}$  mixture. For efficient Feshbach molecule creation and detection, a direct molecular state transfer scheme from the initial  $|f = 1, m_f = -1\rangle_{\text{Na}} + |f = 1, m_f = -1\rangle_{\text{K}}$  states (with  $M_F = -2$ ) into a  $M_F = -3$  channel (thus into one of the channels  $|f = 2, m_f = -2\rangle_{\text{Na}} + |f = 1, m_f = -1\rangle_{\text{K}}$  or  $|f = 1, m_f = -1\rangle_{\text{Na}} + |f = 2, m_f = -2\rangle_{\text{K}}$ ; see Fig. 2.3) is envisioned. First of all this scheme starts from the by default initialized channel, which can be long-lived and where the scattering properties at arbitrary magnetic fields are well known from the previous works [95, 96]; see Fig. 2.4. Second, the open channel of the target  $M_F = -3$  states contains always a stretched atomic state  $|f = 2, m_f = -2\rangle$  and thus allows for easy direct detection of Feshbach molecules in the target state by absorption imaging on the  $|f = 2, m_f = -2\rangle \leftrightarrow |f = 3, m_f = -3\rangle$  closed atomic transition.

Within the previous experiments, only Feshbach resonance in the  $M_F = -2, \dots, 2$  channels have been investigated [96]. However, from theory the scattering and Feshbach properties of the  $M_F = -3$  channels are known; see Fig. 2.3 [92]. The channel  $|f = 2, m_f = -2\rangle_{\text{Na}} + |f = 1, m_f = -1\rangle_{\text{K}}$  possesses high inelastic losses for any magnetic field and no Feshbach resonance up to a magnetic field of 600 G and is therefore unfavorable; see Fig. 2.3 (b). The other one, the  $|f = 1, m_f = -1\rangle_{\text{Na}} + |f = 2, m_f = -2\rangle_{\text{K}}$  state, features only elastic scattering and a Feshbach resonance with a very large width at roughly 200 G; see Fig. 2.3(a). Interestingly, the initial state combination yields decent scattering length for  $^{23}\text{Na}$  atoms ( $\approx 52 a_0$ ),  $^{39}\text{K}$  atoms ( $\approx -20 a_0$ ) and the  $^{23}\text{Na}+^{39}\text{K}$  mixture ( $\approx -110 a_0$ ) at that specific magnetic field

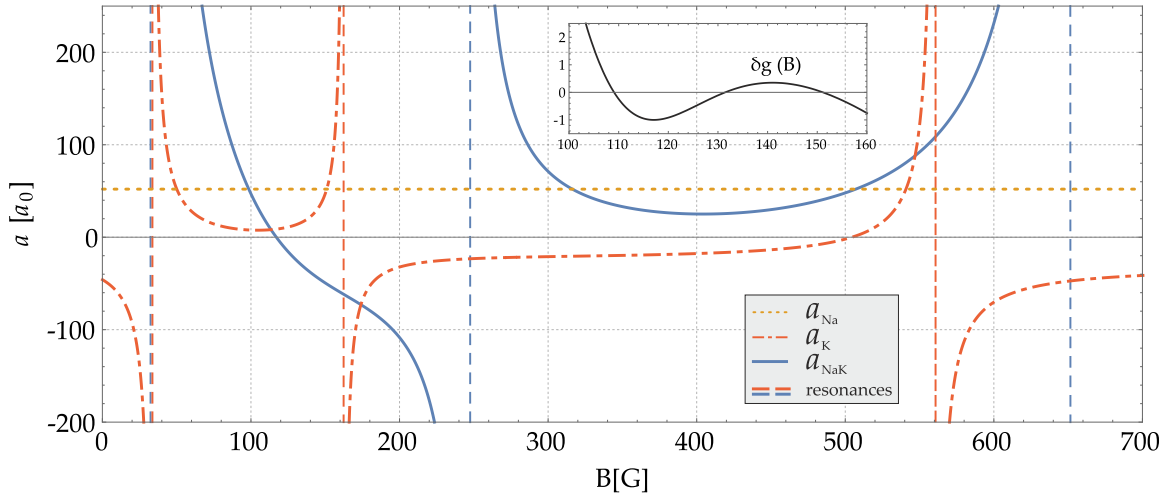


**Figure 2.4:** Intra and interatomic scattering scenario for  $^{23}\text{Na}$  and  $^{39}\text{K}$  atoms both in the  $|f = 1, m_f = -1\rangle$  states. This figure shows the scattering lengths (see legend) dependent on the magnetic field. The position of the scattering poles are shown as dashed lines. This scattering scenario is for the initial atomic mixture and is the starting point for all further experiments with the atoms. The picture is taken from [95].

strength of 200 G; see Fig. 2.4, making it a good candidate for a direct molecule state transfer.

Hence, for Feshbach molecule creation the resonance at 200 G in the channel  $|f = 1, m_f = -1\rangle_{\text{Na}} + |f = 2, m_f = -2\rangle_{\text{K}}$  is chosen. Within the experiments of the publication in Sec. 2.3 [87], first the resonance is characterized by means of magnetic field dependent loss measurements and molecular binding energy spectroscopy. Then, trapped Feshbach molecules are created by rf pulse application and the creation process and the loss rates are analyzed.



## 2.3 P1: *Formation of ultracold weakly bound dimers of bosonic $^{23}\text{Na}^{39}\text{K}$*

**Authors** Kai K. Voges, Philipp Gersema, Torsten Hartmann, Torben A. Schulze, Alessandro Zenesini, Silke Ospelkaus

**Journal** Physical Review A

**Article number** 101, 043704 (2020)

**DOI** 10.1103/PhysRevA.101.042704

**Contributions** **KKV**, PG, TAS and TH performed the measurements. **KKV** analyzed the data. **KKV** and AZ implemented the model for the molecule creation optimization. AZ and SO designed and headed the experiment. All authors contributed to the production of the manuscript.

**Copyright** © American Physical Society (APS). Reprinted with permission from Voges *et al.* Phys Rev. A 101, 042704 (2020), Copyright (2020) by APS.



## Formation of ultracold weakly bound dimers of bosonic $^{23}\text{Na}^{39}\text{K}$

Kai K. Voges , Philipp Gersema , Torsten Hartmann \*, Torben A. Schulze, Alessandro Zenesini , and Silke Ospelkaus <sup>†</sup>  
*Institut für Quantenoptik, Leibniz Universität Hannover, 30167 Hannover, Germany*



(Received 6 November 2019; revised manuscript received 28 February 2020; accepted 9 March 2020; published 20 April 2020)

We create weakly bound bosonic  $^{23}\text{Na}^{39}\text{K}$  molecules in a mixture of ultracold  $^{23}\text{Na}$  and  $^{39}\text{K}$ . The creation is done in the vicinity of a so far undetected Feshbach resonance at about 196 G which we identify in this work by atom-loss spectroscopy. We investigate the involved molecular state by performing destructive radio-frequency binding-energy measurements. For the constructive molecule creation we use radio-frequency pulses with which we assemble up to 6000 molecules. We analyze the molecule creation efficiency as a function of the radio-frequency pulse duration and the atom number ratio between  $^{23}\text{Na}$  and  $^{39}\text{K}$ . We find an overall optimal efficiency of 6 % referring to the  $^{39}\text{K}$  atom number. The measured lifetime of the molecules in the bath of trapped atoms is about 0.3 ms.

DOI: [10.1103/PhysRevA.101.042704](https://doi.org/10.1103/PhysRevA.101.042704)

### I. INTRODUCTION

Feshbach molecule creation from ultracold atomic gases has led to exciting developments ranging from the observation of the BCS-BEC crossover [1,2] to Efimov physics [3] and state-to-state chemistry [4]. Furthermore, Feshbach molecules constitute an important steppingstone for the creation of deeply bound molecules by means of stimulated Raman adiabatic passage (STIRAP). For heteronuclear molecules, this was first demonstrated for fermionic KRb molecules starting from a heteronuclear K and Rb quantum gas mixture [5]. Heteronuclear ground-state molecules are of special interest because of their large electric dipole moment. The anisotropic and tunable dipole-dipole interaction can be used for the control of ultracold chemical reactions [6], quantum simulation [7], and quantum computing [8].

In recent years different alkali heteronuclear ground-state molecules have been produced by association of weakly bound dimers and subsequent STIRAP to the ground state. So far, fermionic KRb [5,9], LiNa [10,11], NaK [12,13], and bosonic RbCs [14,15] and NaRb [16,17] have been created in different experiments. Up to now the bosonic molecule  $^{23}\text{Na}^{39}\text{K}$  has been missing, although it might enable an interesting comparison to its fermionic counterpart, such as the exploration of atom-molecule trimer potential energy surfaces [18] or molecule-molecule collisions in rotational excited states [19]. NaK ground-state molecules have an intrinsic dipole moment of 2.72 D and are known to be chemically stable against two-body exchange reactions [20].

In our experiment we aim for the creation of  $^{23}\text{Na}^{39}\text{K}$  ground-state molecules. Therefore, a detailed investigation of weakly bound dimers is mandatory for an efficient ground-state molecule production. Recently, Feshbach resonances and refined molecular potentials for the  $^{23}\text{Na} + ^{39}\text{K}$  mixture have been reported and a quantum-degenerate Bose-Bose

mixture has been produced [21,22]. Additionally, to transfer the dimers to the ground state, possible STIRAP pathways have been investigated theoretically [23] and experimentally [24].

Weakly bound Feshbach molecules have mainly been created using two different approaches. First of all, magnetic field ramps have been used mostly in the vicinity of Feshbach resonances with small widths. Second, direct state transfer methods have been implemented mostly in the vicinity of Feshbach resonances with a large width. In this case, the bound molecular state is directly populated starting from a nonresonant scattering channel using radio frequencies, microwave radiation, magnetic field modulation [25], or optical Raman transitions [18,26].

Here we report the formation of weakly bound  $^{23}\text{Na}^{39}\text{K}$  dimers from an ultracold mixture of bosonic  $^{23}\text{Na}$  and  $^{39}\text{K}$  by means of rf association. In our experiment we make use of an up-to-now undetected Feshbach resonance in the  $|f = 1, m_f = -1\rangle_{\text{Na}} + |f = 2, m_f = -2\rangle_{\text{K}}$  scattering channel at approximately 196 G. Here  $f$  is the hyperfine quantum number and  $m_f$  its projection on the magnetic field axis. We locate the Feshbach resonance by magnetic-field-dependent atom-loss spectroscopy. We also measure the binding energy of the involved molecular state and characterize the efficiency of the molecule creation process.

In the following we describe our experimental procedure in Sec. II. Characterization measurements of the Feshbach resonance are summarized in Sec. III. Finally, we discuss the formation of weakly bound dimers and the efficiency of the creation process in Sec. IV.

### II. EXPERIMENTAL PROCEDURES

For the presented experiments the atomic mixture is prepared following the procedure described in [21,22]. We start with two precooled atomic beams, the one for  $^{23}\text{Na}$  produced by a Zeeman slower and the one for  $^{39}\text{K}$  produced by a two-dimensional magneto-optical trap (MOT). Atoms from both beams are captured in a three-dimensional MOT. Afterwards

\*torben.alexander@icloud.com

<sup>†</sup>silke.ospelkaus@iqo.uni-hannover.de

both species are individually molasses cooled before they are optically pumped to the  $f = 1$  state and loaded into an optically plugged magnetic quadrupole trap. In the trap  $^{23}\text{Na}$  atoms are cooled by forced microwave evaporation.  $^{39}\text{K}$  atoms are sympathetically cooled in the bath of  $^{23}\text{Na}$  atoms. The cold atomic mixture is loaded from the magnetic trap to a 1064-nm crossed-beam optical dipole trap (cODT). The cODT intensity is increased while the quadrupole field is switched off and a homogeneous magnetic field of about 150 G is applied, yielding favorable inter- and intraspecies scattering lengths. A final optical evaporation step is performed by lowering the intensity in both beams of the cODT. For the experiments both species are cooled to temperatures below  $1\ \mu\text{K}$ . The atom number ratio between the two species is adjusted by the depth of the magnetic trap evaporation before the mixture is loaded to the cODT. During the sympathetic cooling process the phase-space density of  $^{39}\text{K}$  atoms increases and hence three-body losses on  $^{39}\text{K}$  occur [27], reducing drastically the atom number. We can vary the atom number ratio  $N_{\text{Na}}/N_{\text{K}}$  in the  $|f = 1, m_f = -1\rangle_{\text{Na}} + |f = 1, m_f = -1\rangle_{\text{K}}$  channel in the final cODT between 0.3 and 18.

### III. FESHBACH RESONANCE IN THE $|1, -1\rangle_{\text{Na}} + |2, -2\rangle_{\text{K}}$ STATE

The newly found Feshbach resonance in the  $|1, -1\rangle_{\text{Na}} + |2, -2\rangle_{\text{K}}$  state possesses several advantages for the creation of the weakly bound molecules. For  $^{39}\text{K}$  this state is a stretched one which allows for a state-selective imaging of atoms or molecules by utilizing a single laser frequency (see Sec. IV A). In addition, the molecular state can be directly populated using a single rf transfer from a long-lived mixture in the initial  $|1, -1\rangle_{\text{Na}} + |1, -1\rangle_{\text{K}}$  state. The transition itself also is relatively insensitive to magnetic field noise [28].

For a successful creation of weakly bound dimers by rf pulses precise knowledge of the involved molecular state is essential. The Feshbach resonance and therefore the molecular state used here have never been observed before. We first investigate the Feshbach resonance by means of atom-loss spectroscopy (see Sec. III A). For the precise determination of the resonance position we perform destructive binding-energy measurements as a function of magnetic field (see Sec. III B).

#### A. Atom-loss spectroscopy

In the vicinity of Feshbach resonances the atoms experience an increased scattering rate which enhances two- and three-body losses. To determine the position of the Feshbach resonance we use this effect and perform atom-loss spectroscopy. The Feshbach resonance of interest is predicted to be located at a magnetic field of about 196 G in the  $|f = 1, m_f = -1\rangle_{\text{Na}} + |f = 2, m_f = -2\rangle_{\text{K}}$  scattering channel [29]. We prepare the atomic mixture as explained above and finally transfer the  $^{39}\text{K}$  atoms to the  $|f = 2, m_f = -2\rangle_{\text{K}}$  state at 137 G using rapid adiabatic passage (RAP) [21,30]. In this specific case we apply a rf of 256 MHz and sweep the magnetic field by approximately 1 G within 100 ms. At about 137 G the inter- and intraspecies scattering rates for the  $^{23}\text{Na} + ^{39}\text{K}$  mixture for all involved

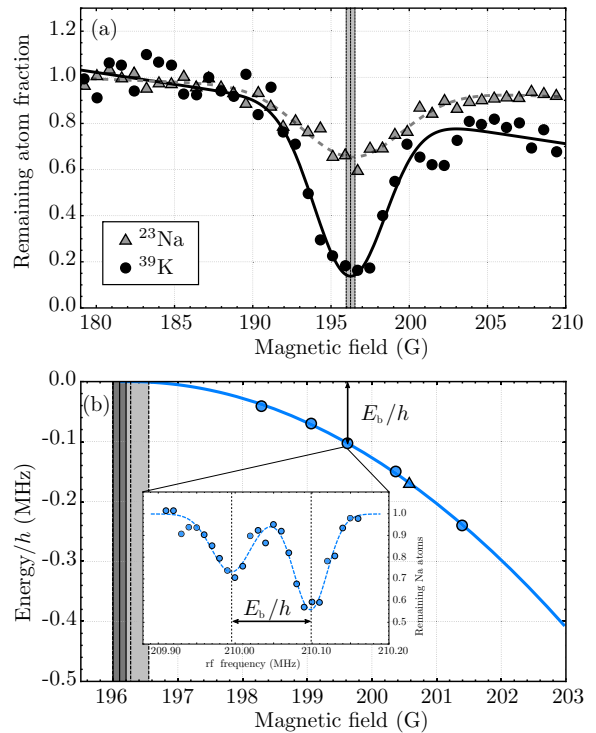


FIG. 1. Feshbach resonance characterization. (a) Atom-loss spectroscopy in the  $|f = 1, m_f = -1\rangle_{\text{Na}} + |f = 2, m_f = -2\rangle_{\text{K}}$  channel. The remaining atom fraction of  $^{23}\text{Na}$  and  $^{39}\text{K}$  for different magnetic field strengths with a holding time of 40 ms. The remaining atom number is normalized to the initial atom number for each species, respectively. Open gray triangles and the dashed gray line refer to the remaining  $^{23}\text{Na}$  atom fraction and solid black circles and the solid black line refer to the  $^{39}\text{K}$  atom number fraction. The vertical lines and corresponding shaded area indicate the resonance position and the standard deviation obtained from the two Gaussian fits. (b) Binding energy of the weakly bound state as obtained from rf spectroscopy. The continuous blue line is a fit to the destructive measurements (blue circles) according to universal binding energy [Eq. (1)]. The triangle is the binding energy extracted from the constructive signal from Fig. 2. The vertical lines are the resonance position with the standard deviation; dashed lines for the atom-loss measurement in (a), and solid lines for the binding-energy measurement. The inset shows a sample rf scan for a binding energy of  $h \times 103\ \text{kHz}$  with a double-Gaussian fit (dashed blue line). The arrows indicate the binding energy. Error bars in both figures are smaller than the plot markers and are not shown.

state combinations are low enough to allow for sufficient long holding time for the RAP [29].

To start atom-loss spectroscopy of the Feshbach resonance, we perform a fast magnetic field ramp to different magnetic field values in the vicinity of the resonance. We hold the mixture at each magnetic field value for 40 ms so that the enhanced scattering rate leads to atom losses. We record the remaining atom number after the hold time resulting in a loss feature as shown in Fig. 1(a). Using a phenomenological Gaussian fit to the data of  $^{23}\text{Na}$  and  $^{39}\text{K}$ , respectively, we

determine the resonance position to be at 196.27(28) G. The value is in good agreement with predictions obtained from our most recent available NaK ground-state potentials [29].

### B. Molecular binding energy

At the position of a Feshbach resonance a molecular state enters from the diatomic continuum into the scattering threshold. As both states are highly coupled close to the Feshbach resonance, the molecular state becomes spectroscopically accessible. To observe the bound state, we perform destructive binding-energy measurements starting from a free diatomic state. We start with the atomic mixture in the  $|f = 1, m_f = -1\rangle_{\text{Na}} + |f = 1, m_f = -1\rangle_{\text{K}}$  state (see Sec. II) and apply rf radiation to bridge the energy gap to the resonant  $|f = 1, m_f = -1\rangle_{\text{Na}} + |f = 2, m_f = -2\rangle_{\text{K}}$  state and the energetically lower-lying bound molecular state. The rf radiation in this experiment is switched on for 40 ms. This ensures that atoms, which are transferred to the resonant  $|f = 2, m_f = -2\rangle_{\text{K}}$  state and which experience a high number of scattering events, are significantly depleted from the trap. The particles transferred to the weakly bound molecular state also experience strong losses (see inset in Fig. 1(b)). The obtained data for different magnetic field strengths is shown in Fig. 1(b). The inset shows an example of a single binding-energy measurement at 199.62 G, where the atom-loss feature (at about 210.1 MHz) serves as a magnetic field calibration and the difference from the molecule-loss feature (at about 210.0 MHz) as binding energy  $E_b/h$ . The smaller depth of the loss signal for the molecular transition can be attributed to a weaker coupling between atoms and molecules than between atoms.

Close to the resonance position and on the positive scattering length side of the Feshbach resonance the binding energy  $E_b(B)$  can be described by the universal formula

$$E_b(B) = \frac{\hbar^2}{2\mu a(B)^2}, \quad (1)$$

with

$$a(B) = a_{\text{bg}} \left( 1 - \frac{\Delta}{B - B_0} \right), \quad (2)$$

where  $a$  is the interspecies scattering length,  $a_{\text{bg}}$  the background scattering length of the entrance channel, and  $\Delta$  and  $B_0$  the width and position of the Feshbach resonance, respectively.  $\mu$  is the reduced mass of the molecular system. The solid blue line in Fig. 1(b) is a fit according to Eq. (1). Using a background scattering length of  $a_{\text{bg}} = -38.1a_0$ ,  $a_0$  being the Bohr radius, as obtained from coupled-channel calculation [31], we determine the resonance width to the zero crossing to be  $\Delta = 105.8(1.6)$  G and the position to be  $B_0 = 196.10(10)$  G, in good agreement with the results from the loss measurement (see Sec. III A).

## IV. WEAKLY BOUND DIMERS

With the knowledge of the exact resonance position and molecular binding energy, the molecular state can be selec-

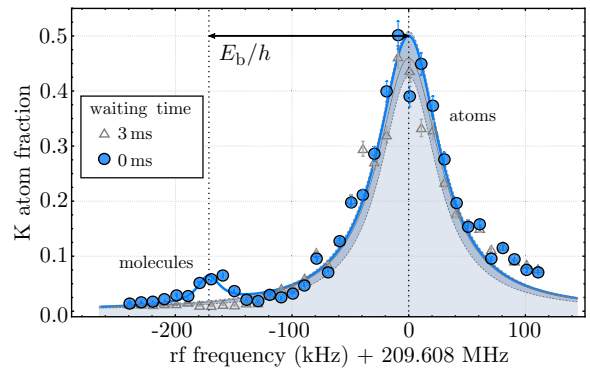


FIG. 2. Constructive molecular signal.  $^{39}\text{K}$  atom number as a function of the applied rf radiation. The blue circles are the detected atom number directly after the rf pulse. Fitting a phenomenological double-Lorentzian function (solid blue line) the atomic transition occurs at 209.608(3) MHz, corresponding to a magnetic field of 200.58(3) G. The extracted binding energy is  $h \times 171(4)$  kHz, shown as the black arrow. The value is displayed also in Fig. 1(b) as a blue triangle. Open gray triangles are the measured background atoms after an additional waiting time of 3 ms (see text) and the solid gray line with the underlying shaded gray area is a Lorentzian fit with the standard error as a darker shaded area. The atom number is normalized to the total number of  $^{39}\text{K}$  atoms. Error bars are the standard deviation and come from different experimental runs.

tively populated by rf radiation. This process requires precisely determined experimental parameters, which are characterized in this section. Also a direct imaging of the molecules is mandatory.

### A. Creation process

We start with an atomic mixture in the  $|f = 1, m_f = -1\rangle_{\text{Na}} + |f = 1, m_f = -1\rangle_{\text{K}}$  state at a temperature of 500 nK and an atom number ratio of  $N_{\text{Na}}/N_{\text{K}} = 3$ . Applying a rf pulse we associate molecules immediately followed by a state-selective imaging of the atoms in the  $|f = 2, m_f = -2\rangle_{\text{K}}$  state. For this purpose the laser frequency for the  $^{39}\text{K}$  imaging is shifted to be on resonance with the  $|S_{1/2}, f = 2, m_f = -2\rangle_{\text{K}} \leftrightarrow |P_{3/2}, f = 3, m_f = -3\rangle_{\text{K}}$  transition for a given magnetic field, which is a closed transition from the Zeeman to the Paschen-Back regime and allows high-field imaging of  $^{39}\text{K}$  atoms at arbitrary magnetic field values. As long as the molecular binding energy is smaller than the linewidth of the atomic transition, this cycling transition can be used to also image weakly bound dimers.

For molecule creation, we switch on the rf source 75 ms before the actual molecule creation takes place with a frequency detuned by  $-120$  kHz with respect to the molecular transition. We then jump the rf frequency for 0.6 ms to the frequency required for molecule creation followed by a hard switch-off. We found this method to be more reliable and stable than a simple switch on and off, accounting for less disturbance of the rf to our magnetic field stabilization system. We populate selectively the atomic and the molecular states as shown in Fig. 2. Both peaks reveal an asymmetric shape on the

positive frequency side originating from this pulse application technique (see Fig. 2). The creation pulse is followed by  $^{39}\text{K}$  imaging as explained above. With this method molecule creation efficiency can be as high as 6% at a binding energy of  $E_b = h \times 100$  kHz. For smaller binding energies the atomic and molecular peaks start to overlap. In this case it is not possible to prepare pure samples of bound dimers and distinguish them from free atoms in a single experimental cycle. In a separated experimental cycle we introduce a waiting time of 3 ms between molecule creation and imaging to distinguish the short-living molecules from atoms (see triangle symbols in Fig. 2).

### B. Characterization and optimization

For an efficient molecule association the duration of the rf pulse as well as the atom number ratio between  $^{23}\text{Na}$  and  $^{39}\text{K}$  is critical.

The dependence on the pulse duration is shown in Fig. 3(a). The maximum appears when the molecule creation is overcome by losses of the molecules due to collisions with atoms. The dynamic is modeled by a set of three differential equations for the time-dependent populations  $N_{\text{mol}}$ ,  $N_{\text{Na}}$ , and  $N_{\text{K}}$ :

$$\begin{aligned} \frac{dN_{\text{mol}}}{dt} &= k_{\text{mol}}g_{\text{Na,K}}N_{\text{Na}}N_{\text{K}} \\ &\quad - k_a(g_{\text{Na,mol}}N_{\text{Na}} + g_{\text{K,mol}}N_{\text{K}})N_{\text{mol}} \\ \frac{dN_{\text{Na}}}{dt} &= -k_{\text{mol}}g_{\text{Na,K}}N_{\text{Na}}N_{\text{K}} - k_a g_{\text{Na,mol}}N_{\text{Na}}N_{\text{mol}} \\ \frac{dN_{\text{K}}}{dt} &= -k_{\text{mol}}g_{\text{Na,K}}N_{\text{Na}}N_{\text{K}} - k_a g_{\text{K,mol}}N_{\text{K}}N_{\text{mol}}, \end{aligned} \quad (3)$$

where  $N_{\text{mol}}$ ,  $N_{\text{Na}}$ , and  $N_{\text{K}}$  are the particle numbers for molecules,  $^{23}\text{Na}$  atoms, and  $^{39}\text{K}$  atoms, respectively;  $g_{i,j}$  is the two-body overlap integral [32]; and  $k_{\text{mol}}$  is the molecular creation coefficient and  $k_a$  the loss coefficient for atom-molecule collisions. The loss coefficient  $k_a$  is set equal for the case of a colliding molecule either with a  $^{23}\text{Na}$  atom or a  $^{39}\text{K}$  atom. Collisions between molecules are excluded from the model as they are expected to be negligibly small. The solid line in Fig. 3(a) shows a fit using the rate model system [Eqs. (3)] with  $k_{\text{mol}}$  and  $k_a$  as free parameters. According to the fit,  $k_{\text{mol}} = 1.18(16) \times 10^{-9} \text{ cm}^3 \text{ s}^{-1}$  and  $k_a = 4.54(45) \times 10^{-9} \text{ cm}^3 \text{ s}^{-1}$ . The maximal creation efficiency is found at a pulse duration of about  $350 \mu\text{s}$ . By accounting for the initial atom numbers the loss rate obtained from the second line in Eq. (3) is  $k_a(g_{\text{Na,mol}}N_{\text{Na}}(0) + g_{\text{K,mol}}N_{\text{K}}(0))$ , corresponding to a calculated lifetime of  $184(23) \mu\text{s}$ .

We have also measured the molecule formation efficiency as a function of the atom number ratio. We find the highest efficiency at  $N_{\text{Na}}/N_{\text{K}} \approx 3$  (see Fig. 3(b)). We use the parameter from the fit in Fig. 3(a) and the specific atom number ratios and total atom number for each experimental data point to calculate the maximal associated molecule fraction. The results are plotted as bars in Fig. 3(b) for a direct comparison to the experimental data. Despite the model not accounting for temperature effects such as antievaporation or temperature disequilibrium, the predictions are in good agreement with the observed dependence on the atom number ratio.

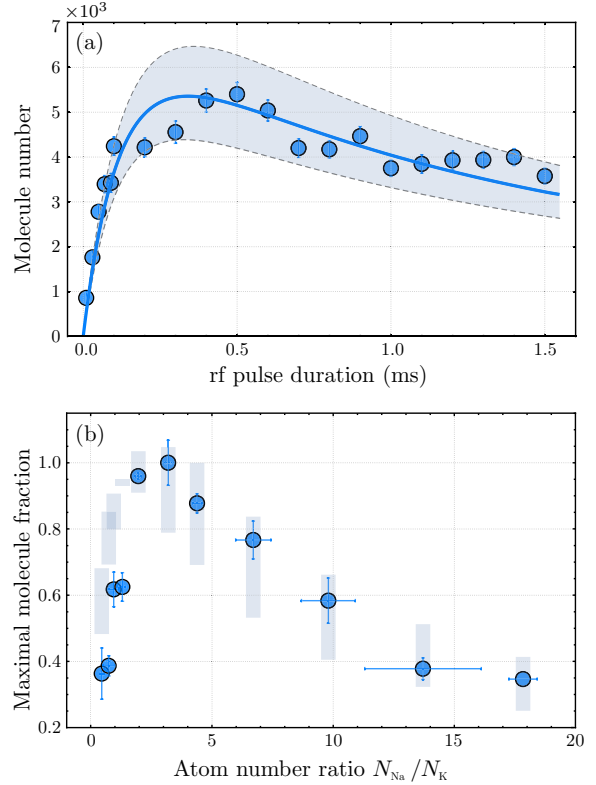


FIG. 3. Characterization of the association process. (a) The molecule number is plotted as a function of the rf pulse duration. The molecules are imaged directly after switching off the rf. The best creation efficiency is reached at a pulse duration around  $350 \mu\text{s}$ . The solid blue line is the fit modeled with the set of differential equations [Eqs. (3)]. The dashed lines with the enclosed shaded area refer to the fit uncertainties. (b) Normalized molecule number as function of the atom number ratio at a creation time of  $500 \mu\text{s}$ . The bars represent the predictions from the fit results in (a) taking the individual starting conditions for each point as well as the fit uncertainties into account. The normalization is done according to the maximal created molecule number. Error bars in both figures are the standard deviation and come from different experimental runs.

### C. Molecule lifetime

We measure the lifetime for molecules immersed in the bath of residual atoms. This measurement is done by introducing a hold time between the rf pulse and the imaging. Figure 4 shows a typical measurement. For this experiment the creation pulse duration is set to  $500 \mu\text{s}$ . During the hold time the rf is set back to the offset detuning to stop molecule creation during the hold time. Using the model from Eq. (3), we determine a lifetime of  $299(17) \mu\text{s}$ , which differs from the one obtained in Sec. IV B. We suggest that the observed difference in lifetime originates from the presence of the resonant rf radiation. For the off-resonant case in Sec. IV C we do not see a difference with or without applied rf. The model from Eqs. (3) does

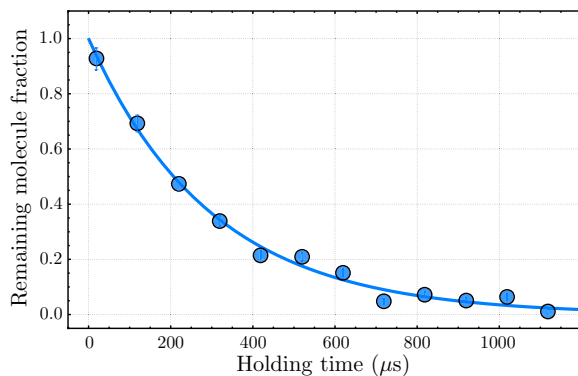


FIG. 4. Lifetime measurement of the molecules in the cODT. The molecule number is normalized to the value of zero waiting time. For this measurement  $^{23}\text{Na}$  and  $^{39}\text{K}$  atoms are not removed. A fit to the data (solid line) results in a lifetime of  $\tau = 299(17)\mu\text{s}$ . Error bars are the standard deviation and come from different experimental runs.

not elucidate or account for the pulse shape and frequency detuning of the rf.

A lifetime of several hundred microseconds is sufficient for subsequent STIRAP transfer of the Feshbach molecules to the molecular ground state, which takes typically  $10\text{--}20\mu\text{s}$  [33,34].

## V. CONCLUSION AND OUTLOOK

In summary we have investigated a Feshbach resonance for the bosonic  $^{23}\text{Na} + ^{39}\text{K}$  mixture in the  $|f = 1, m_f = -1\rangle_{\text{Na}} + |f = 2, m_f = -2\rangle_{\text{K}}$  channel around 196 G. We located the Feshbach resonance using atom-loss spectroscopy as well as destructive binding-energy measurements on the bound molecular state. By applying rf pulses we have been able to populate the bound molecular state and distinguish the dimers from free atoms. We have further characterized and optimized the Feshbach molecule creation efficiency with respect to rf pulse duration and atom number ratio. We have been able to create up to 6000 weakly bound molecules per experimental cycle. The lifetime of the dimers in the presence of background atoms is about 0.3 ms, which is sufficiently long to perform a STIRAP transfer. These dimers serve as an ideal starting point for efficient creation of so far unobserved ultracold chemically stable bosonic  $^{23}\text{Na}^{39}\text{K}$  molecules in their absolute electronic and rovibrational ground state.

## ACKNOWLEDGMENTS

We thank E. Tiemann for enlightening discussions and theory support. We gratefully acknowledge financial support from the European Research Council through ERC Starting Grant POLAR and from the Deutsche Forschungsgemeinschaft (DFG) through CRC 1227 (DQ-mat), project A03, and FOR 2247, project E5. K.K.V. and P.G. thank the DFG for financial support through Research Training Group 1991.

- [1] C. Chin, M. Bartenstein, A. Altmeyer, S. Riedl, S. Jochim, J. H. Denschlag, and R. Grimm, Observation of the pairing gap in a strongly interacting Fermi gas, *Science* **305**, 1128 (2004).
- [2] C. A. Regal, M. Greiner, and D. S. Jin, Observation of Resonance Condensation of Fermionic Atom Pairs, *Phys. Rev. Lett.* **92**, 040403 (2004).
- [3] T. Kraemer, M. Mark, P. Waldburger, J. G. Danzl, C. Chin, B. Engeser, A. D. Lange, K. Pilch, A. Jaakkola, H.-C. Nägerl, and R. Grimm, Evidence for Efimov quantum states in an ultracold gas of caesium atoms, *Nature (London)* **440**, 345 (2006).
- [4] J. Rui, H. Yang, L. Liu, D.-C. Zhang, Y.-X. Liu, J. Nan, Y.-A. Chen, B. Zhao, and J.-W. Pan, Controlled state-to-state atom-exchange reaction in an ultracold atom-dimer mixture, *Nat. Phys.* **13**, 699 (2017).
- [5] K.-K. Ni, S. Ospelkaus, M. H. G. de Miranda, A. Peer, B. Neyenhuis, J. J. Zirbel, S. Kotochigova, P. S. Julienne, D. S. Jin, and J. Ye, A high phase-space-density gas of polar molecules, *Science* **322**, 231 (2008).
- [6] S. Ospelkaus, K.-K. Ni, D. Wang, M. H. G. de Miranda, B. Neyenhuis, G. Quemener, P. S. Julienne, J. L. Bohn, D. S. Jin, and J. Ye, Quantum-state controlled chemical reactions of ultracold potassium-rubidium molecules, *Science* **327**, 853 (2010).
- [7] B. Yan, S. Moses, B. Gadway, J. Covey, K. Hazzard, A. Rey, D. Jin, and J. Ye, Observation of dipolar spin-exchange interactions with lattice-confined polar molecules, *Nature (London)* **501**, 521 (2013).
- [8] D. DeMille, Quantum Computation with Trapped Polar Molecules, *Phys. Rev. Lett.* **88**, 067901 (2002).
- [9] C. Ospelkaus, S. Ospelkaus, L. Humbert, P. Ernst, K. Sengstock, and K. Bongs, Ultracold Heteronuclear Molecules in a 3D Optical Lattice, *Phys. Rev. Lett.* **97**, 120402 (2006).
- [10] M.-S. Heo, T. T. Wang, C. A. Christensen, T. M. Rvachov, D. A. Cotta, J.-H. Choi, Y.-R. Lee, and W. Ketterle, Formation of ultracold fermionic NaLi Feshbach molecules, *Phys. Rev. A* **86**, 021602(R) (2012).
- [11] T. M. Rvachov, H. Son, A. T. Sommer, S. Ebadi, J. J. Park, M. W. Zwierlein, W. Ketterle, and A. O. Jamison, Long-Lived Ultracold Molecules with Electric and Magnetic Dipole Moments, *Phys. Rev. Lett.* **119**, 143001 (2017).
- [12] C.-H. Wu, J. W. Park, P. Ahmadi, S. Will, and M. W. Zwierlein, Ultracold Fermionic Feshbach Molecules of  $^{23}\text{Na}^{40}\text{K}$ , *Phys. Rev. Lett.* **109**, 085301 (2012).
- [13] J. W. Park, S. A. Will, and M. W. Zwierlein, Ultracold Dipolar Gas of Fermionic  $^{23}\text{Na}^{40}\text{K}$  Molecules in Their Absolute Ground State, *Phys. Rev. Lett.* **114**, 205302 (2015).
- [14] T. Takekoshi, M. Debatin, R. Rameshan, F. Ferlaino, R. Grimm, H.-C. Nägerl, C. R. Le Sueur, J. M. Hutson, P. S. Julienne, S. Kotochigova, and E. Tiemann, Towards the production of ultracold ground-state RbCs molecules: Feshbach resonances, weakly bound states, and the coupled-channel model, *Phys. Rev. A* **85**, 032506 (2012).
- [15] T. Takekoshi, L. Reichsöllner, A. Schindewolf, J. M. Hutson, C. R. Le Sueur, O. Dulieu, F. Ferlaino, R. Grimm, and H.-C. Nägerl, Ultracold Dense Samples of Dipolar RbCs Molecules in the Rovibrational and Hyperfine Ground State, *Phys. Rev. Lett.* **113**, 205301 (2014).

- [16] F. Wang, X. He, X. Li, B. Zhu, J. Chen, and D. Wang, Formation of ultracold NaRb Feshbach molecules, *New J. Phys.* **17**, 035003 (2015).
- [17] M. Guo, B. Zhu, B. Lu, X. Ye, F. Wang, R. Vexiau, N. Bouloufa-Maafa, G. Quéméner, O. Dulieu, and D. Wang, Creation of an Ultracold Gas of Ground-State Dipolar  $^{23}\text{Na}^{87}\text{Rb}$  Molecules, *Phys. Rev. Lett.* **116**, 205303 (2016).
- [18] H. Yang, D.-C. Zhang, L. Liu, Y.-X. Liu, J. Nan, B. Zhao, and J.-W. Pan, Observation of magnetically tunable Feshbach resonances in ultracold  $^{23}\text{Na}^{40}\text{K} + ^{40}\text{K}$  collisions, *Science* **363**, 261 (2019).
- [19] S. A. Will, J. W. Park, Z. Z. Yan, H. Loh, and M. W. Zwierlein, Coherent Microwave Control of Ultracold  $^{23}\text{Na}^{40}\text{K}$  Molecules, *Phys. Rev. Lett.* **116**, 225306 (2016).
- [20] P. S. Zuchowski and J. M. Hutson, Reactions of ultracold alkali-metal dimers, *Phys. Rev. A* **81**, 060703(R) (2010).
- [21] T. Hartmann, T. A. Schulze, K. K. Voges, P. Gersema, M. W. Gempel, E. Tiemann, A. Zenesini, and S. Ospelkaus, Feshbach resonances in  $^{23}\text{Na} + ^{39}\text{K}$  mixtures and refined molecular potentials for the NaK molecule, *Phys. Rev. A* **99**, 032711 (2019).
- [22] T. A. Schulze, T. Hartmann, K. K. Voges, M. W. Gempel, E. Tiemann, A. Zenesini, and S. Ospelkaus, Feshbach spectroscopy and dual-species Bose-Einstein condensation of  $^{23}\text{Na}$ - $^{39}\text{K}$  mixtures, *Phys. Rev. A* **97**, 023623 (2018).
- [23] T. A. Schulze, I. I. Temelkov, M. W. Gempel, T. Hartmann, H. Knöckel, S. Ospelkaus, and E. Tiemann, Multichannel modeling and two-photon coherent transfer paths in NaK, *Phys. Rev. A* **88**, 023401 (2013).
- [24] K. K. Voges, P. Gersema, T. Hartmann, T. A. Schulze, E. Tiemann, S. Ospelkaus, and A. Zenesini, A pathway to ultracold bosonic  $^{23}\text{Na}^{39}\text{K}$  ground state molecules, *New J. Phys.* **21**, 123034 (2019).
- [25] C. Chin, R. Grimm, P. Julienne, and E. Tiesinga, Feshbach resonances in ultracold gases, *Rev. Mod. Phys.* **82**, 1225 (2010).
- [26] Z. Fu, L. Huang, Z. Meng, P. Wang, L. Zhang, S. Zhang, H. Zhai, P. Zhang, and J. Zhang, Production of Feshbach molecules induced by spin-orbit coupling in Fermi gases, *Nat. Phys.* **10**, 110 (2014).
- [27] T. A. Schulze, Quantum degenerate mixtures of  $^{23}\text{Na}$ - $^{39}\text{K}$  and coherent transfer paths in NaK molecules, Ph.D. thesis, Leibniz Universität Hannover, 2018.
- [28] The magnetic field stability in our experimental setup is about 20 mG. For the transition in  $^{39}\text{K}$  at 200 G this corresponds to a stability of 10 kHz.
- [29] T. Hartmann, An experiment apparatus for the production of ultracold bosonic dipolar ground state  $^{23}\text{Na}^{39}\text{K}$  molecules and Feshbach spectroscopy in a cold mixture of  $^{23}\text{Na}$  and  $^{39}\text{K}$ , Ph.D. thesis, Leibniz Universität Hannover, 2018.
- [30] J. C. Camparo and R. P. Frueholz, A dressed atom interpretation of adiabatic rapid passage, *J. Phys. B* **17**, 4169 (1984).
- [31] E. Tiemann (private communication).
- [32] For calculating the two-body overlap integral we use the equation  $g_{i,j} = \frac{1}{N_i N_j} \int_V n_i n_j dV$ , where  $i$  and  $j$  denote the atom species or molecules and  $V$  the volume. We assume the densities  $n$  follow a Gaussian distribution.
- [33] N. V. Vitanov, A. A. Rangelov, B. W. Shore, and K. Bergmann, Stimulated Raman adiabatic passage in physics, chemistry, and beyond, *Rev. Mod. Phys.* **89**, 015006 (2017).
- [34] Removing residual atoms before applying the STIRAP is not feasible in our system as any removal would take longer than the molecule lifetime would allow for, resulting in a drastic decrease of the number of ground-state molecules.

## Chapter 3

# A Laser System for STIRAP

With the Feshbach molecules available, the next step on the way to ultracold ensembles of ground-state molecules is the transfer of the Feshbach molecules to the rovibrational ground state. This transfer step is done using STIRAP.

Since each molecular species is highly unique in its properties, the STIRAP pathway has to be specifically designed for each novel molecular species and the chosen quantum states. The specific scheme also requires a specifically designed laser system.

Within this chapter, I will first summarize the theory of STIRAP transfer in an idealized three-level system; see Sec. 3.1. A thorough understanding of the STIRAP theory allows to summarize the technical requirements that a STIRAP laser system has to fulfill. Finally, in Sec. 3.2, I will detail the design, construction and characterization of the STIRAP laser system that is being used in Chap. 4 for the molecular spectroscopy and Chap. 5 for ground-state molecule creation.

### 3.1 Stimulated Raman Adiabatic Passage in a Molecular System

The level structure of molecules is much richer and more complicated compared to the one of atoms. Thus, state control and preparation requires more caution. Molecules, which decay through spontaneous processes to other states are typically lost from the experiment as the variety of decay channels is tremendous. STIRAP can circumvent the decay from excited states during transitions by applying a permanent dressing and producing a dark state with variable state admixtures. The state dressing and the adiabatic state remixing also feature a certain robustness against distortions, either through fluctuations in laser power or frequency.

In the following, I will detail the theoretical framework for the most simple STIRAP application. First, in Sec. 3.1.1, I will give the theoretical description of a three-level system. Then, I introduce the general transfer protocol, which can lead to a high efficient and robust state exchange; see Sec. 3.1.2. In Sec. 3.1.3 I will explain the implementation of losses from excited states in the model. Finally, in Sec. 3.1.4, I evaluate the limits for long and short pulses, providing a starting point for demands on the STIRAP laser system.

#### 3.1.1 A Three-Level $\Lambda$ -System

The STIRAP investigated in this thesis is performed in a molecular system and serves as a path for the transfer of weakly bound molecules to the deeply bound ground state via an excited molecular state and vice versa. The three-level  $\Lambda$ -system; see Fig. 3.1, consists of the Feshbach molecule state  $|f\rangle$ , the excited state  $|e\rangle$  and the ground state  $|g\rangle$ . Transitions are

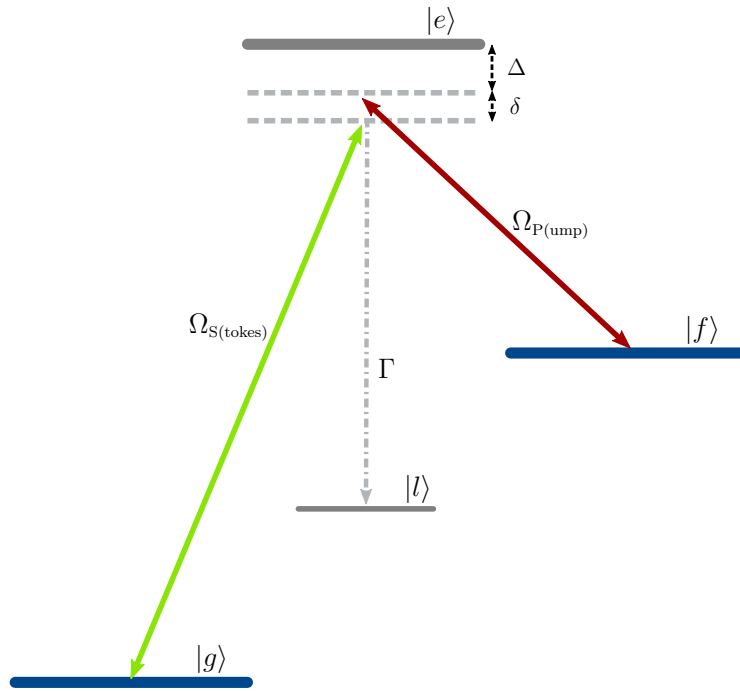


**Figure 3.1:** Three-level  $\Lambda$ -system. This figure shows the molecular  $\Lambda$ -level scheme, including the three states  $|f\rangle$ ,  $|e\rangle$  and  $|g\rangle$ , the possible transitions pump and Stokes with their respective rates  $\Omega_{P(\text{ump})}$  and  $\Omega_{S(\text{tokes})}$  as well as the the loss state  $|l\rangle$  with the loss rate  $\Gamma$ . The scheme is a simplified version analog to the ones presented in the Chaps 4 and 5.

allowed from states  $|f\rangle$  to  $|e\rangle$  and  $|g\rangle$  to  $|e\rangle$  and are name *pump* and *Stokes*, respectively, for the case of a transfer from the state  $|f\rangle$  to the state  $|g\rangle$ . For the backwards transfer, the STIRAP is reversed and so the role and names for the transitions exchange. In the following, the transitions are always labeled for the case of a state transfer from weakly bound molecules to the ground-state molecules. The coupling between the states is described by the Rabi frequencies  $\Omega_{P(\text{ump})}$  and  $\Omega_{S(\text{tokes})}$ .

They depend on the dipole-transition moment  $d_{fe/ge}$  and the electric field strength  $E_{P/S}$  of the laser light [99]. The Rabi frequencies can be expressed as

$$\Omega_P(t) = -d_{fe} \frac{E_P(t)}{\hbar} \quad \text{and} \quad (3.1)$$

$$\Omega_S(t) = -d_{ge} \frac{E_S(t)}{\hbar}, \quad (3.2)$$

where  $\hbar$  is the reduced Planck constant. The frequency detunings of the pump and Stokes laser fields are  $\Delta_P$  and  $\Delta_S$ , respectively, according to Fig. 3.1.

For STIRAP, typically all three states are connected by the induced transitions. In this case the one-photon detuning can be expressed as  $\Delta = \Delta_P$  and the two-photon detuning as  $\delta = \Delta_P - \Delta_S$ . Hence, to model the dynamics of STIRAP by the Schrödinger equation, the Hamiltonian  $H(t)$  in rotating-wave approximation is

$$H(t) = \frac{\hbar}{2} \begin{bmatrix} 0 & \Omega_P(t) & 0 \\ \Omega_P(t) & 2\Delta & \Omega_S(t) \\ 0 & \Omega_S(t) & 2\delta \end{bmatrix}, \quad (3.3)$$

and the corresponding time dependent Schrödinger equation

$$i\hbar \frac{d}{dt} |\Phi\rangle = H(t) |\Phi\rangle, \quad |\Phi\rangle = \begin{pmatrix} \phi_f(t) \\ \phi_e(t) \\ \phi_g(t) \end{pmatrix}. \quad (3.4)$$

Here,  $|\Phi\rangle$  forms the time dependent state vector containing the time dependent amplitude probabilities  $\phi_{f,e,g}(t)$  for the three involved states  $|f\rangle$ ,  $|e\rangle$  and  $|g\rangle$  of the system.

The solution for the complete dressed system is given by the set of eigenstates  $|\chi_0\rangle$ ,  $|\chi_+\rangle$  and  $|\chi_-\rangle$

$$|\chi_0\rangle = \cos \theta(t) |f\rangle - \sin \theta(t) |g\rangle \quad (3.5)$$

$$|\chi_+\rangle = \sin \theta(t) \sin \rho(t) |f\rangle + \cos \rho(t) |e\rangle + \cos \theta(t) \sin \rho(t) |g\rangle \quad (3.6)$$

$$|\chi_-\rangle = \sin \theta(t) \cos \rho(t) |f\rangle - \sin \rho(t) |e\rangle + \cos \theta(t) \cos \rho(t) |g\rangle \quad (3.7)$$

and the respective set of eigenvalues  $\omega_0$ ,  $\omega_+$  and  $\omega_-$

$$\omega_0(t) = 0 \quad (3.8)$$

$$\omega_+(t) = \frac{\hbar}{2} \left[ \Delta + \sqrt{\Delta^2 + \Omega_P^2(t) + \Omega_S^2(t)} \right] \quad (3.9)$$

$$\omega_-(t) = \frac{\hbar}{2} \left[ \Delta - \sqrt{\Delta^2 + \Omega_P^2(t) + \Omega_S^2(t)} \right]. \quad (3.10)$$

The state  $|\chi_0\rangle$  is called *dark state* and the states  $|\chi_+\rangle$  and  $|\chi_-\rangle$  are the *bright states*. The new notation comprises two angles  $\theta(t)$  and  $\rho(t)$ , called mixing angles. Their meaning gets more intuitive in terms of the transfer protocol; see Sec. 3.1.2. They are composed of

$$\tan(2\rho(t)) = \frac{\Omega_0(t)}{\Delta} \quad (3.11)$$

$$\tan(\theta(t)) = \frac{\Omega_P(t)}{\Omega_S(t)}. \quad (3.12)$$

Additionally,  $\Omega_0(t) = \sqrt{\Omega_S^2(t) + \Omega_P^2(t)}$  describes the total eigenfrequency of the dressed system. These equations describe the closed three-level system for the molecular case. The STIRAP itself is a coherent evolution utilizing these states. The protocol for the STIRAP is described in the following section.

### 3.1.2 Transfer Protocol

The eigenstates and eigenvalues of the  $\Lambda$ -system introduced above yield a variety of important features for the STIRAP.

The eigenstates  $|\chi_0\rangle$ ,  $|\chi_+\rangle$  and  $|\chi_-\rangle$  of the dressed system are linear combinations of the bare states  $|f\rangle$ ,  $|e\rangle$  and  $|g\rangle$  and getting admixed via the angle descriptions  $\theta(t)$  and  $\rho(t)$ . Of special interest for STIRAP is the dark state  $|\chi_0\rangle$ ; compare Fig. 3.2. It only consists of the bare states  $|f\rangle$  and  $|g\rangle$ . The state  $|e\rangle$  is associated with incoherent losses; see Sec. 3.1.3, and should never be populated during STIRAP. Therefore, the state  $|\chi_0\rangle$  features a certain robustness against losses paving an elegant pathway between the Feshbach and the ground state. The mixing angle  $\theta(t)$  therefor adjusts the respective state contributions. Its time dependence is given by the time dependent Rabi frequencies  $\Omega_{P/S}(t)$  and governs the adiabatic state exchange, which is the key idea of the STIRAP:

- Before the actual STIRAP transfer starts, the molecule population is initialized in the state  $|f\rangle$ ; see Fig. 3.2 time  $t = t_0$ . The application of Stokes laser ( $t_1$ ) increases the respective Rabi frequency ( $\Omega_S \neq 0$ ,  $\Omega_P = 0$ ) and also raises the eigenfrequency  $\Omega_0$ . The complete three-level system has to be treated now in the dressed state picture. The initialized dark state is only composed of the Feshbach molecule state  $|\chi_0\rangle = |f\rangle$  as the mixing angle is expressed as  $\theta(t_1) = 0$ .

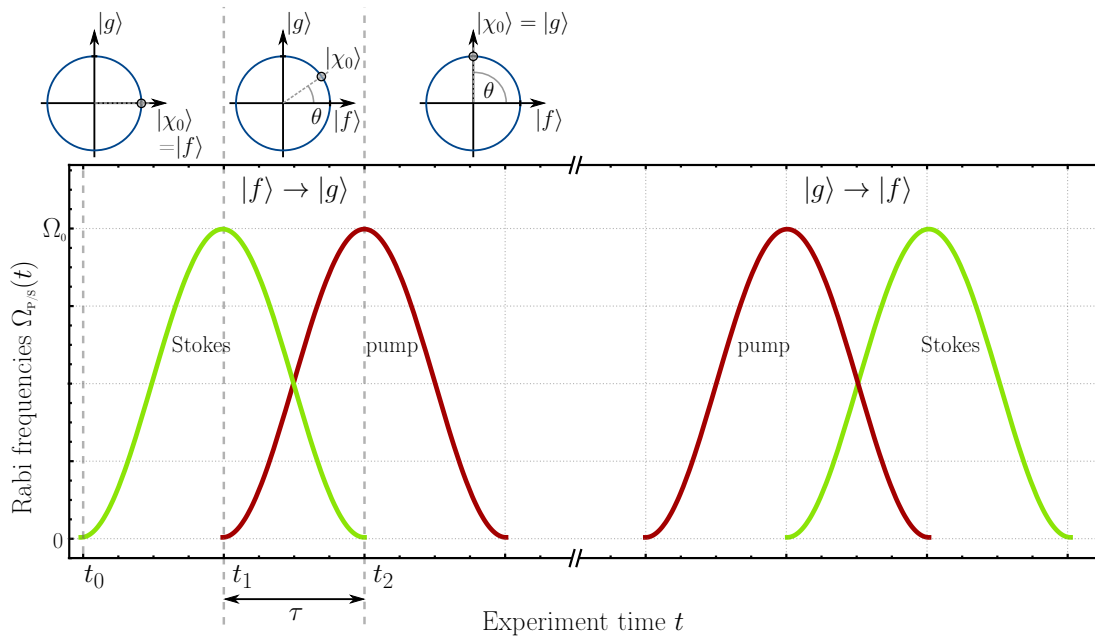


**Figure 3.2:** STIRAP transfer scheme. This plot shows the ideal STIRAP transfer scheme. At  $t = t_0$  all molecules are in state  $|f\rangle$ . From  $t_1$  to  $t_2$  the Stokes laser is ramped down, while the pump laser is ramped up, which represents the typical counterintuitive pulse sequence. After that, the molecule population is in the state  $|g\rangle$ . The representation of the dark state composition  $|\chi_0\rangle$  according to the mixing angle  $\theta$  is shown in the upper part of the picture. The backwards transfer is shown in the right part, where the pulse sequence is time reversed. Note, that the labeling of the pulses is according to the forward STIRAP, see text.

- Admixing the second laser ( $t_1 < t < t_2$ ), the pump laser increases the pump Rabi frequency ( $\Omega_S \neq 0$ ,  $\Omega_P \neq 0$ ). This changes the mixing angle  $\theta$  and the dark state  $|\chi_0\rangle$  becomes a superposition of both the states  $|f\rangle$  and  $|g\rangle$ ; compare Eq. 3.5. This stage is the actual state transfer. To maintain the eigenfrequency of the system,  $\Omega_0$  is kept constant. Therefore, the Stokes laser is lowered in power while the pump laser is increased. Thus, reasonable pulse sequences are sine and cosine functions. The change of Rabi frequency must be adiabatic to allow the dark state to follow the state exchange.
- STIRAP is completed, when  $\Omega_S = 0$  and  $\Omega_P \neq 0$ . The mixing angle is then  $\theta(t_2) = \pi/2$  and the dark state is purely the ground state  $|\chi_0\rangle = |g\rangle$ . Afterwards, the pump laser is ramped down to return to the bare states.

Theoretically, STIRAP works best when  $\Omega_{S,\max} = \Omega_{P,\max}$  and the state exchange ramp is fully symmetric. The pulse sequence can be reversed to transfer ground-state molecules back to the Feshbach-molecule state; see Fig. 3.2. This is typically done in the experiments to image the Feshbach molecules or atoms.

In theory, STIRAP efficiency can reach 100%. In reality, the three-level system is not closed, due to nonadiabatic state admixture of bright states or excitations through phase noise. Moreover, the molecular level structure yields several states, far from or close by the STIRAP transitions, interfering with the STIRAP states or acting as off-resonant loss channels, in which molecules get pumped and consequently get lost. Also the coherence of the entire dressed system can get lost partially when laser phase noise exists. The modeling of irreversible losses from additional states is detailed in the next section below.

### 3.1.3 Losses

Losses during STIRAP are typically associated with spontaneous decay from the molecular  $\Lambda$ -system. The ground state  $|g\rangle$  is assumed to be stable regarding single molecule decay<sup>1</sup>. Feshbach molecules, on the other side, decay relatively fast, yielding lifetimes of several hundreds of  $\mu\text{s}$ ; see Chap.2 [87]. Nevertheless, this loss can be neglected when STIRAP transfer is finished after a few tenth of  $\mu\text{s}$ .

The most critical states for STIRAP are the excited states  $|e\rangle$ . They possess relatively large linewidths of approximately  $\Gamma_{\text{NaK}} \approx \sqrt{\Gamma_{\text{Na}} + \Gamma_{\text{K}}} = 2\pi \times 11.5 \text{ MHz}$ , in case of  $^{23}\text{Na}^{39}\text{K}$ , and corresponding lifetimes of several hundreds of ns. Thus, each excitation to this state leads to an incoherent decay of the molecule to an unobservable state and it is lost in the experiment. To incorporate this spontaneous decay to the aforementioned model, an open quantum system has to be considered. To do so, a new state  $|l\rangle$  is introduced, which is not coupled to other states by means of coherent transitions; see Fig.3.1. The state vector expands to  $|\Phi\rangle = [\phi_f(t), \phi_e(t), \phi_g(t), \phi_l(t)]^T$ . The respective Hamilton operator reads:

$$H_\gamma(t) = \frac{\hbar}{2} \begin{bmatrix} 0 & \Omega_P(t) & 0 & 0 \\ \Omega_P(t) & 2\Delta & \Omega_S(t) & 0 \\ 0 & \Omega_S(t) & \delta & 0 \\ 0 & 0 & 0 & \gamma \end{bmatrix}. \quad (3.13)$$

$\gamma$  is an arbitrary variable. This assures a normalized population during all evaluation processes of the model. Since the Hamilton operator is still unitary, the Schrödinger equation still describes the reversible STIRAP process through the states  $|f\rangle$ ,  $|e\rangle$  and  $|g\rangle$ , while including now a state  $|l\rangle$  for the modeling of losses. The complete process including losses is modeled by a master equation in Lindblad representation. The von-Neumann equation with the time irreversible decay from the states  $|e\rangle$  to  $|l\rangle$  reads

$$\dot{\rho}(t) = -\frac{i}{\hbar}[H_\gamma(t), \rho(t)] + \Gamma D[A_e]\rho(t). \quad (3.14)$$

Here,  $\rho(t) = |\Phi\rangle\langle\Phi|$  is the density matrix and  $D[\cdot]$  is the Lindblad superoperator [101]. The corresponding jump operator  $A_e$ , which induces the state changeover from  $|e\rangle$  to  $|l\rangle$ , is written as

$$A_e = \begin{bmatrix} 0 & 0 & 0 & 0 \\ 0 & 0 & 0 & 0 \\ 0 & 0 & 0 & 0 \\ 0 & 1 & 0 & 0 \end{bmatrix}. \quad (3.15)$$

Note, that the jump operator  $A_e$  is not unitary, representing the irreversibility of the decay.

In the publication P3 in Sec.5.3 [89], a similar model is described, which is extended by two additional excited states.

Note that the effect of phase noise from the laser light fields are not considered in this model. A model for the effect of laser phase noise on the transfer efficiency in STIRAP can be found in [102].

Based on this model, I will now discuss in the following Sec.3.1.4 the limits of the STIRAP pulses regarding the transfer efficiency to find constraints for a later design and construction of the Raman laser system.

<sup>1</sup>Losses from  $|g\rangle$  will occur by sticky collisions [67–70] of two molecules or unwanted excitation of molecules to additional intermediate states [86, 100]. Those losses are recently under investigation in several molecular quantum gas experiment but do not contribute to the investigations concerning molecule preparation.

### 3.1.4 Constraints and Limits

The efficiency of STIRAP is limited by the applied pulse duration, either in the limit of short pulses through adiabaticity or in the limit of long pulses through coherence.

For short pulses, the adiabaticity of the state exchange and pulse overlap constrains the efficiency. If the pulses are too fast, and the transfer time  $\tau$  is too short, the dark state cannot follow and state admixture of the unwanted bright states  $|\chi_+\rangle$  and  $|\chi_-\rangle$  may occur [99]. According to that, the nonadiabatic state coupling between the dark state  $|\chi_0\rangle$  and the bright states  $|\chi_+\rangle$  and  $|\chi_-\rangle$  must be small compared to the separation of their eigenenergies  $\omega_+$  and  $\omega_-$  (Eqs 3.9 and 3.10) [103]. This is expressed by

$$\left| \left\langle \chi_{+/-} \left| \frac{d}{dt} \right| \chi_0 \right\rangle \right|^2 \ll |\omega_{+/-}|^2 . \quad (3.16)$$

The values of the eigenenergies  $|\omega_{+/-}|$ , in case of a resonant STIRAP ( $\Delta = 0$  and  $\delta = 0$ ), are described only by the eigenfrequency  $\Omega_0$  with  $\omega_{+/-} = \hbar\Omega_0/2$ . The STIRAP protocol described in Sec. 3.1.2 uses sine and cosine function which maintains the eigenfrequency  $\Omega_0 = \text{const.}$  during the state exchange. In other words,  $\Omega_0$  dictates the rate, with which a nonadiabatic state exchange may happen. Thus, the STIRAP transfer rate  $1/\tau$  must be faster than  $\Omega_0$  to prevent the system to undergo state changes [104]. The limit can be also expressed as

$$1 \ll \Omega_0 \cdot \tau . \quad (3.17)$$

For STIRAP in molecular systems,  $\Omega_0$  should be of the same order as the linewidth of the excited state. Typically, this is a few MHz, which is also practically feasible from the technical

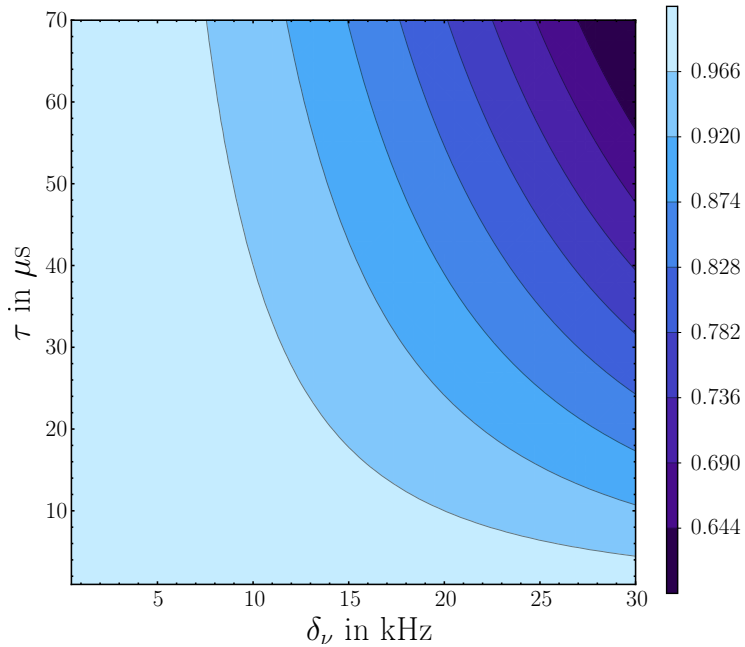


**Figure 3.3:** STIRAP efficiency dependent on the relative laser linewidth and pulse duration. In this figure a contour plot of the STIRAP single-trip efficiency is shown. The efficiency depends on the relative linewidth  $\delta_\nu$  and the pulse duration  $\tau$  and is modeled by applying Eq. 3.18 under the assumption of sine and cosine pulses and uncorrelated phase noise. STIRAP efficiency decreases drastically, when  $\delta_\nu$  or  $\tau$  increases. Maintaining a high efficiency, both should be as small as possible.

point of view; see Sec.3.2.2. When  $\Omega_0 = 2\pi \times 2 \text{ MHz}$  is assumed; e.g. from estimates in Chap. 4, the lower limit for the transfer time is  $\tau \gg 0.5 \mu\text{s}$ .

The upper limit on the pulse duration, on the other hand, is fastened by the relative phase noise of the two independent laser fields. This obstacle is also vastly discussed and researched [105–107]. For the case of sine and cosine pulses and two uncorrelated laser noises the transfer efficiency is expressed by

$$P_{\text{STIRAP}} = \exp\left(\frac{-\delta_\nu^2 \Gamma \tau}{2\Omega_0^2}\right), \quad (3.18)$$

where  $\Gamma$  is the linewidth of the excited state and  $\delta_\nu$  is the two-photon frequency distribution [106]. Figure 3.3 shows a contour plot of Eq.3.18 with  $\tau$  and  $\delta_\nu$  as variables for the ideal case of uncorrelated phase noise and sine and cosine pulse forms [106]. The linewidth is estimated to  $\Gamma = 2\pi \times 10 \text{ MHz}$  and the eigenfrequency to  $\Omega_0 = 2\pi \times 2 \text{ MHz}$ .

One can see that for high transfer efficiencies shorter pulses and narrower two-photon linewidths are required. Note, that this will be in conflict with the adiabaticity criteria for very short transfer times. Anticipating results from Sec.3.2.3, in this case, the mean noise distributions can be estimated to be approximately  $\delta_\nu = 2\pi \times 11 \text{ kHz}$ . Transfer times between 10 and 20  $\mu\text{s}$  should be suitable for high efficient STIRAP. Nevertheless, an increased noise budget may rapidly decrease the transfer efficiency, thus a well understood locking system is required.

## 3.2 Construction of the Raman Laser

The Raman laser system is the key element for the coherent transfer of the weakly bound dimers to the ground state. The laser system was planned and constructed according to the requirements for the STIRAP explained above in Sec. 3.1.4. Hence, the laser should deliver a relative linewidth below 10 kHz with Rabi frequencies for the pump and Stokes transitions of some MHz. Assuming dipole transition matrix elements of 0.056 D [108] and planning for beam foci of 50  $\mu\text{m}$  and Rabi frequencies of 1 MHz, the required laser power is about 0.1 W for each beam.

In theoretical and experimental work [108, 109] pathways for the STIRAP, regarding the singlet-triplet mixing and the Franck-Condon overlap, have been proposed. Relying on these findings, wavelengths of approximately 816 nm for the pump and 573 nm for the Stokes transition are anticipated; see Fig. 3.4. The 816 nm laser light can be easily generated with a high power output by diode laser and tapered amplifier (TA) systems. In case of 573 nm diode lasers are not available. Typically dye lasers can deliver these wavelengths with a high power output. Nevertheless, dye lasers suffer from a bad reputation as they are known to be relatively unstable, require constant maintenance and use hazardous dyes. An alternative way to generate 573 nm laser light is by using a diode laser at 1146 nm and a subsequent second-harmonic generation (SHG) process. The advantage is, that the components rely on solid state materials and are therefore relatively robust and need less maintenance than dye lasers. The major disadvantages are that SHG processes are inefficient and already existing laser noise increases during the SHG.

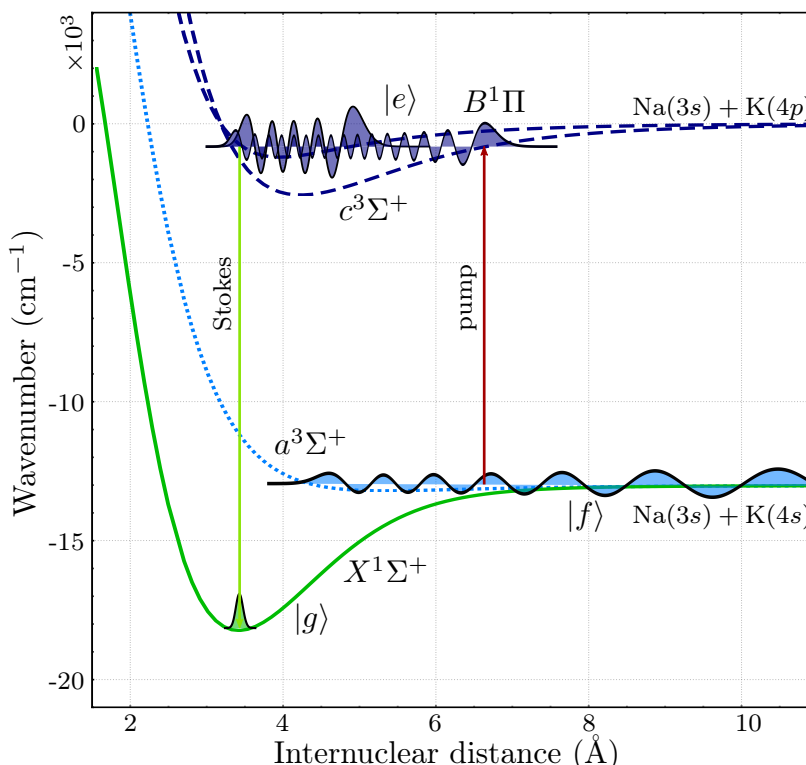


**Figure 3.4:** STIRAP pathway. This picture summarizes the envisioned states for STIRAP. According to the corresponding transition frequencies, the STIRAP Raman laser system was built. Singlet-triplet mixing is assured due to the strongly coupled states  $|B^1\Pi, v=8\rangle$  and  $|c^3\Sigma^+, v=30\rangle$  (dark blue). The wavefunction overlap for the Franck-Condon principle is visualized by the drawn wavefunction for the Feshbach molecule state  $|f\rangle$  (light blue), the excited state manifolds  $|e\rangle$  (dark blue) and the ground state  $|g\rangle$  (green). Wavefunctions are not to scale.

The setup built during this thesis, for a schematic drawing see Fig. 3.5, consists of commercial external-cavity diode lasers and self-built TAs for 816 nm and 1146 nm as well as a self-built bow-tie resonant doubling cavity for the SHG to create 573 nm light; see Sec. 3.2.2. As a relative frequency reference a vacuum housed ultra-low expansion glass (ULE) high finesse cavity is set up, where both infrared lasers are referenced on; see Sec. 3.2.1. For the widely tunable laser locks, side-band Pound-Drever-Hall locking techniques are used; see Sec. 3.2.3.

During the course of this thesis the laser system was intensively used for the excited and ground state spectroscopy; see Sec. 4 and the ground-state molecule preparation; see Sec. 5. In future, it will be an essential part of the experiment to routinely prepare ground-state molecules.

In the following I will detail the construction and characterization of the STIRAP laser. I will begin with the details about the high finesse ultra-low expansion glass cavity in Sec. 3.2.1 and the design of its cavity mount and vacuum housing. In Sec. 3.2.2 I will explain the generation of the laser light for the pump and Stokes transitions. Finally, I will describe the laser locks and their characteristics and the pulse application in Sec. 3.2.3.

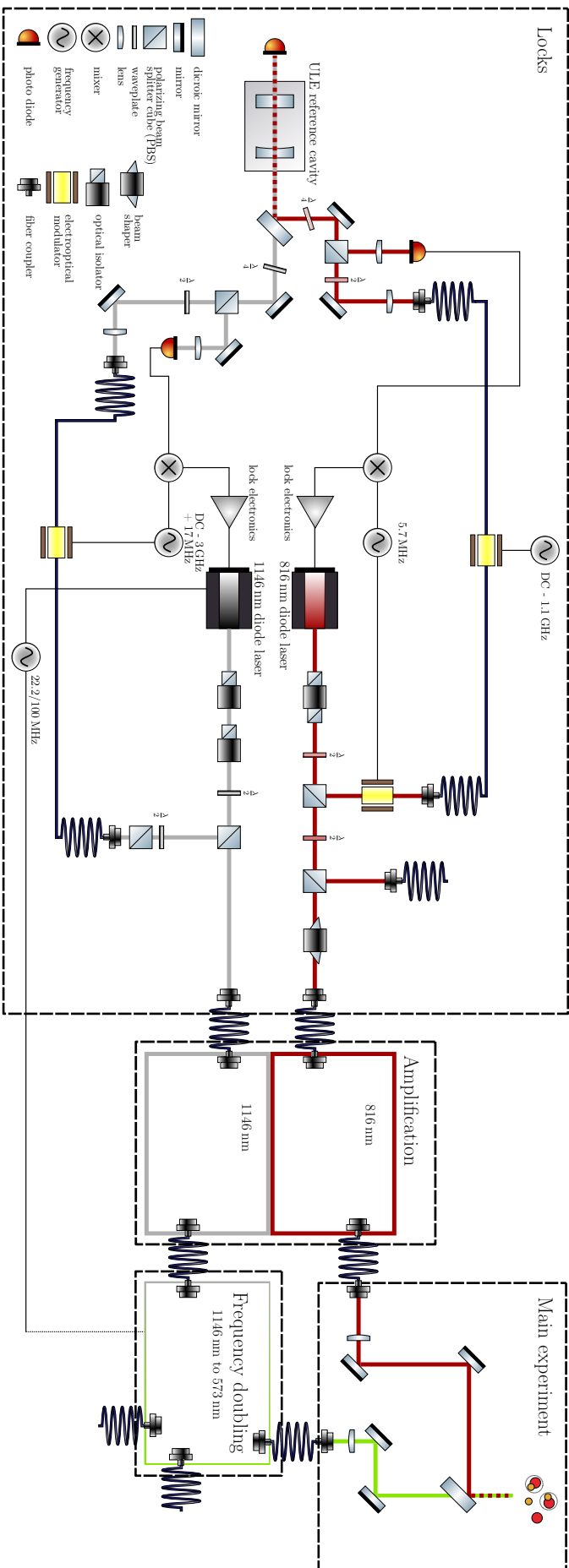


**Figure 3.5:** Overview of the STIRAP laser system. The laser system is divided into three boxes: the box with the laser light generation and locking (details see Fig. 3.17), the amplification box (Fig. 3.11), and the frequency doubling box (Fig. 3.14). 816 nm light is sent to the main table directly after amplification. 573 nm light is created beforehand in a second harmonic generation process. Both lights are focused to the position of the atoms and molecules and overlapped at the main experiment (Fig. 3.21).

### 3.2.1 High Finesse Reference Cavity

To create a coherent laser source from two independent lasers to bridge the frequency gap between the Feshbach molecule state and the ground state of about 155.8 THz, an external reference for stabilization is required. For this experiment a single high finesse ULE cavity is used, to which both lasers are referenced simultaneously. Thus, the lock fastens the relative frequencies of the lasers and narrows their linewidths.

To maintain short term and long term stability of the cavity, the entire ULE setup is housed inside a vacuum chamber to guard the ULE cavity from thermal fluctuations, air turbulence and dust deposition. The cavity itself consists of two ULE mirrors with a high reflection coating for the wavelengths 816 and 1146 nm bonded to a ULE spacer, which is held onto a self-built holder. The vacuum setup, and thus the entire cavity, is permanently heated. All lasers and the cavity setup are housed in a temperature stabilized box which is positioned under a temperature stabilized flow box. The total laser system is built onto an air-damped optical table with additional vibration isolation breadboards for seismic and acoustic noise reduction. In the following the experimental realization is described in detail.

#### ULE-Spacer

The cavity is a commercial cavity assembly bought from *Melles Griot BV* in cooperation with *Advanced Thin Films*. Cavity parameters can be taken from Tab. 3.1. The cavity consists of two mirrors and an open cylinder-like spacer made from ULE glass. The mirrors have a high-reflection coating on the optical surface which is optimized for the wavelengths 816 nm and 1146 nm. The polished surfaces on the mirrors are bonded to the ULE spacer. The curvature of the mirrors and their spacing constitute a semifocal configuration which guarantees optical stability. The expansion coefficient's zero of the ULE glass material is assumed to be at 25 °C. The whole cavity holder and vacuum chamber therefor are stabilized to this value to maximize resonance stability.

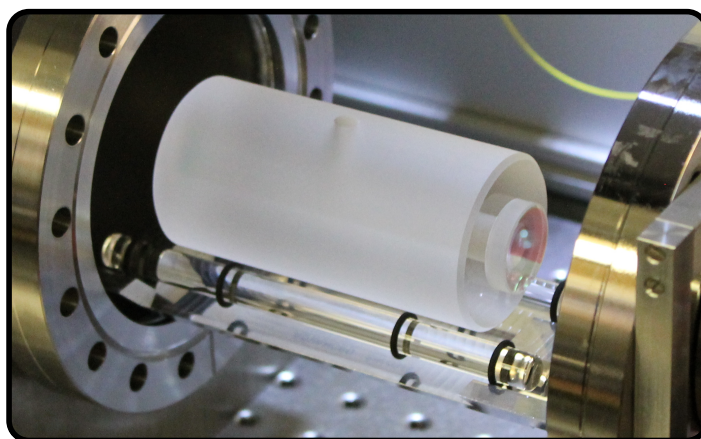


**Figure 3.6:** Real life ULE cavity picture. This picture was taken, when the ULE cavity was placed on the holder during the vacuum assembly process. The cavity holder is mounted to the modified flange, which is held in this picture by the horseshoe-like bar; see Fig.3.10. Later, the flange with the cavity is held by the vacuum chamber itself and the horseshoe is removed from the setup.

**Table 3.1:** Mechanical and optical properties of the ULE reference cavity, taken from the datasheet<sup>a</sup> or measured<sup>b</sup>

	Symbol	Value
outer diameter, spacer <sup>a</sup>	$D_{\text{out}}$	50 mm
inner diameter, spacer <sup>a</sup>	$D_{\text{in}}$	12.7 mm
Length, spacer <sup>a</sup>	$L$	100 mm
Curvature, $M_1$ <sup>a</sup>	$R_1$	500 mm
Curvature, $M_2$ <sup>a</sup>	$R_2$	$\infty$
FSR <sup>a</sup>	$\Delta\nu_{\text{FSR}}$	1.499(1) GHz
Linewidth, 816 nm <sup>b</sup>	$\delta\nu_{1/2_{816}}$	60.2(2) kHz
Finesse, 816 nm <sup>b</sup>	$F_{816}$	24900(85)
Linewidth, 1146 nm <sup>b</sup>	$\delta\nu_{1/2_{1146}}$	40.0(2) kHz
Finesse, 1146 nm <sup>b</sup>	$F_{1146}$	37400(180)

### Vacuum and Cavity Holder

The ULE cavity was purchased without holder or any additional optomechanical element. Consequently, a holder had to be designed, whose realization is described below. For the most stable positioning, the ULE cavity should rest on three points. This promises the highest stability against disposal but is also challenging to realize, especially for a cylindrical spacer. Instead, a symmetric four-point mount is realized, which is cautiously analyzed regarding the mechanical properties of the cavity. The position of the supporting points on the ULE glass can influence the bending of the cylindrical spacer and the attached mirrors due to accelerations. This leads to changes in the total length  $L$  and the angle  $\phi$  of the mirrors; see Fig.3.7, which consequently leads to changes of the cavity resonance frequency and in the worst case to additional noise on the locked lasers. In case of a straight thin cylinder the theories of Bessel and Airy hold [110, 111]. Accordingly, the best supporting point with minimal length change over the entire cylinder would be at  $0.22031 L$  from the cylinder's ends. However, the cavity spacer itself is not a perfect thin cylinder and the supporting points do not touch the symmetry plain of the spacer ( $\theta = 90^\circ$ ; compare Fig. 3.7) as this is mechanically unpractical. Consequently, the mechanical properties are different and a detailed analysis is needed.

To understand the effects of acceleration to the cavity a finite elements method (FEM) simulation with respect to the angular and longitudinal position of the supporting points was carried out. The simulation was executed with the *Environment/Stress Analysis* plug-in of the *Autodesk Inventor Professional 2017* software. An example of the FEM simulation is shown in Fig. 3.7.

A CAD-model of the cavity was not available. Therefore, an own CAD model was developed. Importantly, the mechanical properties of the ULE glass were cautiously implemented. The Young's Modulus was set to  $E = 67.6$  GPa, Poisson's ratio to  $\nu = 0.17$ , the Shear Modulus to  $G = 29.0$  GPa and the density to  $\rho = 2.21$  g/cm<sup>3</sup>. The mirror surface curvatures were not modeled and the ULE parts (two mirrors and spacer) were treated as a single solid object. The positions of the supporting points were always chosen to be symmetric to the cavity center during the entire analysis. As supporting points extruded rings with the dimensions and material properties of commercial rubber Viton rings were used.

The application of the acceleration was set to an overall one of  $g = 9.81$  m/s<sup>2</sup> on all pieces simultaneously, where only the inner surfaces of the Viton rings were fixed in space. From a modal analysis on the ULE cavity the first resonant eigenmode was found to appear above

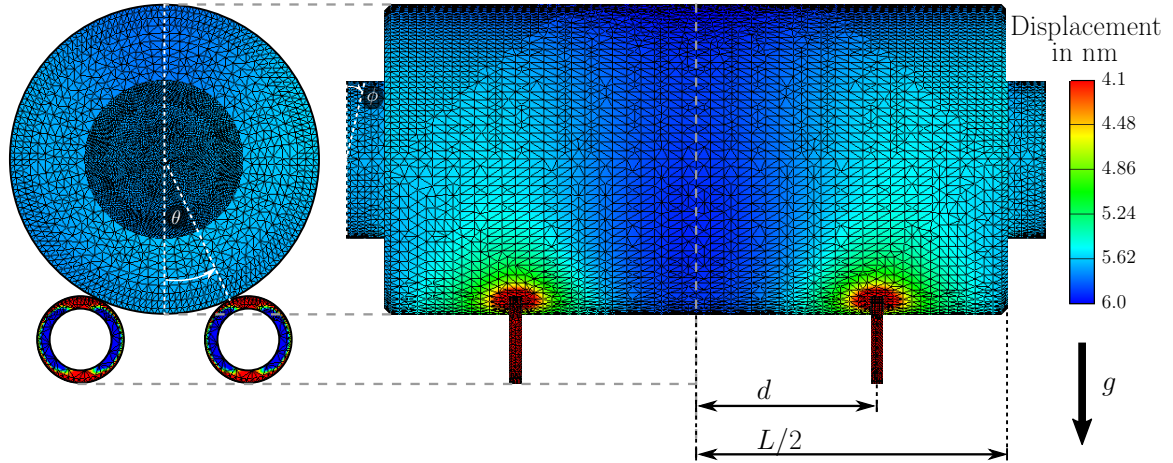


**Figure 3.7:** FEM simulation of the reference cavity. In this picture the displacement of the cavity along the axis of gravity  $g$  is shown, when a constant force of  $g = 9.81 \text{ ms}^{-2}$  is applied to the entire cavity. The displacement is given by the miscolored scale. The position of the supporting points is given by the distance  $d$  to the center of the spacer and the radial angle  $\theta$ . The angle  $\phi$  shows the resulting mirror tilt. Also the mesh, which was used for the simulations, is shown.

16 kHz, which is fast compared to critical noise in the lower acoustic regime. Therefore, it is valid to still use the FEM-simulation as in the applied case changes to the cavity length can be treated as quasi static for low frequencies. The results of the analysis are shown in the figures 3.8 and 3.9 for longitudinal displacements  $d$  of the supporting points along the z-direction relative to the cavity's center plane and as a function of angle  $\theta$  around the optical axis, respectively; compare Fig. 3.7. The frequency change of the cavity resonance for the two relevant laser colors is expressed as acceleration sensitivity  $\kappa_z = [\text{kHz}/\text{ms}^{-2}]$ . For the longitudinal change in position a slowly varying regime was found around  $d = 30 \text{ mm}$ ; see Fig. 3.8 (a). In this region the overall frequency change due to gravity is on the one hand maximal with  $83.5 \text{ kHz}/\text{ms}^{-2}$  for 816 nm and  $59.4 \text{ kHz}/\text{ms}^{-2}$  for 1146 nm light, but also on the other hand insensitive to the supporting point displacement. At the same time the mirror tilt  $\phi$  becomes zero at  $d_{\text{Airy}} = 28.5 \text{ mm}$ , as it is expected from the Airy point at  $0.2113 L$ . The

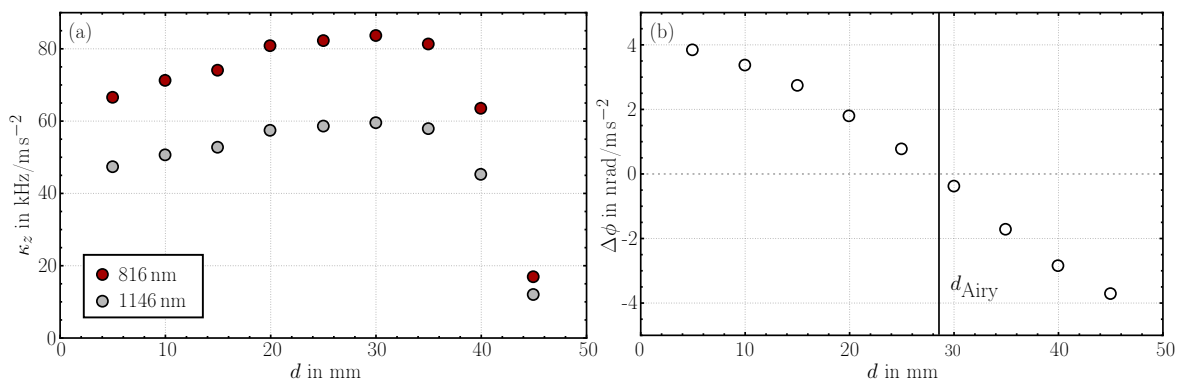


**Figure 3.8:** Results from the FEM simulation with respect to the supporting point position along the optical axis. (a) The acceleration sensitivity for 816 nm (open red circles) and 1146 nm (open gray circles) light in the cavity dependent on the supporting point position  $d$ . The higher sensitivity for 816 nm is due to its shorter wavelength in comparison to 1146 nm light. (b) Angular displacement of the cavity mirrors' surfaces dependent on  $d$ . On the Airy point  $d_{\text{Airy}}$  (solid black line) the angle is zero, which is in agreement with the expectations, see text. The simulation was carried out with a supporting point angle  $\phi = 33^\circ$ .

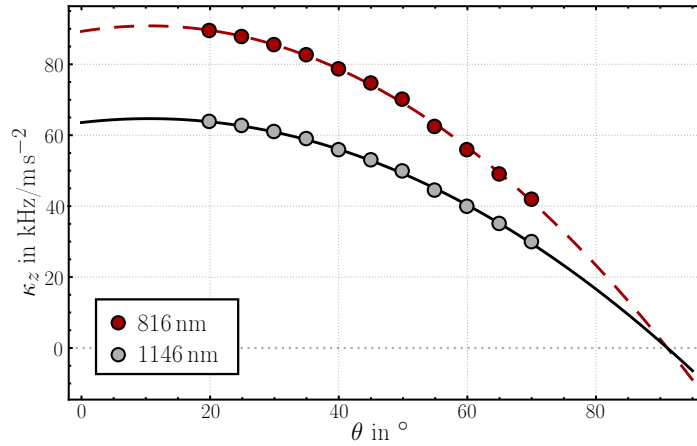


**Figure 3.9:** Results from the FEM simulation with respect to the supporting point angle. The longitudinal supporting point position was chosen to be  $d = d_{\text{Airy}}$ . Clearly, the acceleration sensitivity  $\kappa_z$  decreases with higher angle. Note, that an angle of  $90^\circ$  corresponds to the symmetry position of the cavity; see Fig. 3.7, at which  $\kappa_z$  is expected to be zero. The curves are second order polynomial fits for an estimation on  $\kappa_z$  close to  $90^\circ$ .

fact, that at the Bessel point the acceleration sensitivity has its maximum can be explained by the non-axial placement of the supporting points, thus the push towards and the pull away of the ULE spacer material from the supporting points of accelerations along the direction of gravity do not compensate each other. Therefore, the acceleration sensitivity dependent on the supporting point position angle  $\theta$  to the central plain; see Fig. 3.9. One can see, that for an angle close to  $90^\circ$   $\kappa_z$  approaches zero. As at this point the FEM simulation does not hold due to the construction of the cavity holding system, there are no simulation results for  $\theta > 70^\circ$ . The curves in Fig. 3.9 are simple second order polynomial fits to the FEM simulation results below  $\theta = 70^\circ$  to get a quantitative trend of the results for higher angles.

Nevertheless, for the proposed cavity supporting scheme there is no reasonable point with the acceleration sensitivity vanishing. For geometric stability reasons, the confirmed Airy point at  $d_{\text{Airy}} = 28.5$  mm with an angle  $\theta = 33^\circ$  was chosen for the construction of the cavity holder. A further minimization of the acceleration sensitivity is not necessary because low frequency ( $< 1000$  Hz) seismic noise is damped through the pneumatic vibration isolation of the optical table and additional vibration isolation breadboards by more than two orders of magnitude [112] and acoustic noise ( $> 1000$  Hz) is damped through the minimized surface contact of the cavity through the Viton rings and the vacuum sealed chamber.

According to these considerations, the cavity holder and the vacuum system have been designed. The holder consists of a monolithic aluminum piece with a wide cut-out for the cavity and four smaller cut-outs for two supporting glass rods; see Fig. 3.10. The aluminum holder is attached by three screws to the entrance flange such that the cavity's optical axis fits the middle of the entrance window. On each glass rod four Viton rings are imposed. Two serve as supporting points of the glass rod to the aluminum holder and of the cavity to the glass rod, respectively; see Fig. 3.10. The glass rods were chosen for the low heat conductivity coefficient of glass. The Viton rings further decrease the heat flow through their small contact points and additionally reduce vibrations through their rubber material.

The vacuum chamber consists of a commercial CF 100 pipe with attached CF 40 nipples in a cross configuration. The CF 100 flanges are used as entrance and outlet ports for the laser beams. Two CF 100 blank flanges were customly modified to attach a CF 40 window with centered optical axis to it, respectively. To avoid reflections between the non coated vacuum

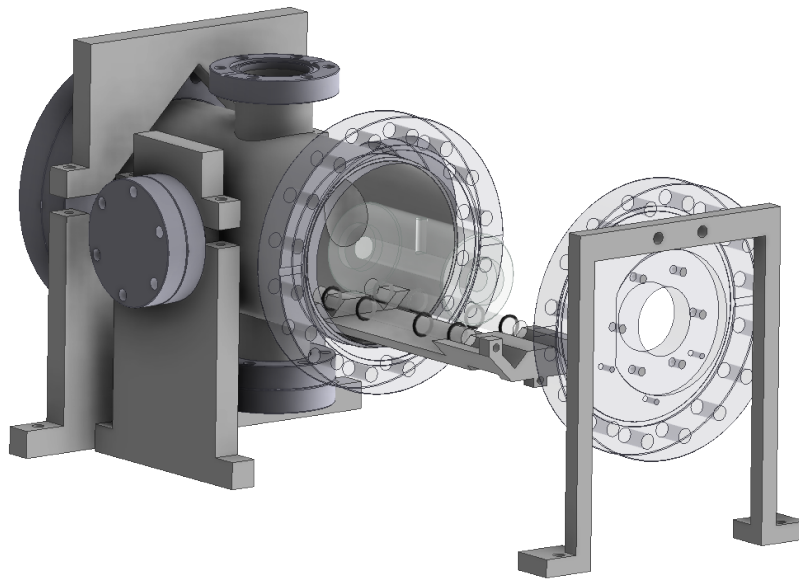


**Figure 3.10:** CAD explosion drawing of the vacuum chamber and the cavity holder. This figure is a drawing of the most important vacuum components and their relations. The center part is the ULE cavity, which rests on the Viton ring covered glass rods. They lay on the newly designed holder, which is screwed to the modified blank flange. The vacuum chamber is held by the chamber carriers. For visibility reasons only two carriers are displayed. Windows, vacuum crosses and pumps are not shown. For further explanations see text.

windows and the flat cavity mirror surfaces the windows are attached at a horizontal angle of  $4^\circ$ ; see Fig. 3.10. Moreover, the entrance blank flange has three mounting holes on the inside to attach the cavity holder to it and a single hole on the outside to place a temperature sensor for stabilization and readout purposes. The chamber is held in place and prevented from rotations by 4 chamber carriers, which are custom made. They consist of V-shaped bars to support the CF 100 and CF 40 nipples and set the optical axis of the ULE cavity to 10 cm above the breadboard. To fix the chamber position, each carrier is closed by an additional V-shaped bar through two screws from the top. The metal horseshoe visible in the front part of Fig. 3.10, and also partially in Fig. 3.6, was only used for the cavity adjustment, as the horseshoe holds the flange and the cavity while assembling the vacuum chamber. It was removed later, when the CF 100 flange supports the entrance flange and thus the cavity holder.

To the upper CF 40 nipple a T-part is connected (not shown in Fig. 3.10), which is used for connecting the pumps. One part is connected to a valve which was used to induce the vacuum through a Turbo molecular pump and was closed afterwards. The other part is connected to a Varian Diode 7 kV ion getter pump which is controlled by a MidiVac controller. It is constantly pumping and holding a pressure of approximately  $p = 3 \cdot 10^{-8}$  mbar which is sufficient to eliminate temperature and air fluctuations. Note, that the MidiVac controller produces disturbing EM-radiation which can couple to the locking circuits for the STIRAP laser lock. Therefore, the controller is placed as far away from the locking electronics as possible.

### Temperature Stability

To protect the STIRAP laser system from temperature fluctuations occurring typically during the course of the day in the laboratory, the entire setup is temperature stabilized in a multiple

stage style. All critical optical components, such as laser sources, locking optics, EOMs and the ULE reference cavity are combined in one box. The vacuum chamber and with this the ULE cavity itself are temperature stabilized by heating the entire chamber to 25 °C through heating pads attached to the outside of the vacuum chamber. For the stabilization, the temperature is referenced by a NTC thermistor glued into the entrance flange and a self-built temperature controller with subsequent output power stage. From the specifications for the ULE material of the cavity, the mean linear thermal expansion coefficient is  $0 \pm 30$  ppb/°C in a range from 5 to 35 °C.

The vacuum chamber serves as the hottest point in the box, so every temperature fluctuation coming from the inside or the outside of the box has to pass at least one regulation circuit.

In the same box also the 816 nm pump laser source and the 1146 nm Stokes laser source are housed; for their description see Sec.3.2.2 below. The 816 nm diode laser is heated to 22.300(1) °C to guarantee single mode operation, the 1146 nm diode laser is stabilized to 19.000(1) °C, both by their own internal temperature controls. The box itself maintains a stable temperature of 23.0(5) °C. The Peltier elements for the box stabilization are implemented into the top covers for two reasons. First, the heated air coming from the vacuum chamber raises upwards, second, the top cover has the best thermal contact to the environment with the continuous laminar air flow with 21.3(1) °C from the flow boxes right above.

The box itself is covered into a pyramid foam to reduce acoustic noise from the environment to the laser system. The foam also serves as thermal isolation. Finally, the optical table is housed in a self-built cover structure to prevent massive air exchange with the laboratory environment.

### 3.2.2 Laser Light Generation

The laser for the STIRAP Raman laser system consists of two infrared laser sources, one with a wavelength of approximately 816 nm and the other one with 1146 nm. For stability and low maintenance purposes, the laser system is built from solid state components only. To further increase the stability for short and long terms, the laser sources are housed in the same box as the ULE cavity, to which both lasers are referenced. To reach the necessary power for the STIRAP, both lasers are amplified by self-built tapered amplifier setups and the 1146 nm laser is subsequently frequency doubled in a self-built resonant bow-tie cavity to 573 nm laser light. A part of the respective light is sent to a wavemeter, for locking and surveillance purposes. The rest of the laser light passes acousto-optical modulators (AOMs) for the control of the power output. Finally, the light is transported through single mode polarization maintaining fibers to the main experiment table, where it is further cleaned in polarization and focused to the position of the molecules and atoms.

In the following the individual components of the laser system are detailed.

#### Diode Laser and Tapered Amplifier Setups

Solid state lasers provide a very good starting point for the generation of laser light for the STIRAP with the desired optical properties such as small linewidth and high laser power. As explained above, the laser linewidth for both lasers should be on the order of some kHz. On the one hand, the linewidth is actively decreased by the laser lock, on the other hand a free running narrow laser is beneficial and eases further experiments. The required powers for the STIRAP; see above; are provided by the TA setup. The laser setup is shown in detail in Fig. 3.5.

**Pump laser** The laser light for the 816 nm laser is generated by a commercial external-cavity diode laser (ECDL) DL pro from *Toptica photonics*. The laser is controlled by the DLC pro Digital Laser Controller. The nominal free running linewidth is < 10 kHz and the output power can reach up to 70 mW. The laser is delivered without internal isolation stage. Accordingly, directly after the laser output a two-stage 60 dB isolator from *Gsänger Elektrooptik* is placed. The polarization is corrected afterwards by a  $\lambda/2$ -waveplate, which is also used to adjust the power ratio at the two output ports of the following polarizing beam splitter cube (PBS). One output is used as a reference for the wavemeter (*High Finesse* WS6-200 with external 8-channel fiber switch), the other port is splitted again. One part is coupled to a polarization maintaining fiber going to the TA setup; see Fig. 3.11, the other part is coupled through a free space resonant electro-optical modulator (EOM) (*QUBIG* EO-6L3-NIR) to imprint the sidebands for the Pound-Drever-Hall (PDH) cavity lock, and afterwards to the EOM (*Photline* NIR-MPX-800-LN-05) fiber input which serves as the adjustable offset-sideband modulation of the laser; see Sec. 3.2.3.

The TA is seeded by the light provided by the fiber coupling coming from the ECDL. The fiber orientation at the outcoupler is chosen such that the outgoing polarization is suitable for the amplification in the TA. The TA chip is a bare c-mount TA-0800-2000-1 from *Toptica Photonics* with a free running spectrum of 786 to 815 nm with 6 dB below the peak output. In the experiment, the maximal seed power reaches 20 mW which is amplified by the TA chip to up to 3 W with an injection current of 3 A. The TA controllers for current and temperature are racked LDC 8040 and TED 8040 controller from *Thorlabs*, respectively, housed in a PRO 8000 rack. The TA mount consists of a self-built housing with integrated Peltier element temperature stabilization and injection and collimation lens holders. For

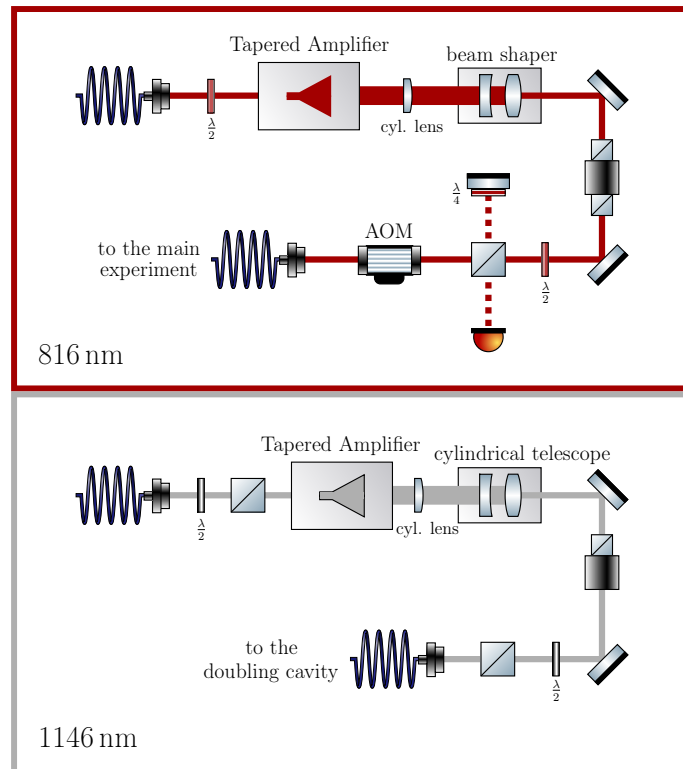


**Figure 3.11:** Drawing of the TA setup. Both setups, for the 816 nm and 1146 nm lasers, are similarly designed, constructed and housed in the same laser box. The 816 nm laser is coupled through an AOM and subsequently to an optical fiber to the main experiment table, the 1146 nm laser is just coupled to a fiber going to the doubling cavity. Consequently, the phase stabilization optics for the 816 nm laser are also housed in this box. Symbols according to Fig. 3.5.

controlling the beam shape a cylindrical  $f = 75$  mm lens is placed after the TA outcoupling lens to collimate the second uncollimated beam direction. An anamorphic beam shaper 5AN-3-V-05 from *Schäfter & Kirchoff* is used to decrease the beam aspect ratio from 3 : 1 to 1 : 1. Afterwards, a 50 dB two-stage FI-810-5SV optical isolator from *Qioptiq Photonics* is used to block back reflections from following optical elements to the TA, which could get amplified and subsequently distort the mode or even lead to the destruction of the TA chip. After the light passed the isolator its polarization is cleaned by a  $\lambda/2$ -waveplate and a PBS and it is coupled through an AOM using the first positive diffraction order. The its coupled to a polarization maintaining optical fiber which goes to the main experiment table. In total, 350 mW of light at 816 nm reach the main experiment table. The AOM is used at a fixed frequency of 200.7 MHz for switching and STIRAP pulse application. The frequency source is an *arduino nano*-based Direct Digital Synthesis (DDS) whose signal is divided and also used for the 573 nm AOM of the Stokes laser setup. This guarantees, that noise coming from the AOM frequency source is modulated to both lasers in the same way, minimizing its effects during STIRAP. On the experimental table, the light is again cleaned in polarization and focused to the position of the atoms and molecules; see Sec. 3.2.3 below.

**Stokes laser** The laser source for the Stokes laser is also a commercial DL pro 1146 nm ECDL provided by *Toptica Photonics*. It is controlled by the same digital controller as the 816 nm laser. The isolation is done directly after the laser output by two independent single stage free-space IO-4-1150-VLP optical isolators from *Thorlabs* with an isolation of 36 dB each. The total output power can reach 100 mW. After the isolation stage the laser power is divided

by using a  $\lambda/2$ -waveplate and a PBS. One part is cleaned in polarization by an additional PBS and coupled into the fiber for the sideband EOM (NIR-MPX-LN-05 from *Photline*) going to the reference cavity. The second part is coupled to a polarization maintaining fiber going towards the TA setup; see Fig. 3.11.

The TA setup is a self-built mount for the commercially bought c-mount TA-1150-0500-1 TA chip from *Toptica Photonics*. The temperature and current is controlled by racked controllers LDC 8040 and TED 8002 from *Thorlabs*, respectively, both housed in the same supply rack as for the 816 nm laser. From the data sheet, the total power can reach up to 500 mW in case of 60 mW incident seed power. The same data sheet, on the other hand, only allows for a maximal seed power of 32 mW lowering the total amount of amplified light to the measured total output power of 360 mW. To maximize the output power, the incident seed light is filtered by a  $\lambda/2$ -waveplate configuration and a PBS. After the integrated TA outcoupling lens a cylindrical  $f = 75$  mm lens is placed to collimate the still divergent light. Using a self-built cylindrical telescope ( $f = 50$  mm and  $f = -30$  mm), the beam's aspect ratio is changed from about 2 : 1 to roughly 1 : 1 to fit it through the aperture of the single stage free-space IO-4-1150-VLP optical isolator. After that, the polarization is cleaned and adjusted by a  $\lambda/2$ -waveplate and PBS combination before it is coupled to a polarization maintaining optical fiber which guides the light to the self-built resonant doubling cavity; see below.

Note, that the coupling between the molecular ground state and the excited state is fairly strong. Thus, only little light, approximately 100  $\mu$ W, is needed; see Chap. 5 [89]. For STIRAP, the TA amplification state is bypassed, to avoid probable noise. Then, the fiber output from the diode laser setup is directly used for the injection into the doubling cavity. Only for the experiments in Chap. 4 the TA was used.

### Resonant Frequency Doubling

The conversion of the fundamental 1146 nm to the second harmonic 573 nm laser light is a nonlinear process of second order. It is highly dependent on the properties of the non-linear medium as well as the fundamental laser field properties, namely laser intensity, beam profile and polarization. These properties are constraining each other for the choice of an accomplished frequency doubling system and have to be considered for the optimization of the effective conversion efficiency.

In general, high-harmonic generation is described by a nonlinear theory of light-matter interaction, which is detailed in several publications [113–119] and therefore is just briefly outlined in this work. Note, that necessary equations are not derived here but proper references with a detailed description are given accordingly.

During second-harmonic generation (SHG) (also known as frequency doubling) two identical photons with frequency  $\omega$  are converted to a single photon with frequency  $2\omega$  through the interaction with a nonlinear optical medium. This second-order process depends on the square of the incident light power and the non-linear properties of the medium. This can be seen in the general description of the polarizability  $P(t)$  of an optical medium through an electric field [119]:

$$\begin{aligned} P(t) &= \epsilon_0 \left[ \chi^{(1)} E(t) + \chi^{(2)} E^2(t) + \chi^{(3)} E^3(t) + \dots \right] \\ &= \underbrace{P^{(1)}(t)}_{\text{linear}} + \underbrace{P^{(2)}(t) + P^{(3)}(t) + \dots}_{\text{non-linear}}, \end{aligned} \quad (3.19)$$

where  $E(t)$  is the electric field and  $\chi^{(n)}$  is the susceptibility of order  $n$ . The first nonlinear term of the polarizability, the second-order term  $P^{(2)}(t)$ , describes the frequency doubling. Consequently, the SHG profits from a high  $\chi^{(2)}$  coefficient, which is given by the material

properties of the non-linear medium, and a high electric field  $E(t)$ , meaning a high laser power.

For an efficient SHG process using laser beams, phase matching has to be considered. It describes the phases relation between the fundamental (here the 1146 nm light) and harmonic mode (the 573 nm light) both propagating through the non-linear medium. For the frequency doubling this can be expressed in the phase mismatch [120]

$$\Delta k = k_2 - 2k_1, \quad (3.20)$$

where  $k_1$  and  $k_2$  are the wavenumbers of the fundamental and the second-harmonic waves, respectively. A good phase matching  $\Delta k \approx 0$  is important, as it means that the amplitude of the harmonic mode adds up through the entire length of the optical medium, which results in a high conversion efficiency. If there is a significant phase mismatch, the process of frequency conversion may reverse through the course of the optical medium.

In the following the mentioned parameters for the non-linear material, laser beam and phase matching are detailed.

**Non-linear crystal** From equation 3.19 one can see that the material for the SHG process determines strictly its efficiency. The choice of a proper crystal material is mandatory. Crystals like BBO (betabarium borate), BiBO (bismuth borate) and LN (lithium niobate) are typical choices for single homogeneous bulk crystals, since they possess high non-linear coefficients. LN for example has a nonlinear coefficient of the contracted nonlinear susceptibility tensor [119]  $d_{33} \gtrsim 20 \text{ pm V}^{-1}$  for the infrared spectrum [121], for which LN is typically used. BBO and BiBO, in contrast, are used for conversions of visible to ultraviolet light due to their transparency in this region of the electromagnetic spectrum. Bulk crystals benefit from the possibility to cut the surfaces in arbitrary configurations, allowing for example for Brewster angle cuts for polarization cleaning and reflection minimization purposes. This also allows to minimize or even compensate astigmatism occurring in a bow-tie cavity configuration; see paragraph below. Phase matching, analog to Eq. 3.20, is typically achieved through angle adjustment between the birefringent crystal axes and the light polarization, also known as critical phase matching. Hence, the phase matching condition is very sensitive to beam misalignment. Especially for frequency doubling applications, such as resonant doubling cavities, this is technically demanding, as both, the phase matching and the cavity's resonance condition and therefore the power build-up are dependent on the geometric beam alignment. On the other hand, noncritical phase matching, where no angle between the light modes exists, can be done by temperature tuning of the crystal's refractive indices.

Periodically poled (PP) crystals often use a kind of noncritical phase matching, although their crystal material normally would only allow for critical phase matching. They consist of a crystal material which is grown periodically with a change of  $90^\circ$  of the poling axis with a certain poling period  $\Lambda$ . In these crystals the fundamental and harmonic light would dephase in the course of their travel through a single poling period. When the dephasing reaches maximum the poling is reversed. Consequently, the dephasing reverses within the next poling period. The harmonic mode is not depleted but still maintained and further acquired by rephasing the fundamental mode until dephasing sets in again. Then the poling is reversed again. The poling period of the crystal has to be matched perfectly with the coherence length  $L_{\text{coh}} = 2/\Delta k$  of the fundamental and harmonic mode which is typically done by adjusting the temperature of the crystal [122]. This process is called quasi-phase matching (QPM). For PP crystals, the nonlinear coefficient is described by an effective one, called  $d_{\text{eff}}$ . Overall, the conversion efficiency in such crystals can overcome easily the one of bulk crystals. This loosens the typical requirements for high-harmonic generation which

**Table 3.2:** Properties of the nonlinear 5 %-doped MgO:PPLN doubling crystal from *Covesion*

	Symbol	Value
crystal dimensions	$L_{c,z}$	10 mm
	$L_{c,x}$	10 mm
	$L_{c,y}$	0.5 mm
lane spacing		0.2 mm
lane thickness (x)		0.5 mm
poling periods	$\Lambda$	8.7, 8.8, 8.9, 9.0, 9.1 $\mu\text{m}$
non-linear coefficient	$d_{\text{eff}}$	14 pm/V
absorption coefficient (fundamental)[123]	$\alpha_f$	0.01 $\text{cm}^{-1}$
absorption coefficient (harmonic)[123]	$\alpha_h$	0.02 $\text{cm}^{-1}$
AR coating (fundamental)	$T_{c,f}$	99.4%
AR coating (harmonic)	$T_{c,h}$	99.3%

are accurate crystal alignment, strong laser powers as well as small beam foci, of which the latter two could cause material damage due to self focusing effects. With PP crystals SHG processes for lasers with moderate laser powers are accessible.

For the SHG in this experiment, a fundamental laser power of approximately 200 mW is accessible. For this purpose a PP crystal is a suitable choice, as it provides the advantages described above. A 1 cm long bare 5 %-doped MgO:PPLN (periodically poled lithium niobate) crystal with an anti-reflection coating for the fundamental and harmonic wavelength from *Covesion* was chosen. The relatively short crystal length results from the constraints coming from the self-built bow-tie cavity, see paragraph below, which is used to further increase the fundamental mode intensity. All crystal properties are summarized in Tab. 3.2.

The choice of the poling period needs a modeling of the QPM by using the phase mismatch condition from Eq. 3.20. The temperature dependence of the phase mismatch originates mostly from the temperature dependent refractive indices  $n_e(T, \lambda)$  for the fundamental and harmonic modes. They are calculated by applying Sellmeier's equation with the corresponding  $a_i$  and  $b_i$  parameters for the 5 %-doped MgO:PPLN from Tab. 3.3 both taken from [124]:

$$n_e(T, \lambda) = a_1 + b_1 f(T) + \frac{a_2 + b_2 f(T)}{\lambda^2 - (a_3 + b_3 f(T))^2} + \frac{a_4 + b_4 f(T)}{\lambda^2 - a_5^2} - a_6 \lambda^2. \quad (3.21)$$

The function  $f(T) = (T - 24.5)(T + 570.82)$  describes the temperature dependence, where temperature  $T$  has to be inserted in units of [ $^{\circ}\text{C}$ ].

**Table 3.3:** Parameters for Sellmeier's equation for the 5 %-doped MgO:PPLN crystal

$a_1$	5.756	$b_1$	$2.86 \times 10^{-6}$
$a_2$	0.0983	$b_2$	$4.7 \times 10^{-8}$
$a_3$	0.2020	$b_3$	$6.113 \times 10^{-8}$
$a_4$	189.32	$b_4$	$1.516 \times 10^{-4}$
$a_5$	12.52		
$a_6$	$1.32 \times 10^{-2}$		

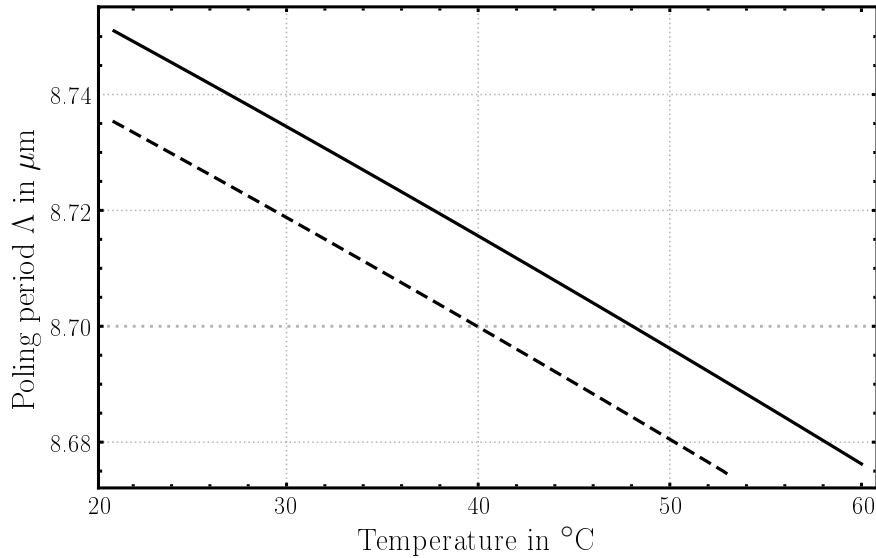


**Figure 3.12:** Simulation of the optimal poling period for the SHG in the 5%-doped MgO:PPLN crystal using 1145.89 nm fundamental light (solid black curve) and 1145.3 nm light (dashed black curve). The crystal provides a 8.7 μm poling period lane, which suits the purpose of SHG at a temperature of 46.6 °C and 39.8 °C, respectively.

With this, the temperature dependent coherence length and therefore the poling period for the PPLN crystal can be calculated. Figure 3.12 shows the dependence of the temperature on the poling period fulfilling the QPM condition, for an assumed fundamental wavelength of 1145.89 nm (solid line in Fig. 3.12), which is used for STIRAP. For moderate temperatures of  $\leq 60$  °C a poling period of  $\Lambda \approx 8.7$  μm is calculated. The crystal from *Covesion* features five different poling periods; see Tab.3.2. Thus, the one with  $\Lambda = 8.7$  μm is perfectly suited. From the calculations the QPM should be fulfilled at a temperature of 46.6 °C. In the experiment, the QPM is performed by changing the temperature of the crystal while the SHG process is ongoing. In this case, the SHG takes place in a resonant bow-tie cavity (description see below). The bare crystal is mounted in a self-built temperature stabilized copper case. The QPM condition is fulfilled, when the harmonic light output is maximal. The results can be seen in Fig. 3.13. The curve is modeled by a sinc function from Eq. 3.22, which describes the power dependence on the temperature [119]:

$$\frac{P_{\text{SHG}}}{P_{\text{max}}} = \left( \frac{\sin(\Delta k L/2)}{\Delta k L/2} \right)^2. \quad (3.22)$$

In this test experiment the laser wavelength was set to the default value set by the company, which is 1145.3 nm. For comparison, the QPM temperature dependence is also shown in Fig. 3.12 as dashed line. In theory, the temperature to match the given 8.7 μm poling period is 39.8 °C. For the later experiments with the atoms or the molecules, the laser frequency was set to the right transition value of about 1145.89 nm; for the detailed values for STIRAP see [89], and therefore the temperature of the crystal had to be changed to the given 46.6 °C. The optimal temperature found for the case of 1145.3 nm is 40.8(1) °C which differs by about 1 K from the theoretical value; see Fig.3.13. This can be explained by a slightly tilted crystal which can cause a shift in poling period and of the refractive index. Besides, the company does not specify the error on the poling period. Nevertheless, the overall line shape of the *sinc*-function fits to the one of the measurement points, but the results in Fig. 3.13 show a qualitative difference of the main peak compared to the theory curve. This can be explained by the decrease of the build-up factor and thus circling laser power in the cavity, when QPM

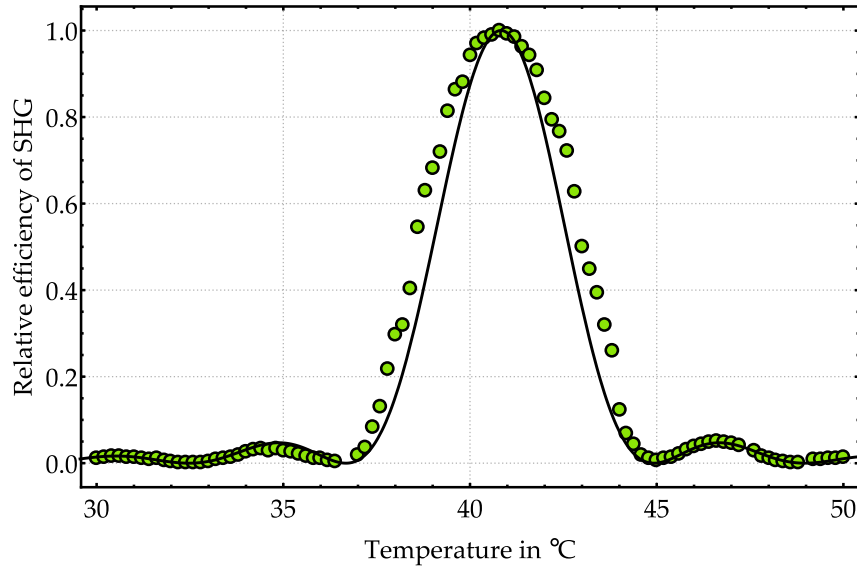


**Figure 3.13:** Temperature dependent QPM. The curve is the function according to Eq. 3.22. The corresponding fundamental wavelength is determined to be 1145.3 nm. This measurement was performed while the doubling cavity was on resonance. The discrepancy of the model curve and the data points can be explained with the change of  $b_{\text{res}}$  (Eq. 3.23) while phase-matching changes the losses of the fundamental mode from the cavity.

is attained; see paragraph below.

**Laser beam properties** For an efficient SHG process the laser beam properties have to be matched. Namely, these are the focus waist  $w_0$  and the polarization. The poled area of the crystal is the limiting parameter for the focus position and size. From Boyd *et al.* [114] it is known, that the focal parameter  $\xi = L/2z_R$  plays a major role for those applications.  $z_R$  is the Rayleigh length of the focused beam and  $L$  is the length of the crystal. For the PPLN crystal, a value of  $\xi = 2.84$  is assumed to give the highest conversion efficiency [114]. This corresponds to a  $1/e^2$  focus radius in air of  $w_c = 25.34 \mu\text{m}$  at the center position of the crystal. The polarization of the laser is also essential for the SHG. Only for horizontally polarized light the SHG will take place.<sup>2</sup> Consequently, the harmonic light is polarized vertically and thus perpendicularly to the fundamental light.

From Eq. 3.19 it is known that a higher intensity leads to higher conversion efficiencies for the SHG. The TA system can deliver up to 200 mW of fiber coupled 1146 nm light. This is fairly small for an efficient single pass SHG. To overcome this obstacle, a stabilized bow-tie cavity is built around the crystal. The challenge is to maintain the laser and crystal properties while the enhancement cavity is on resonance. In the next paragraph, the properties of the enhancement cavity are outlined.

**Bow-tie cavity** For the enhancement of the light a bow-tie ring cavity is chosen. A ring cavity features a running wave preventing spatial hole burning [125] in the crystal and causes a directed output of the harmonic light from the crystal. The cavity consists of four mirrors  $M_{1-4}$ , where  $M_1$  is the 1/2" flat entrance incoupling mirror for the fundamental light,  $M_2$  is a 1/4" flat mirror glued to a piezo actor, which serves as a stabilization element, and  $M_3$  and  $M_4$ , which are 1/2" curved mirrors to focus into the crystal and refocus afterwards; see Fig.3.14. All mirrors are coated with a high reflectivity coating for the fundamental mode.

<sup>2</sup>This is the type-I phase matching condition [119]. It is demanded by the crystal property and the linear polarization of the light.

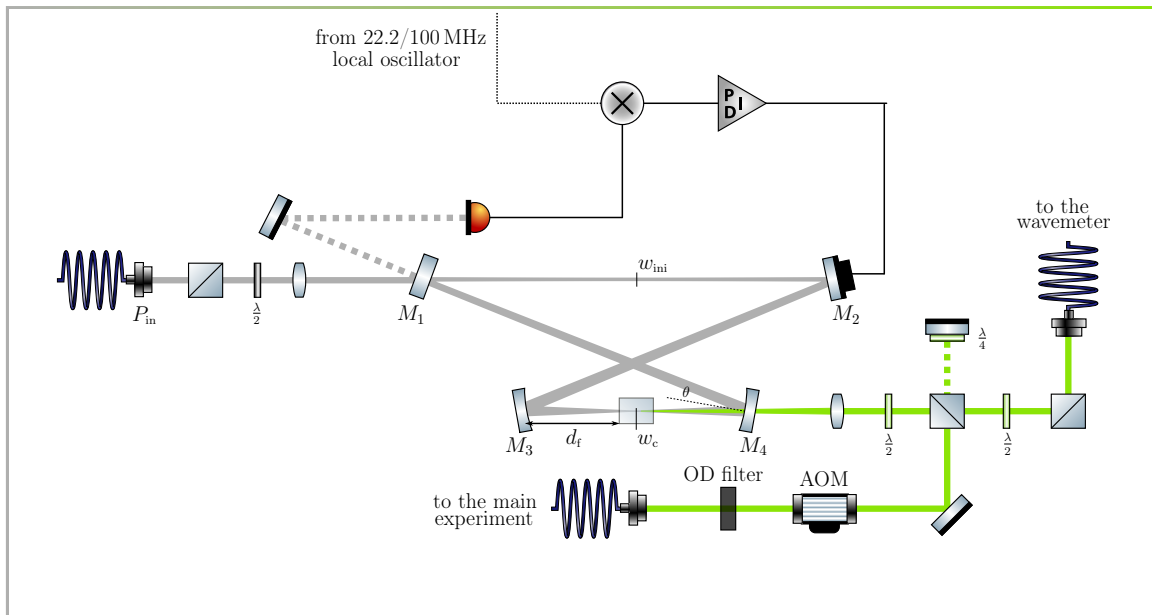


**Figure 3.14:** Bow-Tie cavity. This drawing shows the setup of the frequency doubling cavity with the parameters explained in the text. The generated 573 nm light passes the AOM and is coupled to a fiber to bring the light to the main experiment.

The mirror properties are listed in Tab. 3.4.  $M_1$  has a lower reflectivity, as this mirror is used for impedance matching to compensate losses of the fundamental light in the SHG process and from leakage through all mirrors.  $M_3$  and  $M_4$  have an additional anti-reflectivity coating for the harmonic light to send this light directly after its generation out of the cavity without major losses. For the SHG, the cavity has to support a decent focus, as mentioned in the paragraph above. For this purpose, the cavity possesses two foci. The first one, which is the initial focus with the waist  $w_{ini}$ , is in the middle of the long cavity arm, centered between  $M_1$  and  $M_2$ . The second focus with waist  $w_c$ , the main focus for SHG, is between  $M_3$  and  $M_4$  in the middle of the short cavity arm and thus in the center of the crystal. Besides, the crystal is inserted between the two curved mirrors. The crystal is housed in a self-built copper case which serves as heat reservoir which is permanently stabilized to the desired crystal temperature.

The fundamental light is coupled through  $M_1$  into the bow-tie cavity. For this purpose, the incident light is focused to match the cavity mode at the initial focus. The mirror  $M_2$  folds the beam and directs it to the mirror  $M_3$  with a half open angle  $\theta = 13^\circ$ . The curved mirror  $M_3$  focuses the light into the crystal, where the SHG takes place. The curved mirror  $M_4$  refocuses the fundamental light and directs it back to  $M_1$ . Both mirrors,  $M_4$  and  $M_1$ , are used to overlap the round-trip light with the incident light to close the cavity.

The mode of the cavity is modeled by an ABCD-matrix formalism similar to the one detailed in [117]. It is used to close the cavity and minimize the beam parameter differences for several round-trips of the light. This is done in due consideration of the horizontal and vertical plane of the light. The angle  $\theta$ , with which the beam hits the mirror surfaces, causes astigmatism at the curved mirror surfaces of  $M_{3,4}$ , leading to a shift of the focus position by the factor  $\cos(\theta)$  in the horizontal plane. Both planes have to be treated in conjunction with each other to find a compromise of stability for both axes. For optimization the angle  $\theta$  and the focusing distance  $d_f$  are used. The astigmatism gets smaller, the smaller the chosen angle is. Consequently, the beam ellipticity decreases and mode-matching and SHG efficiency improve. Nevertheless, a small angle makes high demands on the geometric alignment and positioning of the optical

**Table 3.4:** Optomechanical properties of the bow-tie doubling cavity

	Symbol	Value
total length	$L_{\text{tot}}$	0.2787 m
long arm	$l_1$	218.4 mm
short arm	$l_2$	60.6 mm
focusing distance	$d_f$	25.3 mm
crystal length	$L_{c,z}$	10 mm
mirror curvature $M_{1,2}$		$\infty$
mirror curvature $M_{3,4}$		50 mm
half open angle	$\theta$	$13^\circ$
reflectivity $M_1$		$92, 93, 94, 95 \pm 0.2\%$
reflectivity $M_{2,3,4}$		$99.8 \pm 0.2\%$
initial focus	$w_{\text{ini},h}$	$240.0 \mu\text{m}$
	$w_{\text{ini},v}$	$178.5 \mu\text{m}$
crystal focus	$w_{c,h}$	$31.6 \mu\text{m}$
	$w_{c,v}$	$30.1 \mu\text{m}$

elements, such as mirror mounts and crystal holder, increasing the length of the cavity arm drastically. Accordingly, this affects the focus waists of the cavity mode, which are restricted by the crystal for a proper conversion efficiency. To ease the recurring optimization,  $\theta$  is fixed to a decently small value of  $13^\circ$  which allows for an overall compact cavity design. The focusing distance  $d_f$  is used to optimize the focus size of both planes without losing the stability in either of them; see Fig. 3.15 (a). According to the results from Fig. 3.15 (a), the optimal value for  $d_f$  is 25.3 mm. The foci shift from the astigmatism between horizontal and vertical plane is 0.67 mm. The waists after optimization are  $w_{c,h} = 31.6 \mu\text{m}$  and  $w_{c,v} = 30.1 \mu\text{m}$  in air which corresponds to focal parameters  $\xi_h = 1.82$  and  $\xi_v = 2.01$  in the horizontal plane and vertical plane, respectively. The set of all parameters of the cavity is summarized in Tab. 3.4. An optimized light enhancement inside a cavity with additional losses from the SHG requires a proper impedance matching. This is done by changing the incoupling mirror according to the losses of the fundamental mode from the cavity. For this reason, the incoupling mirror  $M_1$  is available with different reflectivities; see Tab. 3.4. Please note at this point, that the reflectivities for all cavity mirrors are not exactly known. The mirrors were generously provided by Piet Schmidt's group, PTB Brunswick, and are specified only for wavelengths of 1120 nm and 560 nm. To understand the cavity enhancement and to select a suitable mirror  $M_1$  the build-up factor  $b_{\text{res}}$  for a resonant cavity is modeled [117, 126] by

$$b_{\text{res}} = \frac{P_{\text{cav}}}{P_{\text{in}}} = \frac{T_1}{\left(1 - \sqrt{(1-T)(1-\gamma)(1-\Gamma P_{\text{cav}})}\right)^2}. \quad (3.23)$$

Here,  $T_1$  is the transmittivity of  $M_1$ ,  $\gamma$  represents the single round-trip losses from leaking mirrors ( $R_{2,3,4}$ ) and reflections on the crystals surface ( $R_c$ ) and the absorption of the fundamental light in the crystal ( $\alpha_f$ ), and  $P_{\text{cav}}$  and  $P_{\text{in}}$  are the power circling inside the cavity and the incident power in front of the cavity, respectively.  $\Gamma$  represents the nonlinear losses from the conversion to the harmonic mode through the SHG conversion process. The conversion efficiency is given by  $\Gamma = kL_{c,z}h_{\text{max}}$ , analog to [114], where  $k = (16\pi^2 d_{\text{eff}}^2)/(c\epsilon_0 n_e \lambda_h^3)$  summarizes constants and  $h_{\text{max}}$  is the focusing parameter function which summarizes the effects coming from the Gaussian beam of the laser, such as focusing parameter  $\xi$  and focus position. In

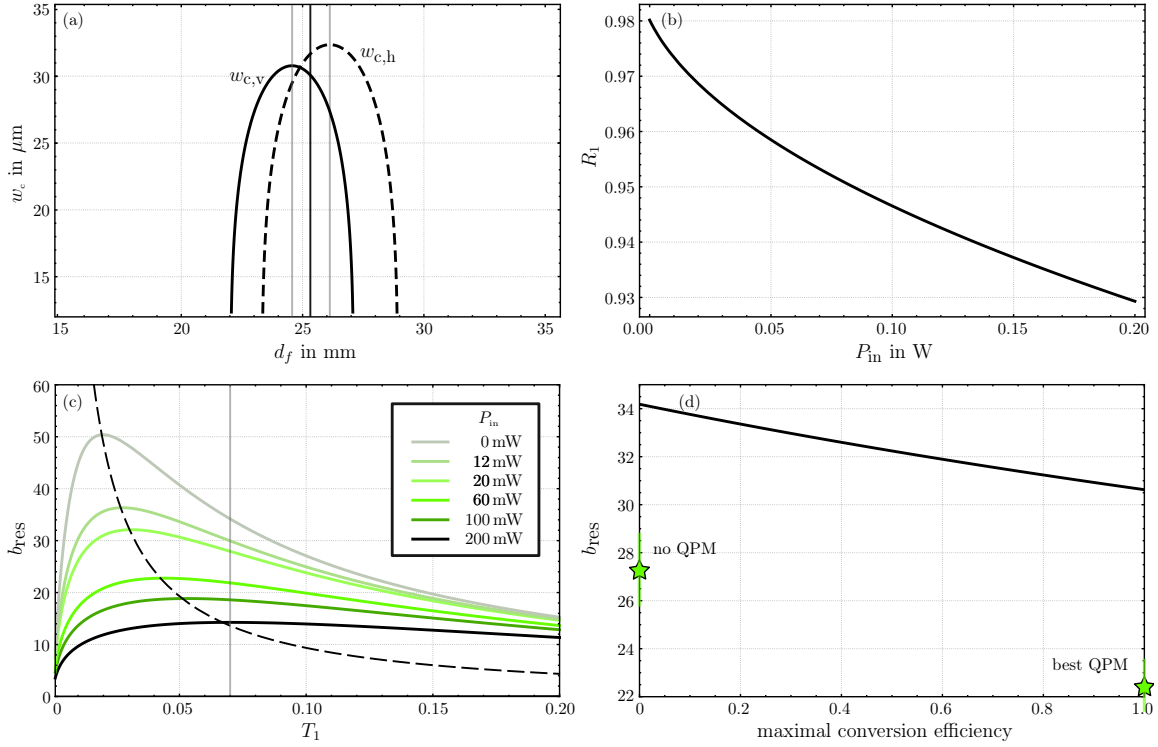


**Figure 3.15:** Calculations for the resonant doubling cavity. (a) Stability in the horizontal and vertical plane. The beam waist  $w_c$  is shown with respect to the focusing distance  $d_f$  to the crystal. The waist vanishes when  $d_f$  gets too small or too large to close the cavity after a few round trips. The gray vertical lines are the optimal positions for the respective plane. The black line is their average  $d_f = 25.3$  mm, which is used for the construction. (b) Choice of  $M_1$ . The reflectivity of the mirror  $M_1$  dependent on the power  $P_{in}$  for perfect impedance matching is shown. For the maximal power of 200 mW the reflectivity should be 0.93. (c) Cavity enhancement. The build-up factor dependent on the transmissivity of  $M_1$  is shown for different powers  $P_{in}$ . The black dashed line is the overall optimum. The vertical gray line shows the chosen  $T_1$  for the construction. (d) Empty and phase-matched cavity. The build-up factor is shown dependent on the maximal QPM for  $P_{in} = 12$  mW. Zero corresponds to no conversion of the fundamental (no QPM), 1 to full conversion (maximal QPM) (according to Eq. 3.23). The green stars show measurements of the build-up factor. The experimental behavior shows the right trend. Nevertheless,  $b_{res}$  is smaller than the calculations due to the unknown mirror properties; see text.

[114] the maximal  $h$  is calculated for several cases of different beam and crystal properties.  $h_{max}$  for optimal  $\xi$  is given as 1.068. Note, that in the case of this thesis,  $\xi_{h,v} < 2.84$ . Still, the dependence of  $h$  on  $\xi$  is negligible (compare [114]) so in the following  $h_{max} = 1.068$  is assumed.

A solution for Eq. 3.23 for the optimal  $T_1$  to maximize  $b_f$  is given by

$$T_{opt} = \frac{\gamma}{2} + \sqrt{\left(\frac{\gamma}{2}\right)^2 + \Gamma P_{in}}. \quad (3.24)$$

Figure 3.15 (b) shows the optimal reflectivity  $R_{opt} = 1 - T_{opt}$  as function of the incident laser power. For the maximal accessible laser power of 200 mW of the fundamental mode, a reflectivity of about 93% is favorable. For lower power, a higher reflectivity might be needed. The behavior of the build-up factor with respect to  $T_1$  is shown in Fig. 3.15 (c), where Eq. 3.23 is solved for incident beam powers  $P_{in} = \{0.012, 0.02, 0.06, 0.1, 0.2\}$  W. The respective maxima of the curves correspond to the values from the curve of Fig. 3.15(b). Most preferably  $T_1$  should be optimal for all possible  $P_{in}$ . As this is obviously never the

case,  $T_1 = 0.07$  ( $R_1 = 0.93$ ) is chosen. This guarantees an optimal build-up factor at maximal power  $P_{\text{in}}$  and at the same time, if  $P_{\text{in}}$  is not maximal, that the impedance matching is done on the slower slope side of  $T_{\text{opt}}$ ; see Fig. 3.15(c), making changes less critical.

The beam alignment of the cavity is done as follows. The main cavity mirror setup is placed on a separate small breadboard as cautiously as possible with respect to the angle  $\theta$  and the distances between the mirrors. This breadboard can be inserted into the incident laser beam. The incident laser beam itself is collimated and afterwards focused to the right position and waist size  $w_{\text{ini}}$ , where the initial focus is suspected. Then the whole cavity on its small breadboard is set in place to match the initial focus. With two mirrors of the incident beam, the laser is adjusted to the center of  $M_1$  and  $M_2$ .  $M_2$  is used to align the beam to the center of  $M_3$ , and  $M_3$  to the center of  $M_4$ . The small focus  $w_c$  becomes visible. Now the crystal in its copper mount is inserted and adjusted as parallel as possible to the laser beam. The diffraction of the beam on the different poling lanes can be used to select the right lane. With a perfectly aligned crystal, the beam still hits the center of  $M_4$ , no adjustment using the mirrors is needed for this step. Then,  $M_4$  is used to hit the center of  $M_1$ .  $M_4$  and  $M_1$  can be used to overlap the round-trip beam with the incident beam. The position and the waist  $w_{\text{ini}}$  should overlap perfectly. Smaller adjustments, when the cavity is closed and scanned, can be done by all mirrors and the crystal alignment to make a perfect mode matching and suppress higher spatial modes. Mode matching for this cavity reaches 95 %.

The closed cavity has to be actively stabilized to a resonant point to maintain the maximal light enhancement inside the cavity. For this goal, the spectral properties are analyzed. This is done by changing the cavity length periodically applying a triangular signal to the piezo actor of  $M_2$ . The cavity length is then shifted periodically on and off resonance. Using this technique, one can access the dimensionless property finesse  $F$  of the cavity by comparing the width and the distance of the resulting spectrum. The finesse is given by

$$F = \frac{\Delta\nu_{\text{FSR}}}{\Delta\nu_{1/2}} = \pi b_{\text{res}} . \quad (3.25)$$

$\Delta\nu_{\text{FSR}}$  is the free spectral range, which is the distance between two sequential resonance signals, and  $\Delta\nu_{1/2}$  is the FWHM linewidth of a resonance signal; see Fig. 3.16. The free spectral range of the cavity can be also calculated by  $\Delta\nu_{\text{FSR}} = c/L_{\text{tot}}$ . With this relation also the cavity linewidth can be deduced. Figure 3.16 shows the cavity's reflection signal for the case of perfect QPM (a) with an incident laser power of  $P_{\text{in}} = 12$  mW. From this measurement, the finesse is  $F_{\text{QPM}} = 70.5(3.5)$  and correspondingly  $b_{\text{res}} = 22.43(1.2)$ , the linewidth is  $\nu_{1/2,\text{QPM}} = 15.3(9)$  MHz and the free spectral range is  $\nu_{\text{FSR}} = 1.076$  GHz. Similarly, for the non-QPM case (not shown in Fig. 3.16 for clarity reasons), the finesse is  $F_{\text{noQPM}} = 85.6(3.9)$  and  $b_{\text{res}} = 27.3(1.5)$ , and the linewidth is  $\nu_{1/2,\text{noQPM}} = 12.6(6)$  MHz. In Fig. 3.15 (d) the dependence of  $b_{\text{res}}$  on the QPM is shown. The measured values for the finesse and for  $b_{\text{res}}$  are smaller than expected from the calculation. This can be explained by the unknown mirror reflectivity. However, the trend of the measurement is correct and shows a higher cavity enhancement when losses from the SHG are switched off.

The cavity lock is done by a Pound-Drever-Hall locking scheme [127, 128]. For a detailed introduction see [129]. The general assembly of the lock is integrated in the overview figures 3.14 and 3.5. To generate the sidebands for the lock, a phase-locked two-output function generator DG4162 from Rigol is used to directly modulate the laser current on the 1146 nm laser head. The frequency is chosen freely to be 22.2 MHz.<sup>3</sup> The second output is used

<sup>3</sup>For later experiments with the STIRAP, the modulation frequency is changed to 100 MHz. This reduces the locking stability but at the same time suppresses the SHG of the sidebands through the doubling cavity.

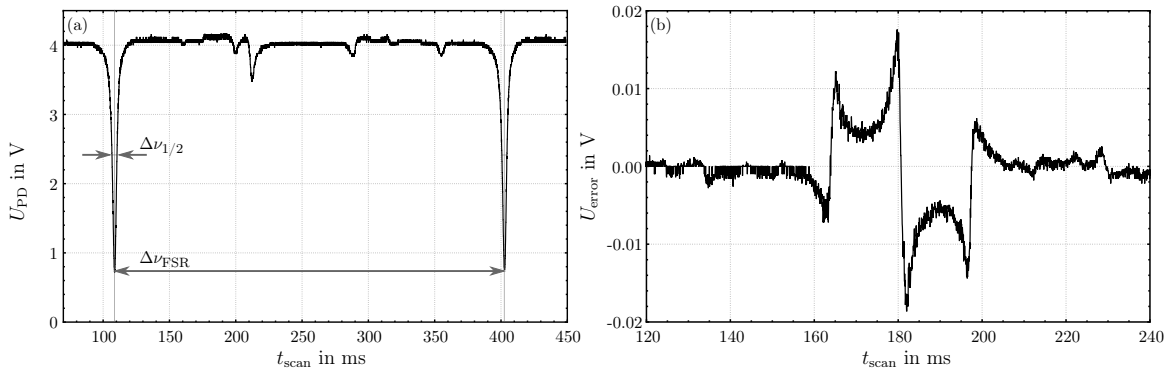


**Figure 3.16:** Characteristics of the doubling cavity (a) Reflection signal of the scanned cavity. The reflection signal of the photo diode is shown dependent on the time while the cavity length is scanned. The two dips are used to extract the finesse; according to the text. The smaller dips are higher order TEM modes. The incident power is 12 mW and the crystal yields perfect QPM. (b) Error signal. The error signal is generated as explained in the text.

as local oscillator for the lock. The reflection signal from  $M_1$  is picked up by an InGaAs photodiode PDA05CF2 from *Thorlabs*. The output is given to a phase detector ZRPD-1+ from *Mini-Circuits* (input L). The local oscillator input is plugged to the input R. The output (I) is used for a self-built PI-controller, which actively stabilizes the cavity length to the laser frequency through the piezo actor of  $M_2$ . Phase and level of the local oscillator for the optimized error signal are adjusted at the function generator. For a proper adjustment of the frequency range to the PI-controller a 11 MHz low pass filter BLP-10.7+ from *Mini-Circuits* is used right before the input of the PI-controller. A typical error signal generated in this way is shown in Fig. 3.16 (b).

The generated frequency doubled light exits the cavity directly after its generation through  $M_3$ , where it is collimated by a lens. It passes the unused fiber phase stabilization part and is divided by the PBS; see Fig. 3.14. The minor amount is coupled to a fiber for the observation on the wavemeter. The major part is coupled to the first diffraction order of an AOM AOMO3200-125 from *Gooch & Housego*. The frequency is set to 200.7 MHz coming from the shared DDS for the 816 nm laser. This AOM is used for switching the laser light and for generating the pulse form during STIRAP. The diffracted light is coupled to an optical fiber for the main experiment. With  $P_{in} = 200$  mW, the optimized and locked cavity setup delivers a harmonic light output at 573 nm of up to 61 mW. This corresponds to an SHG efficiency of  $> 30\%$ . The remaining power on the main experiment is 25 mW. Please note, that for STIRAP less than  $100 \mu\text{W}$  laser power is needed in this setup. For STIRAP the TA is bypassed and the light from the 1146 nm laser is directly fed to the doubling cavity. The cavity parameters do not fit to this low power condition, according to the descriptions from above, but still deliver a proper amount of laser power on a daily base. The fine adjustment of the laser power for STIRAP is done by absorptive filters in front of the last fiber coupling to the main experiment table.

### 3.2.3 Locking and Pulse Application

The coherent transfer demands a stable and low linewidth intensity controlled two-color laser system. The laser light generation is described above in Sec. 3.2.2. In this section, the lock of both lasers to the reference cavity is explained and the characterization is performed. Moreover, the STIRAP pulse generation is explained.

The lock of both lasers is a classical PDH lock [127, 128]. The technique is numerously applied in many laboratories and is not explained in this thesis. For detailed information please refer to [116, 129, 130]. In the following a brief explanation of the laser lock technique is given and its realization and characterization for the two lasers frequencies is detailed.

#### Locking Scheme

The ULE cavity serves as relative frequency reference due to its passive stability of the distance between the mirrors. To maintain the stability, a vibration isolated housing and a carefully designed holding is required, which is described in Sec. 3.2.1.

For locking, light of both laser, the 816 nm and the 1146 nm laser, has to be coupled into the cavity and the resulting signal has to be used to generate an error signal to feed back to the lasers for stabilization.

**Beam alignment** The laser light going to the reference cavity comes from the fiber outputs of the fiber coupled EOMs. The advantage is that the spatial mode from the fibers is a nearly perfect Gaussian TEM<sub>00</sub> mode, which is highly suitable for the incoupling into the cavity. The beam path from the fiber couplers to the cavity is kept as short as possible to minimize long-term spacial displacement. Further, it consists of the lowest amount of optical elements, to minimize unwanted reflections. The entire incoupling setup is mounted to a single breadboard with a beam height of 5 cm. Both paths are similarly set up; see Fig. 3.5. For one beam path, the minimal amount of optical elements are two mirrors for beam walk purposes and one mirror for the adjustment of the reflection signal to the photo diode (DPA05CF2 from *Thorlabs*), one  $\lambda/2$ -waveplate, one  $\lambda/4$ -waveplate, one PBS, one lens for mode matching and one lens for focusing the reflection signal to the photo diode. Both beams are overlapped directly in front of the entrance window of the vacuum chamber by a longpass dichroic mirror DMPL950 from *Thorlabs* held in a solid lens mount. Mode matching between the cavity mode and the incident laser mode is done by focusing the laser into the cavity. The entrance mirror of the ULE cavity is the curved one; see Fig. 3.5. The waist of the cavity mode on the flat mirror of the ULE cavity is calculated by using the evolution of a Gaussian beam by restraining the beam to the cavity parameter; see Tab. 3.1. The radius of curvature  $r$  of a Gaussian beam is given by

$$r = z_1 \left[ 1 + \left( \frac{z_R}{z_1} \right)^2 \right]. \quad (3.26)$$

Here,  $z_1$  is the distance to the focus along the direction of travel of the beam and  $z_R$  is the Rayleigh length. For this cavity the corresponding values are  $z_1 = L$  and  $r = R_1$ . Hence, the cavity mode is completely described. The resulting foci  $w_0$  for wavelength  $\lambda$  of 816 nm and 1146 nm are calculated by

$$w_0 = \sqrt{\frac{\lambda z_R}{\pi}} \quad (3.27)$$

to be  $w_{0,816\text{nm}} = 227.92 \mu\text{m}$  and  $w_{0,1146\text{nm}} = 270.12 \mu\text{m}$ . Using Gaussian beam propagation for both beams mode matching is achieved by using  $f = 11 \text{ mm}$  fiber outcoupler lenses and  $f = 500 \text{ mm}$  focusing lenses placed at distances of 370 mm and 360 mm to the outer flat

surface of the curved entrance mirror of the ULE cavity for the 816 and the 1146 nm light, respectively.

The alignment of both beams was done with care before the vacuum system with the cavity was placed on the breadboard. Due to the characterization of the cavity and the design of the vacuum setup with respect to the beam alignment, the focus positions were strongly restricted. The prealignment eased the incoupling to the cavity drastically. After placing the cavity to the holder, immediately a cavity signal was visible without performing any blind beam walks. Optimization to the cavity signal with respect to incoupling efficiency and spatial mode was done by beam walks resulting in incoupling efficiencies of 48 % and 56 % for the TEM<sub>00</sub> modes of 816 nm and 1146 nm light, respectively.

For the experiments, typically incident laser powers of about 150  $\mu$ W for both wavelengths were used. The wave plates are adjusted to maximize the transmission towards the cavity. The  $\lambda/4$ -waveplates generate circular polarized light from the linear polarized laser light after the PBS. The reflected light from the cavity travels again through the  $\lambda/4$ -waveplates, which generates linear polarized light perpendicular to the incident polarization. At the PBS it is reflected and afterwards focused to the photodiodes for the purpose of PDH locking.

**Sideband lock** For the tunable sideband PDH lock two kinds of sidebands have to be modulated to the laser frequency; see Fig. 3.17. The one kind are widely tunable and freely chosen offset sidebands ( $f_{\text{offset}}$ ) for the control of the laser frequency relative to the arbitrary locking point of the cavity. These sidebands allow to detune the lasers of some GHz within the free spectral ranges of the ULE cavity. In the described setup, the offset sidebands are generated for both wavelengths by the fiber EOM from *phoTline*. As frequency source for the 1146 nm laser a SML01 from *Rohde & Schwarz* is used which can generate arbitrary waves up to 1.1 GHz. For the 816 nm laser, a SME03 function generator is used, also from *Rohde & Schwarz*, delivering frequencies up to 3 GHz. Each source is amplified by a ZHL-1-2W-S+ *Mini Circuits* amplifier. Note, that the nominal amplification range of these amplifiers is 0-500 MHz. Nevertheless, the amplification takes also place to up to about 660 MHz, but requires a higher input power. Using the AOM as additional frequency offset, the entire frequency range of one FSR  $\Delta\nu_{\text{FSR}} = 1.499$  GHz can be probed by scanning the offset sideband frequency  $f_{\text{offset}}$  on both sides of a cavity resonance and reversing the diffraction order of the AOMs.

The second kind of sidebands are the locking sidebands ( $f_{\text{PDH}}$ ) for the PDH lock. They typically have frequencies of several MHz. They are modulated on top of the offset sidebands and are demodulated at the phase detector circuit for the purpose of locking; see Fig. 3.17 part 4. For the 1146 nm light the PDH sidebands are also generated by the fiber EOM but with a fixed frequency of 17 MHz coming from a *Rigol* 4062 function generator. To deliver both frequencies at the same time to the EOM, an electronic circuit consisting of two splitters and a mixer is used; see Fig. 3.17 part 2-3. This is an established solution for a fixed set of frequencies [131], but is improper for changed frequencies, for example during a spectroscopy scan; see Chap. 4. For each frequency the offset sideband wave adds up at the second splitter, but dependent on frequency and circuit length this happens constructively or destructively.

Hence, to generate the PDH sidebands for the 816 nm laser, the free space EOM with a fixed frequency of 5.7 MHz is used; see Fig. 3.5. During the course of this thesis the 816 nm laser is widely tuned, making this method worth to apply. As a frequency source a *Rigol* DG1022 is used. All function generators used for the locking of the STIRAP laser system are simultaneously referenced to a stabilized 10 MHz source from the *Rohde & Schwarz* SMB 100A signal generator, which is used for example for the magnetic trap evaporation or the rf

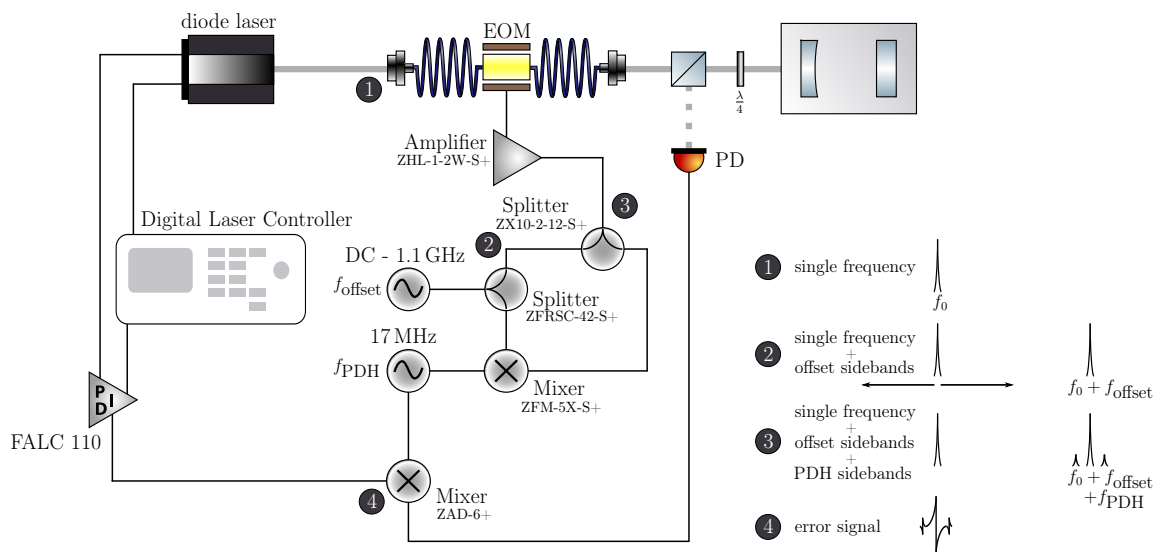


**Figure 3.17:** Drawing of the servo loop with all components. The offset sidebands ( $f_{\text{offset}}$ ) and the PDH sidebands ( $f_{\text{PDH}}$ ) are both modulated by the fiber EOM to the initial laser frequency  $f_0$ . The frequencies are combined by the splitter and mixer circuit shown in the drawing. For the 816 nm servo loop frequency mixing components are missing, because the PDH sidebands for the 816 nm lasers are generated by an additional EOM; see Fig.3.5. The parts 1-4 show the different stages of frequency modulated signals through the circuit and for the laser.

for Feshbach molecule creation.

At the resonance condition of the cavity the modulated light experiences a frequency dependent reflection and phase shift due to the cavity. This effect is used to generate an error signal from it [129]. The reflected light travels backwards through the  $\lambda/4$ -waveplates to the locking photodiodes. There, the PDH sideband frequency is extracted and sent to a phase detector (mixer ZAD-6+ from *Mini Circuits*) for demodulation using the original frequency from the function generator as local oscillator. Depending on the incident laser light frequency to the cavity's resonance a non-vanishing phase shift between the sidebands occurs, which is minimized by use of a servo-loop PID controller; see Fig. 3.17 part 4. Phase and amplitude for an optimized demodulation is adjusted by the local oscillator output of the function generators.

As the PID controllers two commercially bought FALC110 from *Toptica photonics* are used. They are housed in an external DLC ext rack. The slow feedback from the controllers is fed back to the DLC pro Digital Laser Controller using the fast input BNC connectors for each lasers, where the fast feedback directly controls the applied current at the laser head. Figure 3.18 (a) shows an example of a typical error signal of the 816 nm laser. For an open-loop frequency scanned system, the shape of the error signal after the PDH mixer becomes visible. The shape can be adjusted by power and phase of the function generators. The red data corresponds to a closed-loop power system. The frequency spectrum; Fig. 3.18 (b), shows the noise in the system. For the closed loop, the servo bumps get visible. The circuit is limited in bandwidth at the frequency of the servo bumps, approximately 1.8 MHz. This may be increased by shortening the cable length of the entire locking electronics, which would require to compact and move the electronic components closer to the locking photodiodes and laser heads.

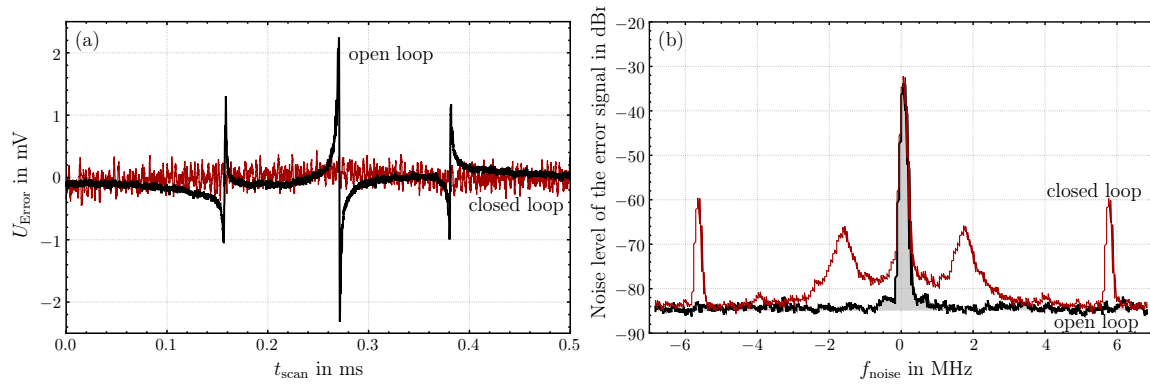


**Figure 3.18:** PDH loop characteristics for the open loop (black) and closed loop (red) for the example of the 816 nm laser. (a) Error signal. The signal is picked up directly after the phase detector and filtered by a 5 MHz low pass filter to be recorded by a *Rohde & Schwarz* HMO724 oscilloscope. The left and right sidebands are both 5.7 MHz apart from the main signal. (b) Spectrum of the error signal. The error signal is mixed by a 17 MHz source to generate an offset (subtracted in this case) and then recorded by a spectrum analyzer *Hameg* HMS3010 using a video bandwidth of 1 kHz. The servo bumps emerge at about 1.8 MHz. The additional closed loop peaks originate from the 5.7 MHz modulation for the PDH lock.

### Finesse and Linewidths

The finesse of the cavity is a reasonable measure to determine the mirror reflectivity and thus the linewidth of the cavity. Differently to the bow-tie cavity from Sec. 3.2.2, the finesse is not easily measured by the ratio between the FSR and linewidth from a cavity scan. To perform the spectroscopic scan for the ULE cavity, the laser frequency has to be scanned. On resonance, the cavity amasses light and builds up the cavity light field. Off resonant, the light field decays and leaks out of the cavity through the mirrors. While the light leaks out, the laser frequency is steadily shifted, which leads to interference effects between the leaking light from the cavity and the incident light which is observed on the reflection signal on the photodiodes, hampering the finesse measurement [132]. This effect is also dependent on the laser linewidth and the scan frequency. Moreover, this issue influences the shape of the error signals of the lock, and for small linewidth lasers and high finesse cavities it should not be neglected. In the case of this setup, the signal for a cavity scan is drastically changed, so that an easy finesse measurement can not be done. The error signal is also affected but by using a slow scan frequency  $f_{\text{scan}} < 5$  Hz, it can still be optimized quantitatively; compare Fig. 3.18.

However, the light decay from the cavity depends on the reflectivity of the mirrors and can therefor be used to calculate the finesse. The cavity ring-down follows an exponential curve

$$P(t) = P_0 \exp\left(-\frac{t}{\tau_{\text{res}}}\right), \quad (3.28)$$

where  $P_0$  is the initial power and  $\tau_{\text{res}}$  is the decay time where the linewidth of the cavity is given by  $\Delta\nu_{1/2} = 1/2\pi\tau_{\text{res}}$  and the free spectral range is  $\Delta\nu_{\text{FSR}} = c/2L$ . The measurement is done separately for the 816 nm and the 1146 nm laser. The respective laser is locked to the cavity, to maintain the cavity build up. The light to the cavity is switched off mechanically by a shutter. The leaking light from the cavity is recorded over time through the converted voltage of the lock photodiodes on an oscilloscope. The results with the respective fits are shown in Fig. 3.19. For 816 nm the resulting finesse is 24900(85), for 1146 nm it is 37400(180). Accordingly, the cavity yields linewidths of 60.2(2) kHz for 816 nm and 40.0(2) kHz for 1146 nm. All cavity parameters are summarized in Tab. 3.1. The PDH lock should be able to decrease

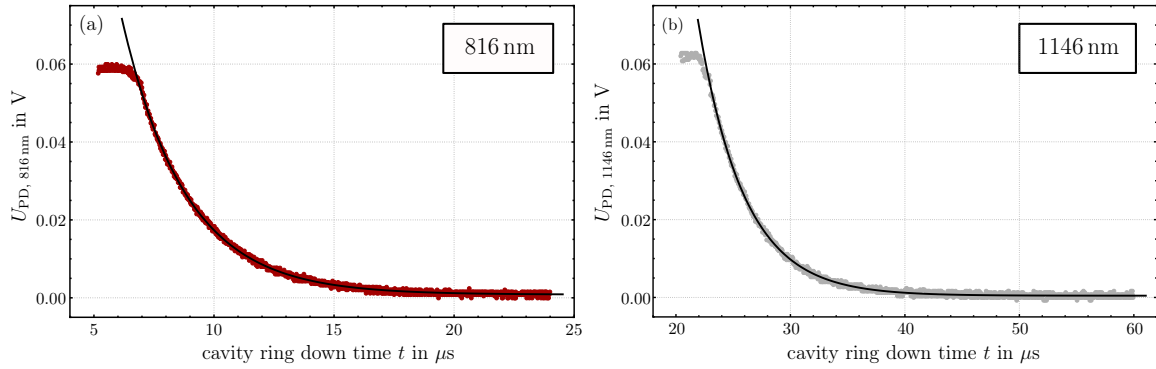


**Figure 3.19:** ULE cavity ring-down. The decays of the light for the 816 nm laser (a) and the 1146 nm laser (b) are shown. The signals are DC voltages from the respective PDH lock photodiode. The lasers are locked to the cavity and mechanically shuttered. The exponential function Eq. 3.28 is used for the fit. The determined ring-down times  $\tau_{\text{res}}$  are  $2.636(9) \mu\text{s}$  and  $3.984(16) \mu\text{s}$  for the 816 nm and the 1146 nm laser, respectively.

the linewidth of the lasers well below the cavity linewidths.

To estimate the linewidth and the noise on the lasers, the error signals already shown in Fig. 3.18 (a) can be further analyzed. The open-loop signal with its PDH locking sidebands are used as frequency references to convert the scale of the scanned piezo of the laser to a frequency one. For this purpose the scan is assumed to be linear over the entire scan range. Thus, the steep linear slope of the open-loop error signal can be calibrated to a frequency reference. The closed-loop signal from Fig. 3.18 (a) can now be converted to a frequency which represents the frequency noise of the locked laser to the cavity. Figure 3.20 shows the frequency converted close-loop error signal and the accumulated histogram plot for an example of the 816 nm laser. The noise in the servo-loop for the 816 nm laser is estimated to a full-width half maximum (FWHM) of a fitted Gaussian curve of  $1.836(86) \text{ kHz}$  for the 816 nm laser and  $5.46(15) \text{ kHz}$  for the 1146 nm laser. The data for the 1146 nm laser is not shown. The closed-loop error signal data; see Fig. 3.20, shows slow<sup>4</sup> variations of its offset. The variation is of the order of the FWHM of the 816 nm laser, which would suggest, that during STIRAP the actual linewidth is even smaller, than the data shows. The slow variations do not affect

<sup>4</sup>slow, compared to the STIRAP pulse time of approximately  $10 \mu\text{s}$ , see Chap. 5

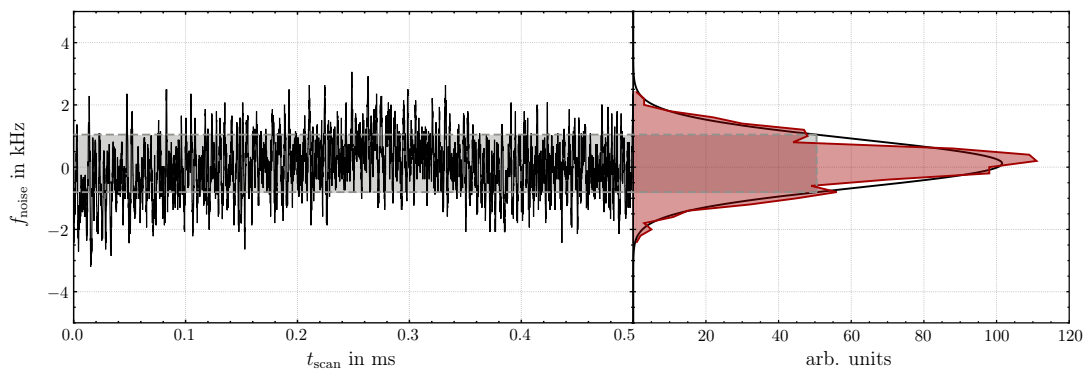


**Figure 3.20:** Frequency distribution of the error signal. (a) The recorded noise spectrum over time is rescaled to the corresponding frequencies; according to Fig. 3.18. (b) Histogram representation of the frequency distribution. The data (red lines) is fitted by a Gaussian function (black curve). The calculated FWHM is  $1.836(86) \text{ kHz}$ .

the STIRAP, because the two-photon detuning for STIRAP is of the order of 100 kHz; see Chap. 5.

For both of the PDH locks, the components of the servo-loops are identical and feature nearly the same sets of control parameters. The more suspicious is the behavior of the 1146 nm laser lock, as it seems not to decrease the linewidth of the laser properly, even after extensive optimization. From previous experiments with self-built lasers to generate wavelengths of 1146 nm and 816 nm, the diodes for 1146 nm always drifted towards multimode behavior and failed to work reliably in the long term. Similar issues can be presumed for the diode in this commercial laser. Moreover, for the generation of the STIRAP light, the 1146 nm laser gets frequency doubled. As a rule of thumb, the resulting linewidth for the 573 nm light can be assumed as the doubled linewidth of the 1146 nm laser, which is then  $> 10$  kHz. Consequently, the linewidth control is explicitly important for the 1146 nm laser, and the more bothersome the uncontrolled laser properties are.

### STIRAP Pulse Application

Both the 573 nm and 816 nm light are coupled through AOMs to optical fibers delivering the light to the main experimental table. The AOMs are used to switch the light on and off, as described in Chap. 4, as well as performing controlled pulses for the STIRAP; see Chap. 5.

**Laser beam properties** The laser light arrives through polarization maintaining fibers at the optical table of the main experiment. Both beams are coupled out from the fiber by  $f = 7.5$  mm lenses producing collimated beams with radii of 0.58 mm and 0.73 mm for the 573 and the 816 nm light, respectively. The foci at the position of the atoms and molecules are achieved by using a  $f = 500$  mm and a  $f = 400$  mm lens; see Fig. 3.21. After the lenses, for each beam separately, a set of two mirrors follows, to make a proper beam walk possible. One of the mirror holders of each path is a high precision Polaris-K1 mount from *Thorlabs* and the other one is equipped with piezo actor Picomotors from *Newport* allowing remote control of the beam position. Both beams are combined by using a fixed mounted shortpass DMSP605 dichroic mirror from *Thorlabs*. Before the beams enter the experimental main chamber, a fast self-built hard drive mechanical shutter is inserted [133].

To achieve maximal Rabi frequencies for a given beam power, the waists of both beams should be on the order of the dipole trap waist, which is in the tightest direction approximately  $42 \mu\text{m}$ . In each beam path a telescope is inserted to increase the initial beam radius before focusing; see Fig. 3.21. For 573 nm, a concave  $f = -50$  mm and convex  $f = 200$  mm with a distance of 150 mm are used, and for 816 nm two convex lenses with  $f = 50$  mm and  $f = 200$  mm with a distance of 250 mm are used. Both telescopes magnify the beam radii by a factor four. The resulting focus waists at the position of the atoms and molecules are 40 and  $35 \mu\text{m}$  respectively.

Polarizations are cleaned and controlled by a PBS and a  $\lambda/2$ -waveplate for the 573 nm laser and by a Glan-Taylor (GT) polarizer GT10-B from *Thorlabs* and  $\lambda/2$ -waveplates for the 816 nm laser. Clean and constant polarizations are crucial for the success of the experiments. A wrong or unclean polarization may lead to undesired coupling to molecular excited or ground states. For this purpose also the fiber alignment of the polarization maintaining fibers for in- and outcoupling were cautiously tuned.

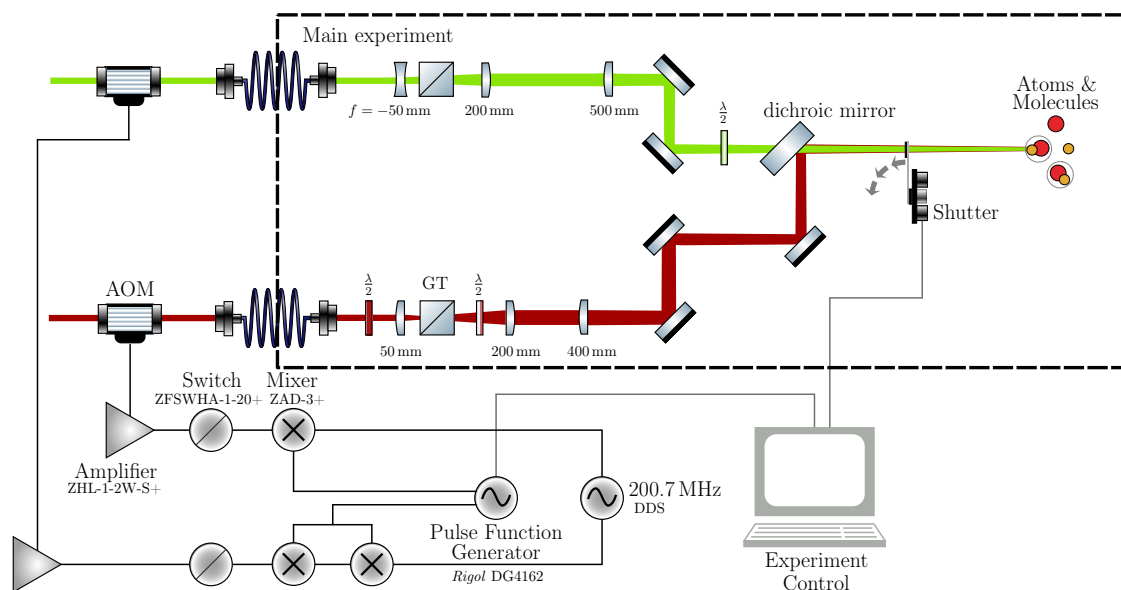


**Figure 3.21: STIRAP beam focusing and pulse generation.** Both laser beams are coupled through an optical fiber. On the main experiment table beam shaping, focusing and polarization control and cleaning is performed. Beam overlap and alignment are done by two separate sets of mirrors and a dichroic mirror. The pulse application is controlled by the experiment control, which creates the pulse sequence and sends it to the pulse function generator which then passes it to the AOMs; see text.

**Pulse generation** The pulse generation is done by using rf amplitude modulation for the AOMs; see Fig. 3.21. The slow STIRAP pulse envelope amplitude is generated by a *Rigol* DG4162 programmable pulse function generator (PFG). It is combined with the radio frequency of 200.7 MHz from the DDS by a mixer array; see Fig. 3.21. For the 573 nm part, two cascaded mixers are used, to increase the amplitude sensitivity for low powers and thus cancel possible leaking light to the diffraction order of the AOM. The amplitude modulated rf signal is then passing a ZFSWHA-1-20+ switch and is amplified by a ZHL-1-2W-S+ amplifier, both from *Mini-Circuits*, before it is fed to the AOMs.

For STIRAP, an adiabatic exchange of Rabi frequencies between the pump and Stokes transition is required. Most commonly, this is done by sine/cosine functions [99]; see Fig. 3.22. The Rabi frequency  $\Omega$  has a non-linear dependence on the applied laser intensity  $I$  with  $\Omega \propto \sqrt{I}$ . Moreover, the signal paths from the PFG to the final laser power for 573 nm and 816 nm on the main experimental table yield an own characteristic response. Both paths were individually calibrated by controlling the rf power at the AOM with the PFG. Both effects have to be considered for designing proper pulses for STIRAP. Fig. 3.22 summarizes the presumed Rabi frequency change seen by the molecules, the pulse form sent to the PFG and the measured presumed laser power change. The overall Rabi frequency is adjusted by the default power of the laser through the optical fiber.

The commands for the PFG are generated by a *Wolfram mathematica* notebook. The inputs are freely designable ramps for the Rabi frequencies for the pump and Stokes transition. The generated output from the notebook contains the explained characteristics and the commands for the PFG. The commands are sent to the PFG via an USB connection where the pulses are applied after receiving an additional trigger from the experiment control.

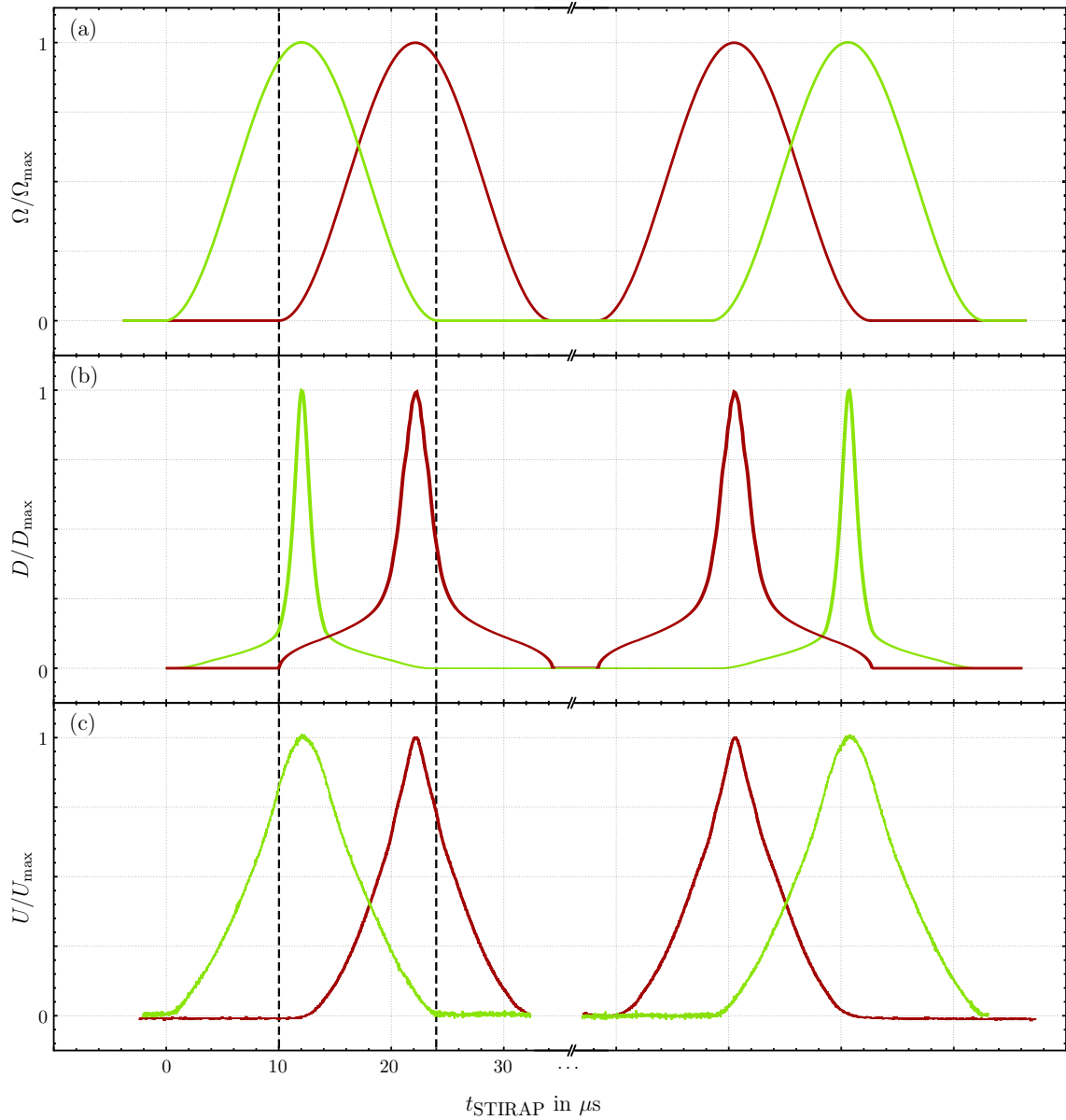


**Figure 3.22:** Pulse shape of the STIRAP. This figure shows the pulse shape of the STIRAP pulses for the different stages in the pulse generation circuit; see Fig. 3.21. (a) Ideal simulated Rabi frequencies for the pump and Stokes pulse. The Rabi frequencies are normalized to their respective maximal value. (b) The normalized output  $P$  of the *Wolfram mathematica* notebook sent to the PFG, with the calibrations for mixers, amplifiers and AOMs response included. (c) Pulse shape measured with a photodiode in front of the main experiment chamber. The powers are normalized to the respective maximal laser powers.

## Chapter 4

# Optical Spectroscopy of the Excited and Ground States

In this chapter the spectroscopy of the excited molecular states for STIRAP in the bosonic  $^{23}\text{Na}^{39}\text{K}$  molecule is carried out. First I will explain the role of the excited state for the STIRAP transfer in Sec. 4.1 and the benefits arising from the involvement of this third state in the molecular state transfer scheme by means of the Franck-Condon principle, singlet-triplet bridging and hyperfine resolution. Then I will summarize the previous findings of cold molecular spectroscopy on the  $^{23}\text{Na}^{39}\text{K}$  molecule and position my work within this frame for its necessity for the successful STIRAP to the ground state; see Sec. 4.2.

The peer-review publication P2: *A pathway to ultracold bosonic  $^{23}\text{Na}^{39}\text{K}$  ground state molecules* in Sec. 4.3 comprises the measurements of the transitions to the excited states and the ground state of the  $^{23}\text{Na}^{39}\text{K}$  molecule and the theoretical model for the description of the excited states.

In Sec. 4.4 I will show additional results of the one-photon excited state spectroscopy, which have been obtained after the publication P2 was accepted. Additionally, I will present all 48 + 48 singlet and triplet hyperfine excited states and give their atomic nuclear spin decomposition for a magnetic field of 200 G, at which the STIRAP is performed.

### 4.1 The Role of the Excited State

The creation of ultracold ground-state molecules essentially relies on STIRAP, the coherent two-photon transfer from the initial weakly bound dimer state to the final deeply bound ground state. Naively, it raises the question, why this relatively complex route to the ground state is the common one, even though it involves two amplitude controlled phase-related narrow-line optical frequencies; compare Chap. 3.

The need for the excited state in the molecular state-transfer scheme originates from the differences between the Feshbach molecule and state the ground state. The Feshbach molecule state possesses mainly triplet character, whereas the ground state is a pure singlet state. Furthermore, the wavefunction of weakly bound Feshbach molecules is located mostly far outside at the rim of the potential, while for the ground-state molecule the wavefunction is located at the minimum of the potential; see Fig. 1.2.

## Franck-Condon Principle

Transitions in a molecular level structure incorporate transitions between different electronic, vibrational and rotational states, which arise from the relative position and motion of the two nuclei. Each state therefore exhibits an individual wavefunction. Transitions between two states, either atomic-molecular or molecular-molecular ones, follow in fact the well known selection rules for angular momentum, energy and parity but additionally experience an adapted transition strength due to the wavefunction overlap of the involved states. This is called the *Franck-Condon principle*. The wavefunction overlap between the well localized ground state and a weakly bound dimer state is fairly small; see Fig. 1.2.

Intuitively, this can be imagined in the following way: The ground-state molecule is a deeply bound diatomic complex, where the two atoms are very close to each other. Accordingly, the wavefunction spread is small and located to the bottom of the potential. The Feshbach molecule, on the other hand, is a loosely bound dimer, where the atoms are far apart from each other and the main part of the wavefunction is located at large internuclear distances and is widespread. Particularly, in the example of Fig. 1.2, the wavefunction for the Feshbach molecule is almost zero at the position of the ground-state wavefunction. In this case no transition is possible at all.

The STIRAP circumvents this issue. The two-photon process introduces a third molecular energy level into the pathway, which has a decent wavefunction overlap with both, the initial and the final state; see Fig. 1.2. Obviously, all the other selection rules also have to be fulfilled. For this reason, it is mandatory to understand the hyperfine level structure of this intermediate state.

The relevance of the Franck-Condon principle is implied by the long exposure times of the one-photon spectroscopy shown in the following publication P2 in Sec. 4.3 [88]. For the presented spectroscopy of atom-molecule transitions, holding times of the atoms in the order of several hundreds of ms have been used, originating from the small Franck-Condon overlap between the diatomic scattering state and the molecular excited state. A conservative estimation of the normalized Rabi frequency results to  $\tilde{\Omega}_{\text{pump,a}} = 2\pi \times 0.004 \text{ kHz} \sqrt{I/(\text{mW cm}^{-2})}$ . In contrast, the normalized Rabi frequency for the molecule-molecule pump transition from the publication P3 in Sec. 5.3 [89] is  $\tilde{\Omega}_{\text{pump,m}} = 2\pi \times 0.66 \text{ kHz} \sqrt{I/(\text{mW cm}^{-2})}$ . The transition strength is increased by a factor of about 150, which comes from the enhanced Franck-Condon overlap from the Feshbach molecule.

## Singlet-Triplet Mixed States

Another very important property of the excited state is its singlet-triplet admixture. The ground state is a pure singlet state in the electronic  $X^1\Sigma^+$  potential and the Feshbach molecule state, on the contrary, possesses a high abundance of triplet character from the  $a^3\Sigma^+$  potential. From symmetry considerations for dipole transitions it is known that changes of the electron spin direction, which are basically transitions from a singlet to a triplet state (and vice versa), are forbidden. To still perform the transition from the Feshbach molecule triplet state to the singlet ground state with a reasonable transition strength, the intermediate state has to have a strong admixture of both spin components.

The singlet-triplet character of the excited state is necessary for the STIRAP. In the following publication P2 in Sec. 4.3 [89], the mixing between the singlet and triplet manifolds are determined by the fit of the local model to the experimental data.

## Hyperfine Resolved Molecular Loss Spectroscopy

The excited state also plays a major role in the creation of spin-polarized ensembles of ground-state molecules and its detailed investigation is fundamentally important [86]. To spectroscopically investigate the excited state the laser for the pump transition is used to selectively populate the hyperfine states in the excited state manifold, causing losses from the ultracold ensemble. Dependent on the choice of the laser light polarization,  $\pi$  or  $\sigma^+/\sigma^-$  transitions can be selectively addressed; see Sec. 5.1.

The spectroscopy can be either done from the diatomic scattering threshold or from the Feshbach molecule state. The advantage of using Feshbach molecules is that the strength of the transition can directly be obtained for the purpose of the STIRAP, as the wavefunctions will be significantly different for scattering atoms and Feshbach molecules. On the other hand, using atomic ensembles simplifies the experimental procedure and therefore makes the entire experiment more reliable, robust and repeatable. Moreover, in the case of a well chosen scattering scenario the atomic mixture can be held for several seconds without significant losses, making it possible to detect weakly coupled states. Anyway, both approaches can be used to spectroscopically explore the excited state hyperfine structure.

Incorporating also the laser for the transition to the ground state, the Stokes transition, into the spectroscopy, information about the ground state can be gathered. When the laser frequency fits the transition energy, the excited state experiences a coupling to the ground state. For a strong dressing of the transition, Autler-Townes effects [134] and constructive state protection [82] can be observed, which can give information about the transition strength and frequency. For low laser beam intensities and short exposure times, electromagnetically induced transparency (EIT) [135] can be observed, which reveals the coherence properties of the coupled molecular three-level system as well as a very precise relative frequency determination of all involved transitions and their corresponding coupling constants.

In the following publication in Sec. 4.3 [88], hyperfine resolved one-photon spectroscopy has been performed. The polarization of the laser light has been changed to select different hyperfine components of the excited states. A theoretical model has been applied to predict the magnetic field dependence of all 48 + 48 hyperfine states of the singlet and triplet manifolds.

Additionally, two-photon Autler-Townes spectroscopy to the  $N = 0$  and  $N = 2$  ground states has been performed to unambiguously identify the rovibrational ground state.

EIT measurements have been performed in the publication P3; see Sec. 5.3 [89].

## 4.2 Spectroscopy of NaK Molecules

The spectroscopy presented in the journal article in Sec. 4.3 [88] focuses on the detection, determination and description of the hyperfine resolved energy level structure of the excited state and the ground state at a bias magnetic field which should be suitable for a STIRAP in the bosonic  $^{23}\text{Na}^{39}\text{K}$  molecule. In previous work [108, 109, 136], the existence of the strongly coupled states  $|B^1\Pi, v = 8\rangle$  and  $|c^3\Sigma^+, v = 30\rangle$  has been proposed theoretically and proven experimentally. In Schulze *et al.* [108], the excited states from the  $B^1\Pi$  and  $c^3\Sigma^+$  potential have been modeled and a suitable pathway to the ground state regarding the singlet-triplet bridge has been identified. In Ferber *et al.* [136] and Temelkov *et al.* [109], the excited states starting from the ground state  $X^1\Sigma^+$  have been observed in an ultrasonic beam experiment at zero magnetic field and with a rotational quantum number of  $N = 6$ . Still, important information for a successful STIRAP was missing, namely the hyperfine structure of the excited states at high bias magnetic fields, transition strengths and the coupling between

the singlet and triplet states. Furthermore, a proper model for the assignment of quantum numbers for selection purposes was missing. In the publication P2 in Sec. 4.3 [88], these issues are addressed.

### 4.3 P2: *A pathway to ultracold $^{23}\text{Na}^{39}\text{K}$ ground state molecules*

**Authors** Kai K. Voges, Philipp Gersema, Torsten Hartmann, Torben A. Schulze, Alessandro Zenesini, Silke Ospelkaus

**Journal** New Journal of Physics

**Article number** 21 (2019) 123034

**DOI** 10.1088/1367-2630/ab5f31

**Contributions** KKV, PG, TAS and SO performed the measurements. KKV and TAS analyzed the data. AZ modeled the excited state hyperfine structure. AZ and SO designed and headed the experiment. All authors contributed to the production of the manuscript.

**Copyright** © 2019 The Author(s). Originally published by IOP Publishing Ltd on behalf of the Institute of Physics and Deutsche Physikalische Gesellschaft. Original content from this work may be used under the terms of the Creative Commons Attribution 3.0 licence.





## PAPER

A pathway to ultracold bosonic  $^{23}\text{Na}^{39}\text{K}$  ground state molecules

Kai K Voges, Philipp Gersema, Torsten Hartmann, Torben A Schulze, Alessandro Zenesini and Silke Ospelkaus

Institut für Quantenoptik, Leibniz Universität Hannover, D-30167 Hannover, Germany

E-mail: [silke.ospelkaus@iqo.uni-hannover.de](mailto:silke.ospelkaus@iqo.uni-hannover.de)

Keywords: STIRAP, molecular spectroscopy, ultracold polar molecules, bosonic quantum gases

## OPEN ACCESS

## RECEIVED

9 September 2019

## REVISED

27 November 2019

## ACCEPTED FOR PUBLICATION

5 December 2019

## PUBLISHED

17 December 2019

Original content from this work may be used under the terms of the [Creative Commons Attribution 3.0 licence](https://creativecommons.org/licenses/by/4.0/).

Any further distribution of this work must maintain attribution to the author(s) and the title of the work, journal citation and DOI.

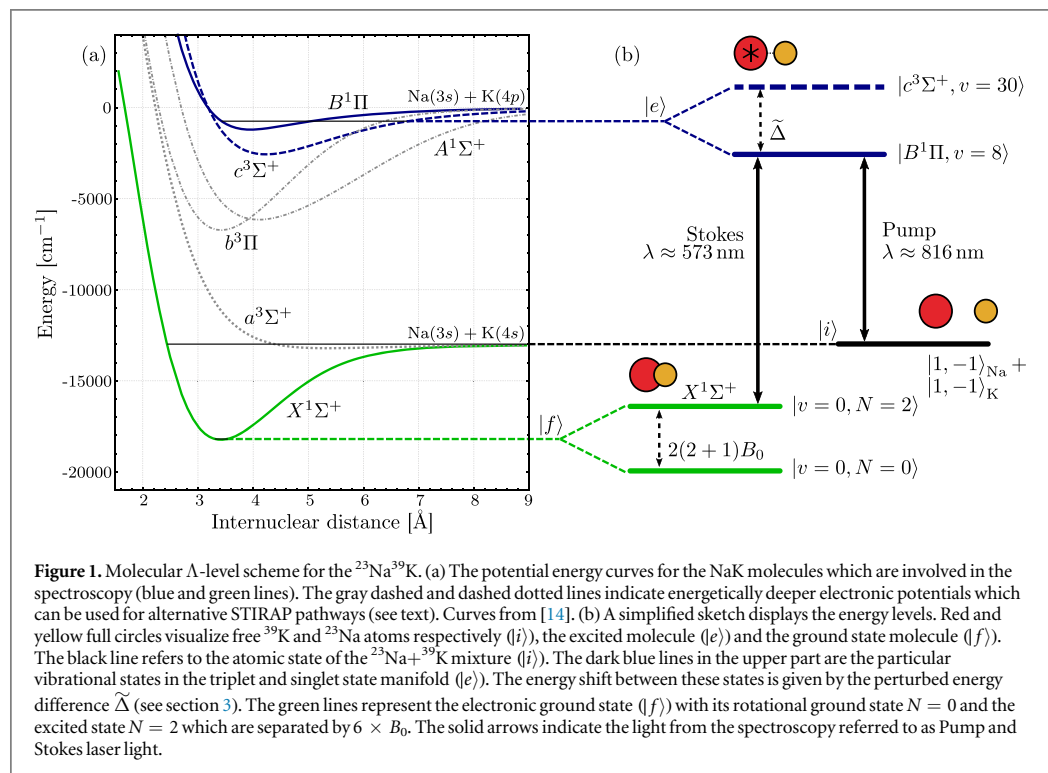


## Abstract

We spectroscopically investigate a pathway for the conversion of  $^{23}\text{Na}^{39}\text{K}$  Feshbach molecules into rovibronic ground state molecules via stimulated Raman adiabatic passage. Using photoassociation spectroscopy from the diatomic scattering threshold in the  $a^3\Sigma^+$  potential, we locate the resonantly mixed electronically excited intermediate states  $|B^1\Pi, \nu = 8\rangle$  and  $|c^3\Sigma^+, \nu = 30\rangle$  which, due to their singlet–triplet admixture, serve as an ideal bridge between predominantly  $a^3\Sigma^+$  Feshbach molecules and pure  $X^1\Sigma^+$  ground state molecules. We investigate their hyperfine structure and present a simple model to determine the singlet–triplet coupling of these states. Using Autler–Townes spectroscopy, we locate the rovibronic ground state of the  $^{23}\text{Na}^{39}\text{K}$  molecule ( $|X^1\Sigma^+, \nu = 0, N = 0\rangle$ ) and the second rotationally excited state  $N = 2$  to unambiguously identify the ground state. We also extract the effective transition dipole moment from the excited to the ground state. Our investigations result in a fully characterized scheme for the creation of ultracold bosonic  $^{23}\text{Na}^{39}\text{K}$  ground state molecules.

## 1. Introduction

Quantum gases of ultracold polar molecules offer unprecedented novel opportunities for the investigation of dipolar collisions, quantum chemical processes and quantum many-body systems [1–5]. The new handle in comparison to atomic systems is given by the electric dipole moment of heteronuclear diatomic ground state molecules. The most successful approach to the creation of ultracold ensembles of polar ground state molecules is based on the association of two chemically different ultracold atomic alkali species. This process starts with magneto-association to weakly bound Feshbach molecules and continues with the coherent transfer of the weakly bound molecules to the rovibrational ground state of polar molecules using a Stimulated Raman Adiabatic Passage (STIRAP) [6]. For the transfer from the initially magneto-associated molecular state  $|i\rangle$  to the final molecular ground state  $|f\rangle$ , the STIRAP transfer consists of an adiabatic change of the dressed state composition by involving two coherent laser beams referred to as Pump and Stokes laser. The Pump laser couples  $|i\rangle$  to a third excited state  $|e\rangle$ , the Stokes laser  $|f\rangle$  to  $|e\rangle$ , resulting in a typical  $\Lambda$ -level scheme; see figure 1. During the time evolution the intermediate state  $|e\rangle$  is not populated and therefore does not contribute to incoherent molecule losses due to spontaneous decay. In the case of bi-alkali molecules, the coupling between  $|i\rangle/|f\rangle$  and  $|e\rangle$  is governed by the Franck–Condon overlap, the singlet–triplet fraction and the hyperfine composition of the states. For bi-alkali heteronuclear molecules the ground state  $|f\rangle$  always belongs to the  $X^1\Sigma^+$  potential while a weakly bound dimer state  $|i\rangle$  exists mainly in the  $a^3\Sigma^+$  potential; see figure 1(a). To act as an efficient coupling bridge, the choice of  $|e\rangle$  is crucial. It needs to be chosen to couple well to the initial triplet as well as to the final singlet state. This can be achieved through the careful choice of mixed states in the  $^3\Pi/1^1\Sigma^+$  or  $^3\Sigma^+/1^1\Pi$  potentials; see figure 1(a). Up to now, the production of trapped ground state molecules, either fermionic, such as  $^{40}\text{K}^{87}\text{Rb}$  [7],  $^{23}\text{Na}^{40}\text{K}$  [8] and  $^6\text{Li}^{23}\text{Na}$  [9], or bosonic, such as  $^{87}\text{Rb}^{133}\text{Cs}$  [10, 11] and  $^{23}\text{Na}^{87}\text{Rb}$  [12] has been reported.  $\text{NaRb}$  [12] and  $\text{RbCs}$  [10, 11] ground state molecules have been prepared by using coupled states in the  $A^1\Sigma^+$  and  $b^3\Pi$  potentials.  $\text{KRb}$  [7] and fermionic  $^{23}\text{Na}^{40}\text{K}$  [8] ground state molecules have been created using states in the  $c^3\Sigma^+$  and  $B^1\Pi$  potentials. Additionally, ground state molecules for fermionic  $^{23}\text{Na}^{40}\text{K}$  have been created using excited states in energetically higher  $D^1\Pi$  and  $d^3\Pi$  potentials [13]; not shown in figure 1(a).



In the case of  $^{23}\text{Na}^{39}\text{K}$ , suitable transitions for the creation of ground state molecules have so far only been investigated experimentally in hot beam experiments accessing rotational states with  $N \geq 6$  [15]. Moreover, the work [15] does not include hyperfine structure and offset magnetic fields. In addition, previous theory work [16] describes a complete spectrum involving spin-orbit, Coriolis and spin-rotation interactions as well as Franck-Condon factors identifying promising singlet-triplet mixed states. However, the hyperfine structure still remains untreated although it is crucial for a successful STIRAP transfer [13]. In this paper, we present hyperfine resolved spectroscopic investigations of the  $^{23}\text{Na}^{39}\text{K}$  molecule at bias magnetic fields for strongly mixed states known from [15, 16].

Using one-photon association spectroscopy, we first locate and characterize the strongly mixed  $|B^1\Pi, \nu = 8\rangle$  and  $|c^3\Sigma^+, \nu = 30\rangle$  states serving as a bridge between the  $a^3\Sigma^+$  and  $X^1\Sigma^+$  potentials. A large Zeeman splitting at 150 G enables us to perform hyperfine resolved optical spectroscopy of the excited molecular state manifold. We present a simple model to determine the singlet-triplet admixtures of the excited states. Furthermore, we perform two-photon Autler-Townes spectroscopy [17] to locate the rovibronic ground state, determine the rotational constants and extract effective dipole transition matrix elements from our measurements. Thus, we present and fully characterize a pathway for the creation of rovibronic ( $\nu = 0, N = 0$ )  $^{23}\text{Na}^{39}\text{K}$  ground state molecules for the first time.

In the following, we give an outline of the experimental setup and procedures; see section 2. In section 3.1 we present the model fit for the coupled excited states, and in section 3.2 we detail the spectroscopic one-photon measurements. This is followed by the two-photon ground state spectroscopy which includes the determination of the rotational constant and the transition dipole element of the Stokes transition in section 4.

## 2. Experimental setup and procedures

The spectroscopic studies presented in this work are based on the preparation of an ultracold mixture of  $^{23}\text{Na}+^{39}\text{K}$ . A description of the experimental setup can be found in [16, 18, 19]. Details of the experimental procedure can be found in [20, 21]. In the following, we briefly summarize the main experimental steps. First,  $^{23}\text{Na}$  and  $^{39}\text{K}$  atoms are loaded into a two-color magneto-optical trap, followed by simultaneous molasses cooling of both species. The atoms are optically pumped to the  $F = 1$  manifold and loaded into an optically plugged magnetic quadrupole trap, where forced microwave evaporative cooling of  $^{23}\text{Na}$  is performed.  $^{39}\text{K}$  atoms are sympathetically cooled by  $^{23}\text{Na}$ . After both atomic species are transferred into a 1064 nm crossed-beam optical dipole trap (cODT), a homogeneous magnetic field of 150 G is applied to ensure favorable scattering properties in the mixture [20]. The atoms are

prepared in the  $|f = 1, m_f = -1\rangle_{\text{Na}} + |f = 1, m_f = -1\rangle_{\text{K}}$  states. Then, forced optical evaporation is performed on both species by lowering the intensity of both beams of the cODT. The forced evaporation process is stopped when the atomic sample has a temperature of about  $1 \mu\text{K}$  and a corresponding phase space density  $\leq 0.1$  for both species. To decrease the differential gravitational sag and assure a significant overlap of the two clouds, the cODT intensity is ramped up again. For the spectroscopy presented in this work, the magnetic field is either set to  $130 \text{ G}$  or left at  $150 \text{ G}$  yielding values at which the inter and intra species scattering properties allow for a long lifetime of the sample by minimizing three-body losses. This allows for a sufficiently long interaction time during photoassociation experiments, as required by the expected weak coupling between the atom pair at the scattering threshold and the electronically excited state molecules. The laser light for the Pump and the Stokes transitions at  $816 \text{ nm}$  and  $573 \text{ nm}$  respectively is generated by diode laser systems. The  $816 \text{ nm}$  light is generated by a commercial external-cavity diode laser (ECDL). The generation of the  $573 \text{ nm}$  light starts from a commercial ECDL operating at  $1146 \text{ nm}$ . The light is amplified by a tapered amplifier and subsequently frequency doubled in a self-built resonant bow-tie doubling cavity. Both lasers are locked to a commercial ultra-low expansion (ULE) glass cavity by using the Pound–Drever–Hall technique [22]. A sideband locking scheme involving widely tunable electro-optical modulators ensure the tunability of both locked lasers within the free spectral range of the ULE cavity which is  $1.499 \text{ GHz}$ . The finesse of the ULE cavity is  $24\,900$  and  $37\,400$  for  $816 \text{ nm}$  and  $1146 \text{ nm}$  light, respectively. The laser system setup is similar to the one described in [23].

Optical fibers spatially filter the light and ensure high quality beam properties. The polarization is set by a half-wave plate for each wavelength. The foci of the two beams on the atoms are adjusted to  $1/e^2$ -beam waists of  $35 \mu\text{m}$  for the Pump laser and  $40 \mu\text{m}$  for the Stokes laser. The maximum laser power is  $25 \text{ mW}$  for each laser. With the Pump beam at full power, the Stokes beam is reduced to  $\leq 10 \text{ mW}$  to avoid a depletion of  $^{23}\text{Na}$  atoms in the trap center, originating from a strong repulsive dipole force. The beams are geometrically superimposed and orientated perpendicularly to the applied magnetic field.

### 3. Excited state spectroscopy

#### 3.1. Local model for the excited state manifold

In our experiment, we are specifically interested in a detailed understanding of the previously located [15] strongly mixed  $|B^1\Pi, \nu = 8\rangle$  and  $|c^3\Sigma^+, \nu = 30\rangle$  states. Hyperfine splitting and spin–orbit coupling for these two states can be modeled by a simple two-manifold coupled system, when neglecting contributions from other vibrational and rotational levels, from nucleus–nucleus interaction and nucleus–rotation coupling. This allows us to treat the two state manifolds separately in the following spectrally local model.

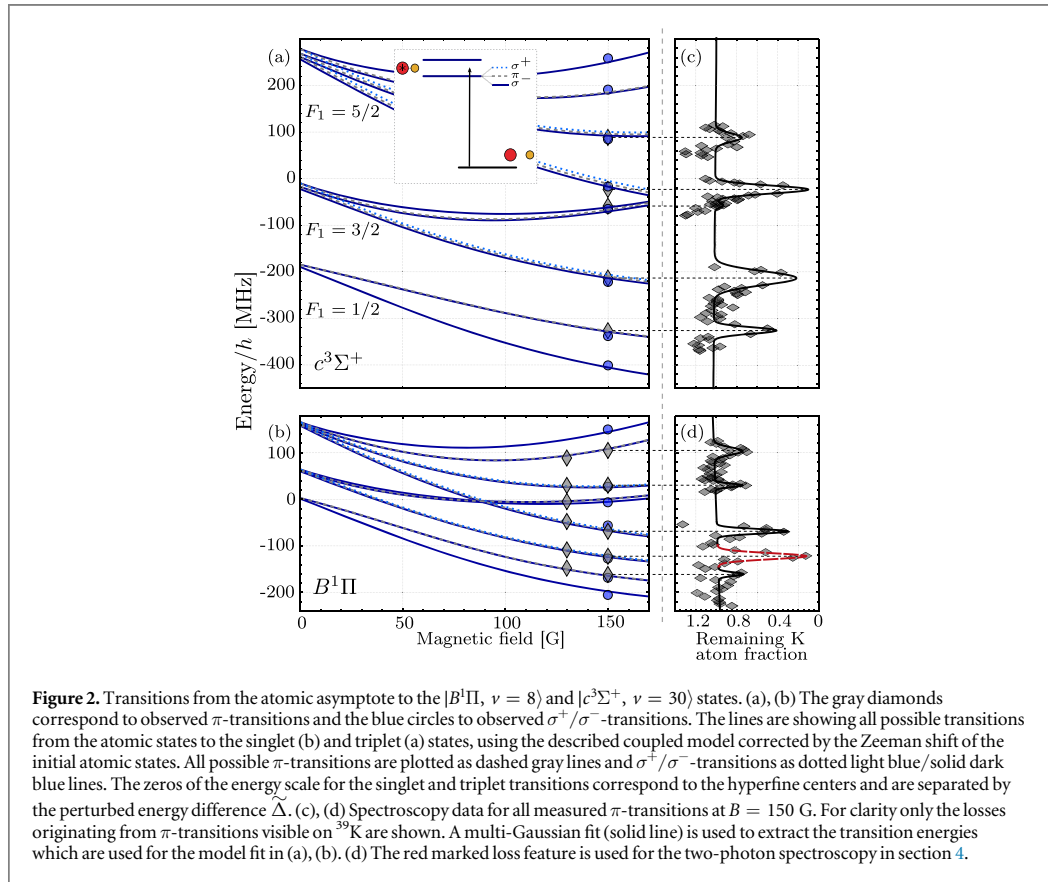
The excited state can be described by Hund’s case (a) and that allows to consider the total angular momentum  $J = 1$  as resulting from the coupling of the rotational angular momentum  $\vec{N}$  and the spin  $\vec{S}$  [24].  $^{23}\text{Na}$  and  $^{39}\text{K}$  nuclear spins are  $i_{\text{Na}} = i_{\text{K}} = 3/2$  leading to  $3 \times 4 \times 4 = 48$  different states in the singlet and triplet channel.

In absence of coupling the Hamiltonians for the investigated states, in the basis of  $|B/c, J, m_J, i_{\text{Na}}, m_{i_{\text{Na}}}, i_{\text{K}}, m_{i_{\text{K}}}\rangle$ , reads as [25]

$$H^B = \mu_0 g_J^B \vec{J} \cdot \vec{B} \quad (1)$$

$$H^c = \Delta + \vec{J} \cdot (A_{\text{K}} \vec{i}_{\text{K}} + A_{\text{Na}} \vec{i}_{\text{Na}}) + \mu_0 g_J^c \vec{J} \cdot \vec{B}, \quad (2)$$

where  $A_{\text{K}}$  and  $A_{\text{Na}}$  are the hyperfine constants,  $\mu_0$  the Bohr magneton and  $\vec{B}$  the applied magnetic field. The energy  $\Delta$  corresponds to the unperturbed energy difference between the two states and we neglect the hyperfine term for the singlet state. The  $^{23}\text{Na}$  hyperfine coupling  $A_{\text{Na}}$  is almost two orders of magnitude larger than  $A_{\text{K}}$  and it was already resolved in previous spectroscopic measurements on cold molecular beams [15]. The hyperfine splitting of  $^{39}\text{K}$  is comparable or even smaller than the molecular state linewidth and remains mainly unresolved. At low field this allows to consider  $F_1 = |\vec{J} + \vec{i}_{\text{Na}}| = (1/2, 3/2, 5/2)$  as a good quantum number, as visible in figure 2, with three groups of states at low magnetic field. Additionally, one can consider the total angular momentum  $\vec{F} = \vec{J} + \vec{i}_{\text{Na}} + \vec{i}_{\text{K}} = \vec{F}_1 + \vec{i}_{\text{K}}$ , where the projection on the quantization axes  $m_F$  is the only preserved quantity even at large magnetic fields. The Zeeman term of equation (2) neglects nuclear contributions and can be expanded as  $\mu_0 m_J g_J B$ , where  $m_J$  is the projection of  $\vec{J}$  on the magnetic field axis and  $g_J$  the Landé factor. In absence of coupling between singlet and triplet, one has  $g_J^B = g_N = g_L/(J(J+1)) = 1/2$  and  $g_J^c = g_s/2 \approx 1$  [25, 26], where  $g_L$  and  $g_s$  are the known electron orbital and spin  $g$ -factors equal to 1 and 2.0023, respectively. Spin–orbit interaction couples singlet and triplet with strength  $\xi_{Bc}$  with selection rules  $\Delta J = 0$ ,  $\Delta m_{i_{\text{Na}}} = 0$  and  $\Delta m_{i_{\text{K}}} = 0$ . The coupling also already incorporates the vibrational wavefunction overlap of the two states. Hence, the problem reduces to solving the following  $(48 + 48) \times (48 + 48)$  matrix



$$\begin{pmatrix} H^B & \xi_{Bc} \\ \xi_{Bc} & H^c \end{pmatrix} \quad (3)$$

Note that the coupling  $\xi_{Bc}$  shows its effect in two ways:

- As the Zeeman term remains significantly smaller than both the unperturbed singlet–triplet energy difference  $\Delta$  and of the coupling strength  $\xi_{Bc}$ , one finds for strong fields compared to the hyperfine splitting (not shown in the later figure 3) the effective Landé factors  $g_{J,\text{eff}}^{B,c}$

$$g_{J,\text{eff}}^{B,c} = \frac{1}{2} \left( g_J^c + g_J^B \mp \Delta \frac{g_J^c - g_J^B}{\sqrt{4\xi_{Bc}^2 + \Delta^2}} \right) \quad (4)$$

$$= g_J^{B,c} \pm \frac{1}{4} \left( 1 - \frac{\Delta}{\tilde{\Delta}} \right), \quad (5)$$

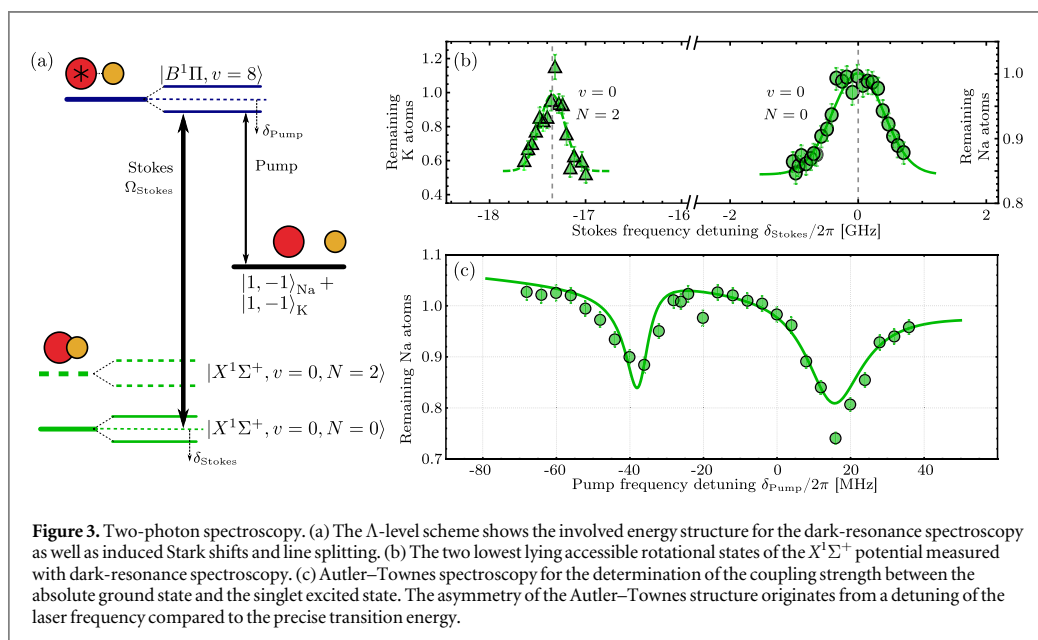
where  $\tilde{\Delta} = \sqrt{4\xi_{Bc}^2 + \Delta^2}$  is the energy difference of the hyperfine centers at  $B = 0$  in the the coupled case.

- The acquired triplet character of the singlet state will lead to a large hyperfine splitting, while the triplet one is decreased.

### 3.2. One-photon spectroscopy

From spectroscopic investigations [15] the transition energies from the atomic scattering threshold in the  $a^3\Sigma^+$  potential to the dominantly  $|B^1\Pi, v = 8\rangle$  and dominantly  $|c^3\Sigma^+, v = 30\rangle$  states are expected to be about  $12\,242.927\text{ cm}^{-1}$  for the triplet state and about  $12\,242.017\text{ cm}^{-1}$  for the singlet state at a magnetic field of 150 G. In the following we will refer to the states with a dominant triplet character as *triplet* and to the ones with dominantly singlet character as *singlet*.

To locate the excited states, we measure the remaining atom number in both species after applying the Pump light for up to 1.6 s for variable detunings from the expected transition frequencies. The atoms associated to



molecules in the excited state collide with the remaining atoms and/or decay to a lower lying molecular state. Both of these effects manifest themselves as a decreased number of atoms in the initial state. The step size for the laser detuning scan is set to a few MHz, which is sufficient to resolve the different structures with an expected linewidth of about  $2\pi \times 6$  MHz. The measurements are performed both for polarizations parallel to the magnetic field (which implies  $\pi$ -transitions from the atomic to the molecular state) and perpendicular to it (leading to both  $\sigma^+$ - and  $\sigma^-$ -transitions). Figures 2(a), (b) shows the positions of the loss features for the triplet and singlet states and  $\pi$ - and  $\sigma^+/\sigma^-$ -transitions. In the case of the singlet state, we perform spectroscopic measurements at two different magnetic field strengths to calibrate our model for the Zeeman splitting. Figures 2(c), (d) show the corresponding atom losses from  $\pi$ -transitions measured on  $^{39}\text{K}$ .

In the magnetic field range at which our measurements are performed, the energy splitting remains in an intermediate region between pure Zeeman and Paschen–Back regime (see figure 2), where  $F$  and  $F_1$  are no good quantum numbers. Selection rules based on the  $m_F$  allow to decrease the number of states to 18 observable ones, 6 for  $\pi$ - and 12 (3/9) for  $\sigma^+/\sigma^-$ -transitions.

Figures 2(a), (b) contains the complete collection of the observed resonant features with a distance of 27.347 GHz ( $\approx 0.913$   $\text{cm}^{-1}$ ) between the manifold zeroes. The lines result from the fit of our model to the experimental observations, where the coupling  $\xi_{B\sigma}$ , the energy difference  $\Delta$  and the hyperfine coupling constants  $A_{\text{Na}}$  and  $A_{\text{K}}$  are used as free parameters. The overall curvature of the lines originates from the atomic state Zeeman effect which is in the intermediate regime for both atoms. From the fit, we obtain  $g_{J,\text{eff}}^B = 0.630(8)$  and  $g_{J,\text{eff}}^c = 0.870(8)$ . The uncertainty comes from the fit and from the ambiguous assignment of few resonances to a precise state, due to the simultaneous presence of  $\sigma^+/\sigma^-$  polarized light. The unperturbed energy difference  $\Delta$  is found to be equal to 13.1(8) GHz ( $=0.437(31)$   $\text{cm}^{-1}$ ) and  $\xi_{Bc}$  to be equal to 12.0(2) GHz ( $=0.400(8)$   $\text{cm}^{-1}$ ). The obtained values correspond to a 26(1)%/74(1)% mixing of singlet and triplet states, which is in agreement with previous predictions [27]. Remarkably the coupling strength  $\xi_{Bc}$  is comparable to the unperturbed energy difference  $\Delta$ . This explains the large mixing. The obtained value for  $A_{\text{Na}}$  of 307(9) MHz ( $\approx 0.0102(3)$   $\text{cm}^{-1}$ ) is in good agreement with previous spectroscopic measurements [28]. Our model provides a value for  $A_{\text{K}} = 6(9)$  MHz ( $\approx 2(3) \times 10^{-3}$   $\text{cm}^{-1}$ ), compatible with previous predictions and measurements [28, 29].

The amplitudes of the loss features depend on the coupling between the atomic and molecular states and are therefore highly dependent on their hyperfine quantum numbers and the wavefunction overlap. The strong mixing of the wavefunctions in the excited states and the scattering wavefunction of the atoms lead to interference effects altering the effective transition dipole strength. Our calculations do not account for the interference and thus do not provide an accurate description of transition amplitudes [16].

#### 4. Two-photon ground state spectroscopy

Using the located excited state as a bridge, we demonstrate two-photon spectroscopy of the rovibrational ground state  $|X^1\Sigma, \nu = 0, N = 0\rangle$ ; as sketched in figure 1. The energy difference between ground and excited state is well known from spectroscopic data [15] and can be predicted within a precision of  $\pm 0.08 \text{ cm}^{-1}$ . To exactly determine the energy of the rovibrational ground state, we fixed the Pump laser frequency on the transition with strongest losses from figure 2(d) within the singlet states which is marked with a red dashed curve. The state originates from the combination of two basis states which are labeled by  $|B/c, 1, -1, 3/2, -1/2, 3/2, -1/2\rangle$  and  $|B/c, 1, 0, 3/2, -1/2, 3/2, -3/2\rangle$  where the quantum numbers are as described in section 3.1.

When the Stokes laser is on resonance, it is inducing a Stark shift on the excited state and a revival of the atom number is expected as sketched in figure 3(a). Figure 3(b) shows this protection when the detuning  $\delta_{\text{Stokes}}$  is scanned with a full width half maximum for the  $|X^1\Sigma^+, \nu = 0, N = 0\rangle$  of about 405(35) MHz for a laser power of 5 mW. The observed peak of the transition energy is at  $17\,452.826(2) \text{ cm}^{-1}$ .

Furthermore, to unambiguously identify the ground state, we performed an atom-loss scan also in the range of frequencies where the second rotationally excited state with  $N = 2$  is expected; see figure 3(b). The observed energy difference of  $\Delta_{N=0 \rightarrow N=2} = h \times 17.3(3) \text{ GHz}$  allows us to deduct the rotational constant to be  $B_{\nu=0} = h \times 2.89(5) \text{ GHz}$  by using the relation  $\Delta_{N=0 \rightarrow N=2} = B_0 \times 2(2 + 1)$ . This value agrees with the one observed by using microwave spectroscopy [30]. The full width of half maximum for the protection is 133(27) MHz. This is smaller than for the  $N = 0$  state, indicating a weaker coupling to the excited states, as expected from theoretical considerations.

To directly determine the coupling strength between the ground and the excited state, we fixed the Stokes laser frequency close to resonance and scanned the Pump laser frequency detuning  $\delta_{\text{Pump}}$ . This scan reveals the well-known Autler–Townes splitting [17], the magnitude of which is proportional to the dipole matrix element of the transition. Figure 3(c) shows the measured remaining atom number with the typical double-loss feature. The asymmetric shape of the splitting originates from a residual detuning to the exact transition frequency of the Stokes laser which is determined to be  $\delta_{\text{Stokes}} = 2\pi \times -22 \text{ MHz}$ . We derive the Rabi frequency  $\Omega_{\text{Stokes}} = 2\pi \times 23.5 \text{ MHz}$  for an applied laser power of 5 mW, corresponding to a normalized Rabi frequency of  $\tilde{\Omega}_{\text{Stokes}} = 2\pi \times 65.2 \text{ kHz} \times \sqrt{I/(m\text{W cm}^{-2})}$  and an effective transition dipole moment of 0.170 D. Both values,  $\delta_{\text{Stokes}}$  and  $\Omega_{\text{Stokes}}$  are derived from a three-level master equation modeling the line shape shown in figure 3(c).

#### 5. Conclusion and outlook

Within this work, we have characterized a two-photon scheme for the coupling of the diatomic scattering threshold in the  $a^3\Sigma^+$  potential to the rovibrational ground state  $|X^1\Sigma^+, \nu = 0, N = 0\rangle$ . Using photoassociation spectroscopy, we have observed and characterized the excited state hyperfine manifolds of the coupled  $|B^1\Pi, \nu = 8\rangle$  and  $|c^3\Sigma^+, \nu = 30\rangle$  states in the bosonic  $^{23}\text{Na}^{39}\text{K}$  molecules at 130 and 150 G, starting from an ultracold atomic quantum gas mixture in the states  $|f = 1, m_f = -1\rangle_{\text{Na}} + |f = 1, m_f = -1\rangle_{\text{K}}$ . By applying a spectral local model fit to the measurements, we have extracted the admixture of these states to be 26%/74%. Due to the strong singlet–triplet mixing, this part of the spectrum serves as an ideal bridge from the triplet atomic scattering threshold to the singlet rovibronic ground state molecules. Making use of this bridge, we have identified the rovibrational ground state and the second rotationally excited state in two-photon spectroscopy. From an Autler–Townes measurement we have extracted the Rabi-coupling between the excited and the ground state. Our work results in a fully characterized scheme for the conversion of  $^{23}\text{Na}^{39}\text{K}$  Feshbach molecules to rovibrational ground state polar molecules and will allow for the efficient creation of ultracold ensembles of chemically stable bosonic  $^{23}\text{Na}^{39}\text{K}$  ground state molecules.

#### Acknowledgments

We thank Eberhard Tiemann for enlightening discussions and suggestions. We gratefully acknowledge financial support from the European Research Council through ERC Starting Grant POLAR and from the Deutsche Forschungsgemeinschaft (DFG) through CRC 1227 (DQ-mat), project A03 and FOR2247, project E5. KKV and PG thank the Deutsche Forschungsgemeinschaft for financial support through Research Training Group (RTG) 1991.

## References

- [1] Ospelkaus S, Ni K K, Wang D, de Miranda M H G, Neyenhuis B, Quéméner G, Julienne P S, Bohn J L, Jin D S and Ye J 2010 *Science* **327** 853–7
- [2] Guo M, Ye X, He J, González-Martínez M L, Vexiau R, Quéméner G and Wang D 2018 *Phys. Rev. X* **8** 041044
- [3] Zuchowski P S and Hutson J M 2010 *Phys. Rev. A* **81** 060703
- [4] Gorshkov A V, Manmana S R, Chen G, Ye J, Demler E, Lukin M D and Rey A M 2011 *Phys. Rev. Lett.* **107** 115301
- [5] Büchler H, Micheli A and Zoller P 2007 *Nat. Phys.* **3** 726–31
- [6] Bergmann K, Theuer H and Shore B W 1998 *Rev. Mod. Phys.* **70** 1003–25
- [7] Ni K K, Ospelkaus S, de Miranda M H G, Peer A, Neyenhuis B, Zirbel J J, Kotochigova S, Julienne P S, Jin D S and Ye J 2008 *Science* **322** 231–5
- [8] Park J W, Will S A and Zwierlein M W 2015 *Phys. Rev. Lett.* **114** 205302
- [9] Rvachov T M, Son H, Sommer A T, Ebadi S, Park J J, Zwierlein M W, Ketterle W and Jamison A O 2017 *Phys. Rev. Lett.* **119** 143001
- [10] Takekoshi T, Reichsöllner L, Schindewolf A, Hutson J M, Le Sueur C R, Dulieu O, Ferlino F, Grimm R and Nägerl H C 2014 *Phys. Rev. Lett.* **113** 205301
- [11] Molony P K, Gregory P D, Ji Z, Lu B, Köppinger M P, Le Sueur C R, Blackley C L, Hutson J M and Cornish S L 2014 *Phys. Rev. Lett.* **113** 255301
- [12] Guo M, Zhu B, Lu B, Ye X, Wang F, Vexiau R, Bouloufa-Maafa N, Quéméner G, Dulieu O and Wang D 2016 *Phys. Rev. Lett.* **116** 205303
- [13] Seeßelberg F, Buchheim N, Lu Z K, Schneider T, Luo X Y, Tiemann E, Bloch I and Gohle C 2018 *Phys. Rev. A* **97** 013405
- [14] Aymar M and Dulieu O 2007 *Mol. Phys.* **105** 1733–42
- [15] Temelkov I, Knöckel H, Pashov A and Tiemann E 2015 *Phys. Rev. A* **91** 032512
- [16] Schulze T A, Temelkov I I, Gempel M W, Hartmann T, Knöckel H, Ospelkaus S and Tiemann E 2013 *Phys. Rev. A* **88** 023401
- [17] Autler S H and Townes C H 1955 *Phys. Rev.* **100** 703–22
- [18] Gempel M W 2016 *PhD Thesis* University of Hannover [www.tib.eu/de/suchen/id/TIBKAT%3A853787425/Towards-ultracold-polar-NaK-molecules-and-the-investigation/](http://www.tib.eu/de/suchen/id/TIBKAT%3A853787425/Towards-ultracold-polar-NaK-molecules-and-the-investigation/)
- [19] Hartmann T 2018 *PhD Thesis* University of Hannover [www.tib.eu/de/suchen/id/datacite%3Adoi-10.15488%252F4699/An-experiment-apparatus-for-the-production-of-ultracold/](http://www.tib.eu/de/suchen/id/datacite%3Adoi-10.15488%252F4699/An-experiment-apparatus-for-the-production-of-ultracold/)
- [20] Schulze T A, Hartmann T, Voges K K, Gempel M W, Tiemann E, Zenesini A and Ospelkaus S 2018 *Phys. Rev. A* **97** 023623
- [21] Hartmann T, Schulze T A, Voges K K, Gersema P, Gempel M W, Tiemann E, Zenesini A and Ospelkaus S 2019 *Phys. Rev. A* **99** 032711
- [22] Drever R W P, Hall J L, Kowalski F V, Hough J, Ford G M, Munley A J and Ward H 1983 *Appl. Phys. B* **31** 97–105
- [23] Gregory P D, Molony P K, Köppinger M P, Kumar A, Ji Z, Lu B, Marchant A L and Cornish S L 2015 *New J. Phys.* **17** 055006
- [24] Ishikawa K 1993 *J. Chem. Phys.* **98** 1916–24
- [25] Townes C H and Schawlow A 1955 *Microwave Spectroscopy* (New York: Dover)
- [26] Semenov M, Yurchenko S N and Tennyson J 2016 *J. Mol. Spectrosc.* **330** 57–62
- [27] Ferber R, Pazyuk E A, Stolyarov A V, Zaitsevskii A, Kowalczyk P, Chen H, Wang H and Stwalley W C 2000 *J. Chem. Phys.* **112** 5740
- [28] Ishikawa K, Kumauchi T, Baba M and Katô H 1992 *J. Chem. Phys.* **96** 6423–32
- [29] Kowalczyk P 1989 *J. Chem. Phys.* **91** 2779–89
- [30] Yamada C and Hirota E 1992 *J. Mol. Spectrosc.* **153** 91

#### 4.4 Additional Results of the Excited States Spectroscopy

The derivation of the hyperfine structure for the singlet and triplet excited states of the journal article P2 in Sec. 4.3 [88] predicts in total 48+48 singlet and triplet states. Nonetheless, the presented measurements in P2 start from an atomic mixture with the states  $|f = 1, m_f = -1\rangle_{\text{Na}} + |f = 1, m_f = -1\rangle_{\text{K}}$  which possess a total angular momentum of  $M_F = -2$ . Dipole transitions to the excited state access only the states with  $M_F = -1, -2, -3$ . Thus, not all predicted states are observable and not all predicted 48 + 48 singlet and triplet states were presented due to clarity reasons in the respective article.

In the course of the experimental progress, spectroscopy from the molecular bound state close to the diatomic  $|f = 1, m_f = -1\rangle_{\text{Na}} + |f = 2, m_f = -2\rangle_{\text{K}}$  states with a total angular momentum  $M_F = -3$  was performed, adding more data points to the data set from P2. An updated version of all found transitions to the triplet manifold is shown in Fig. 4.1. Please note that also the predicted states  $|e_{a,1/2}\rangle$  for a loss-free STIRAP from Chap. 5 [89] have been found. Moreover, the presented data from the journal article in Sec. 4.3 [88] shows the relative transition energies. To adjust the theoretical model of the excited states to the transition data, the atomic ground-state energy was removed. This explains the nonintuitive bending of the lines in the figures of P2 in Sec. 4.3 [88]. The figures 4.2 and 4.3 show the pure theoretical model of the excited state hyperfine structure with all 48 + 48 singlet and triplet levels and a corresponding labeling of the projected atomic quantum numbers.

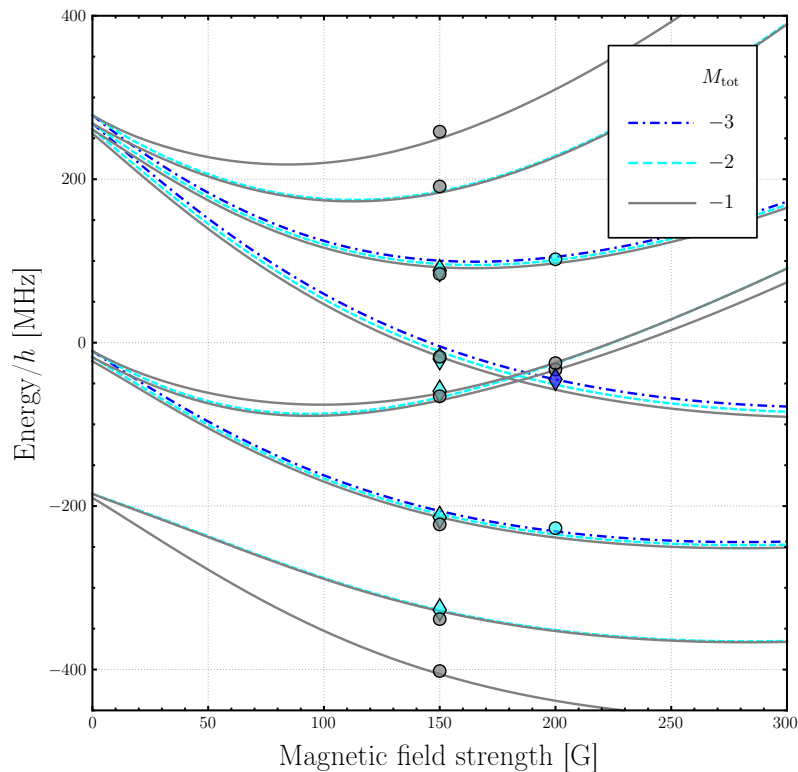


**Figure 4.1:** Transition energies to the triplet manifold. The transitions are shown relative to the line center of the triplet manifold. The curves originate from the model described in [88] but are corrected by the atomic ground-state energy shift. In addition to the measurements at 150 G, which are the ones already presented in [88], measurements at 200 G are presented. Diamonds are observations taken with linearly polarized light and circles are measurements with circularly polarized light. The colors correspond to the assigned states, analogously to the colors in the legend, which are analogous to the ones in Fig. 4.2.

For the triplet  $c^3\Sigma^+$  manifold, the state assignments are listed in Tab. 4.1 with all major contributions of different states in the mixed case at 200 G<sup>1</sup>. The respective first state in the table corresponds to the atomic quantum number decomposition of the excited states in the Paschen-Back regime, which is also valid for the singlet case shown in Fig. 4.3. For both figures the overall ordering becomes clear at higher magnetic fields. The electronic angular momentum separates the manifold into the three  $M_J = [-1, 0, 1]$  branches. Each branch is again divided by the relatively strongly coupled nuclear momentum projection from the sodium nucleus  $m_{i_{\text{Na}}} = [-3/2, -1/2, 1/2, 3/2]$ . The weakly coupling  $m_{i_{\text{K}}} = [-3/2, -1/2, 1/2, 3/2]$  splits each branch again into four components. In total this results in  $3 \times 4 \times 4 = 48$  hyperfine levels for each manifold. The total angular momentum projection is shown by the color and line coding. Their energetic arrangement due to the angular momentum projection can either be seen by the color coding or by the successive number order in Tab. 4.1.

**Table 4.1:** Quantum number assignment for the excited states. The states are labeled according to the ones from Fig. 4.2. The order is kept according to the energies in the Paschen-Back regime. The three  $M_J$  branches are separated in this table by horizontal double lines. Each  $m_{i_{\text{Na}}}$  is combined under a capital letter A - L., where always four successive branches group into one  $M_J$  branch. Within the  $m_{i_{\text{Na}}}$  groups,  $m_{i_{\text{K}}}$  states are aligned. The quantitative state admixtures in this table are the most contributing states for a field of 200 G, where the STIRAP takes place. The states named first correspond to the dominant ones in the Paschen-Back regime. The state, for which STIRAP is reported in [89] is the D.  $|c\rangle = |e_0\rangle$  state. The states for the alternative STIRAP paths are C.  $|c\rangle = |e_{a,1}\rangle$  and H.  $|c\rangle = |e_{a,2}\rangle$ .

State	$ m_{i_{\text{K}}}, m_{i_{\text{Na}}}, M_J, M_F\rangle$
L. $ d\rangle$	$ 3/2, 3/2, 1, 4\rangle$
$ c\rangle$	$ 1/2, 3/2, 1, 3\rangle$
$ b\rangle$	$ -1/2, 3/2, 1, 2\rangle$
$ a\rangle$	$ -3/2, 3/2, 1, 1\rangle$
K. $ d\rangle$	$ 3/2, 1/2, 1, 3\rangle \sim  3/2, 3/2, 0, 3\rangle$
$ c\rangle$	$ 1/2, 1/2, 1, 2\rangle \sim  1/2, 3/2, 0, 2\rangle$
$ b\rangle$	$ -1/2, 1/2, 1, 1\rangle \sim  -1/2, 3/2, 0, 1\rangle$
$ a\rangle$	$ -3/2, 1/2, 1, 0\rangle \sim  -3/2, 3/2, 0, 0\rangle$
J. $ d\rangle$	$ 3/2, -1/2, 1, 2\rangle \sim  3/2, 1/2, 0, 2\rangle$
$ c\rangle$	$ 1/2, -1/2, 1, 1\rangle \sim  1/2, 1/2, 0, 1\rangle$
$ b\rangle$	$ -1/2, -1/2, 1, 0\rangle \sim  -1/2, 1/2, 0, 0\rangle$
$ a\rangle$	$ -3/2, -1/2, 1, -1\rangle \sim  -3/2, 1/2, 0, -1\rangle$
I. $ d\rangle$	$ -3/2, -3/2, 1, -2\rangle \sim  -3/2, -1/2, 0, -2\rangle$
$ c\rangle$	$ -1/2, -3/2, 1, -1\rangle \sim  -1/2, -1/2, 0, -1\rangle$
$ b\rangle$	$ 1/2, -3/2, 1, 0\rangle \sim  1/2, -1/2, 0, 0\rangle$
$ a\rangle$	$ 3/2, -3/2, 1, 1\rangle \sim  3/2, -1/2, 0, 1\rangle$
H. $ d\rangle$	$ -3/2, -3/2, 0, -3\rangle \sim  -3/2, -1/2, -1, -3\rangle$
$ c\rangle$	$ -1/2, -3/2, 0, -2\rangle \sim  -1/2, -1/2, -1, -2\rangle$
$ b\rangle$	$ 1/2, -3/2, 0, -1\rangle \sim  1/2, -1/2, -1, -1\rangle$

<sup>1</sup>A magnetic field of 200 G is chosen, since there the Feshbach molecule creation takes place and thus also the STIRAP.

$ a\rangle$	$ 3/2, -3/2, 0, 0\rangle \sim  3/2, -1/2, -1, 0\rangle$
G. $ d\rangle$	$ -3/2, -1/2, 0, -2\rangle \sim  -3/2, 1/2, -1, -2\rangle \sim  -3/2, -3/2, 1, -2\rangle$
$ c\rangle$	$ -1/2, -1/2, 0, -1\rangle \sim  -1/2, 1/2, -1, -1\rangle \sim  -3/2, 1/2, 0, -1\rangle \sim  -1/2, -3/2, 1, -1\rangle$
$ b\rangle$	$ 1/2, -1/2, 0, 0\rangle \sim  -1/2, 1/2, 0, 0\rangle \sim  -1/2, -1/2, 1, 0\rangle \sim  1/2, -3/2, 1, 0\rangle$
$ a\rangle$	$ 3/2, -1/2, 0, 1\rangle \sim  -1/2, 3/2, 0, 1\rangle \sim  3/2, -3/2, 1, 1\rangle$
F. $ d\rangle$	$ -3/2, 1/2, 0, -1\rangle \sim  -1/2, -1/2, 0, -1\rangle \sim  -3/2, -1/2, 1, -1\rangle \sim  -1/2, -3/2, 1, -1\rangle$
$ b\rangle$	$ -1/2, 1/2, 0, 0\rangle \sim  -3/2, 3/2, 0, 0\rangle \sim  1/2, -1/2, 0, 0\rangle \sim  1/2, -3/2, 1, 0\rangle$
$ b\rangle$	$ 1/2, 1/2, 0, 1\rangle \sim  -1/2, 3/2, 0, 1\rangle \sim  3/2, -1/2, 0, 1\rangle \sim  -1/2, 1/2, 1, 1\rangle$
$ a\rangle$	$ 3/2, 1/2, 0, 2\rangle \sim  1/2, 3/2, 0, 2\rangle \sim  3/2, -1/2, 1, 2\rangle$
E. $ d\rangle$	$ 3/2, 3/2, 0, 3\rangle \sim  3/2, 1/2, 1, 3\rangle$
$ c\rangle$	$ 1/2, 3/2, 0, 2\rangle \sim  3/2, 1/2, 0, 2\rangle \sim  3/2, -1/2, 1, 2\rangle$
$ b\rangle$	$ -1/2, 3/2, 0, 1\rangle \sim  1/2, 1/2, 0, 1\rangle \sim  1/2, -1/2, 1, 1\rangle$
$ a\rangle$	$ -3/2, 3/2, 0, 0\rangle \sim  -1/2, 1/2, 0, 0\rangle \sim  -3/2, 1/2, 1, 0\rangle$
D. $ d\rangle$	$ -3/2, -3/2, -1, -4\rangle$
$ c\rangle$	$ -1/2, -3/2, -1, -3\rangle$
$ b\rangle$	$ 1/2, -3/2, -1, -2\rangle$
$ a\rangle$	$ 3/2, -3/2, -1, -1\rangle$
C. $ d\rangle$	$ -3/2, -1/2, -1, -3\rangle \sim  -3/2, -3/2, 0, -3\rangle$
$ c\rangle$	$ -1/2, -1/2, -1, -2\rangle \sim  -1/2, -3/2, 0, -2\rangle$
$ b\rangle$	$ 1/2, -1/2, -1, -1\rangle \sim  1/2, -3/2, 0, -1\rangle$
$ a\rangle$	$ 3/2, -1/2, -1, 0\rangle \sim  3/2, -3/2, 0, 0\rangle$
B. $ d\rangle$	$ -3/2, 1/2, -1, -2\rangle \sim  -3/2, -1/2, 0, -2\rangle$
$ c\rangle$	$ -1/2, 1/2, -1, -1\rangle \sim  -1/2, -1/2, 0, -1\rangle$
$ b\rangle$	$ 1/2, 1/2, -1, 0\rangle \sim  1/2, -1/2, 0, 0\rangle$
$ a\rangle$	$ 3/2, 1/2, -1, 1\rangle \sim  3/2, -1/2, 0, 1\rangle$
A. $ d\rangle$	$ 3/2, 3/2, -1, 2\rangle \sim  3/2, 1/2, 0, 2\rangle$
$ c\rangle$	$ 1/2, 3/2, -1, 1\rangle \sim  1/2, 1/2, 0, 1\rangle$
$ b\rangle$	$ -1/2, 3/2, -1, 0\rangle \sim  -1/2, 1/2, 0, 0\rangle$
$ a\rangle$	$ -3/2, 3/2, -1, -1\rangle \sim  -3/2, 1/2, 0, -1\rangle$

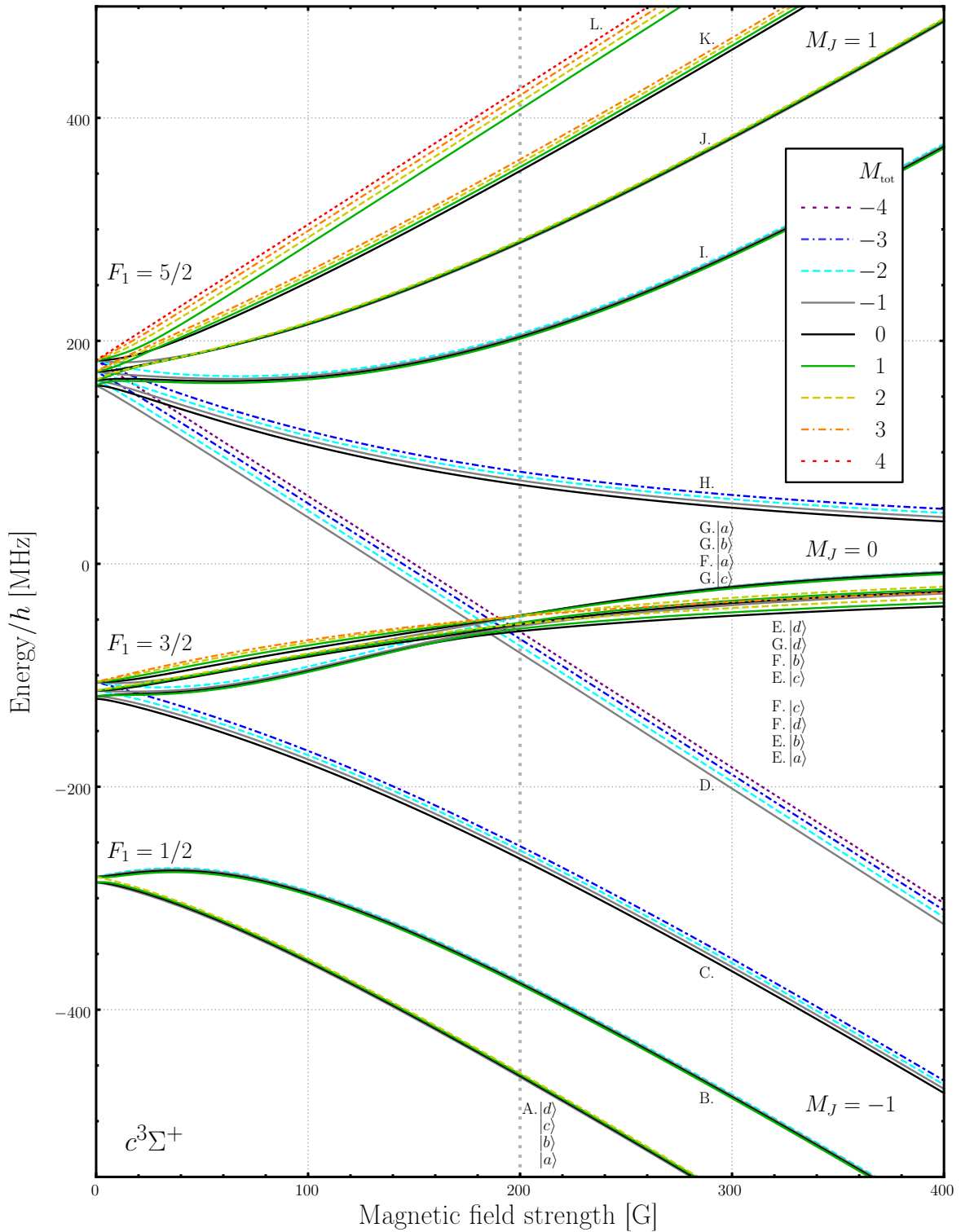


**Figure 4.2:** Hyperfine structure of the excited triplet state manifold. This plot shows all 48 hyperfine states according to the model presented in P2 in Sec. 4.3 [88]. Tab. 4.1 summarizes the corresponding quantum number decomposition for a field of 200 G (thick dotted vertical line). The branches with the same  $m_{i_{\text{Na}}}$  are labeled with A - L, and always consist of four states  $|a\rangle$  -  $|d\rangle$ , where  $a$  corresponds to the lowest energy in the limit of high magnetic fields for the respective  $m_{i_{\text{Na}}}$  branch. The given ordering in this plot is done for a field of 200 G. The plot legend shows the color and line coding for the different  $M_{\text{tot}} = m_{i_{\text{K}}} + m_{i_{\text{Na}}} + M_J$ .

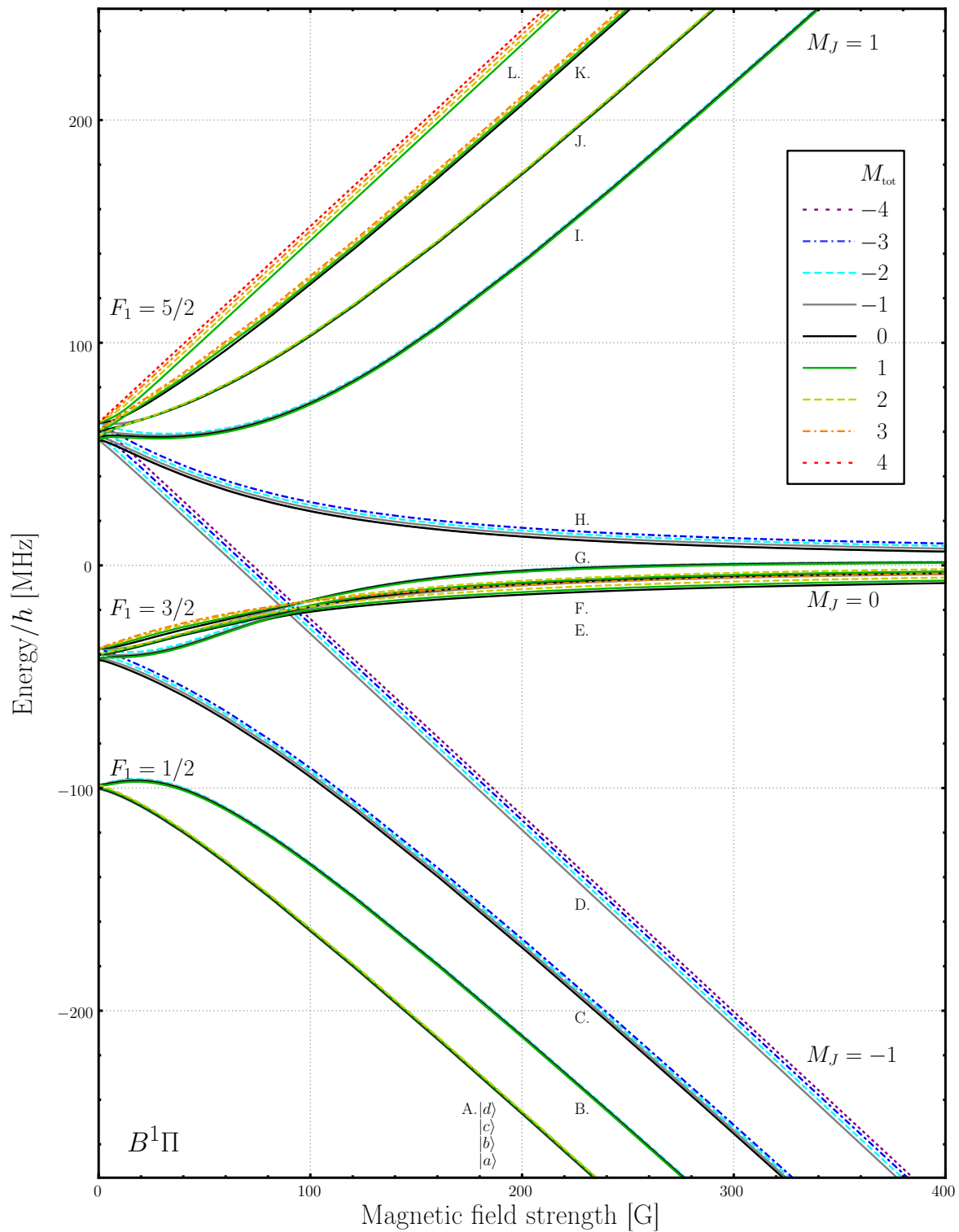


**Figure 4.3:** Hyperfine structure of the excited singlet state manifold. This plot shows all 48 hyperfine states according to the model presented in P2 in Sec. 4.3 [88]. Quantum number assignment is similar to Fig. 4.2 and is the same for the Paschen-Back regime (see corresponding first decomposed state in Tab. 4.1).

## Chapter 5

# Ultracold Trapped $^{23}\text{Na}^{39}\text{K}$ Ground-State Molecules

This chapter is dedicated to the creation process of ultracold ground-state molecules of  $^{23}\text{Na}^{39}\text{K}$  and experimental investigations on the scattering properties of molecule-molecule and molecule-atom collisions. The creation is done by using the STIRAP transfer starting from a Feshbach molecule ensemble, as presented in P1 in Sec. 2.3 [87]. For that purpose the knowledge gained from the molecular spectroscopy is used, as presented in P2 in Sec. 4.3 [88].

In the following Sec. 5.1 I will summarize the physical and technical requirements for the realization of STIRAP in the experiment. This includes a description of the STIRAP pulse sequence, the selection rules in the molecular system, and the STIRAP beam alignment and the choice of laser polarization. Then I will continue with the discussion of scattering properties in molecular collisions in Sec. 5.2, and point out the differences between molecule-molecule and molecule-atom collisions.

Finally, in Sec. 5.3 in the publication P3: *Ultracold Gas of Bosonic  $^{23}\text{Na}^{39}\text{K}$  Ground-State Molecules* the realization of the novel ultracold bosonic ground-state molecule gas and the first collisional loss measurements are presented.

### 5.1 STIRAP in Molecular Systems

The final step for the creation of ground-state molecules is the adiabatic transfer of the weakly bound Feshbach molecules to the absolute rovibrational ground state. The transfer, as already described in the previous Sec. 1.1 and in detail in Chap. 3, is done via the STIRAP transfer. Typically, the STIRAP is performed in a three-level  $\Lambda$ -system. " $\Lambda$ " represents the shape of the pathway as it is typically pictured [99]; see Fig. 3.1. The three states, which are involved in the state exchange, are the initial Feshbach state  $|f\rangle$ , the intermediate excited state  $|e\rangle$  and the final ground state  $|g\rangle$ ; see Chap. 3. They are connected to each other by laser induced dipole transitions. For STIRAP in a bialkali molecular system, the intermediate state  $|e\rangle$  is normally a singlet-triplet mixed excited state to which both the initial state  $|f\rangle$  and final state  $|g\rangle$  must be coupled to. The states  $|f\rangle$  and  $|g\rangle$ , in contrast, are the triplet dominated Feshbach molecule state or the pure singlet ground state, respectively. To obtain a decent coupling, a cautious choice of the excited state is necessary, which was already discussed in Sec. 4.1. The excited state also guarantees a proper wavefunction overlap to satisfy the restrictions from the Franck-Condon principle; see Sec. 4.1.

Beside that, for STIRAP a counter intuitive pulse sequence is used, involving a quantum

mechanical dressed state picture; see Sec.3.1. The selectivity of the transfer to one envisioned hyperfine ground state is done by a carefully chosen laser beam alignment and a corresponding laser light polarization relative to the magnetic field quantization axis.

## Pulse Sequence

STIRAP is a two-photon adiabatic state exchange along which the population of an initial state is transferred to the final state without ever populating the involved intermediate state. This technique is enabled by maintaining a state dressing during the transfer and changing the state admixture by exchanging the dressing laser intensities. This results in the well known counter intuitive pulse sequence as it is shown in Fig. 2b in the journal article P3 below [89] and in Chap. 3.1 in detail. When the molecule population is initially in the state  $|f\rangle$ , the laser which induces the transitions between ground state  $|g\rangle$  and intermediate states  $|e\rangle$ , the Stokes transition, is switched on. Therefore, the state dressing is initiated while the molecule population stays in the state  $|f\rangle$ ; see the derivation in Chap. 3.1. By ramping the Stokes laser down and simultaneously adding a coupling between the  $|e\rangle$  and  $|f\rangle$  states by ramping up the pump laser, the initially populated dressed state is admixed by the state  $|g\rangle$ . When the Stokes laser is ramped down completely and only the pump laser is providing the dressing the molecule population has performed the complete state exchange. Then the dressed state only exists as pure final state  $|g\rangle$ . In theory this technique yields an efficiency of 100 %, under the assumption that the exchange happens in an adiabatic way and that the two lasers are fully phase coherent during the transfer time. In reality, these conditions are not fulfilled. The two lasers differ in frequency by several 100 THz. Thus, the lasers do not originate from the same source which makes them intrinsically incoherent. To circumvent this, both lasers are locked to a highly stable external reference cavity which stabilizes the relative phase of the laser light wave; see Chap. 3.

In the following publication P3 in Sec.5.3, the counter intuitive STIRAP pulse sequence is applied to transfer the ensemble from the Feshbach molecule state to the ground state and vice versa. Moreover, the parameters of the pulse sequence, such as pulse duration and pulse overlap are optimized.

## Selection Rules

Despite the Franck-Condon principle and the singlet-triplet mixing, the selection of suitable states is also restricted by the selection rules for dipole transitions. In general, these are  $\Delta l = \pm 1$  and  $\Delta m_l = 0, \pm 1$ , where  $l$  is the electronic angular momentum and  $m_l$  is its projection to the quantization axis. In case of molecules, this easy selection rule is not directly applicable, since in the molecular frame the quantum state assignment and composition are not always known due to the consideration of the different Hund's cases. Accordingly, the Feshbach molecule state close to the diatomic scattering threshold, excited intermediate states and the deeply bound ground state are described in different cases. Nevertheless, the molecule consists of two coupled alkali atoms which restricts the resulting molecular hyperfine structure to the contributions from the two free electrons and the two nuclei. The hyperfine structure thus can be tracked back to these individual atomic components, if their coupling is neglected. Furthermore, the decoupling of the single atomic angular momenta due to the bias magnetic fields still takes place and is especially valid for the singlet ground state, since it does not possess an electronic angular momentum. At higher magnetic fields, the two nuclear momenta are strongly decoupled, which makes selection rules easy to apply

for the Stokes transition.

In recent publications the behavior of a disturbed STIRAP pathway through the molecular level structure for the fermionic  $^{23}\text{Na}^{40}\text{K}$  molecule has been reported. In the case of Lan *et al.* [100] the STIRAP has been conducted through resonant and non-resonant pathways leading to simultaneous coupling to multiple ground states. Due to the coherent manner of the STIRAP, interference effects have been observed from which coherent ground state super positions have been prepared. In the case of Seeßelberg *et al.* [86] the STIRAP has been performed using states from the excited  $d^3\Pi$  potential. The chosen excited state manifold is not hyperfine resolved. Consequently, the STIRAP was not a selective state transfer and multiple ground states have been populated. Nevertheless, the undesired coupling has been decreased by the choice of appropriate laser polarizations and a large one-photon detuning relative to the excited state manifold.

In the following publication P3 in Sec.5.3 the selection rules are applied to the case of the  $^{23}\text{Na}^{39}\text{K}$  molecule. Since the selection rules are closely related to the applied laser polarization and the experimental beam alignment the chosen STIRAP pathway also considers the latter ones.

## Laser Light Polarization and Beam Alignment

Laser light polarization of the pump and Stokes beam relative to the magnetic field is important, since the geometric configuration of magnetic field axis and laser beam orientation dictates which kind of transition are induced; see Fig. 5.1, left panel. With the laser oriented along the magnetic field axis; Fig. 5.1, left panel (a), only  $\sigma^+$  and  $\sigma^-$  transitions can be induced by applying circularly polarized light.  $\pi$  transitions will never take place in this configuration. Is the laser light direction perpendicular to the magnetic field; Fig. 5.1, left panel (b), both,  $\pi$  and  $\sigma^{+/-}$  transitions can be induced. In this case only linear polarizations of the laser beams are necessary, for  $\pi$  transitions with the polarization parallel to the magnetic field axis, for  $\sigma^{+/-}$  transitions perpendicular to the magnetic field axis. Note that in this configuration, both  $\sigma^+$  and  $\sigma^-$  transitions will occur. Thus, laser polarization is a common tool for the selection of single transitions within the molecular level structure and must be considered for the proper choice of states for the STIRAP pathway.

For STIRAP in ultracold quantum gases only copropagating laser beams are suitable; see Fig. 5.1, right panel. The induced transition in the molecules is a two-photon transition, where momenta between the molecules and the two photons are exchanged. In the simple picture of absorption and emission of photons, a pump laser photon is absorbed by the molecule and a Stokes laser photon is emitted by stimulated emission. Both photons carry energy and momentum. As the photons do not yield the same energy, they also carry different momenta  $|\vec{k}_{\text{pump}}| \neq |\vec{k}_{\text{Stokes}}|$ . A complete canceling of the momenta is not possible, but the momentum transfer can be minimized by using copropagating STIRAP beams. The momentum on the molecule from the pump photon is then facing in the opposite direction as the one gained from the stimulated emitted Stokes photon; see Fig. 5.1. The total momentum on the molecule is then given by  $\Delta k_{\text{STIRAP}} = |\vec{k}_{\text{pump}} - \vec{k}_{\text{Stokes}}|$ . Other laser beam configurations, such as counter-propagating or angled beams, would increase the momentum transfer. If the momentum kick is too high, the molecules might be removed from the optical trap, since for ultracold ensembles the trap depth is very small and atoms and molecules are easily removed from the trap by scattered light.

The restrictions coming from the selection rules, the laser beam alignment and polarization are dependent on each other and have to be chosen in conjunction. A rigorous adoption of

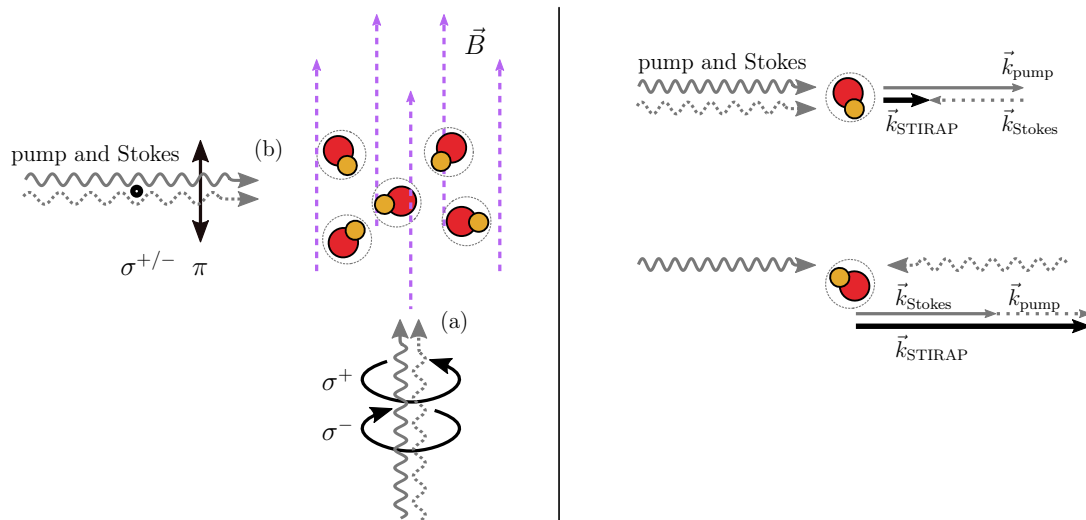


**Figure 5.1:** STIRAP laser beam polarization and alignment. The picture shows the possible laser beam configurations for STIRAP with the induced transitions. The waved arrows represent the incident STIRAP photons. The left panel shows the influence of the polarization with respect to the geometric orientation to the magnetic field on the induced type of transitions. The dashed purple arrows represent the homogeneous magnetic field  $\vec{B}$ . The solid arrows across the waved arrows represent linear or circular polarization, where the respective labels name the type of producible transitions. The cases (a) and (b) show the most common cases with the beams parallel or perpendicular to the magnetic field, respectively. The right panel shows the concept of the reduction of the total momentum transfer to the molecules during STIRAP. The straight arrows are the transferred momenta.

these restrictions can lead to pure and highly efficient state transfers, for example in case of  $^{40}\text{K}^{87}\text{Rb}$  molecules [71]. The adiabatic transfer in their case is done within  $4\ \mu\text{s}$ , which is very fast, and yields a single-trip efficiency of about 90 %.

The publication P3 in Sec. 5.3 [89] presents the successful creation of spin-polarized ground-state molecules of  $^{23}\text{Na}^{39}\text{K}$ . The selection rules for the transitions and the laser beam alignment and polarization adjustment allow for a highly selective state transfer. Nevertheless, due to the geometric alignment of the laser beams, the Stokes laser beam also couples the ground state to two additional excited states, leading to losses during STIRAP. Regarding these restrictions, the STIRAP is optimized and characterized experimentally. A theoretical five-level master equation is used to model the state transfer. To circumvent the losses in future experiments, alternative STIRAP pathways are proposed.

## 5.2 Ultracold Molecular Scattering Physics

Collisions involving ultracold diatomic molecules are more complex than pure atomic ones. Molecule-atom and molecule-molecule collisions are on the verge to many-body problems, since the number of states for the collisional complex proliferates drastically. In recent years, so-called sticky collisions were a topic of high interest in the field of ultracold molecular and atomic collisions. The concept of sticky complexes have been introduced by Mayle *et al.* (2012) [137] for the first time in systems of ultracold colliding molecules and atoms. Later, the theory was extended to the prominent case of molecule-molecule sticky collisions [138] (2013). The density of states and thus the density of Feshbach resonances in such collisions have been estimated as uniformly high and thus have been treated in a statistical way. Due to the high number of states, a collisional complex is formed by the two collisional partners,

which stick together for a finite lifetime. This lifetime is governed by the density of states of the complex. During this time the sticky complex then can either undergo a nuclear spin transition [137], be destroyed or removed from the trap by an additional collisions with an other particle [67, 138] or be excited by light and thus removed from the trap [68–70]. These mechanisms lower the lifetime of even non-reactive collisions close to their universal scattering limit.

The loss measurements from P3 in Sec. 5.3 [89] were performed with consideration to these loss mechanisms. Both non-reactive collisions, the molecule-molecule  $^{23}\text{Na}^{39}\text{K} + ^{23}\text{Na}^{39}\text{K}$ , and molecule-atom  $^{23}\text{Na}^{39}\text{K} + ^{39}\text{K}$  collisions have been investigated.

### Molecule-Molecule Collisions

Sticky molecular collisions have been part of conjectures for a long time and have been recently investigated both theoretically and experimentally. In case of molecule-molecule collisions the density of states for the resulting tetramer complex is very high and can only be modeled by statistical methods. Thus, in Mayle *et al.* (2013) [138] the molecular hyperfine structure was excluded from the model, so that only the ro-vibrational states contributed to the density of states.

From an experimental point of view, tetramers may decay to lower lying states through additional collisions [66, 67, 138] or may be excited by light, for example from optical traps [68–70]. The resulting loss should manifests in a two-body decay of the molecular signal. Evidence on the molecular two-body loss in terms of sticky collisions has been found in the chemically stable bosonic molecule  $^{87}\text{Rb}^{133}\text{Cs}$  [67]. In the pure molecular ensemble, the losses have been assigned to a two-body process and have been compared to universal scattering rates. The temperature dependence of the loss rate has been used to get an insight into the scattering amplitudes and phases for estimations of the contact scattering length from the long-range potential. In further investigations [69], the excitation of collisional complexes through light from the optical trap has been proven.

The situation for chemically reactive molecules is different. For fermionic  $^{40}\text{K}^{87}\text{Rb}$  molecules with the reaction chain  $\text{KRb} + \text{KRb} \rightarrow \text{K}_2\text{Rb}_2 \rightarrow \text{K}_2 + \text{Rb}_2$ , the existence of all reaction products has been proven [66]. This direct prove has been done by photoionization spectroscopy and velocity-map imaging. Additionally, the excitation of the  $\text{K}_2\text{Rb}_2$  intermediates through light has been observed in separate experiments [70].

In the publication P3 in Sec. 5.3 [89] loss measurements for the molecule-molecule collisions of the  $^{23}\text{Na}^{39}\text{K}$  molecules have been carried out. The resulting two-body loss rate coefficients have been compared to the theoretical universal limit, to the loss rate coefficient for the fermionic  $^{23}\text{Na}^{40}\text{K}$  molecule and loss rate coefficients of the two other bosonic molecules  $^{23}\text{Na}^{87}\text{Rb}$  and  $^{87}\text{Rb}^{133}\text{Cs}$ .

### Molecule-Atom Collisions

Besides molecule-molecule collisions, molecule-atom collisions are an effective three-particle process, which is still very challenging to model, but may be feasible within the next years. In Mayle *et al.* (2012) [137], where sticky collisions have been proposed, statistical methods for the model have been used. The hyperfine structure of the molecules and atoms has been incorporated in this theoretical model. Thus, the possibility for nuclear spin transitions for long lived trimer complexes has been discussed. These are more probable in complexes with a high density of states, since the complex lifetime increases with a higher density of states. Besides the light weighted fermionic candidates  $^6\text{Li}^{23}\text{Na} + ^{23}\text{Na}$  and  $^6\text{Li}^{40}\text{K} + ^{40}\text{K}$ , the

$^{23}\text{Na}^{40}\text{K} + ^{40}\text{K}$  mixture possesses one of the lowest spin-transitions portability [137]. The mixture  $^{23}\text{Na}^{40}\text{K} + ^{40}\text{K}$  has been investigated experimentally by means of scattering properties [139]. For several hyperfine states, both for the molecules and the atoms, magnetic field dependent loss features have been observed, which suggest the presence of Feshbach resonances between molecules and atoms. The density of Feshbach resonances is unexpectedly low compared to estimations from [139], which raises the questions of the origin of the found resonances and demands a qualitative model. Molecule-atom Feshbach resonances may offer the possibility to tune interaction of the mixture and use a resonance to prepare selectively trimere states or tune the ratio between elastic and inelastic losses. The latter can be used for sympathetic cooling of molecules on the atoms, as has been realized for fermionic triplet ground-state  $^6\text{Li}^{23}\text{Na}$  molecules immersed in a bath of  $^{23}\text{Na}$  atoms [72]. In the absolute hyperfine ground state, the  $^6\text{Li}^{23}\text{Na} + ^{23}\text{Na}$  mixture possesses very low losses from inelastic scattering. At the same time the elastic collisions are not suppressed which makes the mixture feasible for sympathetic cooling. Such an effect may be used to increase the phase-space density until quantum degeneracy is reached and overcome the obstacle of quantum degenerate atomic gases during the molecule creation as it was shown for  $^{40}\text{K}^{87}\text{Rb}$  molecules [71].

In the following publication P3 in Sec.5.3 [89] loss measurements with molecule-atom mixtures have been performed. The losses from the reactive  $^{23}\text{Na}^{39}\text{K} + ^{23}\text{Na}$  mixture have been compared to the theoretical universal loss rate coefficient. The obtained loss rate coefficient for the  $^{23}\text{Na}^{39}\text{K} + ^{39}\text{K}$  mixture have been compared to the theoretical one and to the experimentally obtained ones for  $^{23}\text{Na}^{40}\text{K} + ^{40}\text{K}$  [139] and  $^6\text{Li}^{23}\text{Na} + ^{23}\text{Na}$  [72] mixtures. Significant discrepancies have been found which have been discussed regarding sticky trimer collisions and sympathetic cooling.

### 5.3 P3: *Ultracold Gas of Bosonic $^{23}\text{Na}^{39}\text{K}$ Ground-State Molecules*

**Authors** Kai K. Voges, Philipp Gersema, Mara Meyer zum Alten Borgloh, Torsten Hartmann, Torben A. Schulze, Alessandro Zenesini, Silke Ospelkaus

**Journal** Physical Review Letters

**Article number** 125, 083401 (2020)

**DOI** 10.1103/PhysRevLett.125.083401

**Contributions** KKV, PG and TH performed the measurements. KKV and AZ analyzed the data. KKV, MMzAB, TAS and AZ implemented the model for EIT, STIRAP, one- and two-photon detuning and molecule-atom losses. AZ and SO designed and headed the experiment. All authors contributed to the production of the manuscript.

**Copyright** © American Physical Society (APS). Reprinted with permission from Voges *et al.* Phys. Rev. Lett. 125, 083401 (2020), Copyright (2020) by APS.



## Ultracold Gas of Bosonic $^{23}\text{Na}^{39}\text{K}$ Ground-State Molecules

Kai K. Voges<sup>1,\*</sup>, Philipp Gersema<sup>1</sup>, Mara Meyer zum Alten Borgloh<sup>1</sup>, Torben A. Schulze,<sup>1</sup>  
Torsten Hartmann<sup>1</sup>, Alessandro Zenesini<sup>1,2</sup> and Silke Ospelkaus<sup>1,†</sup>

<sup>1</sup>*Institut für Quantenoptik, Leibniz Universität Hannover, 30167 Hannover, Germany*

<sup>2</sup>*INO-CNR BEC Center and Dipartimento di Fisica, Università di Trento, 38123 Povo, Italy*



(Received 27 April 2020; accepted 29 July 2020; published 21 August 2020)

We report the creation of ultracold bosonic dipolar  $^{23}\text{Na}^{39}\text{K}$  molecules in their absolute rovibrational ground state. Starting from weakly bound molecules immersed in an ultracold atomic mixture, we coherently transfer the dimers to the rovibrational ground state using an adiabatic Raman passage. We analyze the two-body decay in a pure molecular sample and in molecule-atom mixtures and find an unexpectedly low two-body decay coefficient for collisions between molecules and  $^{39}\text{K}$  atoms in a selected hyperfine state. The preparation of bosonic  $^{23}\text{Na}^{39}\text{K}$  molecules opens the way for future comparisons between fermionic and bosonic ultracold ground-state molecules of the same chemical species.

DOI: 10.1103/PhysRevLett.125.083401

Heteronuclear polar ground-state molecules have attracted considerable attention in recent years. They serve as a new platform for controlled quantum chemistry [1,2], novel many-body physics [3,4], and quantum simulations [5,6]. Their permanent electric dipole moment gives rise to anisotropic and tunable long-range interactions which can be induced in the lab frame via electric fields or resonant microwave radiation [7,8]. This gives exquisite control over additional quantum degrees of freedom. In recent years there has been continuous progress in the production of ultracold bialkali molecules. Fermionic  $^{40}\text{K}^{87}\text{Rb}$  [9],  $^{23}\text{Na}^{40}\text{K}$  [10], and  $^6\text{Li}^{23}\text{Na}$  [11], as well as bosonic  $^{87}\text{Rb}^{133}\text{Cs}$  [12] and  $^{23}\text{Na}^{87}\text{Rb}$  [13] molecules have been prepared.

Up to now, not a single molecule has been available both as a bosonic and a fermionic molecular quantum gas, which makes findings among different species and quantum statistics challenging to interpret and to compare. For bialkali molecules only combinations with Li or K offer the possibility to prepare the bosonic and fermionic molecule, as Li and K are the only alkali metals which possess long-lived fermionic and bosonic isotopes. Among these molecules (LiK, LiNa, LiRb, LiCs, NaK, KRb, KCs) all possible combinations with a Li atom as well as the KRb molecule are known to undergo exothermic atom exchange reactions in molecule-molecule collisions [14]. This leaves only NaK and KCs [15] as chemically stable molecules for a comparison of scattering properties of the same molecular species but different quantum statistics.

Both chemically reactive and nonreactive spin-polarized fermionic molecular ensembles have been reported to be long-lived due to the centrifugal  $p$ -wave collisional barrier limiting the two-body collisional rate to the tunneling rate [1,10]. The lifetime of bosonic molecular ensembles, however, has been observed to be significantly shorter and limited

by the two-body universal scattering rate [13,16]. Two-body collisions involving molecules can lead to the formation of collisional complexes due to a large density of states. The complexes can either decay to new chemical species for chemically reactive molecules [17] or within the lifetime of the complexes are removed from the trap by light excitation [18–20] or collisions with a third scattering partner [16,21].

In this Letter, we report on the production of ultracold bosonic  $^{23}\text{Na}^{39}\text{K}$  rovibrational ground-state molecules. The preparation follows the pioneering experiments for the creation of  $^{40}\text{K}^{87}\text{Rb}$  molecules [9] with Feshbach molecule creation and subsequent stimulated Raman adiabatic passage (STIRAP) transfer [22] to a selected hyperfine state in the rovibrational ground-state manifold. We model our STIRAP transfer through an effective five-level master equation model and work out an efficient pathway to create spin-polarized ground-state molecular ensembles. We prepare pure molecular ensembles as well as molecule-atom mixtures and extract the resulting collisional loss rate coefficients. We find the loss rate for the  $^{23}\text{Na}^{39}\text{K} + ^{39}\text{K}$  mixture to be drastically suppressed, which opens interesting perspectives for sympathetic cooling.

The experiments start from ultracold weakly bound molecules. As previously described in Ref. [23], we associate  $^{23}\text{Na}^{39}\text{K}$  Feshbach dimers by applying a radio frequency pulse to an ultracold mixture of bosonic  $^{23}\text{Na}$  and  $^{39}\text{K}$  held in a 1064 nm crossed-beam optical dipole trap with temperatures below 350 nK. We create  $6 \times 10^3$  dimers in the least bound vibrational state  $|f\rangle$  with a total angular momentum projection  $M_F = -3$  and a binding energy of  $h \times 100$  kHz at a magnetic field of 199.3 G. In terms of atomic quantum numbers the state  $|f\rangle$  is mainly composed of  $\alpha_1|m_{i,\text{Na}} = -3/2, m_{i,\text{K}} = -1/2, M_S = -1\rangle + \alpha_2|m_{i,\text{Na}} = -3/2, m_{i,\text{K}} = -3/2, M_S = 0\rangle$ .  $M_S$  is the total electron spin

projection,  $m_{i,\text{Na}}$  and  $m_{i,\text{K}}$  are the nuclear spin projections, and  $\alpha_{1/2}$  denote the state admixtures. For detection, we use a standard absorption technique of  $^{39}\text{K}$  atoms directly from the weakly bound molecular state.

For the STIRAP transfer, we make use of external-cavity diode laser systems as already described in Ref. [24]. Both lasers are referenced simultaneously to a 10-cm-long high-finesse ultra low expansion cavity using a sideband Pound-Drever-Hall locking scheme [25]. The cavity's finesse for the pump and Stokes laser are 24 900 and 37 400, respectively, and the free spectral range is 1.499 GHz. The linewidths of both locked lasers are estimated to be below 5 kHz. Furthermore, the power of the pump laser is amplified by a tapered amplifier. Both lasers, pump and Stokes, are overlapped and focused to the position of the molecules with  $1/e^2$  Gaussian beam waists of 35 and 40  $\mu\text{m}$ , respectively. The direction of propagation is perpendicular to the direction of the magnetic field; thus,  $\pi$  ( $\sigma^{+/-}$ ) transitions can be addressed by choosing the polarization parallel (perpendicular) to the magnetic field.

Possible transfer pathways to the ground state have been previously investigated theoretically and experimentally [24,26]. Figure 1(a) summarizes the relevant states involved in the transfer scheme. Starting from the weakly bound dimer state  $|f\rangle$  with mainly triplet character, we make use of the triplet-singlet mixed excited state  $|e\rangle$  to transfer the molecules into a selected hyperfine state in the rovibrational ground state  $|g\rangle$  with pure singlet character. For the excited state  $|e\rangle$  we choose the strongly spin-orbit coupled  $B^1\Pi|v=8\rangle/c^3\Sigma^+|v=30\rangle$  state manifolds [see Fig. 1(a)], which have a large state admixture of 26%/74% [24]. The hyperfine structure of the  $|X^1\Sigma^+, v=0, N=0\rangle$  ground state consists of 16 states with a total angular momentum projection  $M_F = m_{i,\text{Na}} + m_{i,\text{K}}$ , which group into four branches with different  $m_{i,\text{Na}}$  at high magnetic fields [see Fig. 1(b)] [27]. At 199.3 G, where the molecule creation is performed, the ground states are deeply in the Paschen-Back regime. In the excited states the  $^{39}\text{K}$  nuclear momenta are also decoupled from the other nuclear and electronic angular momenta [28]. Therefore, dipole transitions only change the latter ones. This limits the number of accessible ground states to three, which are highlighted in Fig. 1(b). Accounting only for  $\pi$  transitions for the pump transition to maximize the coupling strength, only a single state is accessible in the  $c^3\Sigma^+$  hyperfine manifold, namely the  $|e_0\rangle = |c^3\Sigma^+, m_{i,\text{Na}} = -3/2, m_{i,\text{K}} = -1/2, M_J = -1, M_F = -3\rangle$ . The transition yields an energy of  $12242.024(3) \text{ cm}^{-1}$  [which corresponds to a wavelength of  $816.8584(2) \text{ nm}$ ] and is shown in Fig. 1(a). The Stokes transition, with an energy of  $17453.744(3) \text{ cm}^{-1}$  [ $572.94297(10) \text{ nm}$ ], connects the excited state to the ground state. In our case, we use a  $\sigma^-$  transition to the  $|g\rangle = |X^1\Sigma^+, m_{i,\text{Na}} = -3/2, m_{i,\text{K}} = -1/2, M_J = 0, M_i = -2\rangle$  state. Nevertheless, our experimental setup always supports  $\sigma^-$  and  $\sigma^+$  transitions at

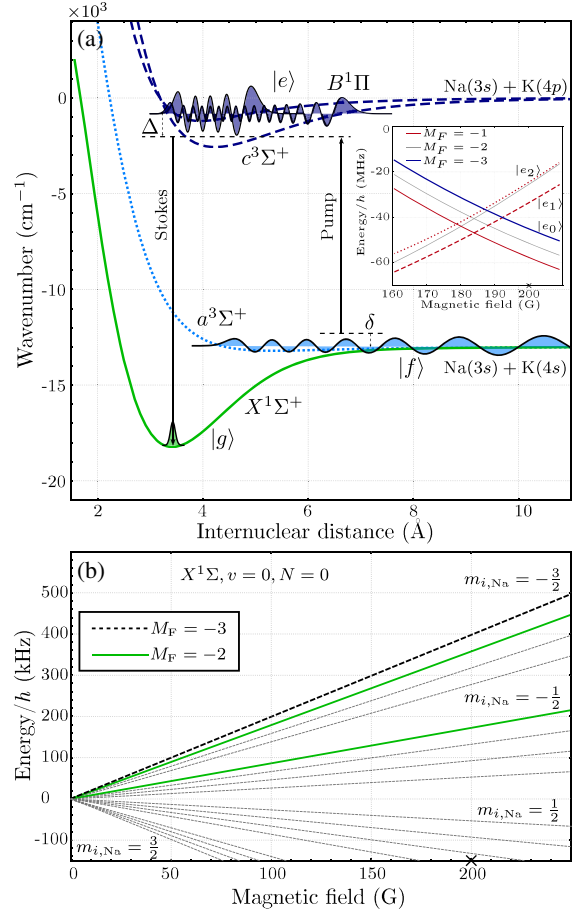


FIG. 1. (a) Potential energy curves of the  $^{23}\text{Na}^{39}\text{K}$  molecule. The energy is shown in  $\text{cm}^{-1}$  as function of the internuclear distance. The solid green curve corresponds to the electronic  $X^1\Sigma^+$ , the dotted light blue to the  $a^3\Sigma^+$ , and the dashed lines to the  $c^3\Sigma^+$  and  $B^1\Pi$  potentials. Wave functions are shown as black lines with the corresponding shading. Amplitudes of the wave functions are not to scale. The black arrows indicate the STIRAP transitions and the one- ( $\Delta$ ) and two- ( $\delta$ ) photon detunings. The inset shows the magnetic field dependence of the pump transition to the excited states from the model in Ref. [24]. (b) Magnetic field dependence of the ground-state hyperfine energy structure. The green lines are the states with  $M_F = -2$  and the black dashed line is the one with  $M_F = -3$ . As the states enter the Paschen-Back regime the four branches for different  $m_{i,\text{Na}}$  become visible. The magnetic field, where the molecule creation process is performed, is marked with a cross on the axis.

the same time. Consequently, the ground state is coupled to two additional states  $|e_{1,2}\rangle$  through  $\sigma^+$  transitions [see inset Fig. 1(a)]. For the experiments and for the modeling we thus have to consider an effective five-level system. The details of the model are described in the Supplemental Material [29].

For STIRAP a high degree of phase coherence between the two independent laser sources is imperative. To prove the coherence and to determine the explicit frequencies for the two-photon Raman transition, we perform electromagnetically induced transparency (EIT) experiments on the selected states. For the measurement shown in Fig. 2(a), Rabi frequencies of  $\Omega_{\text{pump}} = 2\pi \times 0.63(2)$  MHz and  $\Omega_{\text{Stokes}} = 2\pi \times 4.1(2)$  MHz are used. The coherent interaction time is set to  $50 \mu\text{s}$ . The observed asymmetry of the molecule revival arises from a one-photon detuning  $\Delta = 2\pi \times 400(20)$  kHz to the excited state  $|e_0\rangle$ . EIT relies only on coherent dark state effects and never populates the ground state. A coupling between the ground state and the perturbing excited states  $|e_{1,2}\rangle$  does not alter the coupling scheme as the two-photon condition is not fulfilled for these states. Consequently, a three-level scheme is sufficient for its description. Figure 2(a) shows the experimental data and the theoretical prediction (solid black line) using experimentally determined parameters for Rabi frequencies and laser detunings. The errors on the parameters are displayed as dashed lines and gray shaded area. We find very good agreement of our data with the model and consequently good conditions for the STIRAP.

For the creation of ground-state molecules, we perform STIRAP starting from Feshbach molecules. As the Feshbach molecule lifetime is very short, on the order of  $0.3 \text{ ms}$  [23], STIRAP is completed  $25 \mu\text{s}$  after Feshbach molecules creation. The STIRAP process itself takes  $11 \mu\text{s}$  so that no significant loss from a decay of the weakly bound dimers is expected. Figure 2(b) shows a typical signal for ground-state molecule creation. The figure includes the STIRAP light pulse sequence (lower panel) and the populations of the Feshbach molecules as well as the ground-state molecules during the pulse sequence calculated by a five-level master equation. Starting with Feshbach molecules at  $t = 0$ , the molecules are transferred to the ground state at  $t = 14 \mu\text{s}$  where the molecules become dark for the imaging light. To image the molecules, we reverse the STIRAP sequence and transfer ground-state molecules back to the Feshbach state. Because of the additional coupling of the ground state to the excited states  $|e_{1,2}\rangle$ , the STIRAP is highly dependent on the one-photon detuning (see Fig. 3). The states  $|e_{1,2}\rangle$  act as loss channels, into which the ground-state molecules are pumped and consequently get lost. On resonance with one of the  $|e_{1,2}\rangle$  states, nearly no ground-state molecules revive (see Fig. 3). Clearly, in the vicinity of the  $|e_{1,2}\rangle$  states, the STIRAP benefits from fast transfers, which is restricted by the adiabaticity in the limit of small pulse-overlap areas [22]. On the other hand, the pulse-overlap area can be increased by raising the Rabi frequencies of the pulses, which accordingly also increases the undesired coupling to the states  $|e_{1,2}\rangle$ . We find the best results in our system for a pulse duration of  $12 \mu\text{s}$  with a pump pulse delay of  $-2 \mu\text{s}$  and resonant Rabi frequencies of  $\Omega_{\text{pump}} = 2\pi \times 3.0(1)$  MHz and  $\Omega_{\text{Stokes}} = 2\pi \times 2.3(1)$  MHz at a

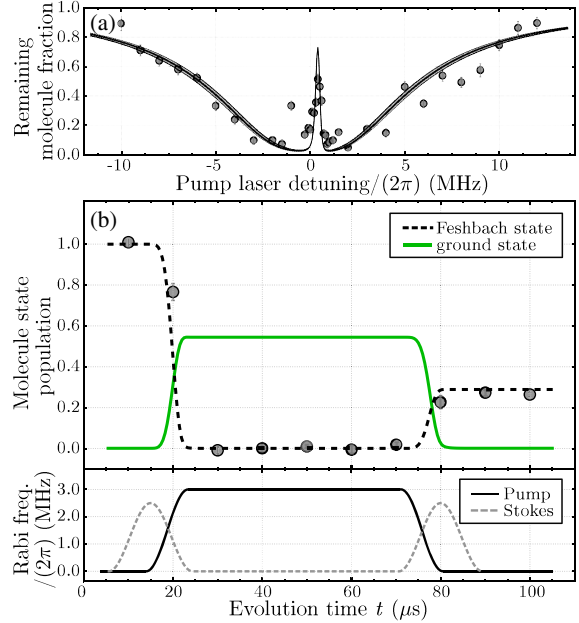


FIG. 2. EIT and time evolution of STIRAP. (a) EIT measurement together with a theory curve. The points are the remaining Feshbach molecule fraction normalized to the initial Feshbach molecule number. The solid black line is the theory curve from a three-level master equation and the dashed lines with the enclosed shaded gray area correspond to the uncertainty of the Rabi frequencies. (b) Time evolution of the Feshbach and ground-state population during a round-trip STIRAP. Data points in the upper panel are the observed Feshbach molecule number normalized to the initial molecule number. The solid green (dashed black) line is a theory curve for the ground-state (Feshbach molecule-state) population using the model described in the text and the pulses from the lower panel. The pulse duration for both lasers is  $10 \mu\text{s}$ . The ramping-up of the pump pulse starts  $1 \mu\text{s}$  before the ramp-down of the Stokes pulse begins. The lower panel shows the pulse sequence of the pump and Stokes laser during the STIRAP. Rabi frequencies are obtained from one-photon loss measurements (not shown here). Error bars are the standard deviation coming from different experimental runs.

one-photon detuning  $\Delta = 2\pi \times 8$  MHz to the center position of  $|e_0\rangle$ . Under these conditions single-trip STIRAP efficiency can get as high as 70%, which corresponds to a ground-state molecule number of about 4200 in a single hyperfine spin state (see inset of Fig. 3). Moreover, we do not observe heating effects of the molecules due to the STIRAP (see Supplemental Material [29]), leading to a phase-space density of up to 0.14. To model the influence of the states  $|e_{1,2}\rangle$  on the STIRAP we apply a five-level master equation model fit (solid curve in Fig. 3) and compare it to an ideal three-level one (dashed curve in Fig. 3). The model is described in detail in the Supplemental Material [29]. In the comparison between the five- and three-level model the influence of the states  $|e_{1,2}\rangle$  gets clear. It indicates that

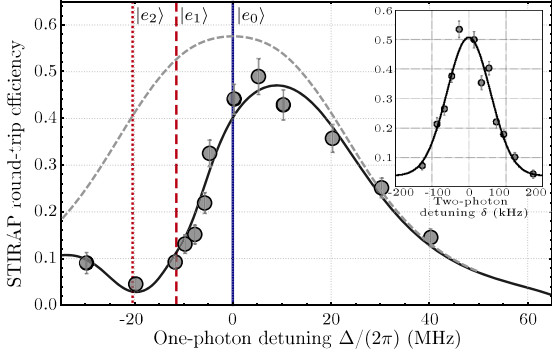


FIG. 3. One- and two-photon detuning for STIRAP. The round-trip efficiency for STIRAP is shown as a function of the one-photon detuning  $\Delta$ . The pulse sequence and laser intensities for these measurements were kept constant corresponding to the optimal values given in the text. The vertical solid blue (dashed red) [dotted red] line is the position of the  $|e_{0(1)2}\rangle$  state deduced from measurements and the model developed in Ref. [24]. The solid black curve is a fit using the five-level master equation model and the individual couplings of the Stokes laser to the  $|e_{1,2}\rangle$  states as free parameters. The dashed gray curve is a theory curve from a three-level model using the same set of parameters. The inset shows the STIRAP round-trip efficiency dependent on the two-photon detuning  $\delta$  with a phenomenological Gaussian fit. The error bars for both plots are the standard error coming from different experimental cycles.

the STIRAP efficiency can be easily increased by choosing a different excited state, experimental geometric condition, such as laser polarization relative to the magnetic field axis, and larger STIRAP pulse overlap areas, which is discussed in the Supplemental Material [29].

After the transfer to the ground state the molecules are still immersed in a gas of  $^{23}\text{Na}$  and  $^{39}\text{K}$  atoms remaining from the creation process of the weakly bound dimers.  $^{23}\text{Na}$  atoms can be removed by applying a  $500\ \mu\text{s}$  resonant light pulse.  $^{39}\text{K}$  atoms can be removed by transferring them to the  $|f=2, m_f=-2\rangle$  state by a rapid adiabatic passage and a subsequent resonant light pulse for  $500\ \mu\text{s}$ . By introducing a variable hold time between the atom removals and the reversed STIRAP pulse, we perform loss measurements, which we analyze assuming a two-body decay model to extract the two-body decay rate coefficient. The model is described in the Supplemental Material [29].

First, we investigate the mixture of molecules and atoms. We observe fast losses from  $^{23}\text{Na}^{39}\text{K} + ^{23}\text{Na}$  collisions (see Fig. 4). The extracted loss rate coefficient is  $1.25(14) \times 10^{-10}\ \text{cm}^3\ \text{s}^{-1}$ , which is close to the theoretical prediction of  $1.3 \times 10^{-10}\ \text{cm}^3\ \text{s}^{-1}$  taken from Ref. [31]. We assign the saturation of the losses to chemical reactions, in which  $^{23}\text{Na}_2$  dimers are formed. Thus,  $^{23}\text{Na}$  atoms are generally removed as fast as possible from the trap as the ground-state molecule number suffers from the strong losses.

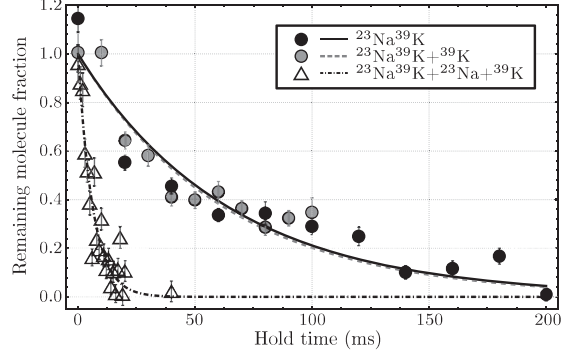


FIG. 4. Loss measurements of pure ground-state molecules and with remaining atoms. The open triangles are measurements without atom removal. The fast loss originates from the chemical reaction with  $^{23}\text{Na}$  atoms. The gray circles are measurements with only  $^{23}\text{Na}$  removed while still  $^{39}\text{K}$  atoms remain in the trap. The solid circles are measurements performed with a pure molecular ensemble. The data are normalized to the molecule number without holding time obtained from the individual fits. The curves are fits using a coupled differential equation system for modeling the losses. For the corresponding loss rate coefficients, see text. All error bars are the standard deviation resulting from different experimental runs.

In a next step, we measure losses in a pure molecular ensemble (see Fig. 4). The two-body loss rate coefficient is measured to be  $4.49(1.18) \times 10^{-10}\ \text{cm}^3\ \text{s}^{-1}$ . This loss rate coefficient is comparable to the universal limit [32] and is possibly resulting from sticky collisions [21] and subsequent removal of the tetramers from the trap. Comparable observations have been made in experiments with other bosonic ground-state molecules, such as  $^{87}\text{Rb}^{133}\text{Cs}$  and  $^{23}\text{Na}^{87}\text{Rb}$  [12,13]. However, the loss rate coefficient for the fermionic counterpart  $^{23}\text{Na}^{40}\text{K}$  is  $6 \times 10^{-11}\ \text{cm}^3\ \text{s}^{-1}$  [10]. The difference can be assigned to the absence of the centrifugal barrier in bosonic  $s$ -wave collisions.

Next, we investigate collisions between the molecules and  $^{39}\text{K}$  atoms. Surprisingly, even a high density of  $^{39}\text{K}$  atoms in the nonstretched  $|f=1, m_f=-1\rangle_{\text{K}}$  state colliding with  $^{23}\text{Na}^{39}\text{K}$  in the nonstretched hyperfine ground state does not increase the molecular loss (compare Fig. 4), although sticky collisions with trimer formation are also expected in mixtures of  $^{23}\text{Na}^{39}\text{K} + ^{39}\text{K}$  [33]. In these collisional trimer complexes nuclear spin transitions can occur leading to subsequent loss of molecules from the prepared hyperfine state. We analyze the observed decay of the molecular cloud using the model fit described in the Supplemental Material [29]. We find the loss rate coefficient for the two-body  $^{23}\text{Na}^{39}\text{K} + ^{39}\text{K}$  collisions to be consistent with zero with an upper limit of  $1.5 \times 10^{-14}\ \text{cm}^3\ \text{s}^{-1}$ . The corresponding universal limit is calculated by using the prediction from Refs. [33,34] and parameters from Ref. [35] and results in  $1.3 \times 10^{-10}\ \text{cm}^3\ \text{s}^{-1}$ . Note that this corresponds to a

suppression of the two-body decay in comparison to the universal limit by more than 3 orders of magnitude. This is in contrast to experiments reported for fermionic molecules in collisions with bosonic atoms ( $^{40}\text{K}^{87}\text{Rb} + ^{87}\text{Rb}$  [1]) and fermionic atoms ( $^{23}\text{Na}^{40}\text{K} + ^{40}\text{K}$  [36]), where such suppression of losses far below the universal limit has not been observed for sticky molecule-atom collisions. The only experiment describing such a suppression has been performed in a mixture of the fermionic molecule  $^6\text{Li}^{23}\text{Na}$  with the bosonic atom  $^{23}\text{Na}$  with both particles in their lowest stretched hyperfine states [37]. Here, we now report collisions in nonstretched states with loss rates far below the universal limit, which might result from a low density of resonant states [33]. Individual resonances might thus be resolvable in this system and demand for further investigations of loss rates in other spin channels and magnetic fields. Moreover, with the low loss rate between  $^{23}\text{Na}^{39}\text{K}$  molecules and  $^{39}\text{K}$  atoms in the named hyperfine state it might be possible to use  $^{39}\text{K}$  atoms as a coolant for bosonic  $^{23}\text{Na}^{39}\text{K}$  molecules to further increase the molecular phase-space density [37].

In conclusion, we have reported the first creation of an ultracold high phase-space density gas of bosonic  $^{23}\text{Na}^{39}\text{K}$  ground-state molecules. We have investigated the creation process and find very good agreement with our five-level model. The spin-polarized molecular ensemble yields up to 4200 molecules and is chemically stable. We extract the two-body decay coefficient for the bosonic  $^{23}\text{Na}^{39}\text{K}$  molecules. For molecule-atom collisions, we find a significant suppression of the two-body decay rate in collisions between  $^{23}\text{Na}^{39}\text{K}$  molecules and  $^{39}\text{K}$  atoms in nonstretched states. This unexpected result demands further experiments including the analysis of collisions between molecules and atoms in different hyperfine states and as a function of magnetic field to identify possible scattering resonances. These experiments can be extended to a detailed comparison of collision properties between same species molecules of different quantum statistics.

We thank M. Siercke for enlightening comments and discussions and the group of P. O. Schmidt, PTB Brunswick, for providing scientific material for the Raman laser system. We gratefully acknowledge financial support from the European Research Council through ERC Starting Grant POLAR and from the Deutsche Forschungsgemeinschaft (DFG) through CRC 1227 (DQ-mat), project A03, and FOR 2247, project E5. P. G. thanks the DFG for financial support through RTG 1991.

\*voges@iqo.uni-hannover.de

†silke.ospelkaus@iqo.uni-hannover.de

- [1] S. Ospelkaus, K.-K. Ni, D. Wang, M. H. G. de Miranda, B. Neyenhuis, G. Quéméner, P. S. Julienne, J. L. Bohn, D. S. Jin, and J. Ye, *Science* **327**, 853 (2010).

- [2] M. Guo, X. Ye, J. He, M. L. González-Martínez, R. Vexiau, G. Quéméner, and D. Wang, *Phys. Rev. X* **8**, 041044 (2018).
- [3] S. A. Moses, J. P. Covey, M. T. Miecinkowski, D. S. Jin, and J. Ye, *Nat. Phys.* **13**, 13 (2016).
- [4] L. De Marco, G. Valtolina, K. Matsuda, W. G. Tobias, J. P. Covey, and J. Ye, *Science* **363**, 853 (2019).
- [5] D. DeMille, *Phys. Rev. Lett.* **88**, 067901 (2002).
- [6] B. Yan, S. Moses, B. Gadway, J. Covey, K. Hazzard, A. Rey, D. Jin, and J. Ye, *Nature (London)* **501**, 521 (2013).
- [7] M. H. G. de Miranda, A. Chotia, B. Neyenhuis, D. Wang, G. Quéméner, S. Ospelkaus, J. L. Bohn, J. Ye, and D. S. Jin, *Nat. Phys.* **7**, 502 (2011).
- [8] S. A. Will, J. W. Park, Z. Z. Yan, H. Loh, and M. W. Zwierlein, *Phys. Rev. Lett.* **116**, 225306 (2016).
- [9] K.-K. Ni, S. Ospelkaus, M. H. G. de Miranda, A. Peer, B. Neyenhuis, J. J. Zirbel, S. Kotochigova, P. S. Julienne, D. S. Jin, and J. Ye, *Science* **322**, 231 (2008).
- [10] J. W. Park, S. A. Will, and M. W. Zwierlein, *Phys. Rev. Lett.* **114**, 205302 (2015).
- [11] T. M. Rvachov, H. Son, A. T. Sommer, S. Ebadi, J. J. Park, M. W. Zwierlein, W. Ketterle, and A. O. Jamison, *Phys. Rev. Lett.* **119**, 143001 (2017).
- [12] T. Takekoshi, L. Reichsöllner, A. Schindewolf, J. M. Hutson, C. R. Le Sueur, O. Dulieu, F. Ferlaino, R. Grimm, and H.-C. Nägerl, *Phys. Rev. Lett.* **113**, 205301 (2014).
- [13] M. Guo, B. Zhu, B. Lu, X. Ye, F. Wang, R. Vexiau, N. Bouloufa-Maafa, G. Quéméner, O. Dulieu, and D. Wang, *Phys. Rev. Lett.* **116**, 205303 (2016).
- [14] P. S. Żuchowski and J. M. Hutson, *Phys. Rev. A* **81**, 060703 (R) (2010).
- [15] M. Gröbner, P. Weinmann, E. Kirilov, H.-C. Nägerl, P. S. Julienne, C. R. Le Sueur, and J. M. Hutson, *Phys. Rev. A* **95**, 022715 (2017).
- [16] P. D. Gregory, M. D. Frye, J. A. Blackmore, E. M. Bridge, R. Sawant, J. M. Hutson, and S. L. Cornish, *Nat. Commun.* **10**, 3104 (2019).
- [17] M.-G. Hu, Y. Liu, D. D. Grimes, Y.-W. Lin, A. H. Gheorghe, R. Vexiau, N. Bouloufa-Maafa, O. Dulieu, T. Rosenband, and K.-K. Ni, *Science* **366**, 1111 (2019).
- [18] A. Christianen, M. W. Zwierlein, G. C. Groenenboom, and T. Karman, *Phys. Rev. Lett.* **123**, 123402 (2019).
- [19] P. D. Gregory, J. A. Blackmore, S. L. Bromley, and S. L. Cornish, *Phys. Rev. Lett.* **124**, 163402 (2020).
- [20] Y. Liu, M.-G. Hu, M. A. Nichols, D. D. Grimes, T. Karman, H. Guo, and K.-K. Ni, *arXiv:2002.05140*.
- [21] M. Mayle, G. Quéméner, B. P. Ruzic, and J. L. Bohn, *Phys. Rev. A* **87**, 012709 (2013).
- [22] N. V. Vitanov, A. A. Rangelov, B. W. Shore, and K. Bergmann, *Rev. Mod. Phys.* **89**, 015006 (2017).
- [23] K. K. Voges, P. Gersema, T. Hartmann, T. A. Schulze, A. Zenesini, and S. Ospelkaus, *Phys. Rev. A* **101**, 042704 (2020).
- [24] K. K. Voges, P. Gersema, T. Hartmann, T. A. Schulze, A. Zenesini, and S. Ospelkaus, *New J. Phys.* **21**, 123034 (2019).
- [25] R. W. P. Drever, J. L. Hall, F. V. Kowalski, J. Hough, G. M. Ford, A. J. Munley, and H. Ward, *Appl. Phys. B* **31**, 97 (1983).
- [26] T. A. Schulze, I. I. Temelkov, M. W. Gempel, T. Hartmann, H. Knöckel, S. Ospelkaus, and E. Tiemann, *Phys. Rev. A* **88**, 023401 (2013).

- [27] J. Aldegunde and J. M. Hutson, *Phys. Rev. A* **96**, 042506 (2017).
- [28] I. Temelkov, H. Knöckel, A. Pashov, and E. Tiemann, *Phys. Rev. A* **91**, 032512 (2015).
- [29] See Supplemental Material at <http://link.aps.org/supplemental/10.1103/PhysRevLett.125.083401> for details about the five-level STIRAP model, the alternative STIRAP pathways, the temperature measurements of molecules, and the models for the calculations of the molecule-atom and molecule-molecule loss rate coefficients, which includes Ref. [30].
- [30] H. J. Carmichael, *Statistical Methods in Quantum Optics I: Master Equations and Fokker-Planck Equations* (Springer-Verlag, Berlin, 1999).
- [31] H. Li, M. Li, C. Makrides, A. Petrov, and S. Kotochigova, *Atoms* **7**, 36 (2019).
- [32] P. S. Julienne, T. M. Hanna, and Z. Idziaszek, *Phys. Chem. Chem. Phys.* **13**, 19114 (2011).
- [33] M. Mayle, B. P. Ruzic, and J. L. Bohn, *Phys. Rev. A* **85**, 062712 (2012).
- [34] G. Quéméner, J. L. Bohn, A. Petrov, and S. Kotochigova, *Phys. Rev. A* **84**, 062703 (2011).
- [35] B. E. Londoño, J. E. Mahecha, E. Luc-Koenig, and A. Crubellier, *Phys. Rev. A* **82**, 012510 (2010).
- [36] H. Yang, D.-C. Zhang, L. Liu, Y.-X. Liu, J. Nan, B. Zhao, and J.-W. Pan, *Science* **363**, 261 (2019).
- [37] H. Son, J. J. Park, W. Ketterle, and A. O. Jamison, *Nature (London)* **580**, 197 (2020).

## Supplemental Material: An ultracold gas of bosonic $^{23}\text{Na}^{39}\text{K}$ ground-state molecules

Kai K. Voges,<sup>1,\*</sup> Philipp Gersema,<sup>1</sup> Mara Meyer zum Alten Borgloh,<sup>1</sup>  
Torben A. Schulze,<sup>1</sup> Torsten Hartmann,<sup>1</sup> Alessandro Zenesini,<sup>1,2</sup> and Silke Ospelkaus<sup>1,†</sup>

<sup>1</sup>*Institut für Quantenoptik, Leibniz Universität Hannover, 30167 Hannover, Germany*

<sup>2</sup>*INO-CNR BEC Center and Dipartimento di Fisica, Università di Trento, 38123 Povo, Italy*

(Dated: July 30, 2020)

In this supplement, we provide additional details on the 5-level STIRAP model, alternative STIRAP pathways for the  $^{23}\text{Na}^{39}\text{K}$  molecules and the temperature measurements of the molecules. Furthermore, we detail on the loss model used for the determination of the two-body decay loss coefficients for molecule-molecule and molecule-atom collisions.

### 5-level STIRAP model

STImulated Raman Adiabatic Passage (STIRAP) for the transfer of weakly bound Feshbach molecules to the ground state, and vice versa, is typically performed in a pure 3-level  $\Lambda$ -system [1]. In our case, the Feshbach molecule state is named  $|f\rangle$ , the ground state  $|g\rangle$  and the excited states are named  $|e_i\rangle$ . The laser beams for the Pump and the Stokes transitions are copropagating and perpendicular to the magnetic field. For both beams, linear polarizations parallel ( $\parallel$ ) to the magnetic field access  $\pi$ -transitions in the molecules and linear polarizations perpendicular ( $\perp$ ) to the magnetic field access always both  $\sigma^+$ - and  $\sigma^-$ -transitions.

The molecular starting state  $|f\rangle$  can be described as a composed state of  $\alpha_1 |m_{i,\text{Na}} = -3/2, m_{i,\text{K}} = -1/2, M_S = -1\rangle + \alpha_2 |m_{i,\text{Na}} = -3/2, m_{i,\text{K}} = -3/2, M_S = 0\rangle$ , where  $M_S$  is the total electron spin projection and  $\alpha_{1/2}$  represent state admixtures. With the goal of maximizing the Rabi frequency  $\Omega_{\text{P(ump)}}$ , we choose excited states from the triplet hyperfine manifold of the coupled triplet-singlet states  $|c^3\Sigma^+, v = 30\rangle$  and  $|B^1\Pi, v = 8\rangle$  [2, 3]. Moreover, we choose the polarization of the Pump beam to be  $\parallel$ . The only possible accessible excited state is the  $|e_0\rangle = |m_{i,\text{Na}} = -3/2, m_{i,\text{K}} = -1/2, M_J = -1, M_F = -3\rangle$ .

Using  $\perp$  polarization for the Stokes laser, we reach the  $|g\rangle = |m_{i,\text{Na}} = -3/2, m_{i,\text{K}} = -1/2, M_J = 0, M_i = -2\rangle$  ground state with a  $\sigma^-$ -transition. Other states in the ground state cannot be reached, because the ground state manifold has pure singlet character and is deeply in the Paschen-Back regime. Thus, nuclear and electronic spins are decoupled so that only the electronic spin projection can be changed by an optical transition.

At the same time  $\sigma^+$ -transitions couple the state  $|g\rangle$  to the excited state  $|e_{1,2}\rangle$  which have both state contributions in the atomic base from  $|m_{i,\text{Na}} = -3/2, m_{i,\text{K}} = -1/2, M_J = 1, M_F = -1\rangle$ . Note that the Pump beam does not couple the state  $|f\rangle$  to the states  $|e_{1,2}\rangle$  due to  $\Delta M_F = 2$ .

In summary, the experimental situation requires to extend the typical 3-level  $\Lambda$ -system (for the state  $|f\rangle$ ,  $|e_0\rangle$  and  $|g\rangle$ ) to a 5-level system (for the states  $|f\rangle$ ,  $|e_0\rangle$ ,

$|g\rangle$  and  $|e_{1,2}\rangle$ ). The model Hamilton operator  $H(t)$  for the light-molecule interaction and the molecular energies in the rotating-wave-approximation is

$$\hbar \begin{bmatrix} 0 & \Omega_{\text{P}}(t)/2 & 0 & 0 & 0 \\ \Omega_{\text{P}}(t)/2 & \Delta_{\text{P}} & \Omega_{\text{S}}(t)/2 & 0 & 0 \\ 0 & \Omega_{\text{S}}(t)/2 & \Delta_{\text{P}} - \Delta_{\text{S}} & \Omega_{\text{S},1}(t)/2 & \Omega_{\text{S},2}(t)/2 \\ 0 & 0 & \Omega_{\text{S},1}(t)/2 & \Delta_{\text{P}} - \Delta_{\text{S},1} & 0 \\ 0 & 0 & \Omega_{\text{S},2}(t)/2 & 0 & \Delta_{\text{P}} - \Delta_{\text{S},2} \end{bmatrix}.$$

The time dependent state vector is represented by  $(c_f(t), c_{e_0}(t), c_g(t), c_{e_1}(t), c_{e_2}(t))^T$ , where  $c_i$  is the probability amplitude of the corresponding state  $|i\rangle$ .  $\Omega_{\text{P}}(t)$  is the Rabi frequency for the Pump transition and  $\Omega_{\text{S(tokes)}}(t)$ ,  $\Omega_{\text{S},1}(t)$  and  $\Omega_{\text{S},2}(t)$  are the Rabi frequencies for the Stokes transition to the excited states  $|e_0\rangle, |e_1\rangle$  and  $|e_2\rangle$ , respectively. Note, that all Rabi frequencies are time dependent and real.  $\Delta_{\text{P}}$  and  $\Delta_{\text{S}}$  are the detunings of the Pump and Stokes laser frequency to the respective molecular transition. The relative positions of the excited states  $|e_{1,2}\rangle$  to  $|e_0\rangle$  are  $\Delta_{\text{S},1} = 2\pi \times (-10)$  MHz and  $\Delta_{\text{S},2} = 2\pi \times (-21)$  MHz, respectively, at 199.3 G and are taken from our excited state model presented in [3]. To additionally model losses of the molecules from the excited states, a sixth state  $|l\rangle$  is introduced, which is not directly coupled to any other state. This is important for the numerical calculation, as it keeps the population normalized during the evaluation. The dynamics of the system can be modeled by solving the master equation in Lindblad representation with the density matrix  $\rho(t)$

$$\dot{\rho}(t) = -\frac{i}{\hbar}[H(t), \rho(t)] + \sum_k \gamma_k D[A_k]\rho(t). \quad (1)$$

The second term denotes the losses from the system, where  $\gamma_k$  are the decay rates of the excited states which we set for all three states to  $\gamma_0 = \gamma_1 = \gamma_2 = 2\pi \times 11$  MHz and  $D[A_k]$  are the corresponding Lindblad superoperators with the jump operator  $A_k$  from the excited state  $|e_k\rangle$  to the loss state  $|l\rangle$  [4].

For the fit of the experimental data in Fig. 3 we use this model with the Rabi frequencies  $\Omega_{\text{S},1}$  and  $\Omega_{\text{S},2}$  as free parameters as well as the STIRAP Rabi frequencies  $\Omega_{\text{P}}$  and  $\Omega_{\text{S}}$  constrained to their experimentally determined uncertainties. We assign the optimum of the fit within

these constrains, confirming the consistency of our data. Furthermore, this model was used to also calculate the STIRAP time dynamics of Fig. 2(b).

The 5-level model can be reduced to a 3-level one by setting the coupling to the excited state  $|e_{1,2}\rangle$  to zero. We use this to calculate the theoretical electromagnetically induced transparency curve in Fig. 2(a) and the optimal curve for the one-photon detuning (gray dashed line) in Fig. 3.

### Alternative STIRAP pathways

Alternative STIRAP pathways using states from the  $c^3\Sigma^+$  potential may be possible with either another STIRAP beam alignment, for example parallel to the magnetic field direction, and/or with other polarizations. In case of a perpendicular alignment, as it is described above, alternative STIRAP pathways to the ground state  $|g\rangle$  are possible when switching the laser polarizations, using now  $\perp$  polarization for the Pump and  $\parallel$  polarization for the Stokes beam; see Fig.S1.

We identify two additional states  $|e_{a,1}\rangle$  and  $|e_{a,2}\rangle$  suiting these pathways, both yielding state contributions from the  $|m_{i,\text{Na}} = -3/2, m_{i,\text{K}} = -1/2, M_J = 0, M_F = -2\rangle$  in the atomic base. Their transitions are +189 and -146 MHz detuned from the original one  $|e_0\rangle$  and do not possess neighboring states close by which may be populated through  $\sigma^-$ -transitions to the state  $|f\rangle$ . The additional STIRAP pathways are identified based on the model of the excited states [3]. Simulations, utilizing the model described above suggest round-trip efficiencies of more than 80%. These states will be object of future investigation.

### Loss coefficients

Two-body loss coefficients for molecule-molecule and molecule-atom collisions are extracted from the decay of the  $^{23}\text{Na}^{39}\text{K}$  ground-state molecule ensemble.

In a pure molecular ensemble, losses can be assigned to two-body losses with tetramer formation and subsequent removal or loss of the tetramers, see [5]. We obtain an analytic solution for the two-body loss of the ground-state molecule number  $N_{\text{NaK}}(t)$  [6]

$$N_{\text{NaK}}(t) = \frac{N_{\text{NaK},0}}{\left(1 + \frac{11}{8} \epsilon k_{\text{NaK},2} t\right)^{8/11}}, \quad (2)$$

where  $N_{\text{NaK},0}$  is the initial ground-state molecule number,  $k_{\text{NaK},2}$  the molecular two-body loss coefficient and  $\epsilon = (m_{\text{NaK}} \bar{\omega} / (2\pi k_B))^{3/2}$  with  $\bar{\omega}$  the average trap frequency and  $k_B$  the Boltzmann constant.  $N_{\text{NaK},0}$  and  $k_{\text{NaK},2}$  were used as free parameters for the fit. For the model of the loss from molecule-atom collisions

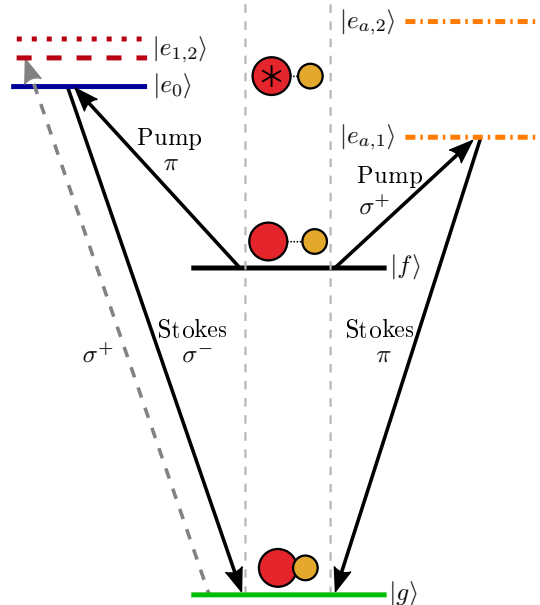


FIG. S1. STIRAP pathways. This figure shows the current (left) and the alternative (right) STIRAP pathway. Pathways start from the Feshbach molecule state  $|f\rangle$  (black solid line) and end in the ground state  $|g\rangle$  (green solid line). The excited states  $|e_i\rangle$  are the ones described in the text. For the current STIRAP the Pump beam drives  $\pi$ -transitions and the Stokes beam  $\sigma^-$ -transitions, displayed as solid arrows. On contrary, the Stokes beam couples also with  $\sigma^+$ -transition to the excited states  $|e_{1,2}\rangle$  (dashed arrow). The alternative STIRAP pathways use  $\sigma^+$ -transitions for the Pump and  $\pi$ -transitions for the Stokes beam. The states  $|e_{a,1,2}\rangle$  are shown as orange dashed-dotted lines.

we use the coupled differential equation system:

$$\begin{aligned} \dot{N}_{\text{NaK}}(t) &= -\epsilon k_{\text{NaK},2} \frac{N_{\text{NaK}}(t)^2}{T_{\text{NaK}}(t)^{3/2}} - \eta k_a N_{a,0} N_{\text{NaK}}(t) \\ \dot{T}_{\text{NaK}}(t) &= \epsilon k_{\text{NaK},2} \frac{N_{\text{NaK}}(t)}{4\sqrt{T_{\text{NaK}}(t)}}. \end{aligned} \quad (3)$$

$\eta$  is the density overlap between molecules and atoms,  $k_a$  the loss coefficient for the molecule-atom collision,  $N_{a,0}$  the initial atom number and  $T_{\text{NaK}}$  the temperature of the ground-state molecules.

Note, that in the model anti-evaporation effects may be considered for molecules only, or for both, molecules and atoms. The difference of these two cases is smaller than our experimental uncertainties. The presented data only consider effects on molecules.

### Temperature measurement for molecular clouds

Temperature measurements for atomic clouds are typically done through time-of-flight (TOF) measurements after releasing them from the trap and fitting a temperature dependent expansion curve to the clouds width. For ground-state molecules, this technique is limited by the free expansion time, as the molecules might leave the region of the STIRAP laser beams which is needed to transfer the ground-state molecules back to the Feshbach state for imaging. In our experiment, the STIRAP beam foci have  $1/e^2$  radii of 35 and 40  $\mu\text{m}$ , respectively, allowing for almost no free expansion time of the molecules before leaving the STIRAP beam area.

To still measure the temperature of the ground-state molecule ensemble we reverse the entire molecule creation process, by means of STIRAP and Feshbach molecule dissociation, before performing the TOF and imaging on the dissociated atoms. Note, that for our Feshbach molecules, imaging normally takes place from the Feshbach molecule state itself, as the linewidth of the imaging transition in  $^{39}\text{K}$  is larger than the binding energy of the weakly bound dimers [7]. A temperature measurement in TOF with Feshbach molecules is also not possible, because the Feshbach molecule lifetime is very short, about 1 ms in a pure molecular ensemble, and an appropriate signal would be lost very fast. A complete dissociation within 600  $\mu\text{s}$  using a resonant radio frequency of 210.0 MHz to the  $|f = 1, m_f = -1\rangle_{\text{Na}} + |f = 1, m_f = -1\rangle_{\text{K}}$  is performed immediately after the

backwards STIRAP. Temperature TOF measurements are then performed on the long living atomic ensemble. All atoms involved in the temperature measurement come originally from deeply bound molecules.

The extracted temperature from the atoms show the same temperature as the initial atoms measured before the molecule creation happened. Consequently, all transfers in between (Feshbach molecule creation, STIRAPs, atom state preparations and removals, Feshbach molecule dissociation) do not heat the molecule ensemble.

---

\* voges@iqo.uni-hannover.de

† silke.ospelkaus@iqo.uni-hannover.de

- [1] N. V. Vitanov, A. A. Rangelov, B. W. Shore, and K. Bergmann, *Rev. Mod. Phys.* **89**, 015006 (2017).
- [2] T. A. Schulze, I. I. Temelkov, M. W. Gempel, T. Hartmann, H. Knöckel, S. Ospelkaus, and E. Tiemann, *Phys. Rev. A* **88**, 023401 (2013).
- [3] K. K. Voges, P. Gersema, T. Hartmann, T. A. Schulze, A. Zenesini, and S. Ospelkaus, *New Journal of Physics* **21**, 123034 (2019).
- [4] H. J. Carmichael, Springer-Verlag Berlin Heidelberg 10.1007/978-3-662-03875-8 (1999).
- [5] P. D. Gregory, M. D. Frye, J. A. Blackmore, E. M. Bridge, R. Sawant, J. M. Hutson, and S. L. Cornish, *Nature Communications* **10** (2019).
- [6] The derivation of the analytical solution will be presented in a future publication.
- [7] K. K. Voges, P. Gersema, T. Hartmann, T. A. Schulze, A. Zenesini, and S. Ospelkaus, *Phys. Rev. A* **101**, 042704 (2020).



## Chapter 6

# Conclusion and Outlook

In this thesis, the creation of a novel quantum gas of ultracold bosonic  $^{23}\text{Na}^{39}\text{K}$  ground-state molecules and the first experimental findings regarding ultracold collisions is presented.

The creation pathway follows along the line of the pioneering experiments with  $^{40}\text{K}^{87}\text{Rb}$  molecules [49]: weakly bound molecule creation (see Chap. 2), hyperfine resolved spectroscopy of singlet-triplet mixed molecular states (see Chap. 4) and the high efficient ground-state transfer by STIRAP (see Chap. 5).

Starting from an ultracold heteronuclear atomic mixture, a cautious selection of a suitable Feshbach resonance for the formation of weakly bound dimers is outlined. Close to the chosen resonance in the  $|f = 1, m_f = -1\rangle_{\text{Na}} + |f = 2, m_f = -2\rangle_{\text{K}}$  at 200 G, the Feshbach molecules are created and the creation procedure is characterized [87]. Up to 6000 molecules can be created in a single experimental run which feature a lifetime of about  $300 \mu\text{s}$  immersed in a bath of residual atoms.

For the purpose of state transfer of the Feshbach molecules to their ground state, the STIRAP process is utilized. According to the preselection of the singlet-triplet mixed excited state manifolds  $|B^1\Pi, v = 8\rangle \sim |c^3\Sigma^+, v = 30\rangle$  a two-color low-linewidth laser system for 816 nm and 573 nm is required. In this thesis, the design and construction as well as characterization of this laser system is detailed (see Chap. 3). During the course of this work, it is intensively used. The hyperfine resolved spectroscopy of the excited state is performed by using the 816 nm laser. The experiment are performed starting from the atomic threshold. The found transitions to the bound molecular excited state are described by a quantum mechanical model involving the singlet-triplet mixing of both coupled state manifolds. The respective singlet-triplet admixture is determined to be 26%/74%. Including the 573 nm laser into the spectroscopy, the ground state is identified, first by the introduction of strong Stark shifts and later by coherent dark-state effects. The relative position of the excited states are known within a few MHz from the one-photon experiments [88].

The ground-state energy relative to the initial Feshbach molecule state is on the other hand known within a few kHz due to its strong two-photon dependence [89]. The acquired knowledge about the molecular hyperfine structure is used to perform STIRAP from the Feshbach molecule state to the ground state with an efficiency of 70%. The resulting 4200 ground-state molecules are prepared in a single hyperfine state and possess long lifetimes expected from ultracold bosonic nonreactive ground-state molecules [89].

The molecular quantum gas is prepared as a pure molecular ensemble and shows significant losses from two-body processes. The respective loss rate coefficient is in accordance with the universal scattering limit. This indicates towards sticky collisions and light induced sticky complex removals, analog to the prominent case of RbCs [67, 69]. Moreover, the ground-state molecules are prepared in a mixture together with  $^{23}\text{Na}$  and  $^{39}\text{K}$  atoms. Similar to the magnetic field dependent measurements performed for the ultracold fermionic

$^{23}\text{Na}^{40}\text{K} + ^{40}\text{K}$  mixture [139], a hyperfine state dependent scattering scenario is suggested. In contrast to predictions from Mayle *et al.* (2012) [137], the losses from a distinguished non-stretched collisional hyperfine channel in the  $^{23}\text{Na}^{39}\text{K} + ^{39}\text{K}$  mixture is not observed. The resulting loss rate coefficient is smaller than  $1.5 \times 10^{-14} \text{ cm}^3 \text{ s}^{-1}$ . This unexpected result demands more investigations in an extended parameter range and eventually an extended model for molecule-atom collisions.

The entire creation process, from the atomic mixture to the ground state, is highly unique for any selected molecular species. This thesis hallmarks the first successful creation of the novel molecular bosonic quantum gas of rovibrational ground-state  $^{23}\text{Na}^{39}\text{K}$ .

Since the experimental machine was originally designed for experiments with heteronuclear polar ground-state molecules [90–92], it features a few experimental add-ons, namely an integrated optical lattice beam path, a single-site quantum gas microscope area [93] and an in-vacuum versatile ITO electrode structure for inducing the electric dipole moment of the molecules [94]. In forthcoming investigations, these features will be used to extend the variety of physical systems with polar molecules. The optical lattice will be used to pin the molecules to individual sites of the lattice preventing them from forming four-body complexes [67, 68]. The lattice will be also a worthy tool in terms of efficient molecule creation inside the optical lattice [62, 63]. Atoms, in case of bosonic  $^{23}\text{Na}$  and  $^{39}\text{K}$ , can form a double Mott-insulator [140] which is an ideal starting point for the high-efficient Feshbach molecule creation and the subsequent STIRAP for a highly filled lattice.

The ITO electrodes are essential for experiments with directed dipoles along the electric field. Polarized molecules experience attractive and repulsive long-range interaction respective to their head-to-tail or side-by-side orientation [141]. This can alter the scattering properties drastically, especially, when the confinement forbids collisions in selected directions [57]. Chemical reaction control and advanced dipolar collisional studies lie ahead [59]. In combination with an optical lattice, it allows the observation of dipolar effects between neighboring lattice sites or even spin-exchanges and excitation diffusion within the lattice particles [64].

At this point the high resolution objective comes into play. It allows for single-site read out of the particles and even single-site addressing and manipulation [142]. Analog to the pioneering experiments with arrays of atoms, one- and two-dimensional arrays of polar molecules can be engineered. The dipole-dipole interaction will be an advanced tool for mediating interactions between quantum particles and study their behavior in few and many-particle systems in very controlled and pure environment.

# Bibliography

- [1] X. Chen and B. Fan, *The emergence of picokelvin physics*, Reports on Progress in Physics, **83**(7) 076401, 2020, DOI: 10.1088/1361-6633/ab8ab6.
- [2] T. Hänsch and A. Schawlow, *Cooling of gases by laser radiation*, Optics Communications, **13**(1) 68 – 69, 1975, DOI: [https://doi.org/10.1016/0030-4018\(75\)90159-5](https://doi.org/10.1016/0030-4018(75)90159-5).
- [3] W. D. Phillips and H. Metcalf, *Laser Deceleration of an Atomic Beam*, Phys. Rev. Lett., **48**(9) 596 – 599, 1982, DOI: <https://doi.org/10.1103/PhysRevLett.48.596>.
- [4] E. L. Raab, M. Prentiss, A. Cable, S. Chu, and D. E. Pritchard, *Trapping of Neutral Sodium Atoms with Radiation Pressure*, Phys. Rev. Lett., **59**(23) 2631–2634, 1987, DOI: 10.1103/PhysRevLett.59.2631.
- [5] P. D. Lett, R. N. Watts, C. I. Westbrook, W. D. Phillips, P. L. Gould, and H. J. Metcalf, *Observation of Atoms Laser Cooled below the Doppler Limit*, Phys. Rev. Lett., **61**(2) 169–172, 1988, DOI: 10.1103/PhysRevLett.61.169.
- [6] W. Petrich, M. H. Anderson, J. R. Ensher, and E. A. Cornell, *Stable, Tightly Confining Magnetic Trap for Evaporative Cooling of Neutral Atoms*, Phys. Rev. Lett., **74**(17) 3352–3355, 1995, DOI: 10.1103/PhysRevLett.74.3352.
- [7] S. Chu, J. E. Bjorkholm, A. Ashkin, and A. Cable, *Experimental Observation of Optically Trapped Atoms*, Phys. Rev. Lett., **57**(3) 314–317, 1986, DOI: 10.1103/PhysRevLett.57.314.
- [8] The Royal Swedish Academy of Science, *The Nobel prize in Physics 1997*.
- [9] M. H. Anderson, J. R. Ensher, M. R. Matthews, C. E. Wieman, and E. A. Cornell, *Observation of Bose-Einstein Condensation in a Dilute Atomic Vapor*, Science, **269**(5221) 198–201, 1995, DOI: 10.1126/science.269.5221.198.
- [10] B. DeMarco and D. S. Jin, *Onset of Fermi Degeneracy in a Trapped Atomic Gas*, Science, **285**(5434) 1703–1706, 1999, DOI: 10.1126/science.285.5434.1703.
- [11] G. Roati, M. Zaccanti, C. D’Errico, J. Catani, M. Modugno, A. Simoni, M. Inguscio, and G. Modugno,  *$^{39}\text{K}$  Bose-Einstein Condensate with Tunable Interactions*, Phys. Rev. Lett., **99**(1) 010403, 2007, DOI: 10.1103/PhysRevLett.99.010403.
- [12] C. Chin, R. Grimm, P. Julienne, and E. Tiesinga, *Feshbach resonances in ultracold gases*, Rev. Mod. Phys., **82**(2) 1225–1286, 2010, DOI: 10.1103/RevModPhys.82.1225.
- [13] C. R. Cabrera, L. Tanzi, J. Sanz, B. Naylor, P. Thomas, P. Cheiney, and L. Tarruell, *Quantum liquid droplets in a mixture of Bose-Einstein condensates*, Science, **359**(6373) 301–304, 2017, DOI: 10.1126/science.aao5686.
- [14] C. D’Errico, A. Burchianti, M. Prevedelli, L. Salasnich, F. Ancilotto, M. Modugno, F. Minardi, and C. Fort, *Observation of quantum droplets in a heteronuclear bosonic mixture*, Phys. Rev. Research, **1**(3) 033155, 2019, DOI: 10.1103/PhysRevResearch.1.033155.

- [15] C.-L. Hung, V. Gurarie, and C. , *From Cosmology to Cold Atoms: Observation of Sakharov Oscillations in a Quenched Atomic Superfluid*, *Science*, **341**(6151) 1213–1215, 2013, DOI: 10.1126/science.1237557.
- [16] J. R. Abo-Shaeer, C. Raman, J. M. Vogels, and W. Ketterle, *Observation of Vortex Lattices in Bose-Einstein Condensates*, *Science*, **292**(5516) 476–479, 2001, DOI: 10.1126/science.1060182.
- [17] M. J. H. Ku, B. Mukherjee, T. Yefsah, and M. W. Zwierlein, *Cascade of Solitonic Excitations in a Superfluid Fermi gas: From Planar Solitons to Vortex Rings and Lines*, *Phys. Rev. Lett.*, **116**(4) 045304, 2016, DOI: 10.1103/PhysRevLett.116.045304.
- [18] J. Rui, H. Yang, L. Liu, D.-C. Zhang, Y.-X. Liu, J. Nan, Y.-A. Chen, B. Zhao, and J.-W. Pan, *Controlled state-to-state atom-exchange reaction in an ultracold atom-dimer mixture*, *Nature Physics*, **13**(7) 699–703, 2017, DOI: 10.1038/nphys4095.
- [19] C. Chin, M. Bartenstein, A. Altmeyer, S. Riedl, S. Jochim, J. H. Denschlag, and R. Grimm, *Observation of the Pairing Gap in a Strongly Interacting Fermi Gas*, *Science*, **305**(5687) 1128–1130, 2004, DOI: 10.1126/science.1100818.
- [20] C. A. Regal, M. Greiner, and D. S. Jin, *Observation of Resonance Condensation of Fermionic Atom Pairs*, *Phys. Rev. Lett.*, **92**(4) 040403, 2004, DOI: 10.1103/PhysRevLett.92.040403.
- [21] T. Kraemer, M. Mark, P. Waldburger, J. G. Danzl, C. Chin, B. Engeser, A. D. Lange, K. Pilch, A. Jaakkola, H.-C. Nägerl, and R. Grimm, *Evidence for Efimov quantum states in an ultracold gas of caesium atoms*, *Nature*, **440**(7082) 315–318, 2006, DOI: 10.1038/nature04626.
- [22] D. Savoie, M. Altorio, B. Fang, L. A. Sidorenkov, R. Geiger, and A. Landragin, *Interleaved atom interferometry for high-sensitivity inertial measurements*, *Science Advances*, **4**(12) eaau7948, 2018, DOI: 10.1126/sciadv.aau7948.
- [23] D. Schlippert, J. Hartwig, H. Albers, L. L. Richardson, C. Schubert, A. Roura, W. P. Schleich, W. Ertmer, and E. M. Rasel, *Quantum Test of the Universality of Free Fall*, *Phys. Rev. Lett.*, **112**(20) 203002, 2014, DOI: 10.1103/PhysRevLett.112.203002.
- [24] R. Wynands and S. Weyers, *Atomic fountain clocks*, *Metrologia*, **42**(3) 64–79, 2005, DOI: 10.1088/0026-1394/42/3/s08.
- [25] T. Bothwell, D. Kedar, E. Oelker, J. M. Robinson, S. L. Bromley, W. L. Tew, J. Ye, and C. J. Kennedy, *JILA SrI optical lattice clock with uncertainty of  $2.0 \times 10^{-18}$* , *Metrologia*, **56**(6) 065004, 2019, DOI: 10.1088/1681-7575/ab4089.
- [26] D. Greif, M. F. Parsons, A. Mazurenko, C. S. Chiu, S. Blatt, F. Huber, G. Ji, and M. Greiner, *Site-resolved imaging of a fermionic Mott insulator*, *Science*, **351**(6276) 953–957, 2016, DOI: 10.1126/science.aad9041.
- [27] P. M. Preiss, R. Ma, M. E. Tai, A. Lukin, M. Rispoli, P. Zupancic, Y. Lahini, R. Islam, and M. Greiner, *Strongly correlated quantum walks in optical lattices*, *Science*, **347**(6227) 1229–1233, 2015, DOI: 10.1126/science.1260364.
- [28] M. Endres, H. Bernien, A. Keesling, H. Levine, E. R. Anschuetz, A. Krajenbrink, C. Senko, V. Vuletic, M. Greiner, and M. D. Lukin, *Atom-by-atom assembly of defect-free one-dimensional cold atom arrays*, *Science*, **354**(6315) 1024–1027, 2016, DOI: 10.1126/science.aah3752.
- [29] N. Šibalić and C. S. Adams, *Rydberg Physics*, 2399-2891. IOP Publishing, 2018, DOI: 10.1088/978-0-7503-1635-4.

- [30] J. A. Sedlacek, A. Schwettmann, H. Kübler, and J. P. Shaffer, *Atom-Based Vector Microwave Electrometry Using Rubidium Rydberg Atoms in a Vapor Cell*, *Phys. Rev. Lett.*, **111**(6) 063001, 2013, DOI: 10.1103/physrevlett.111.063001.
- [31] C. S. Adams, J. D. Pritchard, and J. P. Shaffer, *Rydberg atom quantum technologies*, *Journal of Physics B*, **53**(1) 012002, 2019, DOI: 10.1088/1361-6455/ab52ef.
- [32] E. Urban, T. A. Johnson, T. Henage, L. Isenhower, D. D. Yavuz, T. G. Walker, and M. Saffman, *Observation of Rydberg blockade between two atoms*, *Nature Physics*, **5**(2) 110–114, 2009, DOI: 10.1038/nphys1178.
- [33] T. Wilk, A. Gaëtan, C. Evellin, J. Wolters, Y. Miroshnychenko, P. Grangier, and A. Browaeys, *Entanglement of Two Individual Neutral Atoms Using Rydberg Blockade*, *Phys. Rev. Lett.*, **104**(1) 010502, 2010, DOI: 10.1103/PhysRevLett.104.010502.
- [34] A. Omran, H. Levine, A. Keesling, G. Semeghini, T. T. Wang, S. Ebadi, H. Bernien, A. S. Zibrov, H. Pichler, S. Choi, and et al., *Generation and manipulation of Schrödinger cat states in Rydberg atom arrays*, *Science*, **365**(6453) 570–574, 2019, DOI: 10.1126/science.aax9743.
- [35] T. Niederprüm, O. Thomas, T. Eichert, C. Lippe, J. Pérez-Ríos, C. H. Greene, and H. Ott, *Observation of pendular butterfly Rydberg molecules*, *Nature Communications*, **7**(1), 2016, DOI: 10.1038/ncomms12820.
- [36] A. Griesmaier, J. Werner, S. Hensler, J. Stuhler, and T. Pfau, *Bose-Einstein Condensation of Chromium*, *Phys. Rev. Lett.*, **94**(16) 160401, 2005, DOI: 10.1103/PhysRevLett.94.160401.
- [37] M. Lu, N. Q. Burdick, S. H. Youn, and B. L. Lev, *Strongly Dipolar Bose-Einstein Condensate of Dysprosium*, *Phys. Rev. Lett.*, **107**(19) 190401, 2011, DOI: 10.1103/PhysRevLett.107.190401.
- [38] K. Aikawa, A. Frisch, M. Mark, S. Baier, A. Rietzler, R. Grimm, and F. Ferlaino, *Bose-Einstein Condensation of Erbium*, *Phys. Rev. Lett.*, **108**(21) 210401, 2012, DOI: 10.1103/PhysRevLett.108.210401.
- [39] E. T. Davletov, V. V. Tsyganok, V. A. Khlebnikov, D. A. Pershin, D. V. Shaykin, and A. V. Akimov, *Machine learning for achieving Bose-Einstein condensation of thulium atoms*, *Phys. Rev. A*, **102**(1) 011302, 2020, DOI: 10.1103/PhysRevA.102.011302.
- [40] J. Miao, J. Hostetter, G. Stratis, and M. Saffman, *Magneto-optical trapping of holmium atoms*, *Phys. Rev. A*, **89**(4) 041401, 2014, DOI: 10.1103/PhysRevA.89.041401.
- [41] L. Chomaz, S. Baier, D. Petter, M. J. Mark, F. Wächtler, L. Santos, and F. Ferlaino, *Quantum-Fluctuation-Driven Crossover from a Dilute Bose-Einstein Condensate to a Macrodroplet in a Dipolar Quantum Fluid*, *Phys. Rev. X*, **6**(4) 041039, 2016, DOI: 10.1103/PhysRevX.6.041039.
- [42] H. Kadau, M. Schmitt, M. Wenzel, C. Wink, T. Maier, I. Ferrier-Barbut, and T. Pfau, *Observing the Rosensweig instability of a quantum ferrofluid*, *Nature*, **530**(7589) 194–197, 2016, DOI: 10.1038/nature16485.
- [43] I. Ferrier-Barbut, M. Wenzel, F. Böttcher, T. Langen, M. Isoard, S. Stringari, and T. Pfau, *Scissors Mode of Dipolar Quantum Droplets of Dysprosium Atoms*, *Phys. Rev. Lett.*, **120**(16) 160402, 2018, DOI: 10.1103/PhysRevLett.120.160402.
- [44] M. Wenzel, F. Böttcher, T. Langen, I. Ferrier-Barbut, and T. Pfau, *Striped states in a many-body system of tilted dipoles*, *Phys. Rev. A*, **96**(5) 053630, 2017, DOI: 10.1103/PhysRevA.96.053630.

- [45] F. Böttcher, J.-N. Schmidt, M. Wenzel, J. Hertkorn, M. Guo, T. Langen, and T. Pfau, *Transient Supersolid Properties in an Array of Dipolar Quantum Droplets*, *Phys. Rev. X*, **9**(1) 011051, 2019, DOI: 10.1103/PhysRevX.9.011051.
- [46] L. Chomaz, D. Petter, P. Ilzhöfer, G. Natale, A. Trautmann, C. Politi, G. Durastante, R. M. W. van Bijnen, A. Patscheider, M. Sohmen, M. J. Mark, and F. Ferlaino, *Long-Lived and Transient Supersolid Behaviors in Dipolar Quantum Gases*, *Phys. Rev. X*, **9**(2) 021012, 2019, DOI: 10.1103/PhysRevX.9.021012.
- [47] L. Chomaz, R. M. W. van Bijnen, D. Petter, G. Faraoni, S. Baier, J. H. Becher, M. J. Mark, F. Wächtler, L. Santos, and F. Ferlaino, *Observation of roton mode population in a dipolar quantum gas*, *Nature Physics*, **14**(5) 442–446, 2018, DOI: 10.1038/s41567-018-0054-7.
- [48] M. Wenzel, F. Böttcher, J.-N. Schmidt, M. Eisenmann, T. Langen, T. Pfau, and I. Ferrier-Barbut, *Anisotropic Superfluid Behavior of a Dipolar Bose-Einstein Condensate*, *Phys. Rev. Lett.*, **121**(3) 030401, 2018, DOI: 10.1103/PhysRevLett.121.030401.
- [49] K.-K. Ni, S. Ospelkaus, M. H. G. de Miranda, A. Peer, B. Neyenhuis, J. J. Zirbel, S. Kotochigova, P. S. Julienne, D. S. Jin, and J. Ye, *A High Phase-Space-Density Gas of Polar Molecules*, *Science*, **322**(5899) 231–235, 2008, DOI: 10.1126/science.1163861.
- [50] J. W. Park, S. A. Will, and M. W. Zwierlein, *Ultracold Dipolar Gas of Fermionic  $^{23}\text{Na}^{40}\text{K}$  Molecules in Their Absolute Ground State*, *Phys. Rev. Lett.*, **114**(20) 205302, 2015, DOI: 10.1103/PhysRevLett.114.205302.
- [51] T. M. Rvachov, H. Son, A. T. Sommer, S. Ebadi, J. J. Park, M. W. Zwierlein, W. Ketterle, and A. O. Jamison, *Long-Lived Ultracold Molecules with Electric and Magnetic Dipole Moments*, *Phys. Rev. Lett.*, **119**(14) 143001, 2017, DOI: 10.1103/PhysRevLett.119.143001.
- [52] T. Takekoshi, L. Reichsöllner, A. Schindewolf, J. M. Hutson, C. R. Le Sueur, O. Dulieu, F. Ferlaino, R. Grimm, and H.-C. Nägerl, *Ultracold Dense Samples of Dipolar RbCs Molecules in the Rovibrational and Hyperfine Ground State*, *Phys. Rev. Lett.*, **113**(20) 205301, 2014, DOI: 10.1103/PhysRevLett.113.205301.
- [53] P. K. Molony, P. D. Gregory, Z. Ji, B. Lu, M. P. Köppinger, C. R. Le Sueur, C. L. Blackley, J. M. Hutson, and S. L. Cornish, *Creation of Ultracold  $^{87}\text{Rb}^{133}\text{Cs}$  Molecules in the Rovibrational Ground State*, *Phys. Rev. Lett.*, **113**(25) 255301, 2014, DOI: 10.1103/PhysRevLett.113.255301.
- [54] A. Zaitsevskii, S. O. Adamson, E. A. Pazyuk, A. V. Stolyarov, O. Nikolayeva, O. Docenko, I. Klincare, M. Auzinsh, M. Tamanis, R. Ferber, and R. Cimiraglia, *Energy and radiative properties of the low-lying NaRb states*, *Phys. Rev. A*, **63** 052504, 2001, DOI: 10.1103/PhysRevA.63.052504.
- [55] M. Aymar and O. Dulieu, *Calculation of accurate permanent dipole moments of the lowest  $^{1,3}\Sigma^+$  states of heteronuclear alkali dimers using extended basis sets*, *The Journal of Chemical Physics*, **122**(20) 204302, 2005, DOI: 10.1063/1.1903944.
- [56] P. S. Żuchowski and J. M. Hutson, *Reactions of ultracold alkali-metal dimers*, *Phys. Rev. A*, **81** 060703, 2010, DOI: 10.1103/PhysRevA.81.060703.
- [57] S. Ospelkaus, K.-K. Ni, D. Wang, M. H. G. de Miranda, B. Neyenhuis, G. Quémener, P. S. Julienne, J. L. Bohn, D. S. Jin, and J. Ye, *Quantum-State Controlled Chemical Reactions of Ultracold Potassium-Rubidium Molecules*, *Science*, **327**(5967) 853–857, 2010, DOI: 10.1126/science.1184121.

- [58] K.-K. Ni, S. Ospelkaus, D. Wang, G. Quéméner, B. Neyenhuis, M. H. G. de Miranda, J. L. Bohn, J. Ye, and D. S. Jin, *Dipolar collisions of polar molecules in the quantum regime*, *Nature*, **464**(7293) 1324–1328, 2010, DOI: 10.1038/nature08953.
- [59] M. Guo, X. Ye, J. He, M. L. González-Martínez, R. Vexiau, G. Quéméner, and D. Wang, *Dipolar Collisions of Ultracold Ground-State Bosonic Molecules*, *Phys. Rev. X*, **8**(4) 041044, 2018, DOI: 10.1103/PhysRevX.8.041044.
- [60] A. V. Gorshkov, P. Rabl, G. Pupillo, A. Micheli, P. Zoller, M. D. Lukin, and H. P. Büchler, *Suppression of Inelastic Collisions Between Polar Molecules With a Repulsive Shield*, *Phys. Rev. Lett.*, **101**(7) 073201, 2008, DOI: 10.1103/PhysRevLett.101.073201.
- [61] T. Karman and J. M. Hutson, *Microwave Shielding of Ultracold Polar Molecules*, *Phys. Rev. Lett.*, **121**(16) 163401, 2018, DOI: 10.1103/PhysRevLett.121.163401.
- [62] S. A. Moses, J. P. Covey, M. T. Miecnikowski, B. Yan, B. Gadway, J. Ye, and D. S. Jin, *Creation of a low-entropy quantum gas of polar molecules in an optical lattice*, *Science*, **350**(6261) 659–662, 2015, DOI: 10.1126/science.aac6400.
- [63] L. Reichsöllner, A. Schindewolf, T. Takekoshi, R. Grimm, and H.-C. Nägerl, *Quantum Engineering of a Low-Entropy Gas of Heteronuclear Bosonic Molecules in an Optical Lattice*, *Phys. Rev. Lett.*, **118**(7), 2017, DOI: 10.1103/physrevlett.118.073201.
- [64] B. Yan, S. A. Moses, B. Gadway, J. P. Covey, K. R. A. Hazzard, A. M. Rey, D. S. Jin, and J. Ye, *Observation of dipolar spin-exchange interactions with lattice-confined polar molecules*, *Nature*, **501**(7468) 521–525, 2013, DOI: 10.1038/nature12483.
- [65] M. Lemeshko, R. V. Krems, and H. Weimer, *Nonadiabatic Preparation of Spin Crystals with Ultracold Polar Molecules*, *Phys. Rev. Lett.*, **109**(3), 2012, DOI: 10.1103/physrevlett.109.035301.
- [66] M.-G. Hu, Y. Liu, D. D. Grimes, Y.-W. Lin, A. H. Gheorghe, R. Vexiau, N. Bouloufa-Maafa, O. Dulieu, T. Rosenband, and K.-K. Ni, *Direct observation of bimolecular reactions of ultracold KRb molecules*, *Science*, **366**(6469) 1111–1115, 2019, DOI: 10.1126/science.aay9531.
- [67] P. D. Gregory, M. D. Frye, J. A. Blackmore, E. M. Bridge, R. Sawant, J. M. Hutson, and S. L. Cornish, *Sticky collisions of ultracold RbCs molecules*, *Nature Communications*, **10**(1), 2019, DOI: 10.1038/s41467-019-11033-y.
- [68] A. Christianen, M. W. Zwierlein, G. C. Groenenboom, and T. Karman, *Photoinduced Two-Body Loss of Ultracold Molecules*, *Phys. Rev. Lett.*, **123**(12), 2019, DOI: 10.1103/physrevlett.123.123402.
- [69] P. D. Gregory, J. A. Blackmore, S. L. Bromley, and S. L. Cornish, *Loss of Ultracold  $^{87}\text{Rb}^{133}\text{Cs}$  Molecules via Optical Excitation of Long-Lived Two-Body Collision Complexes*, *Phys. Rev. Lett.*, **124**(16) 163402.
- [70] Y. Liu, M.-G. Hu, M. A. Nichols, D. D. Grimes, T. Karman, H. Guo, and K.-K. Ni, *Steering ultracold reactions through long-lived transient intermediates*, *arXiv*, **(2002.05140)**, 2020.
- [71] L. De Marco, G. Valtolina, K. Matsuda, W. G. Tobias, J. P. Covey, and J. Ye, *A degenerate Fermi gas of polar molecules*, *Science*, **363**(6429) 853–856, 2019, DOI: 10.1126/science.aau7230.
- [72] H. Son, J. J. Park, W. Ketterle, and A. O. Jamison, *Collisional cooling of ultracold molecules*, *Nature*, **580**(7802) 197–200, 2020, DOI: 10.1038/s41586-020-2141-z.

- [73] N. V. Vitanov, A. A. Rangelov, B. W. Shore, and K. Bergmann, *Stimulated Raman adiabatic passage in physics, chemistry, and beyond*, Rev. Mod. Phys., **89**(1) 015006, 2017, DOI: 10.1103/RevModPhys.89.015006.
- [74] C. Ospelkaus, S. Ospelkaus, L. Humbert, P. Ernst, K. Sengstock, and K. Bongs, *Ultracold Heteronuclear Molecules in a 3D Optical Lattice*, Phys. Rev. Lett., **97**(12) 120402, 2006, DOI: 10.1103/PhysRevLett.97.120402.
- [75] C. Klempt, T. Henninger, O. Topic, M. Scherer, L. Kattner, E. Tiemann, W. Ertmer, and J. J. Arlt, *Radio-frequency association of heteronuclear Feshbach molecules*, Phys. Rev. A, **78**(6), 2008, DOI: 10.1103/physreva.78.061602.
- [76] J. J. Zirbel, K.-K. Ni, S. Ospelkaus, T. L. Nicholson, M. L. Olsen, P. S. Julienne, C. E. Wieman, J. Ye, and D. S. Jin, *Heteronuclear molecules in an optical dipole trap*, Phys. Rev. A, **78**(1), 2008, DOI: 10.1103/physreva.78.013416.
- [77] A.-C. Voigt, M. Taglieber, L. Costa, T. Aoki, W. Wieser, T. W. Hänsch, and K. Dieckmann, *Ultracold Heteronuclear Fermi-Fermi Molecules*, Phys. Rev. Lett., **102**(2) 020405, 2009, DOI: 10.1103/PhysRevLett.102.020405.
- [78] C.-H. Wu, J. W. Park, P. Ahmadi, S. Will, and M. W. Zwierlein, *Ultracold Fermionic Feshbach Molecules of  $^{23}\text{Na}^{40}\text{K}$* , Phys. Rev. Lett., **109**(8) 085301, 2012, DOI: 10.1103/PhysRevLett.109.085301.
- [79] M.-S. Heo, T. T. Wang, C. A. Christensen, T. M. Rvachov, D. A. Cotta, J.-H. Choi, Y.-R. Lee, and W. Ketterle, *Formation of ultracold fermionic NaLi Feshbach molecules*, Phys. Rev. A, **86**(2) 021602, 2012, DOI: 10.1103/PhysRevA.86.021602.
- [80] M. P. Köppinger, D. J. McCarron, D. L. Jenkin, P. K. Molony, H.-W. Cho, S. L. Cornish, C. R. Le Sueur, C. L. Blackley, and J. M. Hutson, *Production of optically trapped  $^{87}\text{RbCs}$  Feshbach molecules*, Phys. Rev. A, **89**(3), 2014, DOI: 10.1103/physreva.89.033604.
- [81] F. Wang, X. He, X. Li, B. Zhu, J. Chen, and D. Wang, *Formation of ultracold NaRb Feshbach molecules*, New Journal of Physics, **17**(3) 035003, 2015, DOI: 10.1088/1367-2630/17/3/035003.
- [82] J. W. Park, S. A. Will, and M. W. Zwierlein, *Two-photon pathway to ultracold ground state molecules of  $^{23}\text{Na}^{40}\text{K}$* , New Journal of Physics, **17**(7) 075016, 2015, DOI: 10.1088/1367-2630/17/7/075016.
- [83] B. Zhu, X. Li, X. He, M. Guo, F. Wang, R. Vexiau, N. Bouloufa-Maafa, O. Dulieu, and D. Wang, *Long-range states of the NaRb molecule near the  $\text{Na}(3^2\text{S}_{1/2})+\text{Rb}(5^2\text{P}_{3/2})$  asymptote*, Phys. Rev. A, **93**(1) 012508, 2016, DOI: 10.1103/PhysRevA.93.012508.
- [84] M. Guo, R. Vexiau, B. Zhu, B. Lu, N. Bouloufa-Maafa, O. Dulieu, and D. Wang, *High-resolution molecular spectroscopy for producing ultracold absolute-ground-state  $^{23}\text{Na}^{87}\text{Rb}$  molecules*, Phys. Rev. A, **96**(5) 052505, 2017, DOI: 10.1103/PhysRevA.96.052505.
- [85] A. Yang, S. Botsi, S. Kumar, S. B. Pal, M. M. Lam, I. Čepaitė, A. Laugharn, and K. Dieckmann, *Singlet Pathway to the Ground State of Ultracold Polar Molecules*, Phys. Rev. Lett., **124**(13) 133203, 2020, DOI: 10.1103/PhysRevLett.124.133203.
- [86] F. Seeßelberg, N. Buchheim, Z.-K. Lu, T. Schneider, X.-Y. Luo, E. Tiemann, I. Bloch, and C. Gohle, *Modeling the adiabatic creation of ultracold polar  $^{23}\text{Na}^{40}\text{K}$  molecules*, Phys. Rev. A, **97**(1) 013405, 2018, DOI: 10.1103/PhysRevA.97.013405.

- [87] K. K. Voges, P. Gersema, T. Hartmann, T. A. Schulze, A. Zenesini, and S. Ospelkaus, *Formation of ultracold weakly bound dimers of bosonic  $^{23}\text{Na}^{39}\text{K}$* , Phys. Rev. A, **101**(4) 042704, 2020, DOI: 10.1103/PhysRevA.101.042704.
- [88] K. K. Voges, P. Gersema, T. Hartmann, T. A. Schulze, A. Zenesini, and S. Ospelkaus, *A pathway to ultracold bosonic  $^{23}\text{Na}^{39}\text{K}$  ground state molecules*, New Journal of Physics, **21**(12) 123034, 2019, DOI: 10.1088/1367-2630/ab5f31.
- [89] K. K. Voges, P. Gersema, M. Meyer zum Alten Borgloh, T. A. Schulze, T. Hartmann, A. Zenesini, and S. Ospelkaus, *Ultracold Gas of Bosonic  $^{23}\text{Na}^{39}\text{K}$  Ground-State Molecules*, Phys. Rev. Lett., **125**(8) 083401, 2020, DOI: 10.1103/PhysRevLett.125.083401.
- [90] M. W. Gempel, *Towards Ultracold Polar NaK Molecules and the Investigation of Dipolar Quantum Gases*, PhD thesis, 2016, DOI: <https://doi.org/10.15488/8680>.
- [91] T. A. Schulze, *Quantum degenerate mixtures of  $^{23}\text{Na}$ - $^{39}\text{K}$  and coherent transfer paths in NaK molecules*, PhD thesis, 2018, DOI: <https://doi.org/10.15488/3429>.
- [92] T. Hartmann, *An experiment apparatus for the production of ultracold bosonic dipolar ground state  $^{23}\text{Na}^{39}\text{K}$  molecules and Feshbach spectroscopy in a cold mixture of  $^{23}\text{Na}$  and  $^{39}\text{K}$* , PhD thesis, 2018, DOI: <https://doi.org/10.15488/4699>.
- [93] M. Gempel, T. Hartmann, T. Schulze, K. Voges, A. Zenesini, and S. Ospelkaus, *An adaptable two-lens high-resolution objective for single-site resolved imaging of atoms in optical lattices*, Review of Scientific Instruments, **90** 053201, 2019, DOI: 10.1063/1.5086539.
- [94] M. W. Gempel, T. Hartmann, T. A. Schulze, K. K. Voges, A. Zenesini, and S. Ospelkaus, *Versatile electric fields for the manipulation of ultracold NaK molecules*, New Journal of Physics, **18**(4) 045017, 2016, DOI: 10.1088/1367-2630/18/4/045017.
- [95] T. A. Schulze, T. Hartmann, K. K. Voges, M. W. Gempel, E. Tiemann, A. Zenesini, and S. Ospelkaus, *Feshbach spectroscopy and dual-species Bose-Einstein condensation of  $^{23}\text{Na}$ - $^{39}\text{K}$  mixtures*, Phys. Rev. A, **97**(2) 023623, 2018, DOI: 10.1103/PhysRevA.97.023623.
- [96] T. Hartmann, T. A. Schulze, K. K. Voges, P. Gersema, M. W. Gempel, E. Tiemann, A. Zenesini, and S. Ospelkaus, *Feshbach resonances in  $^{23}\text{Na}+^{39}\text{K}$  mixtures and refined molecular potentials for the NaK molecule*, Phys. Rev. A, **99**(3) 032711, 2019, DOI: 10.1103/PhysRevA.99.032711.
- [97] E. Tiemann, P. Gersema, K. K. Voges, T. Hartmann, A. Zenesini, and S. Ospelkaus, *Beyond Born-Oppenheimer approximation in ultracold atomic collisions*, Phys. Rev. Research, **2**(1) 013366, 2020, DOI: 10.1103/PhysRevResearch.2.013366.
- [98] Z. Fu, L. Huang, Z. Meng, P. Wang, L. Zhang, S. Zhang, H. Zhai, P. Zhang, and J. Zhang, *Production of Feshbach molecules induced by spin-orbit coupling in Fermi gases*, Nature Physics, **10**(2) 110–115, 2013, DOI: 10.1038/nphys2824.
- [99] K. Bergmann, H. Theuer, and B. W. Shore, *Coherent population transfer among quantum states of atoms and molecules*, Rev. Mod. Phys., **70**(3) 1003–1025, 1998, DOI: 10.1103/RevModPhys.70.1003.
- [100] L. Liu, D.-C. Zhang, H. Yang, Y.-X. Liu, J. Nan, J. Rui, B. Zhao, and J.-W. Pan, *Observation of Interference between Resonant and Detuned stirap in the Adiabatic Creation of  $^{23}\text{Na}^{40}\text{K}$  Molecules*, Phys. Rev. Lett., **122**(25) 253201, 2019, DOI: 10.1103/PhysRevLett.122.253201.
- [101] H. J. Carmichael, Springer-Verlag Berlin Heidelberg, 1999, DOI: 10.1007/978-3-662-03875-8.

- [102] M. Meyer zum Alten Borgloh.  
*Bachelor thesis*, 2018.
- [103] U. Gaubatz, P. Rudecki, S. Schiemann, and K. Bergmann, *Population transfer between molecular vibrational levels by stimulated Raman scattering with partially overlapping laser fields. A new concept and experimental results*, *The Journal of Chemical Physics*, **92**(9) 5363–5376, 1990, DOI: 10.1063/1.458514.
- [104] J. R. Kuklinski, U. Gaubatz, F. T. Hioe, and K. Bergmann, *Adiabatic population transfer in a three-level system driven by delayed laser pulses*, *Phys. Rev. A*, **40**(11) 6741–6744, 1989, DOI: 10.1103/PhysRevA.40.6741.
- [105] A. Kuhn, G. W. Coulston, G. Z. He, S. Schiemann, K. Bergmann, and W. S. Warren, *Population transfer by stimulated Raman scattering with delayed pulses using spectrally broad light*, *The Journal of Chemical Physics*, **96**(6) 4215–4223, 1992, DOI: 10.1063/1.462840.
- [106] L. P. Yatsenko, V. I. Romanenko, B. W. Shore, and K. Bergmann, *Stimulated Raman adiabatic passage with partially coherent laser fields*, *Phys. Rev. A*, **65**(4) 043409, 2002, DOI: 10.1103/PhysRevA.65.043409.
- [107] L. P. Yatsenko, B. W. Shore, and K. Bergmann, *Detrimental consequences of small rapid laser fluctuations on stimulated Raman adiabatic passage*, *Phys. Rev. A*, **89**(1) 013831, 2014, DOI: 10.1103/PhysRevA.89.013831.
- [108] T. A. Schulze, I. I. Temelkov, M. W. Gempel, T. Hartmann, H. Knöckel, S. Ospelkaus, and E. Tiemann, *Multichannel modeling and two-photon coherent transfer paths in NaK*, *Phys. Rev. A*, **88**(2) 023401, 2013, DOI: 10.1103/PhysRevA.88.023401.
- [109] I. Temelkov, H. Knöckel, A. Pashov, and E. Tiemann, *Molecular beam study of the  $a^3\Sigma^+$  state of NaK up to the dissociation limit*, *Phys. Rev. A*, **91**(3) 032512, 2015, DOI: 10.1103/PhysRevA.91.032512.
- [110] F. W. Bessel, *Darstellung der Untersuchungen und Maaßregeln, welche, in den Jahren 1835 bis 1838, durch die Einheit des Preußischen Längenmaaßes veranlasst worden sind*. Druckerei der Königlichen Akademie der Wissenschaften, 1839.
- [111] G. B. Airy, *On the flexure of a uniform bar supported by a number of equal pressures at equi-distant points*, *Monthly Notices of the Royal Astronomical Society*, **6** 143, 1845, DOI: 10.1093/mnras/6.12.143.
- [112] J. Wöhler.  
*Bachelor thesis*, 2012.
- [113] J. A. Armstrong, N. Bloembergen, J. Ducuing, and P. S. Pershan, *Interactions between Light Waves in a Nonlinear Dielectric*, *Phys. Rev.*, **127**(6) 1918–1939, 1962, DOI: 10.1103/PhysRev.127.1918.
- [114] G. D. Boyd and D. A. Kleinman, *Parametric Interaction of Focused Gaussian Light Beams*, *Journal of Applied Physics*, **39**(8) 3597–3639, 1968, DOI: 10.1063/1.1656831.
- [115] D. A. Kleinman, A. Ashkin, and G. D. Boyd, *Second-Harmonic Generation of Light by Focused Laser Beams*, *Phys. Rev.*, **145**(1) 338–379, 1966, DOI: 10.1103/PhysRev.145.338.
- [116] J. Mielke.  
*Master thesis*, 2016.

- [117] K. K. Voges.  
*Master thesis*, 2014.
- [118] J. E. M. Frits Zernike, *Applied Nonlinear Optics*. Courier Corporation, 2006.
- [119] R. W. Boyd, *Nonlinear Optics*. Academic Press, 2008.
- [120] G. J. Edwards and M. Lawrence, *A temperature-dependent dispersion equation for congruently grown lithium niobate*, *Optical and Quantum Electronics*, **16** 373–375, 1984.
- [121] R. Schiek and T. Pertsch, *Absolute measurement of the quadratic nonlinear susceptibility of lithium niobate in waveguides*, *Opt. Mater. Express*, **2**(2) 126–139, 2012, DOI: 10.1364/OME.2.000126.
- [122] M. M. Fejer, G. A. Magel, D. H. Jundt, and R. L. Byer, *Quasi-phase-matched second harmonic generation: tuning and tolerances*, *IEEE Journal of Quantum Electronics*, **28**(11) 2631–2654, 1992, DOI: 10.1109/3.161322.
- [123] J. R. Schwesyg, A. Markosyan, M. Falk, M. C. C. Kajiyama, D. H. Jundt, K. Buse, and M. M. Fejer, *Optical loss mechanisms in magnesium-doped lithium niobate crystals in the 300 to 2950 nm wavelength range*, *Advances in Optical Materials*, page AIThE3, 2011, DOI: 10.1364/AIOM.2011.AIThE3.
- [124] O. Gayer, Z. Sacks, E. Galun, and A. Arie, *Temperature and wavelength dependent refractive index equations for MgO-doped congruent and stoichiometric LiNbO<sub>3</sub>*, *Applied Physics B*, **91**, 2008, DOI: 10.1007/s00340-008-2998-2.
- [125] T. Kimura, K. Otsuka, and M. Saruwatari, *Spatial hole-burning effects in a Nd<sup>3+</sup>:YAG laser*, *IEEE Journal of Quantum Electronics*, **7**(6) 225–230, 1971, DOI: 10.1109/JQE.1971.1076746.
- [126] R. Le Targat, J.-J. Zondy, and P. Lemonde, *75%-Efficiency blue generation from an intracavity PPKTP frequency doubler*, *Optics Communications*, **247**(4) 471–481, 2005, DOI: <https://doi.org/10.1016/j.optcom.2004.11.081>.
- [127] R. V. Pound, *Electronic Frequency Stabilization of Microwave Oscillators*, *Review of Scientific Instruments*, **17**(11) 490–505, 1946, DOI: 10.1063/1.1770414.
- [128] R. W. P. Drever, J. L. Hall, J. Kowalski, F. V. and Hough, G. M. Ford, A. J. Munley, and H. Ward, *Laser phase and frequency stabilization using an optical resonator*, *Applied Physics B*, **31** 97–105, 1983, DOI: 10.1007/BF00702605.
- [129] E. D. Black, *An introduction to Pound-Drever-Hall laser frequency stabilization*, *American Journal of Physics*, **69**(1) 79–87, 2001, DOI: 10.1119/1.1286663.
- [130] Z. Fang, H. Cai, G. Chen, and R. Qu, *Single Frequency Semiconductor Lasers*. Springer, 2017.
- [131] J. Gerschmann.  
*Master thesis*, 2015.
- [132] M. J. Lawrence, B. Willke, M. E. Husman, E. K. Gustafson, and R. L. Byer, *Dynamic response of a Fabry–Perot interferometer*, *J. Opt. Soc. Am. B*, **16**(4) 523–532, 1999, DOI: 10.1364/JOSAB.16.000523.
- [133] K. Diedrich.  
*Bachelor thesis*, 2017.

- [134] S. H. Autler and C. H. Townes, *Stark Effect in Rapidly Varying Fields*, *Phys. Rev.*, **100**(2) 703–722, 1955, DOI: 10.1103/PhysRev.100.703.
- [135] M. Fleischhauer, A. Imamoglu, and J. P. Marangos, *Electromagnetically induced transparency: Optics in coherent media*, *Rev. Mod. Phys.*, **77**(2) 633–673, 2005, DOI: 10.1103/RevModPhys.77.633.
- [136] R. Ferber, E. A. Pazyuk, A. V. Stolyarov, A. Zaitsevskii, P. Kowalczyk, H. Chen, H. Wang, and W. C. Stwalley, *The  $c^3\Sigma$ ,  $b^3\Pi$  and  $a^3\Sigma$  states of NaK revisited*, *J. Chem. Phys.*, **112** 5740, 2000, DOI: 10.1063/1.481149.
- [137] M. Mayle, B. P. Ruzic, and J. L. Bohn, *Statistical aspects of ultracold resonant scattering*, *Phys. Rev. A*, **85**(6) 062712, 2012, DOI: 10.1103/PhysRevA.85.062712.
- [138] M. Mayle, G. Quémener, B. P. Ruzic, and J. L. Bohn, *Scattering of ultracold molecules in the highly resonant regime*, *Phys. Rev. A*, **87**(1) 012709, 2013, DOI: 10.1103/PhysRevA.87.012709.
- [139] H. Yang, D.-C. Zhang, L. Liu, Y.-X. Liu, J. Nan, B. Zhao, and J.-W. Pan, *Observation of magnetically tunable Feshbach resonances in ultracold  $^{23}\text{Na}^{40}\text{K} + ^{40}\text{K}$  collisions*, *Science*, **363**(6424) 261–264, 2019, DOI: 10.1126/science.aau5322.
- [140] M. Greiner, O. Mandel, T. Esslinger, H. T. W., and I. Bloch, *Quantum phase transition from a superfluid to a Mott insulator in a gas of ultracold atoms*, *Nature*, **415**(7) 39–44, 2002, DOI: 10.1038/415039a.
- [141] T. Lahaye, C. Menotti, L. Santos, M. Lewenstein, and T. Pfau, *The physics of dipolar bosonic quantum gases*, *Reports on Progress in Physics*, **72**(12) 126401, 2009, DOI: 10.1088/0034-4885/72/12/126401.
- [142] W. S. Bakr, J. I. Gillen, A. Peng, S. Fölling, and M. Greiner, *A quantum gas microscope for detecting single atoms in a Hubbard-regime optical lattice*, *Nature*, **462**(7269) 74–77, 2009, DOI: 10.1038/nature08482.

# Danksagung

Eine Doktorarbeit, insbesondere in unserem Fachgebiet, ist niemals das Werk einer einzelnen Person alleine. Und auch diese Arbeit ist stark von meinen Freunden und Kollegen geprägt. Ich möchte also an dieser Stelle schon einmal all denjenigen danken, die mir geholfen haben, diese Arbeit zu verwirklichen.

Zuallererst möchte ich natürlich meine Betreuerin, Silke, erwähnen. Sie hat mich in ihre Arbeitsgruppe aufgenommen und mir zugetraut am POLAR-Experiment zu arbeiten. Mit ihrer freundlichen und ruhigen Art hat sie auch in den kritischen Zeiten immer die passenden Worte gefunden und mit ihrem schnellen logischen Denkvermögen uns immer wieder auf die richtige Bahn gelenkt.

Auch Alessandro hat sich als hervorragender „Miniboss“ erwiesen. Zum einen besitzt er die Fähigkeit andere Leute zu ermutigen, selbstständig an neuen Projekten zu arbeiten und daran zu wachsen, zum anderen hat er mit seinem großartigen italienischen Physik- und Technikverständnis immer eine hilfreiche Idee gehabt (und sei es nur „try to change something drastically“- was erstaunlich oft geholfen hat...!).

Ebenso war Herr Tiemann eine Quelle unschätzbaren Wissens und wurde nie müde auch komplizierte Sachverhalten immer und immer wieder zu erklären.

Meinen direkten Arbeitskollegen gebührt hier besondere Aufmerksamkeit. Da gibt es die „Generation 1“ mit MATThias, TorBen, TorSten und KEVin und die „Generation 2“ mit Vasko/Gerke/Baby und Mr. Monday (a.k.a. Philipp und Jannis). Wir haben uns gegenseitig geholfen, wo immer es ging. Jeder einzelne von uns wäre wohl in seiner Arbeit untergegangen, wenn nicht jeder mit Rat und Tat den anderen unter die Arme gegriffen hätte. Dabei hat die Generation 1 die unglaubliche Herausforderung gemeistert, das POLAR-Experiment zu designen und aufzubauen. Die Generation 2 hat die gewaltige Aufgabe vollbracht, Macken und Kinderkrankheiten des Experiments auszumerzen und die Maschine immer weiterzuentwickeln und zu verbessern.

Matthias hat sich immer durch sein Elektronik- und Optikwissen und seine Lösungsorientiertheit und Zielstrebigkeit ausgezeichnet und war ein ständiger Pool an Wissen und Erfahrung. Torben war immer mit seinem offenen Ohr, seinen ehrlichen Worten und seinem Theoriewissen zu Hilfe. Torsten zeichnen seine Beharrlichkeit, sein ruhiges Wesen und seine klaren Denkstrukturen aus.

Philipp und Jannis haben dem Lab einen neuen Wind gebracht, mehr Manpower, neue Ideen und Gedankenansätze. Mit ihrer großen Motivation und freundlichen Gemütern haben sie die alten Lab-Rats wieder auf Schwung gebracht.

Später kamen dann noch unsere Youngsters („Generation 3“?) Jule, Jakob und Mara dazu, die mit ihrem Wissensdurst und ihrer Sorgfalt dem Experiment bestimmt noch ihren Stempel aufdrücken werden.

Nach all den gemeinsamen Stunden im Lab, bei den Gruppen- und Paperbesprechungen, den Reisen zu Konferenzen und Seminaren, den Meilensteinabenden, Spielerunden, Weihnachtsmarktbesuchen ... bin ich euch allen in guter Freundschaft verbunden. An euch

alle von POLAR: Vielen Dank für all eure unersetzbare Unterstützung und Hilfe!

Abseits der direkten Arbeitskollegen finden hier auch die „indirekten“ Arbeitskollegen ihren Platz, die SLOMOs (Maurice, Paul, Mariia, Timo und Mirco), die Spektroskopiker (Erik, Julia, Horst und Wuying) und die Ionen (Teresa, Malte, Jojo, Timko, AGP, Sebastian ...). Sie sind hervorragende Labornachbarn und Arbeitskollegen, mit denen man unglaublich viel Spaß hat. Gleichzeitig sind sie wahnsinnig hilfsbereit und helfen einem gerne aus misslichen Lagen. Im Laufe der Jahre habe ich mich mit sehr vielen von ihnen angefreundet. Dank an euch alle für die tolle Zeit und die viele Hilfe. Großen Dank an Mirco für seine immerwährende Genialität und Geduld (und die schlechten Wortspiele), an Teresa für ihre Freundschaft und Bodenständigkeit, an Paul für sein umfassendes Technik- und Regelwissen und an Erik fürs Eriksein (und den Laserschutz). Auch den anderen Mitarbeitern des Instituts möchte ich großen Dank aussprechen, insbesondere dem Sekretariat mit Elke, Katrin und Stephanie, und den Mitarbeitern der Feinmechanikwerkstatt, die mir mit ihrer Erfahrung viel Ärger vom Hals gehalten haben.

Auch meine Familie und meine Freunde außerhalb des Instituts möchte ich erwähnen, denn sie haben geholfen, dass ich mit dem Stress der letzten Jahre fertig geworden bin. Zuvorderst ist da Ilka, die sich immer um mich gekümmert hat. Auch Mareike, Lars und Steffi waren immer da und haben sich meine Nörgeleien angehört und mir Halt und Mut gespendet. Und dann sind da noch viele mehr, die mich in den letzten Jahren ständig begleitet und mir Freude und Kraft gegeben haben: Aylin, Justus, Batti, Christian, Max, Maike, Rieke, Isi, Nadine, Tatjana, ...

Zu guter Letzt, danke ich noch meiner Familie, auf die ich mich in Notzeiten immer verlassen konnte und immer können werde: Anna-Maria und Konrad, Barbara und Konrad, Tini und Con und natürlich Bärbel.

Ich danke euch allen aus tiefstem Herzen. Ohne eure Nähe und Geduld, Freundschaft und Treue wäre dies nicht möglich gewesen.

# Curriculum Vitae

## Personal Details

Name	Kai Konrad Voges
Date of birth	January 2, 1990
Place of birth	Gehrden
Current address	Sedanstraße 43 30161 Hannover

## Education

### Research

Apr. 2015 – Oct. 2020	Doctoral studies at Institute of Quantum Optics, University of Hanover, Germany Group: Prof. Dr. S. Ospelkaus
Jul. 2017 – Aug. 2017	Visiting Scientist at University of Innsbruck, Austria Group: Prof. Dr. H.-C. Nägerl
Dec. 2014 – Mar. 2015	Employee at Institute of Quantum Optics, University of Hanover, Germany Group: Prof. Dr. S. Ospelkaus

### Studies

Oct. 2012 – Nov. 2014	Master of Science (Physics) University of Hanover, Germany Thesis with Prof. Dr. C. Ospelkaus
Jan. 2013 – Jun. 2013	Master studies Chalmers University of Technology, Sweden
Oct. 2009 – Sep. 2012	Bachelor of Science (Physics) University of Hanover, Germany Thesis with Prof. Dr. K. Danzmann
Jun. 2009	Allgemeine Hochschulreife (Abitur), Otto-Hahn-Gymnasium Springe, Germany



# List of Publications (complete)

- **K.K.V.**, *Charakterisierung einer NIR-Kamera für den Aufbau eines Scatterometers*, Bachelor thesis, Leibniz Universität Hannover, 2012
- **K.K.V.**, *Lasersysteme für Einzel-Ionen-Experimente mit  $^9\text{Be}^+$* , Master thesis, Leibniz Universität Hannover, 2014
- M.W. Gempel, T. Schulze, T. Hartmann, **K.K.V.**, A. Zenesini, S. Ospelkaus, “*Versatile electric fields for the manipulation of ultracold NaK molecules*”, *New J. Phys.* **18** 045017, 2016
- T. Meiners, M. Niemann, A.-G. Paschke, M. Borchert, A. Idel, J. Mielke, **K.K.V.**, A. Bautista-Salvador, R. Lehnert, S. Ulmer and C. Ospelkaus, *Towards Sympathetic Laser Cooling and Detection of Single (Anti-)Protons*, *Proceedings of the Seventh Meeting on CPT and Lorentz Symmetry (CPT’16)*, 85-88, 2017
- T. Meiners, M. Niemann, A.-G. Paschke, J. Mielke, A. Idel, **K.K.V.**, M. Borchert, A. Bautista-Salvador, S. Ulmer, C. Ospelkaus, *Towards Quantum Logic Inspired Cooling and Detection for Single (Anti-)Protons*, *JPS Conf. Proc.* **18**, 011006, 2017
- T. Schulze, T. Hartmann, **K.K.V.**, M.W. Gempel, A. Zenesini, E. Tiemann, S. Ospelkaus, “*Feshbach spectroscopy and dual-species Bose-Einstein condensation of  $^{23}\text{Na}$ - $^{39}\text{K}$  mixtures*”, *Phys. Rev. A* **97** 023623, 2018
- T. Hartmann, T. Schulze, **K.K.V.**, P. Gersema, M.W. Gempel, E. Tiemann, A. Zenesini, S. Ospelkaus, “*Feshbach resonances in  $^{23}\text{Na}$ + $^{39}\text{K}$  mixtures and refined molecular potentials for the NaK molecule*”, *Phys. Rev. A* **99** 032711, 2019
- M.W. Gempel, T. Hartmann, T. Schulze, **K.K.V.**, A. Zenesini, S. Ospelkaus, “*An adaptable two-lens high-resolution objective for single-site resolved imaging of atoms in optical lattices*”, *Rev. Sci. Instrum.* **90**, 053201, 2019
- **K.K.V.**, P. Gersema, T. Hartmann, T. Schulze, A. Zenesini, S. Ospelkaus, “*A pathway to ultracold bosonic  $^{23}\text{Na}$ - $^{39}\text{K}$  ground state molecules*”, *New J. Phys.* **21** 123034, 2019

- E. Tiemann, P. Gersema, **K.K.V.**, T. Hartmann, A. Zenesini, S. Ospelkaus, “*Beyond Born-Oppenheimer approximation in ultracold atomic collisions*”, Phys. Rev. Res. **2** 013366, 2020
- **K.K.V.**, P. Gersema, T. Hartmann, T. Schulze, A. Zenesini, S. Ospelkaus, “*Formation of ultracold weakly bound dimers of bosonic  $^{23}\text{Na}^{39}\text{K}$* ”, Phys. Rev. A **101** 042704, 2020
- **K.K.V.**, P. Gersema, M. Meyer zum Alten Borgloh, T. Schulze, T. Hartmann, A. Zenesini, S. Ospelkaus, “*Ultracold Gas of Bosonic  $^{23}\text{Na}^{39}\text{K}$  Ground-State Molecules*”, Phys. Rev. Lett. **125** 083401, 2020